LASER-INDUCED FLUORESCENCE SPECTROSCOPY AS A NON-DESTRUCTIVE TECHNIQUE FOR MINERAL AND ORGANIC DETECTION IN CARBONACEOUS CHONDRITES

ELIZABETH A. LYMER

A THESIS SUBMITTED TO THE FACULTY OF GRADUATE STUDIES IN PARTIAL FULFILLMENT OF THE REQUIREMENTS FOR THE DEGREE OF MASTERS OF SCIENCE

GRADUATE PROGRAM IN EARTH AND SPACE SCIENCE
YORK UNIVERSITY
TORONTO, ONTARIO

November, 2017

© Elizabeth A. Lymer, 2017

Abstract

With continuing interest in asteroid sample return and remote sensing missions, the need for non-destructive, bulk composition and organic detection and analyses is paramount. Laser-induced fluorescence (LIF) spectroscopy is a time efficient, non-destructive technique that is capable of identifying mineral and organic constituents within a sample. To investigate the capabilities of a LIF instrument for an asteroid mission, LIF was used to collect maps of millimetre-sized features within carbonaceous chondrite samples and conduct point analyses. A Raman spectrometer and a scanning electron microscope (SEM) with electron dispersive spectroscopy (EDS) capabilities were used to collect maps of the same features for comparison. The Royal Ontario Museum (ROM) provided four carbonaceous chondrite samples for analysis: Allende CV3, Murchison CM2, DGR-034, and DGR-035. Samples DGR-034 and DGR-035 were classified during this study and full petrographic and geochemical information are discussed in this work. The purpose of this work was to investigate the applicability and quality of LIF for mapping millimetre-sized features in asteroid analog material. Chondrules and calcium-aluminum-rich inclusions were visible in three out of four spectral images, and many minerals were identified using time-resolved LIF data. Minerals identified using LIF, were also identified using Raman spectroscopy, and electron dispersive X-ray spectroscopy (EDS). LIF spectroscopy is an ideal candidate for time-efficient mapping or point analyses for carbonaceous chondrites. This technique could be valuable for future asteroid sample return or *in-situ* missions where non-destructive mineral and organic detection techniques are needed.

Acknowledgments

I would like to acknowledge my supervisor Dr. Michael Daly for supporting my research and building my personal and professional confidence. This thesis would not be possible without Dr. Daly's continual support and encouragement. Thank you Dr. Kim Tait, Veronica DiCecco, Ian Nicklin, and Brendt Hyde at the ROM for their contributions to this project. Special thanks to Dr. Evan Eshelman for laying the foundations for this work and his daily lunch tutorials about Raman, LIF and physics. I would also like to thank my colleagues and friends at York. I would finally like to thank my family, whose support in all aspects of my life that I am eternally grateful for.

Contents

Abstract ii

Acknowledgments iii

Table of Contents vi

List of Tables vii

List of Figures x

1 Introduction 1

1.1 Study objectives . . . 1

2 Background 2

2.1 Chondritic asteroids and carbonaceous chondrites . . . 2

2.2 Meteorite classification . . . 3

2.3 Laser-induced fluorescence spectroscopy . . . 4

2.4 Raman spectroscopy . . . 5

3 Experimental apparatuses 8

3.1 Petrographic Microscope . . . 8

3.2 Electron Probe Micro-analyzer . . . 8

3.3 Raman Spectrometer . . . 9

3.4 Scanning electron microscope . . . 9

3.5 UV laser-induced fluorescence spectrometer setup . . . 10

3.5.1 Instrument optimization . . . 10

3.5.2 Spot size and power . . . 12

4 Samples 13

4.1 Monomineralic samples . . . 13

4.2 Carbonaceous chondrite samples . . . 13

4.3 Sample preparation . . . 13

4.4 Meteorite slab descriptions . . . 14

4.5 Introduction to classification of meteorites . . . 14

4.6 Methods for classification . . . 14

4.7 Classification of ROM sample DGR-034 . . . 18

4.7.1 Collection History . . . 18

4.7.2 Hand Sample Examination . . . 18

4.7.3 Petrography . . . 18

4.7.4 Chondrules . . . 18

4.7.5 Calcium-aluminum-rich-inclusions . . . 21

4.7.6 Matrix . . . 21

4.7.7 Shock features . . . 21

4.7.8 Weathering features . . . 22
4.7.9 Electron probe micro-analysis geochemistry . . . 22
4.7.10 Discussion and Classification . . . 24
4.7.11 Conclusion . . . 25
4.8 Classification of ROM sample DGR-035 . . . 27
4.8.1 Collection History . . . 27
4.8.2 Hand Sample Examination . . . 27
4.8.3 Petrography . . . 27
4.8.4 Chondrules . . . 27
4.8.5 Calcium-aluminum-rich inclusions . . . 28
4.8.6 Matrix . . . 28
4.8.7 Shock features . . . 28
4.8.8 Weathering features . . . 30
4.8.9 EPMA geochemistry . . . 30
4.8.10 Discussion and Classification . . . 33
4.8.11 Conclusion . . . 34

5 Methodology and experimental techniques **35**
5.1 Laser-induced fluorescence (LIF) spectroscopy . . . 36
5.1.1 Acquisition techniques for single spectra . . . 37
5.1.2 Time resolved fluorescence . . . 37
5.1.3 LIF 2D mapping techniques . . . 37
5.1.4 LIF mapping analyses . . . 38
5.1.5 LIF monomineralic database spectra . . . 38
5.2 Raman Spectroscopy . . . 39
5.2.1 Raman 2D mapping techniques . . . 39
5.2.2 Raman spectral analyses . . . 39
5.3 Scanning electron microscope (SEM) . . . 39
5.3.1 Back-scattered electron images . . . 39
5.3.2 Electron dispersive spectroscopy (EDS) mapping . . . 40
5.3.3 EDS point analyses . . . 40

6 Results **41**
6.1 EDS maps and quantification results . . . 41
6.2 Raman spectroscopy maps and spectral analyses . . . 49
6.3 LIF mineral database . . . 58
6.4 LIF 2D maps, time-resolved fluorescence and spectral analyses . . . 62
6.4.1 Allende chondrule: LIF maps, individual, and time-resolved spectra . . . 62
6.4.2 Allende CAI: LIF maps, idividual, and time-resolved spectra . . . 65
6.4.3 Murchison chondrule: LIF maps, idividual, and time-resolved spectra . . . 68
6.4.4 Murchison CAI: LIF maps, idividual, and time-resolved spectra . . . 71
6.4.5 DGR-035 chondrule: LIF maps, idividual, and time-resolved spectra . . . 74
6.4.6 DGR-035 CAI: LIF maps, idividual, and time-resolved spectra . . . 77
6.4.7 DGR-034 chondrule: LIF maps, idividual, and time-resolved spectra . . . 80

6.4.8 DGR-034 CAI: LIF maps, idividual, and time-resolved spectra . . . 81
6.5 Overview of spectral maps . . . 82
6.5.1 Allende chondrule maps . . . 82
6.5.2 Allende CAI maps . . . 83
6.5.3 Murchison chondrule maps . . . 84
6.5.4 Murchison CAI maps . . . 85
6.5.5 DGR-035 chondrule maps . . . 86
6.5.6 DGR-035 CAI maps . . . 87
6.5.7 DGR-034 chondrule maps . . . 88
6.5.8 DGR-034 CAI maps . . . 89
6.6 Mineral ID result summary . . . 90

7 Discussion **91**
7.1 Characterization . . . 91
7.2 Spectral investigation . . . 91
7.3 Database creation . . . 92
7.4 Identification . . . 93
7.5 Fluorescence quenching . . . 93
7.6 Raman and LIF as a combined instrument . . . 94

8 Conclusions **95**

9 Future work **96**

References **97**

Appendices **101**
Appendix A: Amino acids database . . . 101
Appendix B: Modal abundance determinations using Olympus STREAM . . . 104
Appendix C: Chondrule and CAI measurements for DGR-034 and DGR-035 . . . 106
Appendix D: Electron probe micro-analysis standards and calibration . . . 111

List of Tables

1 Monomineralic samples used to create LIF mineral database from the ROM. 13
2 EPMA results for olivine, pyroxene and plagioclase in DGR-034 24
3 EPMA results for olivine, pyroxene and plagioclase in DGR-035 33
4 EDS mineral ID for Allende chondrule 42
5 EDS mineral ID for Allende CAI 42
6 EDS mineral ID for Murchison chondrule 43
7 EDS mineral ID for Murchison CAI 44
8 EDS mineral ID for DGR-035 chondrule 45
9 EDS mineral ID for DGR-035 CAI 46
10 EDS mineral ID for DGR-034 chondrule 47
11 EDS mineral ID for DGR-034 CAI 48
12 Mineral identification from EDS, Raman and LIF maps 90
13 Amino acids pelletized for LIF amino acids database. 101
14 DGR-034 matrix versus features quantification 104
15 DGR-035 matrix versus features quantification 104
16 Chondrule measurements in DGR-034 108
17 CAI measurements in DGR-034 109
18 CAI measurements in DGR-035 109
19 CAI measurements in DGR-035 110
20 EPMA standards for olivine 111
21 EPMA standards for pyroxene 112
22 EPMA standards for plagioclase 112

List of Figures

1 Fluorescence emission . . . 5
2 Time-resolved fluorescence demonstration. . . . 6
3 Raman vs. Rayleigh scattering . . . 6
4 York University's Olympus BX-53P petrographic microscope. . . . 8
5 Horiba LabRAM Aramis micro-Raman instrument at the ROM. . . . 9
6 York University's Tescan VEGA3 scanning electron microscope. . . . 10
7 Simplified schematic of UV Raman/LIF breadboard setup at York University. . . . 11
8 Beam size measurement . . . 12
9 Cut sections of carbonaceous chondrite samples from the ROM. . . . 14
10 Petrologic types and their relationship to metamorphic and aqueous alteration levels . . . 15
11 Meteorite Classes . . . 16
12 Parameters determining petrographic type of chondrites . . . 17
13 Hand sample of DGR-034 . . . 18
14 DGR-034 thin section images . . . 19
15 DGR-034 chondrule images . . . 20
16 DGR-034 chondrules with dusty rim and inclusions . . . 21
17 DGR-034 CAI images . . . 22
18 DGR-034 opaque matrix images . . . 22
19 Enstatite, ferrosilite, and wollastonite end member plot for pyroxene in DGR-034 . . . 23
20 Albite, anorthite and orthoclase end member plot for feldspar in DGR-034 . . . 24
21 Flow chart of meteorite classification for DGR-034 and DGR-035 . . . 26
22 Hand sample of DGR-035 . . . 27
23 DGR-035 thin section images . . . 28
24 DGR-035 chondrule images . . . 29
25 DGR-035 chondrule images with poorly defined rim and inclusions . . . 30
26 DGR-035 CAI images . . . 30
27 DGR-035 matrix images . . . 31
28 Shock feature in DGR-035 . . . 31
29 Enstatite, ferrosilite, and wollastonite end member plot for pyroxene in DGR-035. . . . 32
30 Albite, Anorthite and Orthoclase end member plot for feldspar in DGR-035. . . . 32
31 Four-step method for completion of study. . . . 35
32 Relative intensity correction factor . . . 36
33 EDS spectral map with mineral labels for Allende chondrule . . . 41
34 EDS spectral map with mineral labels for Allende CAI . . . 42
35 EDS spectral map with mineral labels for Murchison chondrule . . . 43
36 EDS spectral map with mineral labels for Murchison CAI . . . 44
37 EDS spectral map with mineral labels for DGR-035 chondrule . . . 45
38 EDS spectral map with mineral labels for DGR-035 CAI . . . 46
39 EDS spectral map with mineral labels for DGR-035 chondrule . . . 47
40 EDS spectral map with mineral labels for DGR-034 CAI . . . 48
41 Raman Allende chondrule . . . 50

42 Raman Allende cCAI . . . 51
43 Raman Murchison chondrule . . . 52
44 Raman Murchison CAI . . . 53
45 Raman DGR-035 chondrule . . . 54
46 Raman DGR-035 CAI . . . 55
47 Raman DGR-034 chondrule . . . 56
48 Raman DGR-034 CAI . . . 57
49 Mineral database: long fluorescence (100 ns gate width) spectra. . . . 59
50 Mineral database: time-resolved fluorescence surface plots. . . . 60
51 Mineral database: time-resolved fluorescence contour plots. . . . 61
52 Allende chondrule LIF 2D map . . . 62
53 Allende chondrule LIF point of interest P1464 . . . 63
54 Allende chondrule LIF point of interest P943 . . . 63
55 Allende chondrule LIF point of interest P1464 . . . 63
56 Allende chondrule LIF P112 mineral ID . . . 64
57 Allende chondrule LIF P943 mineral ID . . . 64
58 Allende chondrule LIF P1464 mineral ID . . . 64
59 Allende CAI LIF 2D map . . . 65
60 Allende CAI LIF point of interest 1333 . . . 66
61 Allende CAI LIF point of interest 1494 . . . 66
62 Allende chondrule LIF P1333 mineral ID . . . 66
63 Allende chondrule LIF P1494 mineral ID . . . 67
64 Murchison chondrule LIF 2D map . . . 68
65 Murchison chondrule LIF point of interest P673 . . . 69
66 Murchison chondrule LIF point of interest P473 . . . 69
67 Murchison chondrule LIF point of interest P813 . . . 69
68 Murchison chondrule LIF P673 mineral ID . . . 70
69 Murchison chondrule LIF P473 mineral ID . . . 70
70 Murchison chondrule LIF P813 mineral ID . . . 70
71 Murchison CAI LIF 2D map . . . 71
72 Murchison CAI LIF point of interest 250 . . . 72
73 Murchison CAI LIF point of interest P241 . . . 72
74 Murchison CAI LIF point of interest P231 . . . 72
75 Murchison CAI LIF P250 mineral ID . . . 73
76 Murchison CAI LIF P241 mineral ID . . . 73
77 Murchison CAI LIF P231 mineral ID . . . 73
78 DGR-035 chondrule LIF 2D map . . . 74
79 DGR-035 chondrule LIF point of interest P990 . . . 75
80 DGR-035 chondrule LIF point of interest P1308 . . . 75
81 DGR-035 chondrule LIF P990 mineral ID . . . 75
82 DGR-035 chondrule LIF P1308 mineral ID . . . 76
83 DGR-035 CAI LIF 2D map . . . 77
84 DGR-035 CAI LIF point of interest P170 . . . 78

85 DGR-035 CAI LIF point of interest P252 . . . 78
86 DGR-035 CAI LIF point of interest P325 . . . 78
87 DGR-035 CAI LIF P170 mineral ID . . . 79
88 DGR-035 CAI LIF P252 mineral ID . . . 79
89 DGR-035 CAI LIF P325 mineral ID . . . 79
90 DGR-034 chondrule LIF 2D map . . . 80
91 DGR-034 CAI LIF 2D map . . . 81
92 Spectral map acquisitions for Allende chondrule. . . . 82
93 Spectral map acquisitions for Allende CAI. . . . 83
94 Spectral map acquisitions for a Murchison chondrule. . . . 84
95 Spectral map acquisitions for a Murchison CAI. . . . 85
96 Spectral map acquisitions for a DGR-035 chondrule. . . . 86
97 Spectral map acquisitions for a DGR-035 CAI. . . . 87
98 Spectral map acquisitions for a DGR-034 chondrule. . . . 88
99 Spectral map acquisitions for a DGR-034 CAI. . . . 89
100 LIF amino acid spectra . . . 102
101 Time-resolved LIF of amino acids . . . 103
102 DGR-034 modal abundance of matrix versus features . . . 105
103 DGR-035 modal abundance of matrix versus features . . . 105
104 Chondrules measured in DGR-034 . . . 106
105 CAIs measured in DGR-034 . . . 106
106 Chondrules measured in DGR-035 . . . 107
107 CAIs measured in DGR-035 . . . 107
108 Olivine weight percent oxide point results from EPMA . . . 113
109 Olivine point precision results from EPMA . . . 114
110 Olivine limit of detection results from EPMA . . . 115
111 Pyroxene weight percent oxide point results from EPMA . . . 116
112 Pyroxene point precision results from EPMA . . . 117
113 Pyroxene limit of detection results from EPMA . . . 118
114 Plagioclase weight percent oxide point results from EPMA . . . 119
115 Plagioclase point precision results from EPMA . . . 120
116 Plagioclase limit of detection results from EPMA . . . 121
117 Olivine end member (forsterite-fayalite) results . . . 121
118 Orthopyroxene ferrosilite-enstatite-wollastonite results . . . 121
119 Clinopyroxene clinoferrosilite-clinoenstatite-wollastonite results . . . 122
120 Plagioclase ende member (anorthite-albite-orthoclase) results . . . 122

1 Introduction

York University's standoff UV Raman and laser-induced fluorescence (LIF) spectrometer enables non-destructive analyses of rock, mineral, and organic samples. With asteroid missions gaining popularity amongst international space agencies (eg. OSIRIS-REx [Lauretta et al., 2017], Hayabusa [Fujiwara et al., 2006] and Hayabusa 2 [Tsuda et al., 2013]) due to their potential insights into the history of our solar system, it will continue to be a challenge to assemble an instrument suite that can provide the most amount of useful information *in-situ*. LIF spectroscopy has the potential to identify mineralogic and organic constituents within a sample, and spatially map where the features are within the sample in a non-destructive way. LIF spectroscopy has been proven useful for Mars relevant material and can detect organics relevant to astrobiology in such work as Eshelman [Eshelman, 2016], Hamilton [Hamilton, 2016], and others. In this study, Raman spectroscopy and laser-induced fluorescence spectroscopy will be used in combination to collect a series of high-resolution maps of millimetre-sized chondrules, Calcium-Aluminum-rich Inclusions (CAIs) and some surrounding matrix within carbonaceous chondrites. Current practice to obtain petrographic information from a sample is to cut the sample into thin and polished sections for use in petrographic microscopes, scanning electron microscopes, electron microprobe analyses, etc. These instruments provide excellent geochemical and petrographic data, however they do require or inflict some minor destruction of a sample or are not practical for *in-situ* analysis. This study is focused on fundamental research of the applicability and quality of UV Raman and LIF for in mapping millimetre-sized features on asteroid-like material. This research has the potential to aid in the non-destructive analysis of samples from asteroid sample return missions such as OSIRIS-REx, and other future remote sensing missions to asteroids. LIF could be used as a tool to aid in the curation of material returned from asteroid missions by providing stand-off, non-destructive, mineral and organic detection. This technique could help determine areas of interest, areas of higher organic content within the samples, which samples should be preserved, which samples should be studied immediately, and which techniques or instruments should be used for analyses based on the resulting constituents.

The purpose of this study was to determine the capabilities and limitations of LIF to be used as a flight instrument or non-destructive laboratory instrument for sample return missions. The effectiveness of LIF as a mineral and organic carbon detection tool is tested using carbonaceous chondrites as asteroid analog material. 2D compositional LIF maps were obtained and compared to more established spectral identification techniques such as Raman spectroscopy, and electron-dispersive X-ray spectroscopy (EDS) on millimetre-sized features within the carbonaceous chondrites.

1.1 Study objectives

To determine the capabilities and limitations of a laser-induced fluorescence spectrometer to be used as a flight or non-destructive laboratory instrument for sample return missions, a five step systematic approach was used. The objectives for this study were to characterize carbonaceous chondrite samples, investigate millimetre-sized features within those samples using Raman, LIF and EDS, create a LIF spectral database to identify mineral and organic constituents within the features, and finally, compare the value of a LIF instrument to that of Raman and EDS for asteroid studies.

2 Background

2.1 Chondritic asteroids and carbonaceous chondrites

Chondrites are optimal analog material to test prospective non-destructive flight or laboratory instruments for robotic missions to asteroids, and to prepare for the analysis of asteroid sample returns. This is due to their relative abundance on Earth and their distinctive relationship with chondritic asteroids. Chondritic asteroids are of special interest because they are believed to contain some of the oldest and most primitive material in our solar system. This type of asteroid has a chemical composition that is similar to that of the sun's photosphere, suggesting they have not changed in composition from the formation of our solar system [Weisberg et al., 2006]. It is believed that the material in chondritic asteroids was formed in primitive bodies which are precursors to the planets as we know them today. As such, chondritic asteroids offer a looking glass into the beginning stages of our solar system [Hutchison, 2004, Michel et al., 2015].

Our solar system is thought to have formed shortly after the formation of the sun. At the beginning stages of our solar system, dust and gas began to condense and primitive bodies called planetismals began accreting material through gravitational attraction. As these planetismals grew large, heat created through compression in the core along with impaction, began melting accreted material. Melting enables differentiation, a process which separates metals from silicates, creating dense cores and outer layers of lighter rock. Chondrites are leftover building materials of planetismals. Because this material did not become part of a large body, it has not undergone any major melting or differentiation and is thought to retain the characteristics of the material that existed at the beginning stages of our solar system formation.

The defining feature of chondrites are millimetre-sized, spherical, mineral globules called chondrules. There are many theories surrounding how chondrules are formed, Johnson et al. [2015] suggests chondrules are formed primarily through impact jetting, a process where protoplanetary impacts occur, creating enough energy to melt and eject material back into space.

Chondrites are separated into three groups: ordinary, carbonaceous and enstatite. Carbonaceous, or C-type asteroids, are a type of chondritic asteroid of particular interest to the scientific community currently because they have been found to contain organic carbon and water [Campins et al., 2010, Becker and Bunch, 1997, Oró et al., 1971, Wing and Bada, 1991]. C-type asteroids could help decipher the evolution of our solar system and of Earth, but may also be the key to understanding how the essential building blocks of life such as water and organic carbon, evolved through time and formed on Earth. Carbonaceous asteroids have been studied in depth using remote sensing tools due to their organic content and their relative abundance in proximity to Earth. Bulk composition can be determined using telescopic spectroscopy, however fine-scale mineralogy and composition cannot be easily determined. Efforts have been made to obtain mafic (high magnesium and iron content) mineral abundances on small bodies using visible or near inrared spectra of olivine and pyroxene with some success. [Reddy et al., 2015].

The most accessible way for Earth-bound researchers to study the fine scale mineralogy and composition of carbonceous asteroids is by using carbonaceous meteorites, pieces of carbonaceous asteroids that fell through Earth's atmosphere and were collected on the surface of Earth. Chemical and petrographic analysis using

instruments not yet capable of space flight can be completed on Earth, and inferences can then be made about different chondritic asteroids in our solar system.

Some carbonaceous chondritic meteorites such as Murchison and Allende have been found to contain non-terrestrial amino acids, which could provide insight into how life started on Earth [Wing and Bada, 1991, Becker and Bunch, 1997]. Amino acids are essential in the formation of life, and are located on carbonaceous asteroids with the other foundational elements of life such as carbon, nitrogen and water. These carbonaceous asteroids play a key role in understanding how complex life began and evolved, by providing a unique insight into preserved environments with all the correct ingredients. The search for the genesis of life on earth is ongoing through new missions such as OSIRIS-REx and Hyabusa-2 [Lauretta et al., 2017, Tsuda et al., 2013], that are collecting samples from chondritic asteroids and returning the samples back to Earth.

Carbonaceous chondritic meteorites (aka carbonaceous chondrites) contain the oldest features dated in our solar system, calcium-aluminum-rich inclusions (CAIs) at 4.567 Ga [Hutchison, 2004]. These features are amoeboid-shaped and contain fine-grained silicates that are rich in calcium and aluminum. millimetre-sized chondrules and CAIs are the defining features of carbonaceous chondrites and are set in a fine-grained, dark matrix that often contains carbon and silicates. Carbonaceous chondrites are separated into eight groups: CI, CM, CV, CK, CO, CR, CH, and CB. The 'C' represents the carbonaceous class, while the second letter represents a meteorite in which the group is based on. For example, 'CV' represents carbonaceous Vigarano-like after the meteorite 'Vigarano' [Weisberg et al., 2006]. Meteorites are placed into the eight different classes based on petrologic, and geochemical characteristics such as chondrule, matrix, and CAI abundance and size.

It is valuable to study and understand chondritic meteorites due to their relationship with C-type asteroids, and the importance that C-type asteroids may have in the understanding of the formation of our solar system and life on Earth. Because of their relative abundance on Earth, Chondrites are an optimal analog material to experiment and test the performance and characteristics of prospective non-destructive flight or laboratory instruments for asteroid missions, and to prepare for the analysis of asteroid sample returns from missions such as OSIRIS-REx and Hyabusa-2.

2.2 Meteorite classification

Meteorites are pieces of extra-terrestrial bodies such as asteroids, comets, or other planets that have traveled through our atmosphere and impacted on the surface of Earth. There are two ways meteorites are collected: as falls, or finds. A 'fall' is when a meteorite was observed falling through the atmosphere and collected shortly after impact. A 'find' is when meteorites have been found on the surface of Earth without being observed prior to their find. Meteorite falls are particularly interesting because the time and location of impact are known, and collection of samples usually happens very quickly after impaction, leading to minimal terrestrial weathering and timely preservation resulting in more pristine samples. Visible petrographic differences among meteorites lead to the idea of different types, or classifications, of meteorites. Meteorites are classified into three major types: chondrites, primitive achondrites, and achondrites. Chondrites are undifferentiated, meaning they have not undergone significant melting or alteration from their original composition [Weisberg et al., 2006]. Chondrites, considered to be the most primitive type of meteorite, contain pre-solar grains and calcium-aluminum-rich inclusions (CAIs), which have been dated as the oldest material in our solar system (4.567 Byr) thus far [Connelly et al., 2012]. Achondrites are metoerites that have come

from parent bodies that have undergone differentiation such as in planets, moons or large asteroids. Primitive achondrites have undergone partial differentiation from bodies that had just started differentiating or were undergoing local heating events. Primitive achondrites look as if they have been differentiated from achondritic bodies because of their brecciated nature, but when their oxygen isotope ratios are analyzed, they seem so be similar to that of carbonaceous chondrites [Weisberg et al., 2006].

Meteorites are assigned types and classes based on petrologic, chemical and isotopic characteristics such as: chondrule abundance and average diameter, CAI abundance, matrix composition and grain size, oxygen isotope ratio, olivine composition (fayalite number) etc. When a meteorite is classified and assigned a 'type' the short hand (i.e. 'CV') portrays a reasonable amount of information to the reader about the defining characteristics of the sample. More information on the sample is provided in nomenclature by determining the level of shock and weathering. The amount of shock a meteorite has undergone may create discrepancies from typical composition of a group, and is therefore informative. For example, when a sample has undergone extreme pressure change, the mineral plagioclase may convert to maskelynite. A sample can be assigned a shock stage from S1 - S6 based on characteristics visible using a petrographic microscope [Scott et al., 1992]. Terrestrial weathering can have large effects on the geochemistry of a sample by aqueous alteration and the mobilization of trace elements. Terrestrial weathering creates oxidation of the meteorites and may infill cracks with secondary alteration minerals such as carbonates. Each meteorite can be assigned a weathering scale from W1 - W6 [Wlotzka, 1993].

The classification scheme for meteorites may be convoluted, but is extremely important for establishing language and standardization for scientific meteorite studies. The classification scheme for chondrites, pioneiered by Van Schmus [1969], was created in hopes of understanding genetic relationships and to determining parent bodies amongst chondritic groups [Weisberg et al., 2006]. Once a meteorite is classified, further studies can be preformed. The classification of these samples will provide fundamental information on the geochemistry, petrology and texture. In this work, two meteorite samples from the Royal Ontario Museum will be classified before further LIF, Raman and EDS analyses are preformed.

2.3 Laser-induced fluorescence spectroscopy

Laser-induced fluorescence (LIF) has been incorporated into a UV Raman instrument at the Planetary Exploration Instrumentation Laboratory at York University [Eshelman, 2016]. Raman spectroscopy often results in fluorescence emissions, which are unwanted and overwhelm Raman spectra. Incorporating fluorescence spectroscopy into a preexisting Raman system is simple, only requiring a change of diffraction grating and gating capabilities within the camera. LIF can be used as a non-destructive tool for detecting minerals and organics in materials. It has the advantage of being even more time efficient than Raman spectroscopy, allowing spectra to be acquired in a couple of seconds. Fluorescence data compliments UV Raman spectra well, which does not have a large fluorescence component, and green Raman after fluorescence has been subtracted. The fluorescence component from these data is useful in its own right for identifying minerals and organics using known fluorescence decay curves. Fluorescence lifetime, shape overtime, and wavelength spread may provide a fingerprint for different organic compounds [Eshelman, 2016].
Fluorescence emission is produced when a photon excites an electron within a molecule to some vibrational level in a higher electronic state (Figure 1). When the electron settles back towards ground state, a photon

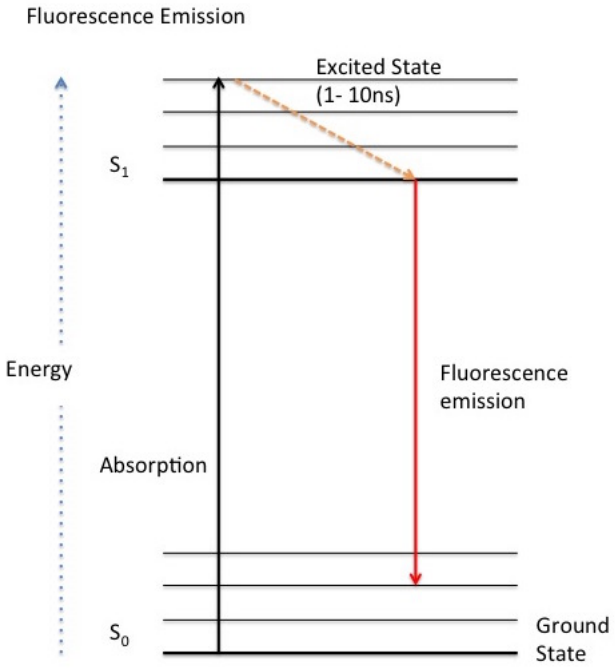


Figure 1: Fluorescence emission diagram.

will be emitted at specific wavelengths, different from the excitation wavelength [Eshelman et al., 2015]. UV excitation is particularly good for obtaining organic fluorescence because UV energies are between the highest occupied molecular orbital (HOMO) and the lowest unoccupied molecular orbital (LUMO) for many organic compounds, which is required to create fluorescence spectra [Sauer et al., 2011]. The fluorescence window we have used is between 268 nm and 530 nm when using a 300 lines/mm grating. With UV excitation, we can collect Raman and fluorescence data because the Raman spectrum lies very close to the laser line (266 nm), whereas fluorescence occurs mainly above 270 nm and longer wavelengths. Therefore fluorescence can be energetically separated from Raman spectra, allowing the two components to be viewed separately to better identify organics within a sample [Skulinova et al., 2014, Eshelman et al., 2014].
Fluorescence is produced over several nanoseconds to microseconds, which enables time-resolved fluorescence analysis (Figure 2). Fluorescence lifetimes can be very useful for determining the constituents of the sample because decay curves for most organics are well quantified. Fast fluorescence, on the order of $<$10 ns, can be indicative of organic material; whereas long fluorescence on the order of 1 µs, can be indicative of mineral fluorescence or impurities [Eshelman et al., 2015].

2.4 Raman spectroscopy

Raman spectroscopy is a time efficient, non-destructive tool used to detect and identify mineral and organic constituents in a material. The Planetary Exploration Instrumentation Laboratory's Raman instrument, which incorporates the UV LIF setup, mainly operates at 266 nm (UV), with 532 nm capabilities. For this study Raman spectroscopy was completed at the Royal Ontario Museum using a Horiba LabRAM Aramis micro-Raman spectrometer with an excitation wavelength of 532 nm. UV Raman spectroscopy creates minimal fluorescence when collecting mineral and organic spectra, compared to visible and near infrared

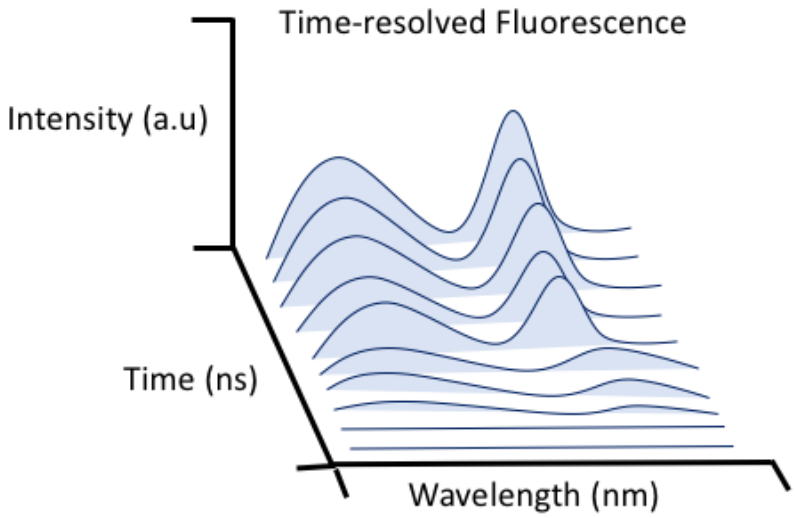


Figure 2: Time-resolved fluorescence demonstration.

wavelengths [Eshelman, 2016]. This is beneficial for cases where the fluorescence component of a sample is more intense than the Raman spectrum, which can occur when analyzing minerals with longer wavelengths, making identification with Raman spectra difficult. However, the Raman spectrometer at the ROM has a smaller spot size, creating higher resolution maps and Raman spectra. Spectral images with clear peaks are crucial for identifying minerals and organics within a sample.

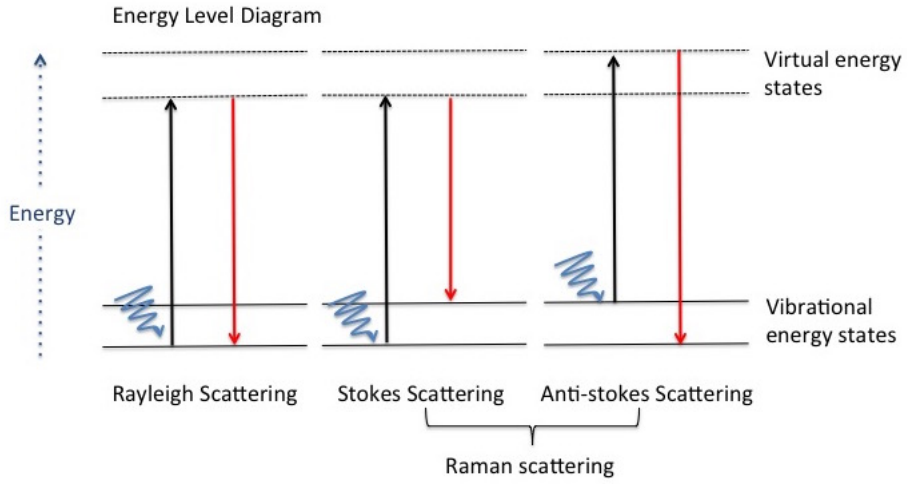


Figure 3: Physical difference between Rayleigh scattering and Raman scattering within molecules.

Raman spectroscopy takes advantage of the physical characteristics of molecular bonds to create a unique spectral signature for each compound. The signature is a compilation of the measured wavelengths of photons that are emitted during Raman scattering. Raman scattering occurs when a molecule is excited by a laser source, which causes vibration within the molecule (Figure 3). This vibration leads to the inelastic scattering of a photon, which has a shift in frequency due to change in energy in the molecule [Long, 2002].

In this study, we view stokes scattering (Figure 3), where the resulting photons have a lower energy (longer wavelength) than the incident photon (266 nm). Raman spectra is measured using wavenumber (cm^{-1}) as the x-axis, which describes the Raman shift, or the change in wavenumber from the incident wavelength; and intensity as the y-axis, often an arbitrary unit. A Raman spectrum displays peaks in locations related to the energies of the vibrational frequencies of molecules. Each molecule has a unique vibrational frequency, allowing spectra to be used as an identification tool [Eshelman, 2016].

3 Experimental apparatuses

3.1 Petrographic Microscope

An Olympus BX-53P petrographic microscope (Figure 4) was used to analyze DGR-034 and DGR-035 thin sections. This microscope was vital in the classification of these samples, by allowing observations of textures and features within the samples. The BX-53P has a polarizer, enabling quick mineral identification through interference colors, cleavage and crystal shape. The software package Olympus STREAM was used simultaneously to capture images, measure, and analyze features of interest. STREAM was used to obtain modal percentages of features and matrix within the unclassified samples.

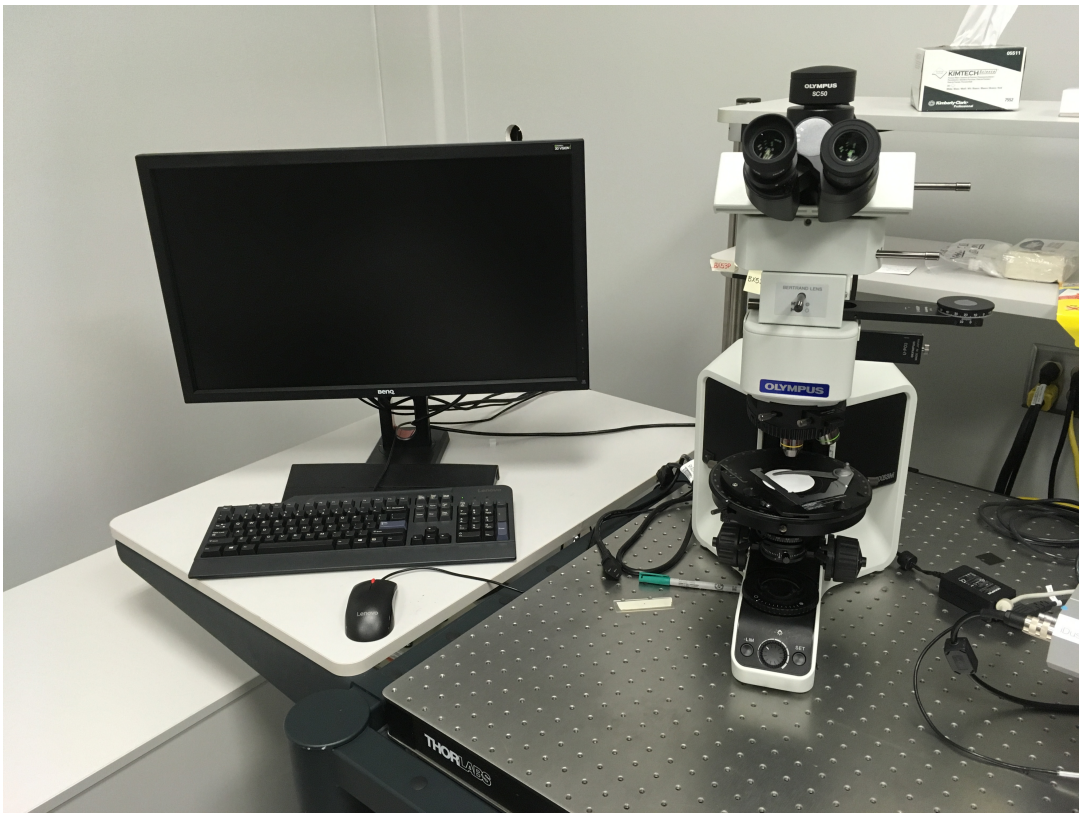


Figure 4: York University's Olympus BX-53P petrographic microscope.

3.2 Electron Probe Micro-analyzer

A JEOL JXA-8230 electron probe microanalyzer (EPMA) was used at Queen's University, Kingston, Canada to obtain major and minor element data for olivine, pyroxene and plagioclase in each sample. These data were used to calculate forsterite-fayalite composition in olivine, ferrosilite–enstatite–wollastonite compositions for orthopyroxene and clinopyroxene, and albite–anorthite–orthoclase compositions for plagioclase.

3.3 Raman Spectrometer

Raman spectra were collected at the Royal Ontario Museum using a Horiba LabRAM Aramis micro-Raman spectrometer with an excitation wavelength of 532 nm (Figure 5). The Raman window observed when using the ROM's 532 nm excitation laser is from 286 cm^{-1} to 3805 cm^{-1} when using a 2400 lines/mm grating. This window allows us to observe important molecular bonds such as in organics and minerals which we wish to identify in the search for life on Mars and analyze other bodies such as asteroids.

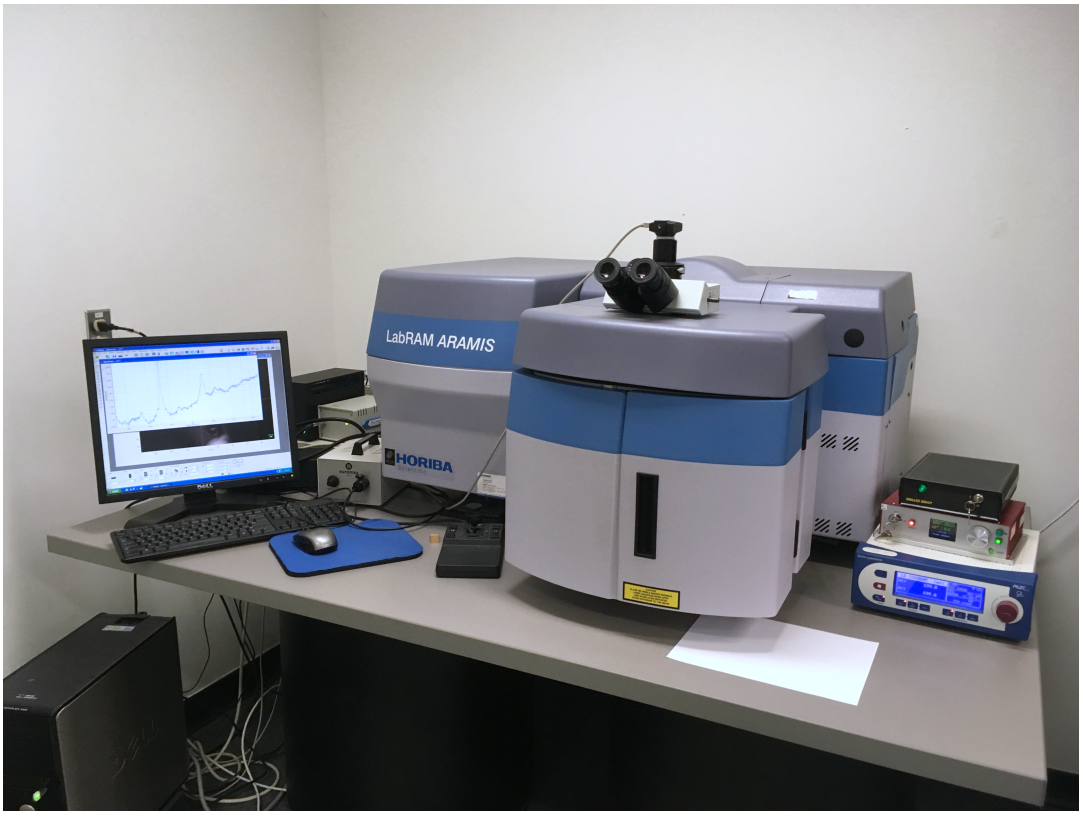


Figure 5: Horiba LabRAM Aramis micro-Raman instrument at the ROM.

3.4 Scanning electron microscope

A Tescan VEGA3 scanning electron microscope (SEM) was used to collect elemental maps of the same feature areas acquired by LIF and Raman. York University's SEM is equipped with a back-scattered electron detector (BSE), a Bruker electron-dispersive X-ray spectrometer (QUANTAX EDS) and a secondary electron detector (SE). The secondary electron detector is used to analyze suface topography, whereas the BSE detector is dependent on mean atomic weight, creating a grey-scale image based on composition. The EDS detector is used to obtain semi-quantitative atomic data.



Figure 6: York University's Tescan VEGA3 scanning electron microscope.

3.5 UV laser-induced fluorescence spectrometer setup

3.5.1 Instrument optimization

The UV (266 nm) Raman spectrometer in the Planetary Exploration Instrumentation Laboratory has been modified to include time-resolved laser-induced fluorescence (LIF) capabilities as shown in Figure 7. This instrument has been optimized over the course of this study to include a reflectance microscope objective (UV 15x), allowing a small laser spot-size and high resolution mapping. The system has also been modified to include rotating mirrors that allow quick transition between LIF and Raman spectroscopy without changing the position of the sample. By changing the diffraction grating in the spectrometer and adjusting camera settings, the system can be used for UV LIF or Raman spectroscopy interchangeably on the same sample.
The LIF system described in Eshelman [Eshelman, 2016], operates with a ALPHALAS Nd:YAG laser with 266-1064 nm capabilities. Modifications were made from Eshelman [2016] to incorporate a UV 15x (Thorlabs LMM-15x-P01) reflective microscope objective. To optimize the LIF system to incorporate the UV reflective mirror, the laser beam had to be refocused and expanded to fill as much of the objective aperture as possible to obtain a focused spot on the sample stage. In the system, UV light (266 nm) is emitted from the Nd:YAG source and interacts first with a quartz beam splitter (Figure 7), where a portion of the light is picked off and redirected to an external camera trigger. The trigger enables imaging of Raman and fluorescence phenomena at an optimized time after the laser pulse reaches the sample stage. At the beam splitter, some of the light continues toward the sample stage, being refocused smaller at L_1, expanded between L_2 and L_3, and reflected off the UV coated mirrors (M_i). The mirrors allow the external trigger enough time to interface with the

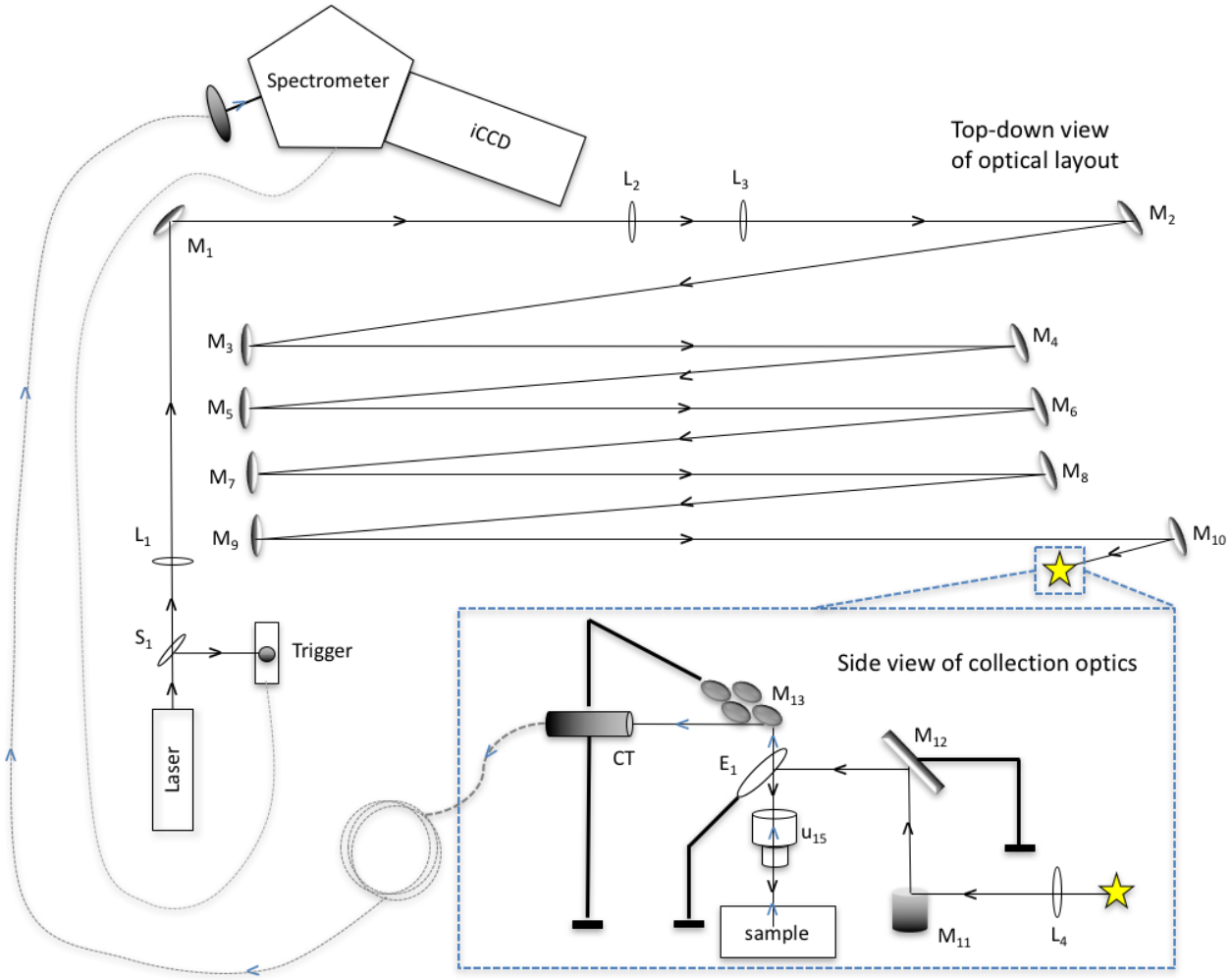


Figure 7: Simplified schematic of UV Raman/LIF breadboard setup at York University. M: UV coated mirrors, S: beam splitter, L: lenses, E: edge filter.

iCCD camera and capture Raman and fluorescence phenomena at the correct time. Once the light is focused through the microscope objective it will interact with the sample on the 3-axis, motorized, sample stage. A 3-axis stage facilitates 2D mapping, and refocusing of the spot on different sized, unprepared samples. Light re-emitted from the sample passes through an edge filter, which reflects 266 nm light (Rayleigh scattered), and passes wavelengths >266 nm into the collection optics. Within the collection optics tube there is another 266 nm filter and a lens focusing the light to the fiber cable. The bundled fiber cable transmits collimated light to the Andor Shamrock 163 spectrograph through a vertically aligned fiber bundle and redirected with an internal mirror towards a 2400 lines/mm diffraction grating with a 300 nm blaze when obtaining Raman spectra, and 300 lines/mm diffraction grating when obtaining fluorescence spectra. The wavelength separated light is then refocused into the Andor iStar DH334t, where is light is directed towards a ϕ18 mm photocathode. The photocathode generates photoelectrons, which are then amplified and intensified by the intensifier tube and microchannel plate (MCP). The photoelectrons are converted into visible photons by a phosphore for a 1024 x 1024 pixel CCD with 13 µm pixels to detect. When using a 300 line/mm diffraction grating with a 300 line blaze to obtain fluorescence spectra, the spectral resolution estimated for the Andor

Shamrock 163 spectrograph is 1.16 nm. This estimate is assuming a 10 µm slit. The slit in this setup is measured to be 0.07 mm wide, or 70 µm, reducing the spectral resolution by roughly a factor of 7. The estimated spectral resolution when collecting fluorescence spectra is therefore 8 nm. The Andor iStar iCCD has nanosecond scale gating capabilities by controlling the voltage across the intensifier. The iStar camera is equipped software (Andor Solis) enabling digital gate delay and cooling control.

3.5.2 Spot size and power

The beam size was measured to better understand the laser power at the sample and to determine the optimal step-size for spectral maps. The laser beam before entering the microscope objective is very elliptical, and is roughly 1 cm long, and 0.5 cm wide. Beam size was measured using a knife edge after passing through the objective.

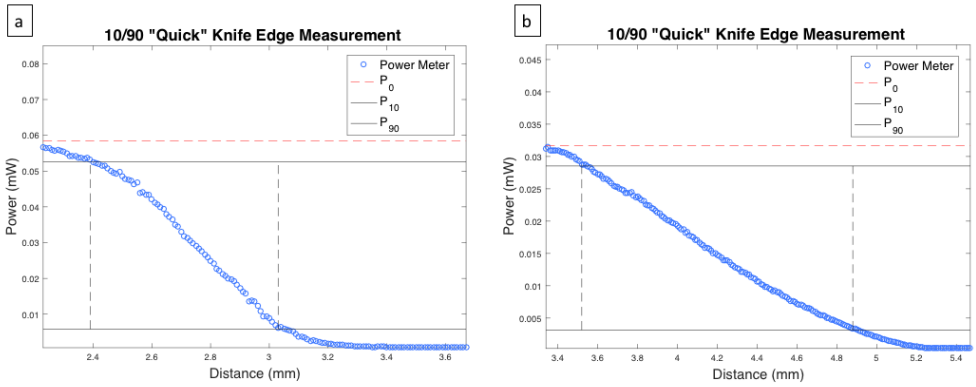


Figure 8: Beam size measurements between 10% and 90% of laser power when inserting knife edge for x (a) and y axis (b).

The knife edge was moved at 0.01 mm increments and the power was recorded at each step using a Thorlabs power meter. The power at each increment was plot using Matlab, and trimmed to include the power values slightly before drop off, and while completely blocked from the knife edge. The difference in positions at 10% and 90% of the laser power was found to obtain an approximate spot size. The beam was measured to be approximately 1.36 mm in the y-axis, and approximately 0.64 mm in the x-axis when slightly out of focus (Figure 8). When the laser is operated at a pulse repetition frequency of 5 kHz, the power is 0.8 W near the source output, and 0.1 mW where the sample is placed.

4 Samples

4.1 Monomineralic samples

A sample suite of common minerals found in carbonaceous chondrites was assembled to create a fluorescence spectra database to better identify mineral constituents in the meteorite samples. 10 minerals were borrowed from the Royal Ontario Museum to complete this database: anorthite, augite, diopside, forsterite, graphite, labradorite, nepheline, olivine, orthopyroxene and spinel (Table 1).

Table 1: Monomineralic samples used to create LIF mineral database from the ROM.

Mineral	**Mass (g)**	**Locality**
Augite	0.68	Borislav, Czech Republic
Nepheline	1.34	Kishangarh, India
Anorthite	0.67	Mesam Peublo Forest, New Mexico, USA
Orthopyroxene (Hedenbergite)	5.63	Hanover County, New Mexico, USA
Forsterite	0.65	Bernardmyo, Myanmar
Diopside	0.31	Outukumpu, Finland
Olivine	0.17	Bernardmyo, Mogok, Myanmar
Spinel	0.27	Mogok, Myanmar
Labradorite	1.08	Nain, Labrador, Canada
Graphite	45.7	Ottawa County, Quebec, Canada

4.2 Carbonaceous chondrite samples

Four carbonaceous chondrites were borrowed from the Royal Ontario Museum (ROM) for this study. Carbonaceous chondrites are considered to be pieces of C-type asteroids that have been collected on Earth, making them ideal analogs for asteroid studies. Carbonaceous chondrites contain many millimetre-sized features such as chondrules and calcium-aluminum-rich inclusions (CAIs) in a fine-grained, carbon-rich matrix. Pieces of Allende (CV3), Murchison (CM2), and two unclassified meteorites: DGR-034, and DGR-035 were chosen for this study to obtain results on well known and unknown carbonaceous chondrites. Allende and Murchison were observed falls, resulting in a large collection of material and extensive study of the meteorites. The mineral consituents and geochemistry of these two samples are well known due to extensive studies of these meteorites continuing since in the 1970s [Grossman, 1975, Clarke Jr et al., 1971, Marvin et al., 1970, Kvenvolden et al., 1970, Jarosewich, 1971]. Samples DGR-034 and DGR-035 are new carbonaceous chondrites to the ROM's collection and therefore have not yet been classified or studied.

4.3 Sample preparation

All four carbonaceous chondrite samples were cut using a Wells diamond wire saw at the ROM. the samples were cut into flat slabs for spectral analyses (Figure 9). These slabs were lightly polished with aluminum oxide paper, and dusted using pure compressed oxygen to obtain relatively flat, uncontaminated surfaces after cutting. Raman and laser-induced fluorescence (LIF) do not require flat surfaces, however for this study flat slabs were cut for ease of use of all instruments including an scanning electron microscope (SEM). Thin sections (30 μm) were prepared from DGR-034 and DGR-035 for electron probe microanalyzer (EPMA)

geochemistry and petrographic microscopy work. Thin sections were covered with a carbon coat for the EPMA analyses, which was later removed using aluminum oxide powder and ethanol.

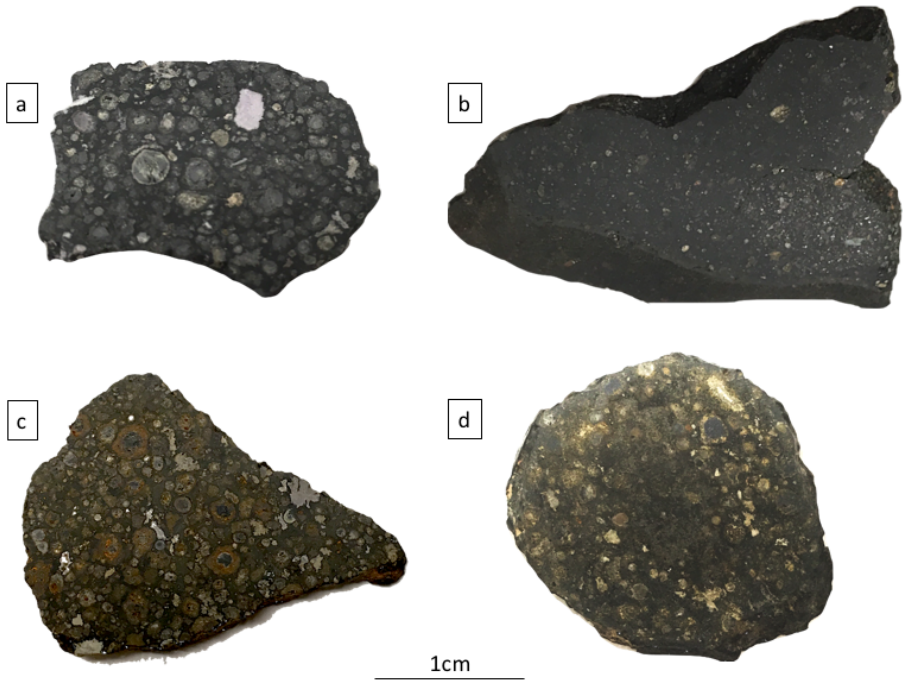


Figure 9: Cut sections of carbonaceous chondrite samples from the ROM. (a) Allende CV3, (b) Murchison CM2, (c) DGR-034, (d) DGR-035.

4.4 Meteorite slab descriptions

All four samples have visible millimetre sized chondrules and CAIs on the flat surface of the slabs (Figure 9). Allende is roughly 2 cm in diameter and contains abundant chondrules and CAIs with a dark, fine grained matrix. Murchison is about 4 cm long with small (1 mm) chondrules and CAIs with abundant matrix. DGR-034 has abundant, large (1-2 mm) chondrules and CAIs visible on the surface of the slab, with a fine-grained oxidized matrix. DGR-035 has a greenish-yellow matrix with less abundant chondrules and matrix than DGR-034.

4.5 Introduction to classification of meteorites

Classification of new meteorites in a collection is essential for future scientific studies, and provides a naming scheme for the specimen that includes a shorthand for basic chemical, petrographic, shock, and weathering characteristics. Two samples from the ROM that were on loan for this study were previously unidentified, DGR-034 and DGR-035. Classification of these two samples was necessary to obtain scientific meaning from any other instrument results. Classification is formal and registered with the Meteoritical Society.

4.6 Methods for classification

To establish a full understanding of the samples, they were examined in hand-sample, cut sections (cut at the ROM), and thin section (30 µm thickness). Hand samples were observed using a binocular microscope to

better understand whole rock composition and to analyze the fusion crust. Cut sections allowed observation of the abundance of calcium-aluminium-rich inclusions (CAIs), chondrules and metallic constituents. Optical petrography on the thin sections were completed using an Olympus BX53P petrographic microscope with a SC50 5x camera attachment, and Olympus STREAM software capabilities. A JEOL JXA-8230 electron probe microanalyzer (EPMA) was used at Queen's University, Kingston, Canada to obtain major and minor element data for olivine, pyroxene and plagioclase in each sample. These data were used to calculate forsterite-fayalite composition in olivine, ferrosilite–enstatite–wollastonite compositions for orthopyroxene and clinopyroxene, and albite–anorthite–orthoclase compositions for plagioclase. Plagioclase and pyroxene data were then plot on ternary diagrams to determine what mineral within the pyroxene, and plagioclase groups are represented in the sample. The ternary diagrams represent the three element ideal end-members for each group. For pyroxene, ferrosilite–enstatite–wollastonite end members are calculated by determining the ratio of Fe-Mg-Ca ions within a grain by dividing one element by the sum of the others. Similarly, the albite–anorthite–orthoclase ratios for plagioclase are calculated using Na-An-K ions. Modal mineralogy was determined using Olympus STREAM software, where minerals were differentiated using colour thresholds (Appendix B). These data were used to determine class, clan and group of each meteorite sample (Figure 11). 'Petrographic type' was determined using these data and Figure 12 which represents the level of metamorphic or aqueous alteration a meteorite has undergone within the parent body (Figure 10) [Weisberg et al., 2006].

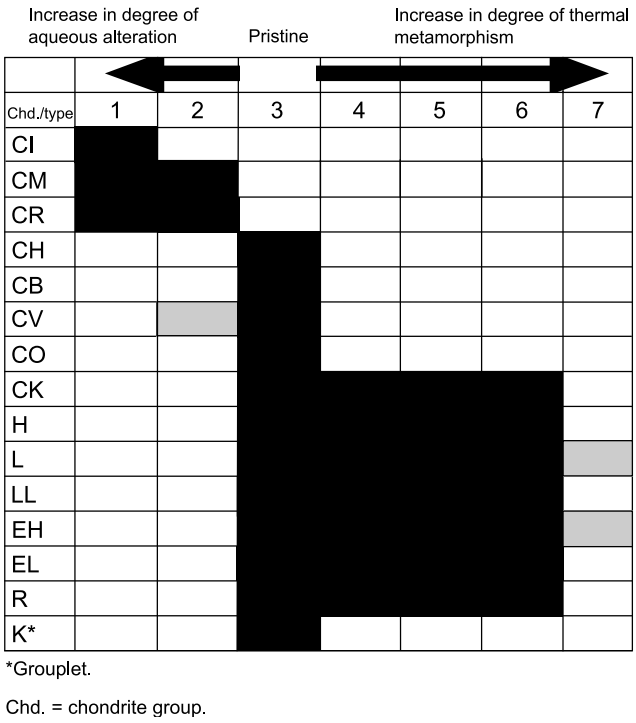


Figure 10: Petrologic types and their relationship to metamorphic and aqueous alteration levels from Weisberg (2006). Black boxes indicate average petrologic type for each group.

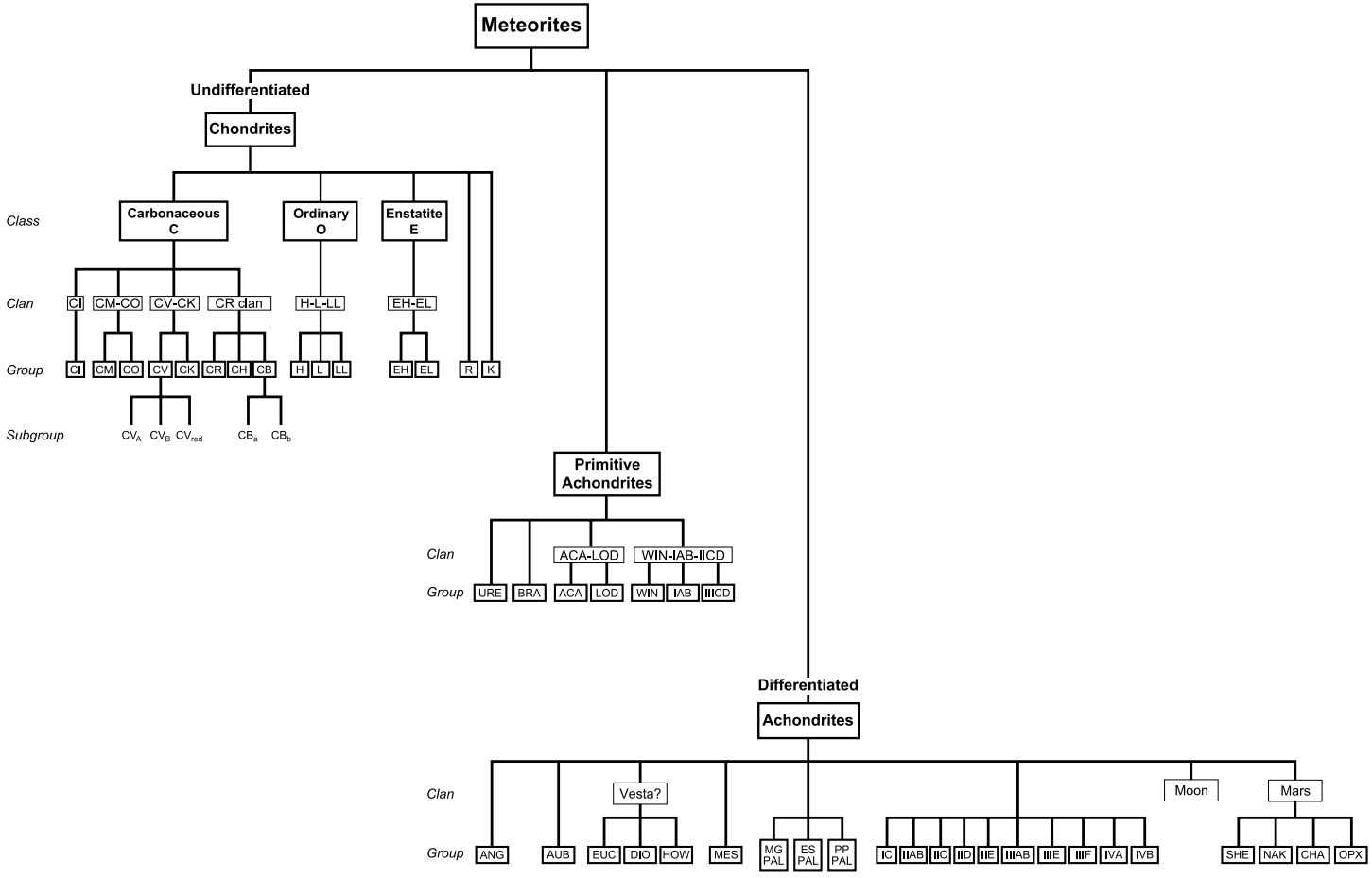


Figure 11: Classification chart displaying genetic relationships between meteorites and parent bodies. Classes, clans, groups and subgroups are presented from the three types of meteorites: chondrites, achondrites and primitive achondrites from [Weisberg et al., 2006].

Criterion	1	2	3	4	5	6	7
Homogeneity of olivine compositions	—	>5% mean deviations		≤5%	Homogeneous		
Structural state of low-Ca pyroxene	—	Predominantly monoclinic		>20% monoclinic	≤20% monoclinic	Orthorhombic	
Feldspar	—	Minor primary grains		Secondary <2-μm grains	Secondary 2–50-μm grains	Secondary >50-μm grains	
Chondrule glass	Altered or absent	Mostly altered, some preserved	Clear, isotropic	Devitrified	Absent		
Metal: Maximum Ni (wt%)	—	<20 taenite minor or absent	>20 kamacite and taenite in exsolution relationship				
Sulfides: Mean Ni (wt%)	—	>0.5	<0.5				
Matrix	Fine grained opaque	Mostly fine-grained opaque	Opaque to transparent	Transparent, recrystallized			
Chondrule-matrix integration	No chondrules	Sharp chondrule boundaries		Some chondrules can be discerned, fewer sharp edges	Chondrules poorly delineated	Primary textures destroyed	
Carbon (wt%)	3–5	0.8–2.6	0.2–1	<0.2			
Water (wt%)	18–22	2–16	0.3–3	<1.5			

Figure 12: Parameters aiding in the determination of petrographic type for chondrites from Weisberg (2006), modified from Van Shmus and Wood (1967).

4.7 Classification of ROM sample DGR-034

4.7.1 Collection History

DGR-034 was collected in Morocco and has a total known weight of 39 g. The sample was purchased by Dr. Gregory in September, 2013 in Denver, colourado, USA. The piece of sample used to study and classify the meteorite is located at the ROM and the main mass remains with Dr. Gregory.

4.7.2 Hand Sample Examination

The type sample for DGR-034 was examined at the ROM. The hand sample has minimal visible fusion crust, but very noticeable oxidation on the outside of the sample as reddish-brown dust (Figure 13). millimetre-sized chondrules and CAIs are visible on the outside of the hand sample and are seen clearly in the cut section of the sample. The matrix is very dark in colour and extremely fine-grained. The chondrule boundaries appear to be well defined, and CAIs are abundant. Metals do not appear to be readily abundant in the hand sample.



Figure 13: Hand sample (type sample) of DGR-034 at the ROM. Oxidation is noticeable on the outside of the sample, with no fusion crust.

4.7.3 Petrography

DGR-034 was analyzed in thin section using optical microscopy to determine mineralogy and relative abundance of matrix, chondrules, and CAIs within the sample. The sample was viewed in plane-polarized light (PPL), crossed polarized (XPL) and reflected light (RL) to determine bulk rock context (Figure 14).

DGR-034 contains abundant chondrules (about 40-50% modal) and calcium-aluminum-rich inclusions (CAIs) (10% modal), with an extremely fine-grained, opaque matrix (40% modal). DGR-034 has very little (<1%) metal and sulphide content, which mainly occur as small inclusions within chondrules. Modal mineralogy percentages are reported in Appendix B.

4.7.4 Chondrules

DGR-034 is abundant in well-defined chondrules (40-50% modal) with visible rims. Chondrules range in size from 0.3-3.3 mm, with the average chondrule size being 1 mm (n:51). The chondrules contain mostly olivine and pyroxene, and some interstitial plagioclase. Most of the chondrules were porphyritic olivine (PO) texture. Barred olivine chondrules (BO) were also present, as well as porphyritic pyroxene (PP) and several other textures as seen in Figure 15. These textures were classified based on the chondrule texture classifications outlined in Hutchison (2004)[Hutchison, 2004].

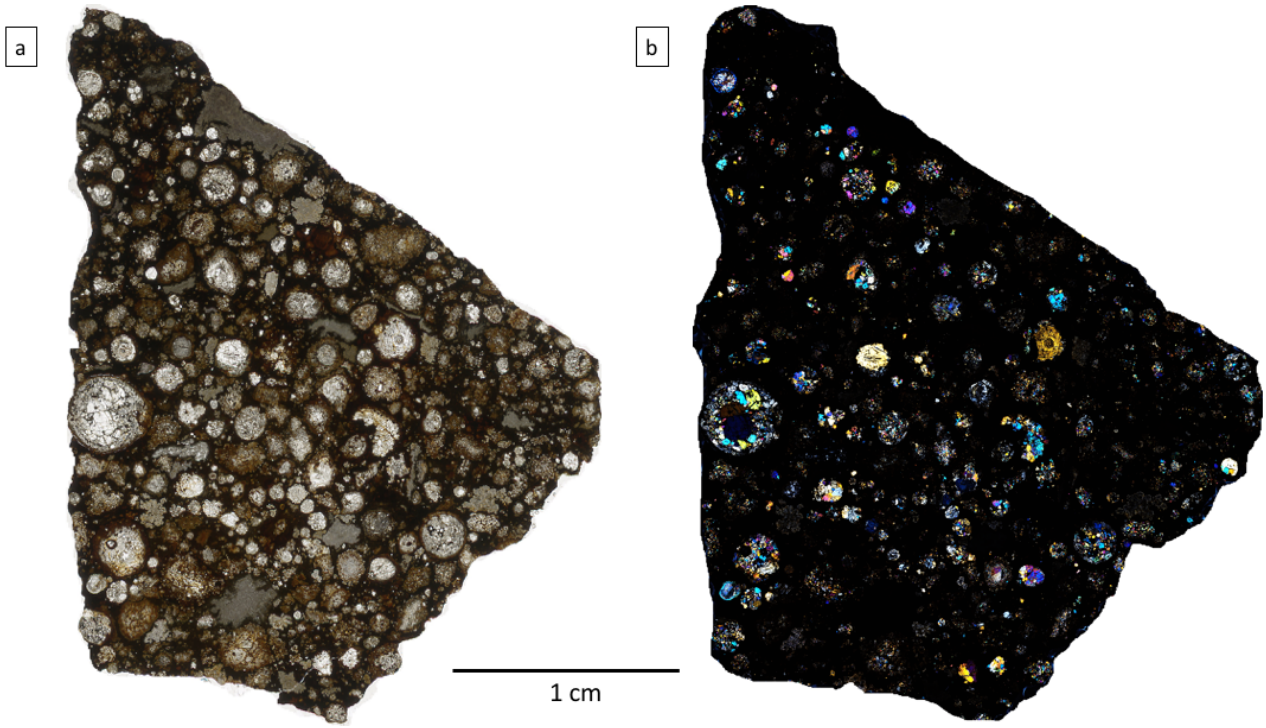


Figure 14: DGR-034 thin section: (a) Plane-polarized light (PPL) microscopy image; (b) Crossed-polarized light microscopy (XPL) image.

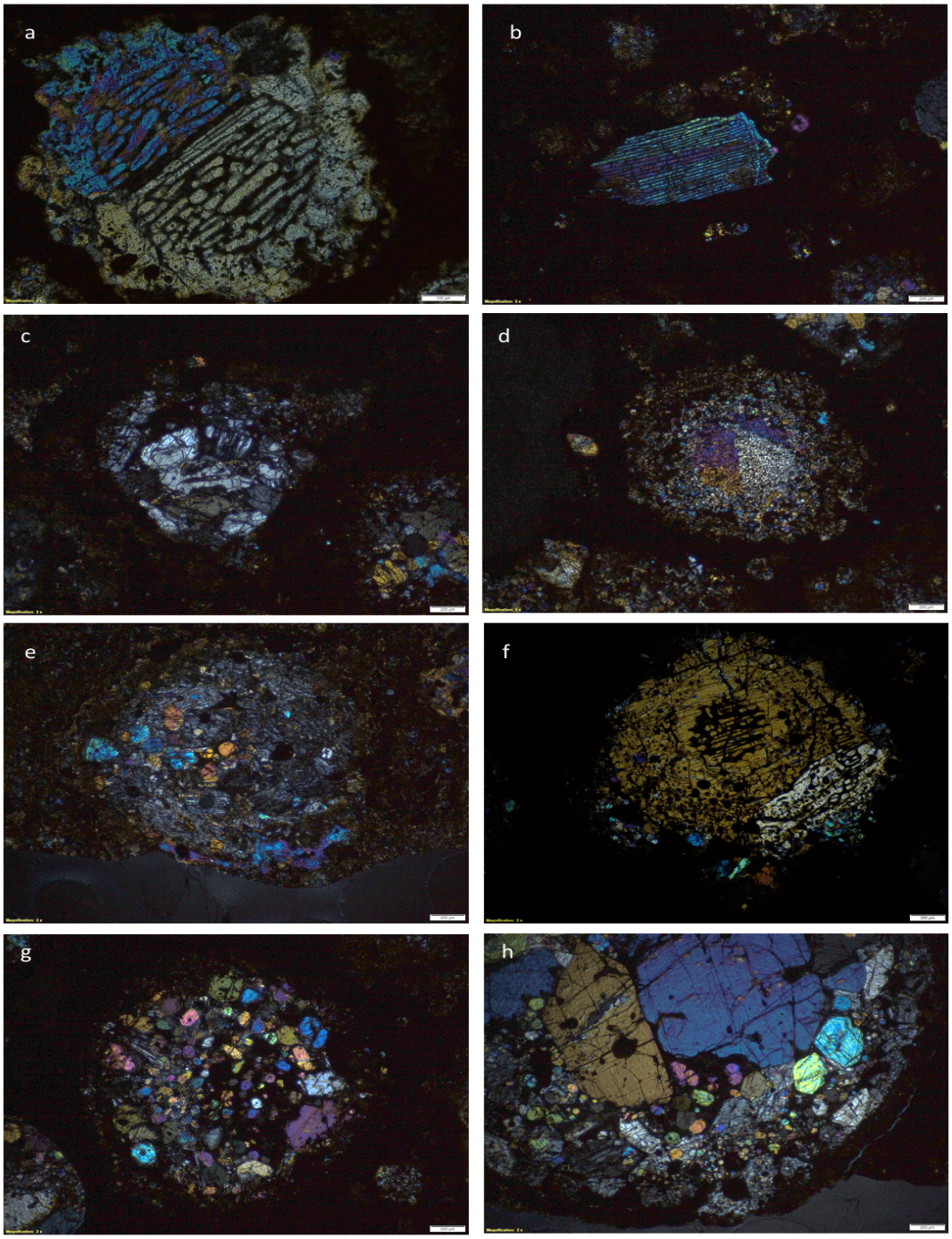


Figure 15: Chondrules imaged in DGR-034. (a) Barred olivine and pyroxene chondrule. Scale bar: 100 µm; (b) Barred olivine chondrule (BO). Scale bar 200 µm; (c) Porphyritic pyroxene chondrule (PP). Scale bar 200 µm; (d) Broken Pyroclastic pyroxene chondrule. Scale bar 200 µm; (e) Porphyritic olivine - pyroxene chondrule (POP). Scale bar 200 µm; (f) Porphyritic pyroxene chondrule (PP) with some barred texture. Scale bar 200 µm; (g) Porphyritic olivine chondrule with plagioclase laths. Scale bar 200 µm; (h) Porphyritic pyroxene - olivine chondrule. Scale bar 200 µm.

Most chondrules in the sample have defined, and even 'dusty' rims of oxidized material clearly visible in plain polarized light. Most chondrules display a 'spongy' texture as described by Van Schmus (1969), where the silicate grains within the chondrules are surrounded by opaques, metal and sulphide inclusions that are visible in reflected light (Figure 16). Some turbid glass was found interstitially within barred olivine chondrules.

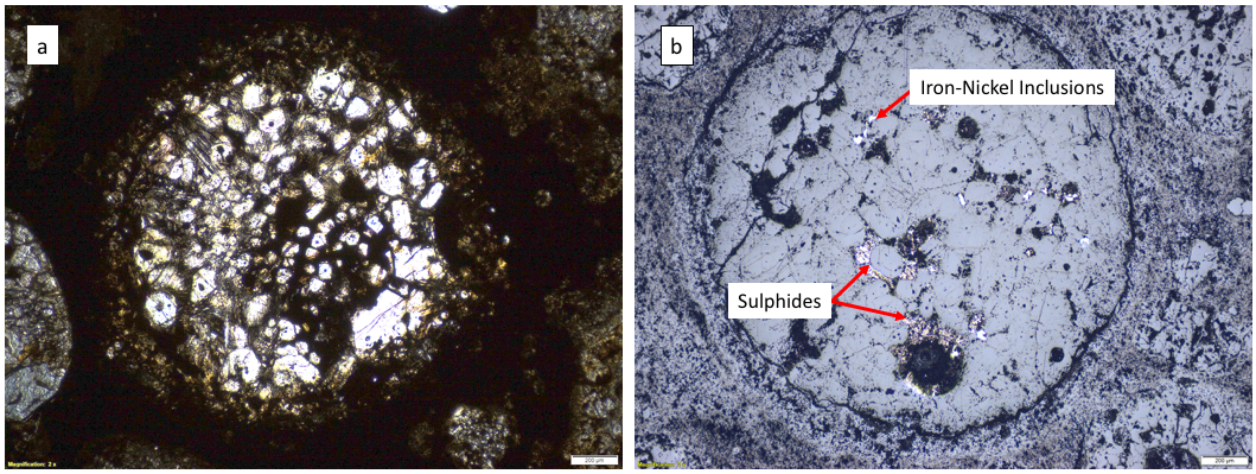


Figure 16: (a) Plane-polarized image of a chondrule in DGR-034 with well defined 'dusty' rim. (b) Reflected light image of a chondrule in DGR-034 with sulphide and iron-nickel inclusions. Scale bars: 200 μm.

4.7.5 Calcium-aluminum-rich-inclusions

Calcium–aluminum–rich inclusions are present in DGR-034, with a modal abundance of about 10%. The CAIs ranged in size from 0.5-2.1 mm, with an average size (long axis length) of 1.17 mm (n:16) Most CAIs were crypto-crystalline, with some larger grains (<10 μm) that were identified as plagioclase and orthopyroxene using optical microscopy (Figure 17). About 85% of CAIs in DGR-034 are crypto-crystalline, and the other 15% are coarser grained (<20 μm). There are some features (making up <5% of the sample) that resemble amoeboid olivine aggregate (AOA). Such features have similar compositions to that of CAIs but formed at possibly lower temperature conditions and can contain olivine, nepheline, sodalite and perovskite [Grossman and Steele, 1976].

4.7.6 Matrix

The matrix of DGR-034 was almost entirely opaque in PPL, due to the amount of fine-grained silicates and oxides present.The matrix consisted of about 85% very fine-grained olivine, 7% plagioclase, 5% opaque minerals, and <1% metal. The opaque matrix in PPL and XPL is visible in reflected light as discernible, metallic looking grains (Figure 18).

4.7.7 Shock features

Shock levels were assessed by examination of olivine grains. There were no planar shock features, and all grains had very sharp extinction in crossed-polarized light. There was very little to no mosaicism and undulatory extinction occurring in olivine in the sample. No alteration of plagioclase to maskelynite was found within this sample.

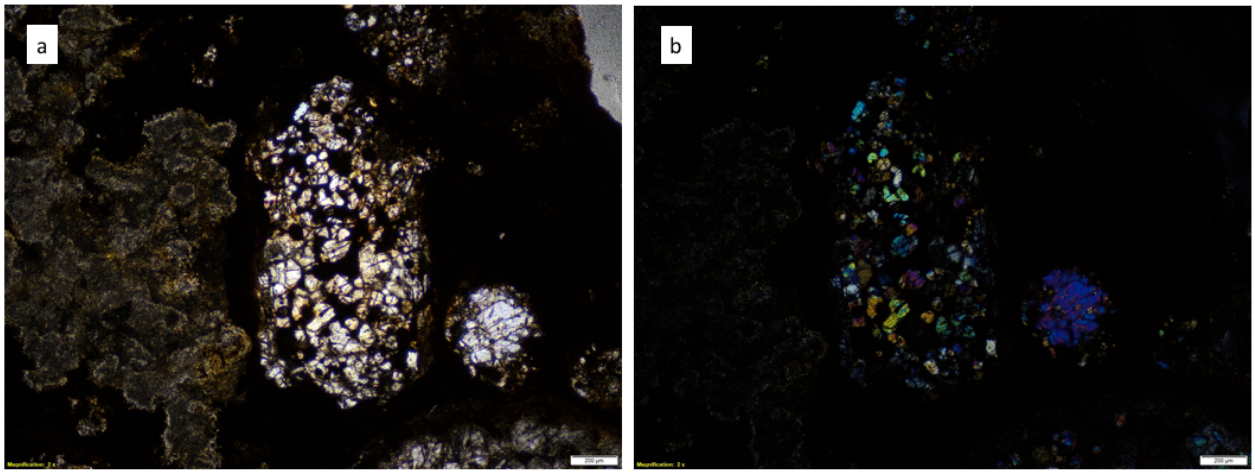


Figure 17: (a)Plane-polarized light image of a cryptocrystalline CAI on the left, and a coarse-grained AOA in the centre of the image. (b) Crossed-polarized light (XPL) image of the same CAI area. The cryptocrystalline CAI is opaque in XPL most likely due to density. Scale bars: 200 μm.

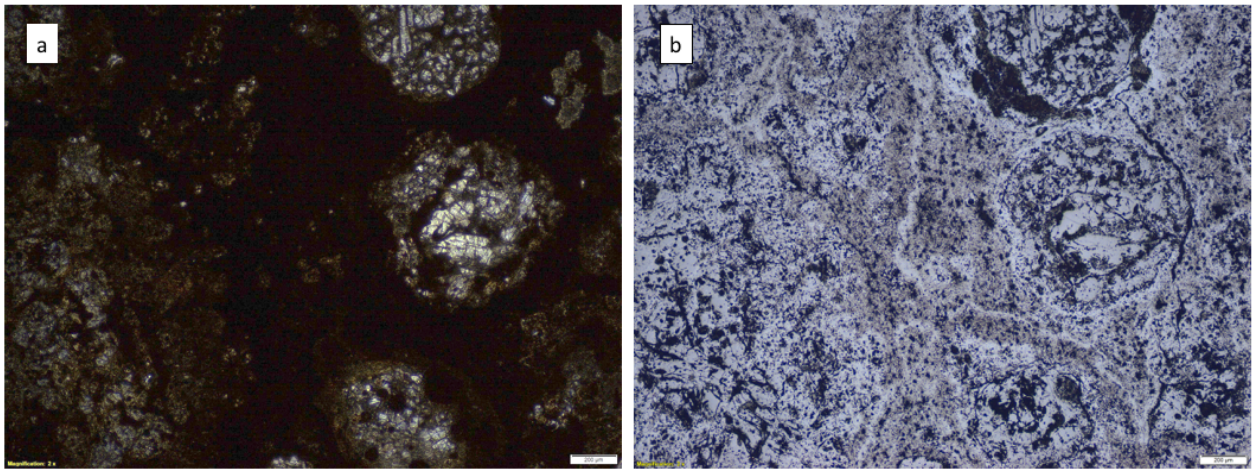


Figure 18: (a) Plane-polarized light microscopy image of opaque matrix between features; (b) Reflected light microscopy image of matrix. Scale bars: 200 μm.

4.7.8 Weathering features

The presence of a reddish brown weathering rind on the surface of DGR-034 indicates that terrestrial weathering has occurred (Figure 13). This red-brown staining of the thin section was visible in PPL, as well as slight staining of some silicate grains. Some iron oxides were present within the sample as inclusions and as very fine grains around the rims of chondrules within the sample (Figure 16). Aside from some oxidation staining of grains and around the rims of chondrules, weathering evidence was limited. There were no veins infilled with carbonates or phylosillicates in the sample, through cracks filled with oxides were present.

4.7.9 Electron probe micro-analysis geochemistry

Electron probe micro-analyses (EPMA) were used to obtain quantitative geochemical data from the sample. Major and minor elements were analyzed in olivine, pyroxene and plagioclase grains within the matrix,

chondrules and CAIs when present. Fayalite compositions for olivine were calculated, and ranged from $Fa_{0.36-51.91}$ with an average of $Fa_{23.544}$ (Table 2). Olivine homogeneity was calculated using equation 1, where σ_{Fa} represents the standard deviation fayalite number, and $\overline{Fa}$ represents the mean fayalite number calculated for the sample. Olivine homogeneity for DGR-034 was found to be 83%.

$$Homogeneity = \frac{\sigma_{Fa}}{\overline{Fa}} * 100\% \tag{1}$$

Orthopyroxene and clinopyroxene were abundant in this sample and both were analyzed using EMPA (Table 2). Pyroxene (orthopyroxene and clinopyroxene) geochemistry was plot on an enstatite-ferrosilite-wollastonite ternary diagram to determine composition for grains within chondrules, CAIs and the whole rock. Ternary diagram calculations are described in section 4.6. The orthopyroxene in DGR-034 was mainly enstatite, whereas the clinopyroxene compositions ranged from augite to diopside, with the whole rock average being augite composition (Figure 19).

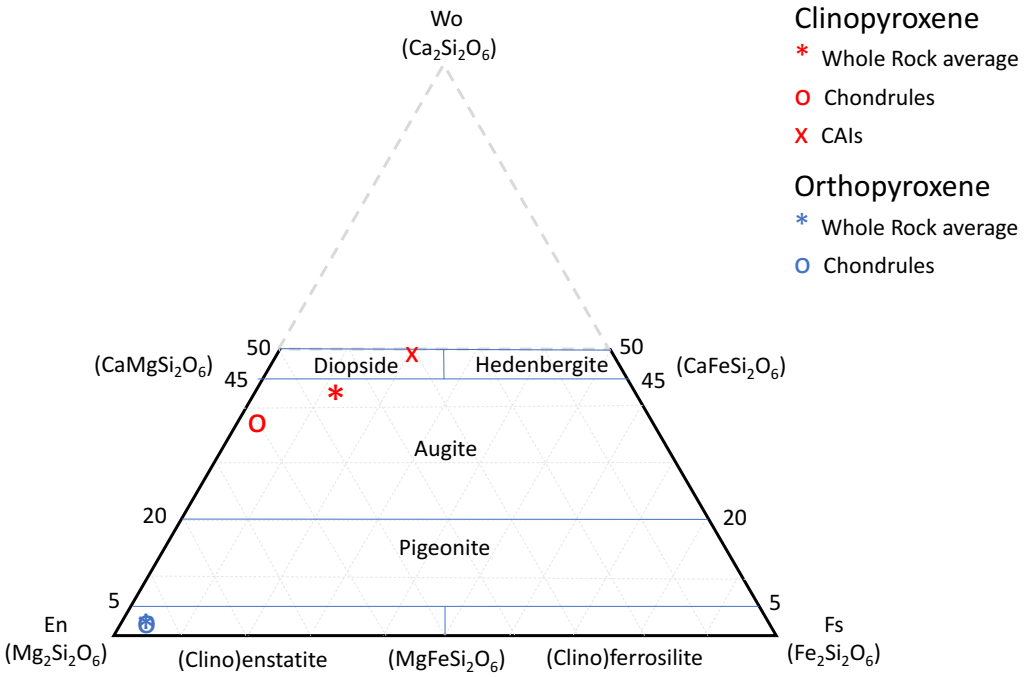


Figure 19: Enstatite, ferrosilite, and wollastonite end member plot for pyroxene in DGR-034 after [Deer et al., 1992]. Pyroxene grains from CAIs, chondrules and whole rock average were plot.

Feldspar was found within the chondrules and CAIs of DGR-034 and was analyzed using EPMA (Table 2). Feldspar geochemistry was plot on an albite-anorthite-orthoclase ternary diagram to determine composition for grains within chondrules, CAIs and the whole rock. The average feldspar within the sample fell into the composition range of bytownite. The plagioclase from the CAIs however were almost pure anorthite in composition (Figure 20). All feldspars were in the plagioclase range within DGR-034 and no alkali feldspars were found.

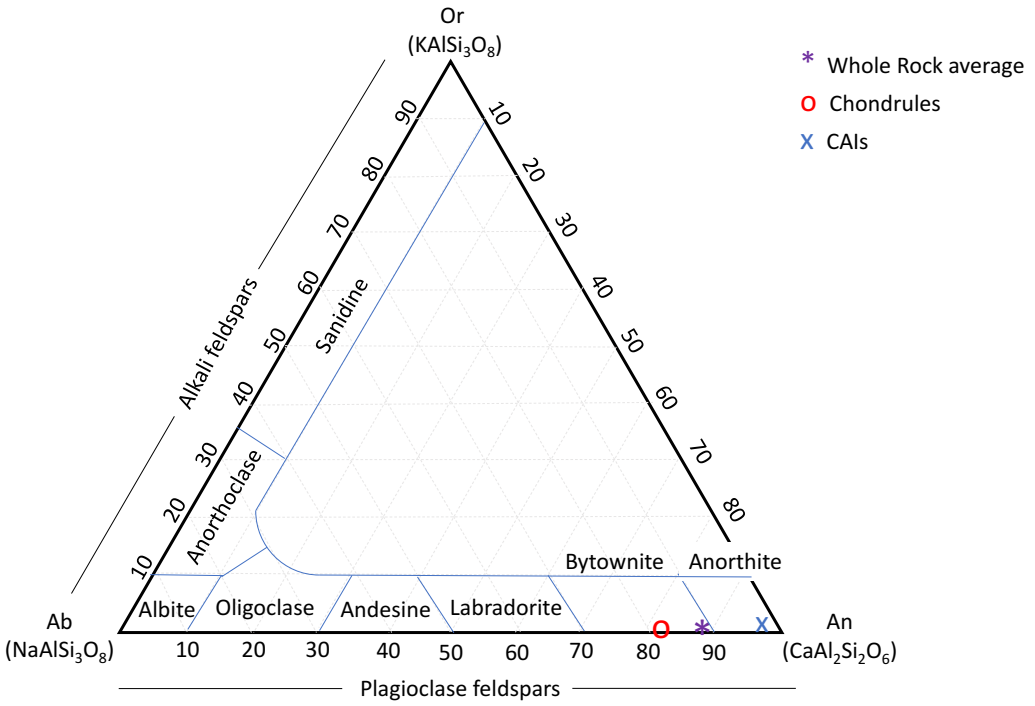


Figure 20: Albite, anorthite and orthoclase end member plot for feldspar in DGR-034 after [Deer et al., 1992]. Feldspar grains from CAIs, chondrules and whole rock average were plot.

Table 2: EPMA results for olivine, pyroxene and plagioclase in DGR-034

Mineral	Number of Samples	Compositional Range (Mol%)	Average (Mol%)	Mean Deviation (Mol%)
Olivine	35	$Fa_{0.36-51.91}$	23.54	18.30
Orthopyroxene	17	$Fs_{0.50-41.43}$ - $En_{50.12-98.41}$ - $Wo_{0.76-8.45}$	$Fs_{5.02}$ - $En_{91.66}$ - $Wo_{3.32}$	$Fs_{5.03}$ - $En_{6.95}$ - $Wo_{1.93}$
Clinopyroxene	10	$Fs_{0.77-50.15}$ - $En_{0.47-60.46}$ - $Wo_{35.28-50.79}$	$Fs_{16.43}$ - $En_{39.47}$ - $Wo_{44.10}$	$Fs_{16.3}$ - $En_{17.01}$ - $Wo_{5.45}$
Plagioclase	16	$An_{79.03-99.46}$ - $Ab_{0.54-20.96}$ - $Or_{0-0.12}$	$An_{85.87}$ - $Ab_{14.12}$ - $Or_{0.03}$	$An_{5.62}$ - $Ab_{5.62}$ - $Or_{0.03}$

4.7.10 Discussion and Classification

A classification workflow (Figure 21) summarizes the steps taken to determine a group for each meteorite. Petrologic type was then determined using Figure 12 and McSween (1977). Based on the presence of chondrules and CAIs within the sample DGR-034, it is confirmed to be a carbonaceous chondrite. With the size (average 1 mm), and abundance of chondrules (about 40-50 modal %), and a dark fine-grained matrix occurring in about 40% of the sample, DGR-034 falls into the category of a CV type carbonaceous chondrite based on average petrologic characteristics of the major chondrite groups [Weisberg et al., 2006].

To determine petrographic type, the modal mineralogy of the matrix, chondrules, and CAIs were assessed.

Olivine was abundant and mainly euhedral to subhedral. Olivine homogeneity was calculated using equation 1, and was found to be 83.47%. Such a high result indicates that the olivine grains are not homogenous, and therefore the sample is not in equilibrium. This result is consistent with petrographic type 3, considering the higher the petrologic type, the more equilibrated the olivines will be. Clinopyroxene and orthopyroxene were present in the sample, as well as some <10 μm anorthite laths. The matrix was extremely fine-grained and opaque, mostly containing oxide minerals and some iron and sulphide. Calcium-aluminum inclusions were present and contained mostly fine-grained to cryptocrystalline minerals. Based on this evidence, DGR-034 is classified as petrographic type 3. Little to no shock evidence places DGR-034 in the S1 shock category, being subjected to minimal amounts of pressure (<4-5 GPa) according to the classification guidelines for CK chondrites [Scott et al., 1992]. Minimal weathering evidence was found within the sample beyond some iron oxide inclusions and staining. The main evidence of terrestrial weathering was 60-95% of metals have been replaced by oxides, placing the sample at W3 on the chondritic weathering scale [Wlotzka, 1993]. This suggests DGR-034 was minimally altered by terrestrial weathering.

4.7.11 Conclusion

By observing and analyzing the type hand sample, cut section, and thin section of ROM chondritic sample DGR-034, the classification was determined to be a carbonaceous chondrite type CV3 with S1 shock and W3 weathering. This classification has been submitted to the Meteoritical Society to be approved for naming. This classification will allow future scientific study and reporting on this sample and provide more information about the rare meteorite group, carbonaceous chondrites.

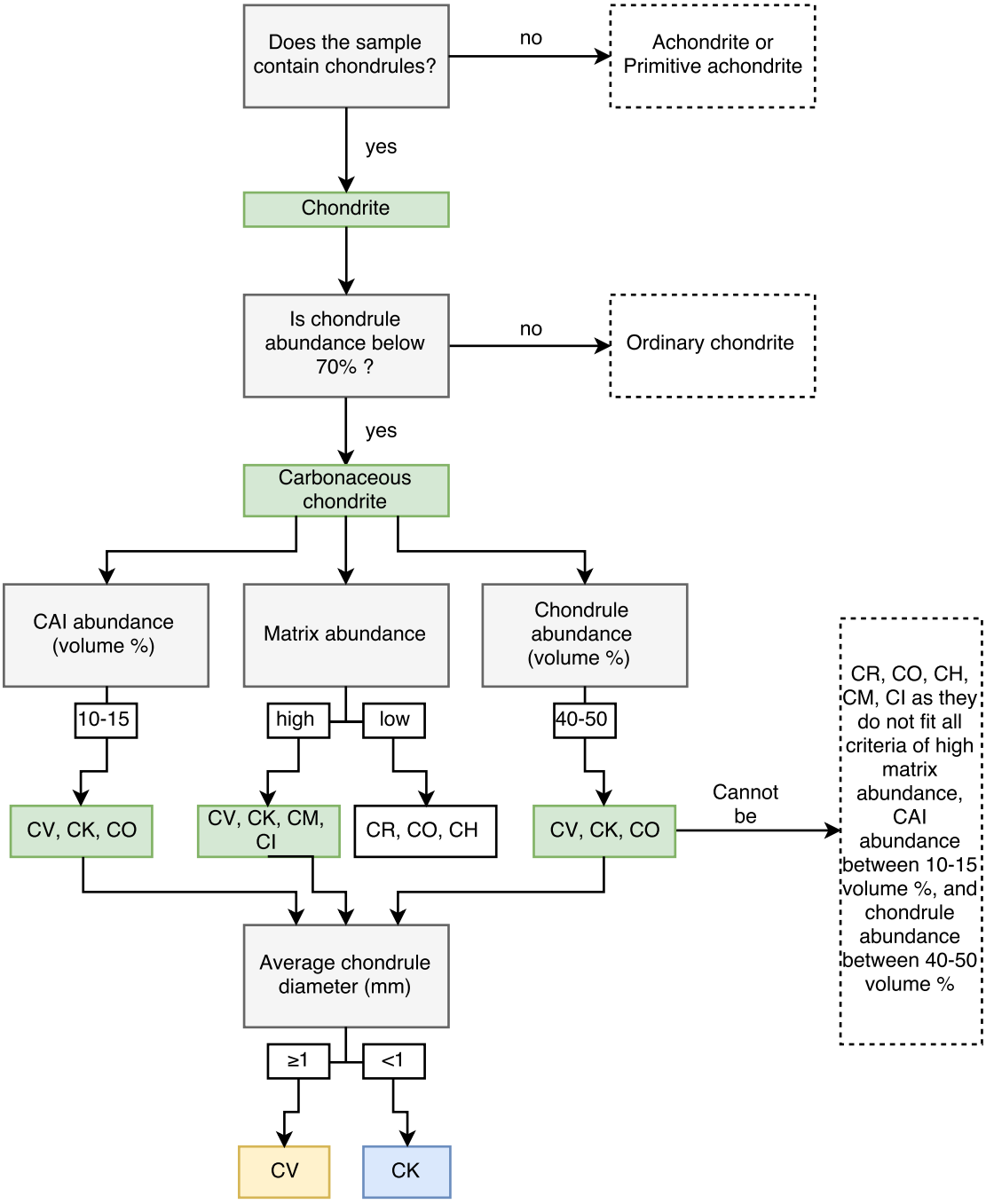


Figure 21: Flow chart of meteorite classification for DGR-034 and DGR-035. Petrographic type was determined after groups were determined through this flow chart. Characterization were based off of Sears (2004), and Weisberg (2006).

4.8 Classification of ROM sample DGR-035

4.8.1 Collection History

DGR-035 was collected in Morocco and has a total known weight of 91 g. Sample DGR-035 was purchased by Dr. Gregory in September, 2013 in Denver, colourado, USA. The type mass is located at the ROM and the main mass remains with Dr. Gregory.

4.8.2 Hand Sample Examination

The type sample for DGR-035 was examined at the ROM. The hand sample has a visible fusion crust, but minimal oxidation on the outside of the sample (Figure 22). Chondrules and CAIs are partially visible on the outside of the hand sample, and are seen clearly in the cut section of the sample. The matrix is light greyish-green in colour and fine-grained. The chondrule boundaries appear to range between defined and poorly defined. CAIs are large, and darker in colour (grey) as apposed to stark white in some carbonaceous chondrites. There are some chondrules that appear to be more metallic than others.



Figure 22: Hand sample (type sample) of DGR-035 at the ROM. A fusion crust is noticeable on the outside of the sample, with minimal terrestrial weathering.

4.8.3 Petrography

DGR-035 was analyzed using optical microscopy to determine petrology. The sample was viewed in plane-polarized (PPL), crossed polarized (XPL) and reflected light (RL). The thin section of this sample was imaged in plane-polarized and crossed polarized light (Figure 23).

DGR-035 contains abundant chondrules (about 15-20% modal) and CAIs (10% modal), with a coarse grained (<10-100 μm) matrix (70% modal). DGR-035 has very little metal content (<5%), which occurs in the matrix and as inclusions within chondrules.

4.8.4 Chondrules

DGR-035 contains a range of chondrules that are well-defined to poorly defined. The chondrules make up about 15-20% of the sample. Chondrules range in size from 0.4-3.0 mm, with the average size being 0.88 mm (n:30). Chondrules contain mostly olivine and pyroxene, and some plagioclase. Most of the chondrules were porphyritic pyroxene (PP) texture. Barred olivine chondrules (BO) were also present, as well as porphyritic olivine (PO) and several other textures as seen in Figure 24. Chondrule textures were classified based on chondrule characteristic textures described in Hutchison [2004]. Mesostasis or turbid glass, was found in barred olivine chondrules.
Most chondrules in the sample do not have well-defined rims, with some chondrules being poorly defined and broken into the matrix. Some of the chondrules, especially with barred texture have well-defined rims, whereas others appear to 'melt' into the matrix. Some chondrules in DGR-035 contain metal inclusions, but sulphides are not abundant within chondrules.

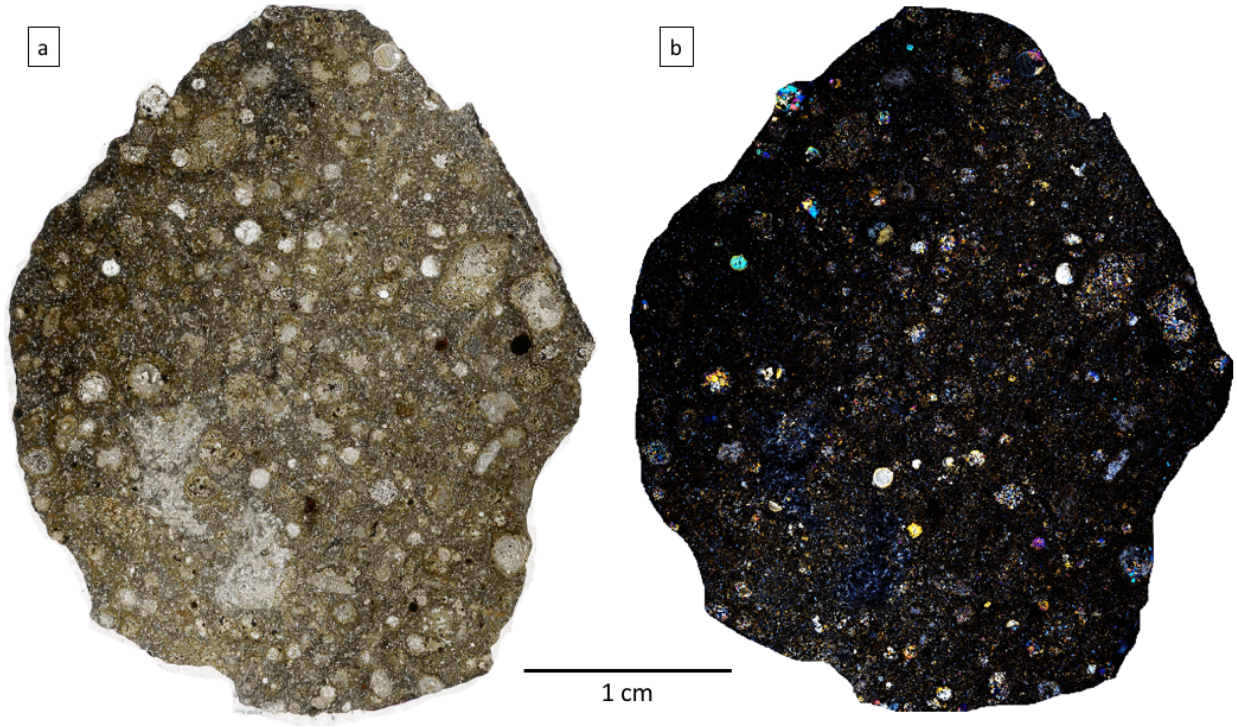


Figure 23: DGR-035 thin section: (a) Plane-polarized light (PPL) microscopy image; (b) Crossed-polarized light microscopy (XPL) image.

4.8.5 Calcium-aluminum-rich inclusions

Calcium–aluminum–rich inclusions are present in DGR-035, with a modal abundance of approximately 10%. CAIs in DGR-035 ranged from 0.75-5 mm (long axis length), with an average size of 2.2 mm (n:10). Most CAIs contained silicate grains the same size or larger than that of the matrix (<20-100 μm), with some larger grains that were identified as plagioclase and orthopyroxene using optical microscopy (Figure 26).

4.8.6 Matrix

The matrix of DGR-034 was almost entirely recrystallized, consisting of mostly silicate grains <10-100 μm in size. The matrix is comprised of about 75% olivine, 15% pyroxene, 8% plagioclase and 2% opaque minerals. The opaque minerals are mostly iron-nickel alloys with that are visible in reflected light as defined, metallic grains (Figure 27).

4.8.7 Shock features

Shock features were observable within DGR-035. Olivine grains were subhedral - anhedral on average, with undulose extinction and some mosaicism within the sample. Barred olivine chondrules were present and abundant within the sample with euhedral olivine and pyroxene grains and undulose extinction. No maskelynite was found within the sample. Planar shock fractures could be seen in large, more euhedral grains of olivine shown in Figure 28. Overall, planar fractures were visible in <25% of all olivine grains.

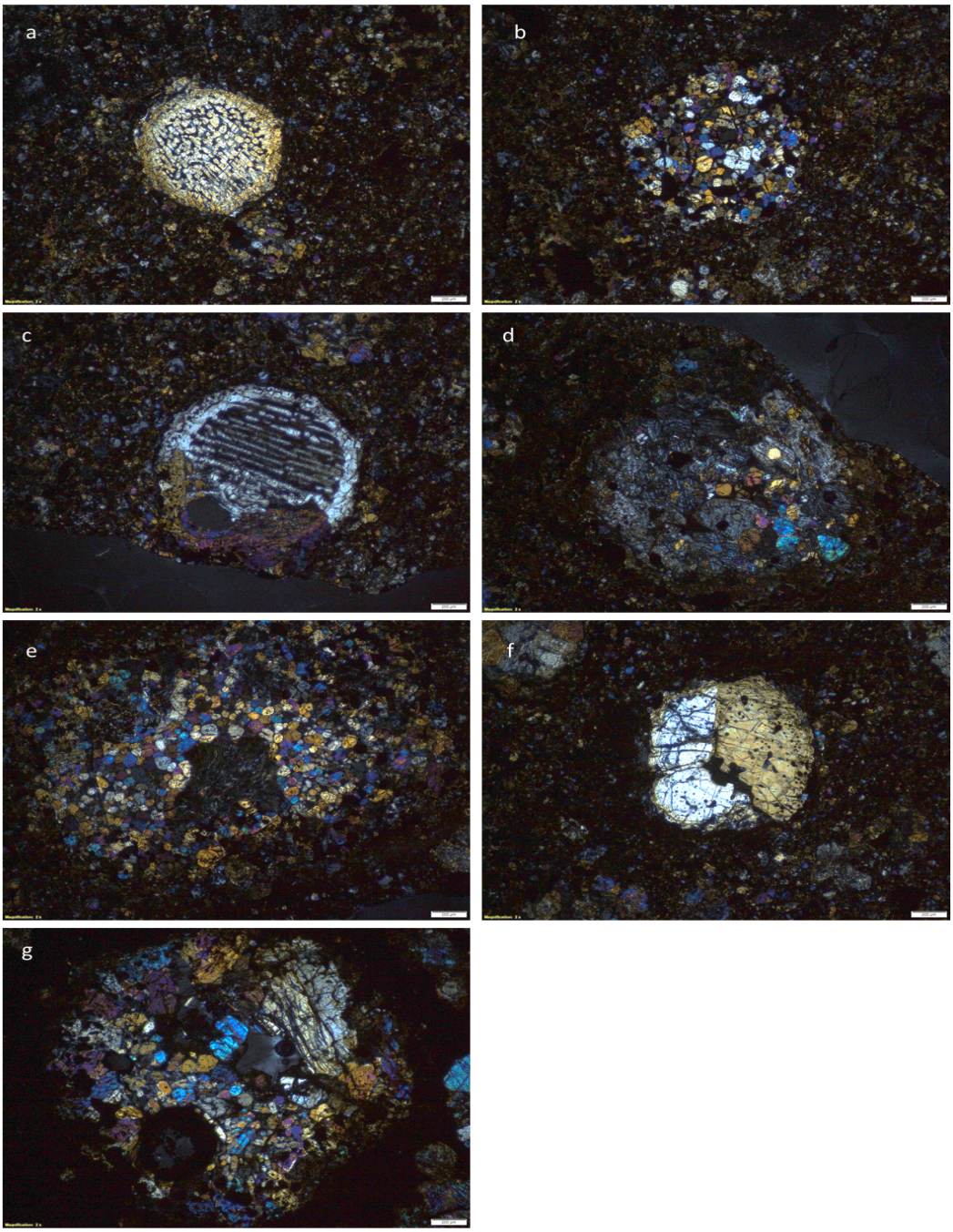


Figure 24: Chondrules imaged in DGR-035. (a) Barred pyroxene (BP) chondrule with interstitial plagioclase. Scale bar: 200 µm; (b) Porphyritic olivine chondrule (PO). Scale bar 200 µm; (c) Barred olivine and pyroxene chondrule (BOP). Scale bar 200 µm; (d) Pyroclastic pyroxene (PP) chondrule with plagioclase and olivine. Scale bar 200 µm; (e) Porphyritic olivine (PO) chondrule with interstitial pyroxene. Scale bar 200 µm; (f) Porphyritic pyroxene chondrule (PP). Scale bar 200 µm; (g) Porphyritic pyroxene - olivine chondrule. Scale bar 200 µm.

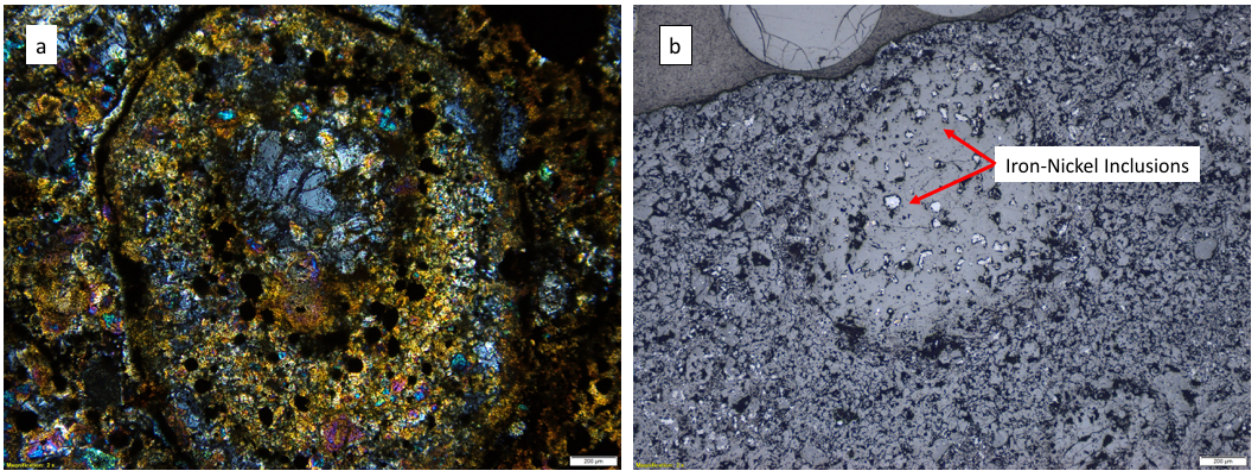


Figure 25: (a) Crossed-polarized image of a chondrule in DGR-035 with not well defined rim. (b) Reflected light image of a chondrule in DGR-035 with iron-nickel inclusions. Scale bars: 200 μm.

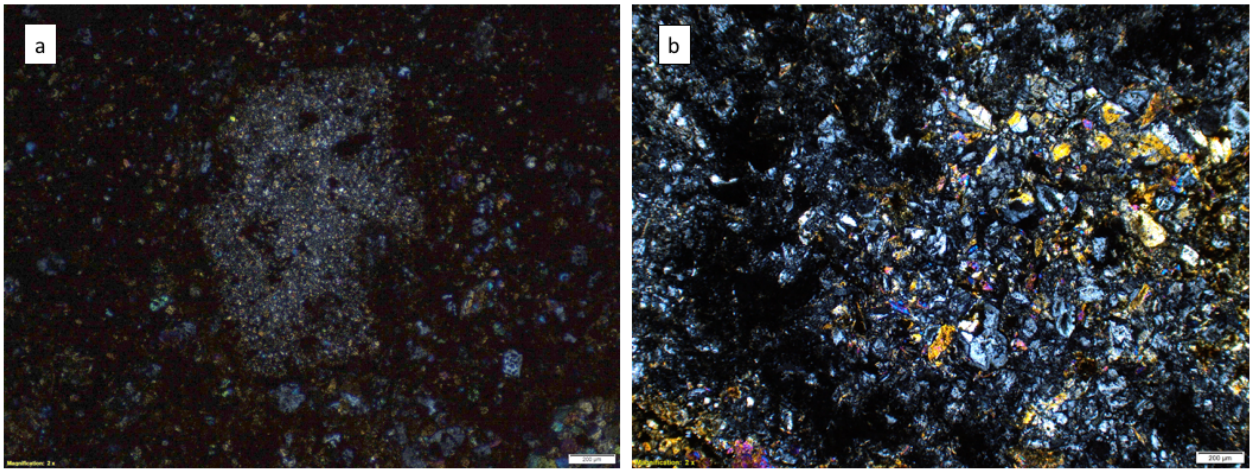


Figure 26: (a)Crossed-polarized light image of a fine-grained CAI in DGR-035. (b) Crossed-polarized light image of a coarser grained CAI in DGR-035. Scale bars: 200 μm.

4.8.8 Weathering features

Red-brown staining of the thin section of DGR-035 was visible in PPL, as well as slight staining of some silicate grains. Other than some oxidation staining on grains and around the rims of chondrules, weathering evidence was limited. There were no veins infilled with carbonates or phylosillicates in the sample.

4.8.9 EPMA geochemistry

Major and minor elements were analyzed in olivine, pyroxene and plagioclase grains within the matrix, chondrules and CAIs when present. Fayalite compositions for olivine were calculated in mol% and ranged from $Fa_{0.34-35.49}$ with an average of $Fa_{20.83}$ (Table 3). Olivine homogeneity was calculated using Eq. 1, and was found to be 60-90%.

Orthopyroxene and clinopyroxene were abundant in this sample and both were analyzed using EMPA (Table

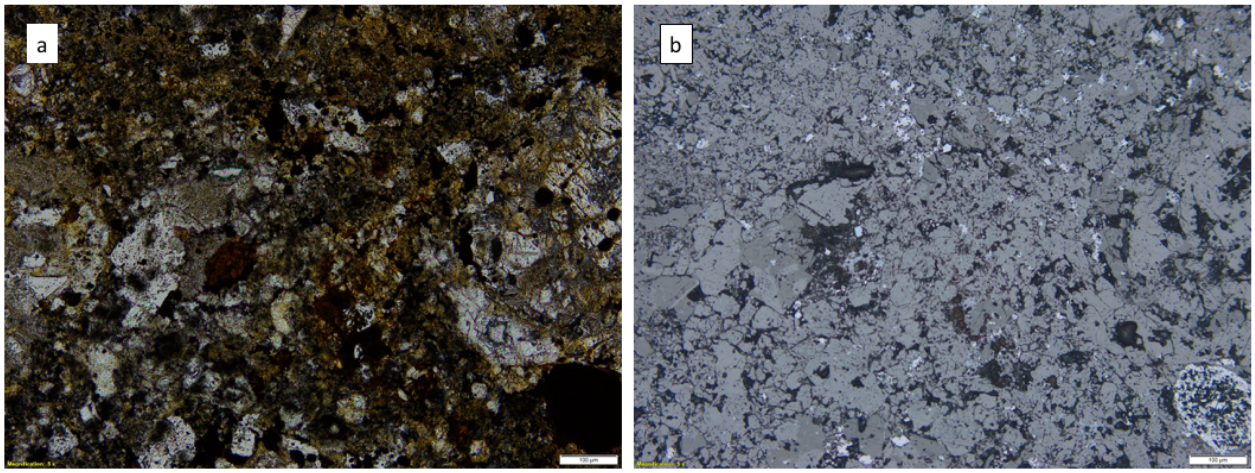


Figure 27: (a) Plane-polarized light microscopy image of matrix in DGR-035; (b) Reflected light microscopy image of matrix in DGR-035 in same location. Scale bars: 100 μm.

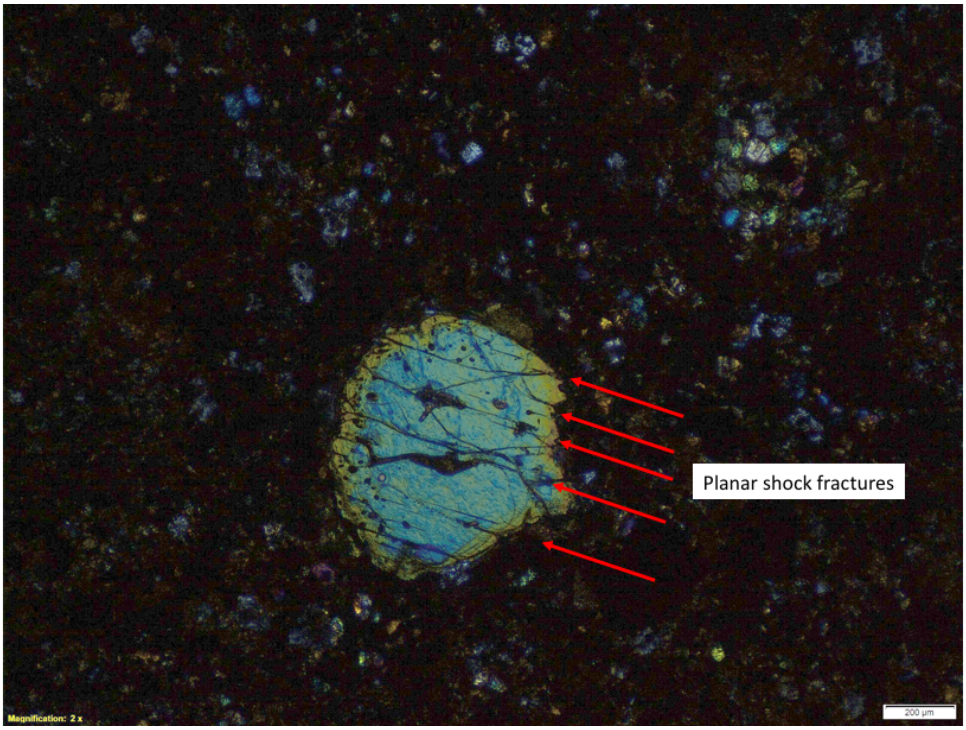


Figure 28: Olivine in DGR-035 displaying planar shock fractures. Scale bar: 200 μm.

3). Pyroxene geochemistry was plot on a enstatite-ferrosilite-wollastonite ternary diagram to determine composition from chondrules, matrix and the average whole rock. The orthopyroxene in DGR-035 was mainly enstatite, where as the clinopyroxene compositions ranged from augite to diopside, with the whole rock average being augite in composition (Figure 29).

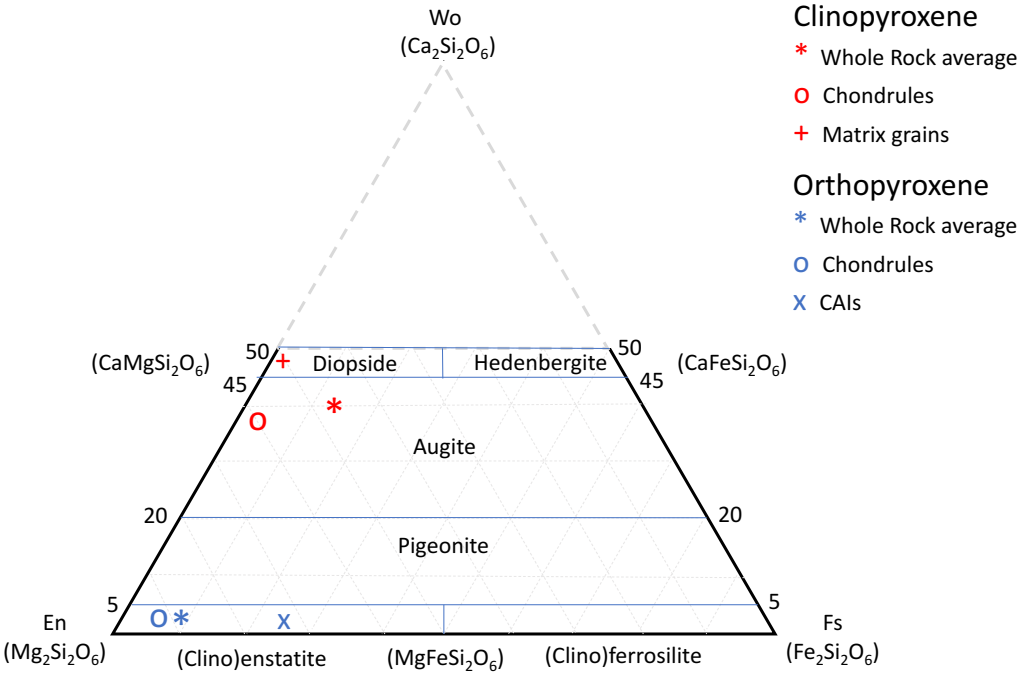


Figure 29: Enstatite, ferrosilite, and wollastonite end member plot for pyroxene in DGR-035. Image modified from [Deer et al., 1992]. Pyroxene grains from CAIs, chondrules and whole rock average were plot.

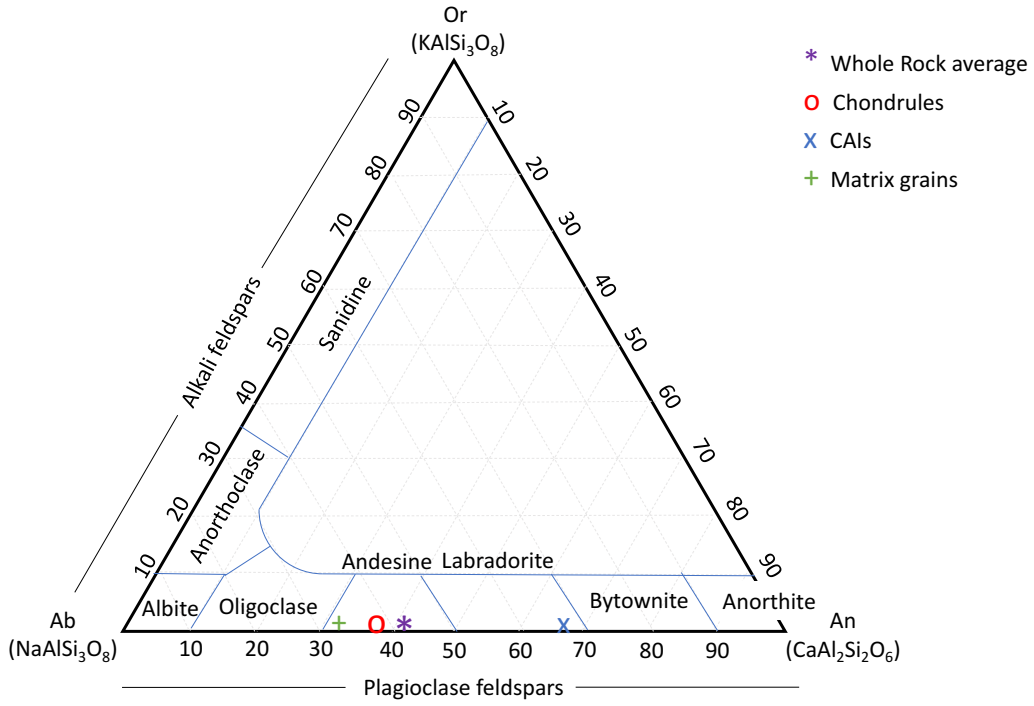


Figure 30: Albite, Anorthite and Orthoclase end member plot for feldspar in DGR-035. Image modified from [Deer et al., 1992]. Feldspar grains from CAIs, chondrules and whole rock average were plot.

Feldspar was found within the chondrules and CAIs of DGR-035 and was analyzed using EPMA (Table 3).

Feldspar geochemistry was plot on a albite-anorthite-orthoclase ternary diagram to determine composition from chondrules, matrix and the everage whole rock. The average feldspar within the sample fell into the composition range of andesine. The plagioclase from the CAIs however were labradorite in composition (Figure 30). All feldspars were in the plagioclase range within DGR-035, no alkali feldspars were found.

Table 3: EPMA results for olivine, pyroxene and plagioclase in DGR-035

Mineral	Number of Samples	Compositional Range (Mol%)	Average (Mol%)	Mean Deviation (Mol%)
Olivine	35	$Fa_{0.34-35.49}$	20.83	11.34
Orthopyroxene	9	$Fs_{0.66-23.06}$ - $En_{76.32-98.27}$ - $Wo_{0.63-15.30}$	$Fs_{9.44}$ - $En_{86.86}$ - $Wo_{3.70}$	$Fs_{5.78}$ - $En_{6.50}$ - $Wo_{2.61}$
Clinopyroxene	18	$Fs_{1.19-15.93}$ - $En_{34.13-86.47}$ - $Wo_{12.17-49.93}$	$Fs_{6.67}$ - $En_{52.88}$ - $Wo_{7.30}$	$Fs_{4.08}$ - $En_{10.32}$ - $Wo_{7.30}$
Plagioclase	28	$An_{19.94-99.90}$ - $Ab_{0.10-78.15}$ - $Or_{0-2.17}$	$An_{42.41}$ - $Ab_{56.47}$ - $Or_{0.52}$	$An_{19.65}$ - $Ab_{19.21}$ - $Wo_{0.52}$

4.8.10 Discussion and Classification

A classification workflow (Figure 21) summarizes the steps taken to determine a group for each meteorite. Petrologic type was then determined using Figure 12 and Mcsween [1977]. Based on the presence of chondrules and CAIs within the sample DGR-035, it is confirmed to be a Carbonaceous chondrite. With the size (average 0.88 mm), and abundance of chondrules (about 15 modal %), and a recrystallized matrix occurring in about 70% of the sample, DGR-034 falls into the category of a CK type carbonaceous chondrite based average petrologic characteristics of the major chondrite groups table in Weisberg et al. [2006].

To determine petrographic type, the modal mineralogy of the matrix, chondrules and CAIs were assessed. DGR-035 appears to be a petrographic type 4 based on the texture and compositional analyses of the sample [Kallemeyn et al., 1991]. Olvine was not at equillibrium within this sample, which is not expected of a type 4 CK chondrite. However, due to texture and features visible in the sample discussed in this section, it was concluded that DGR-035 was of petrographic type 4. Olivine was abundant and mainly subhedral with planar shock fractures and undulose extinction. Clinopyroxene and orthopyroxene were present in the sample with undulose extinction, as well as some 5-50 μm plagioclase grains. The matrix was <20-100 μm in size and consisted mostly of recrystallized olivine, pyroxene and plagioclase grains. Calcium-aluminum-rich inclusions were present and contained fine-grained to 100 μm sized grains of pyroxene and plagioclase. The diameter of plagioclase measured by EMPA was between 5 and 50 μm, with an average of about 20 μm. Chondrules ranged from well-defined to poorly defined with turbid glass within barred chondrules, indicating that the sample was going through metamorphic alteration but not enough to destroy the shape of all the chondrules. If the sample was a petrographic type 5, we would expect to see recrystallized glass starting to form in chondrules instead of mesostasis glass, and very poorly defined chondrules. Calcium-aluminum-rich inclusions are still present in the sample suggesting petrographic type 4. Shock evidence places the sample DGR-035 in the S2 shock category, having been subjected to <5-10 GPa of pressure [Scott et al., 1992]. Minor oxidation suggests DGR-035 has been minimally altered by terrestrial weathering, with the main

weathering evidence being 20-60% of metal content being replaced by oxides, making the sample W2 on the weathering scale for chondrites [Wlotzka, 1993].

4.8.11 Conclusion

By observing and analyzing the type hand specimen, cut section, and thin section of ROM chondritic sample DGR-035, a classification was made of a carbonaceous chondrite type CK4 with S2 shock and W2 weathering. This classification has been submitted to the Meteoritical Society to be reported and approved for renaming. This classification will allow future scientific study and reporting on this sample and provide more information about the rare meteorite group, carbonaceous chondrites.

5 Methodology and experimental techniques

This study was accomplished using a four-step approach (Figure 31). The first stage of this study was characterization. During this stage a range of carbonaceous chondrites were chosen for this study. The samples range in classification from CV, CM and CK. Allende and Murchison have been extremely well studied, whereas DGR-034 and DGR-035 were unclassified samples, with no previous publications. The unclassified samples were characterized during this study to better understand composition before spectral analysis. Second, investigation using spectral techniques was accomplished. Raman spectroscopy, LIF spectroscopy and EDS were used to complete this phase. Spectral maps using these techniques were created for two, millimter-sized features (one chondrule and one CAI) for each sample. It was important for this study to not only use techniques that were possible flight instruments, but also a technique that was fairly standard in laboratories on Earth. This was accomplished by using EDS, an instrument standard for geologic samples in laboratory settings, in addition to Raman and LIF techniques. Thirdly, because there are no LIF mineral databases available at the time of this study, a mineral database and small amino acids database were created in order to identify constituents within LIF spectral maps. Finally, identification of constituents were accomplished for each feature. Identification of minerals was completed using the RRUFF mineral database [Lafuente et al., 2016] for Raman spectra, and the LIF mineral database from this study for LIF spectra. EDS point analyses were quantified and converted from atomic percent to weight percent oxide stoichiometrically and compared to known concentrations for common minerals within Deer et al. [1992].

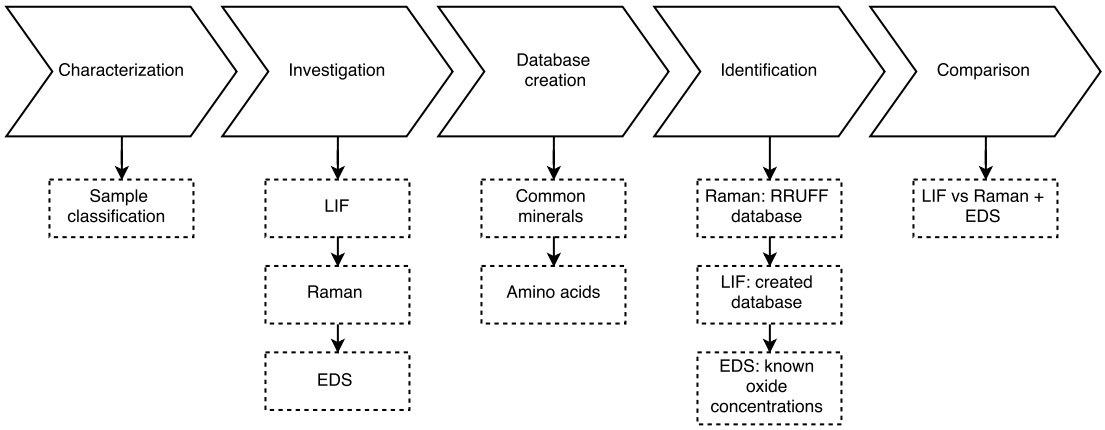


Figure 31: Four-step method for completion of study: Characterization of samples; investigation of samples using LIF, Raman and EDS; database creation for LIF identification; identification of minerals in samples using different databases; and comparison of investigation techniques.

5.1 Laser-induced fluorescence (LIF) spectroscopy

The LIF spectroscopy setup described in Chapter 3.5 was used for all fluorescence spectra and maps acquired in this study. A pulsed UV laser at 266 nm was used at a repetition rate of 5 kHz. Andor Solis was used to manage the digital iCCD setting and cooling. The iCCD was cooled to -25°C for most analyses, unless there was significant noise, then the camera was cooled to -35°C using a ThermoTek T255P solid state recirculating chiller set to 16°C. Full vertical binning (FVB) was used to create all fluorescence spectra, which assigns a value to each of the 1024 pixel columns on the CCD sensor to create a linear sensor. FVB allows multiple accumulations to be combined into a single spectra. The x-axis was calibrated using an Ocean Optics HG-1,

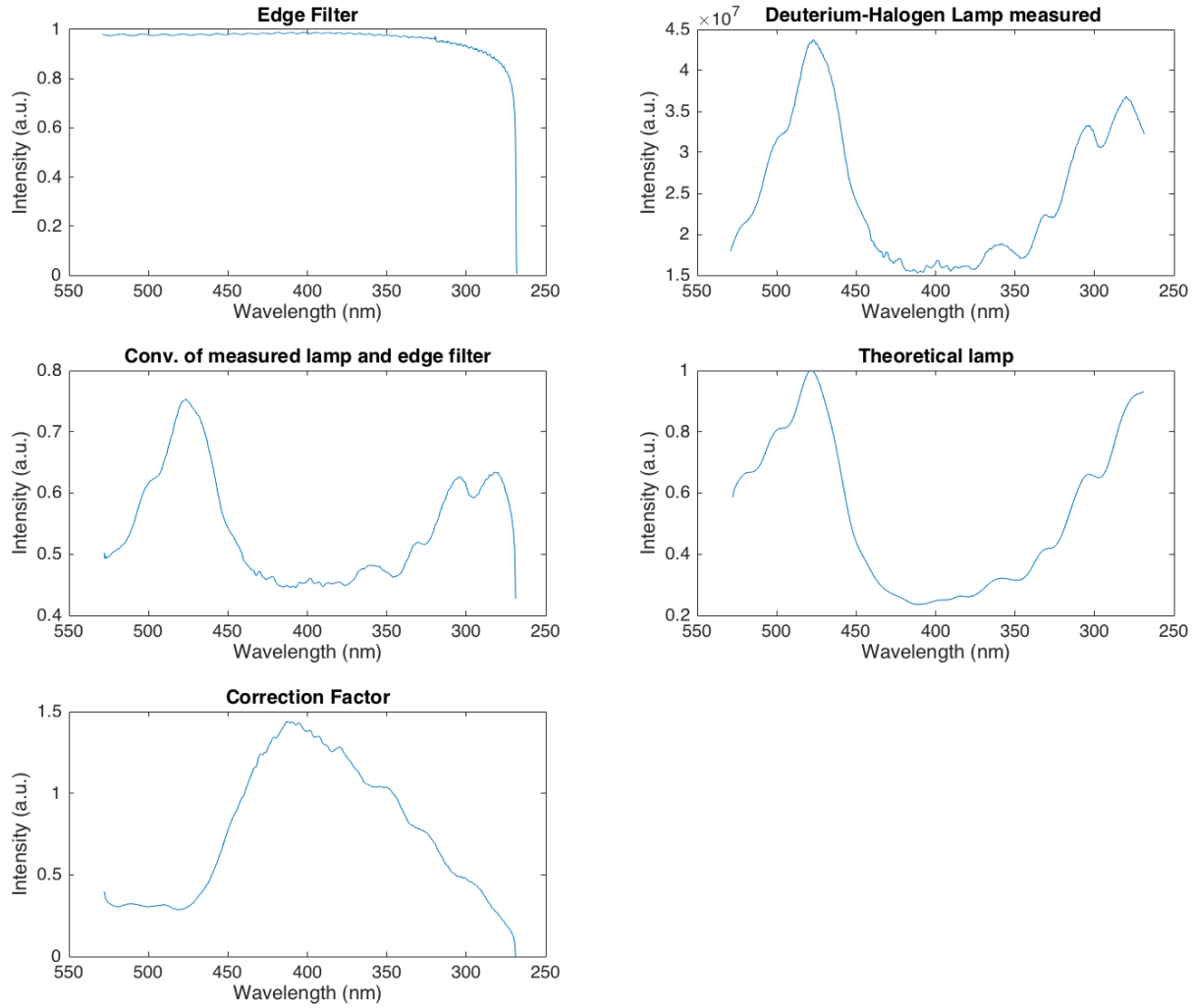


Figure 32: SEMRock Edge filter 266 nm transmission; Deuterium-Halogen lamp measured using Shamrock spectrograph; convolution of measured lamp and edge filter transmission to mimic spectra collected through full LIF setup; theoretical lamp standard from Ocean Optics; correction factor, calculated by Eq. 2.

mercury-argon calibration source with lines from 266-922 nm. An Ocean Optics DH3 Plus UV-VIS-NIR deuterium-halogen calibration source was used to obtain a relative intensity correction factor to offset the response curve from the edge filter, and correct for any discrepancies from the spectrometer. The fiber cable from the collection optics in the LIF setup was connected to the DH3 deuterium-halogen lamp to obtain

spectra. This spectra was then convolved with transmission data from the SEMRock 266 nm edge filter. This convolved spectra was used as a representation of our 'measured' data. This measured data was then divided by the theoretical lamp output provided by Ocean Optics to obtain a correction factor (Equation 2). Each spectra and time-resolved plot presented in this work has been corrected using this correction factor by multiplying the measured spectra by the correction factor (CF) (Figure 32).

$$\begin{aligned} \text{measured lamp} &= \text{measured lamp spectra} \circledast \text{edgefilter response} \\ \text{CF} &= \frac{\text{measured lamp}}{\text{theoretical lamp}} \\ \text{corrected spectra} &= \text{CF} * \text{measured spectra} \end{aligned} \tag{2}$$

5.1.1 Acquisition techniques for single spectra

Single acquisitons of spectra were taken at points of interest in spectral maps, and of the monomineralic samples. Organics tend to have shorter fluorescence lifetimes than minerals, and often have sharper peaks, therefore organics are usually imaged better with a short gate width to reduce noise. Minerals on the other hand, tend to have longer fluorescence lifetimes than organics, and have broader fluorescence peaks. Therefore, minerals are imaged better with a longer gate width setting. Points of interest from 2D maps were analyzed using both short (10 ns) and long (100 ns) gate widths to ensure proper identification. The monomineralic samples for the fluorescence database were analyzed with a gate width of 100 ns, with 1200 accumulations, meaning the acquisition was made over one minute. All spectra were acquired using a gain of 3000, and exposure time of 0.05 seconds.

5.1.2 Time resolved fluorescence

Time-resolved fluorescence spectra were collected at points of interest from spectral maps, and of each monomineralic sample. 'Kinetic' mode in Andor Solis allows spectra to be taken over a set period of time by defining a gate step and the length of the series. Kinetic mode is essentially a series of freeze-frames of a long gate width spectral accumulation, where the spectra can be viewed in three dimensions: time, wavelength and intensity. Kinetic mode was used in the Andor Solis software, with 200 accumulations per spectra, a series length of 200, and a gate step of 0.1 ns. These parameters yielded 200 spectra over the course of 20 ns. TTL gate width was set between 3 ns and 5 ns depending on the sample. These data are saved as a text file with 1024 rows of wavelength data in the first column, and 1024 rows of intensity values in columns 2-21. Each column (after the first) represents a 0.1 ns time step. These data are then processed using Matlab, and displayed as 3D surface maps, or 2D contour maps showing the relationship of fluorescence intensity at different wavelengths with respect to time.

5.1.3 LIF 2D mapping techniques

Two-dimensional spectral maps were created using LIF for this study by collecting spectra at many points over an area of interest. Each spectra makes up 1 pixel in a mapping grid. 2D maps were acquired using a Labview interface built by Eshelman [2016]. The program interfaces to the iCCD, motorized stage and a THUM humidity sensor. Within the program, the iCCD can be turned off and on and cooled, while also providing the same digital gating and acquistion settings as the Andor Solis software. This way, gate width, gain, and gate delay can all be adjusted for map acquisitions. A Point Grey Flea 3 webcam with Flycap2

software is used to observe the laser interaction point on the sample. Once a feature of interest is chosen (such as a chondrule or CAI) the laser spot is moved to the top right corner of that feature to begin mapping. For the 2D maps in this study, the laser would be positioned to create a rectangular map as close to the feature borders as possible, while including some matrix material. The feature of interest on the sample was measured prior to LIF analysis using a stereoscopic microscope and ruler to determine the path length for the laser. The path length was set using number of rows and columns in the Labview software, while maintaining a fixed step size. The optimal step size for this system was determined to be 60 μm when considering the spot size and average distance that is traveled when imaging features to limit acquisition time. The mapping area changed for each feature depending on size, however spot size, step size and iCCD parameters remained the same for each. Gain was set to 3000, no gate delay was used, and exposure was 0.05 seconds. Gate width was set to 100 ns, to ensure that all fluorescence was imaged. Multiple accumulations were taken for each spectra, which helps with noise reduction, but no background subtraction was used. Between 40 and 80 accumulations were used depending on the sample, with an exposure time of 0.05 seconds, therefore each point or spectra in the map takes 2 or 4 seconds to collect. The map is then automated by the Labview program, collecting spectra at each point down each column and across the consecutive rows until it reaches the final point. The motors are then returned to the starting position at (0,0). The files are then viewed at the same time to differentiate peaks of interests. Points of interest were chosen based on unique peaks, or intense peaks of main components to be analyzed further using longer single acquisitions with different gate widths, and time-resolved fluorescence. LIF spectral maps had a collection time between 1 and 5 hours.

5.1.4 LIF mapping analyses

Once the map is completed, each spectra is saved with its coordinates as the title as text files. The text files are made up of two columns: wavelength (nm) and intensity (arbitrary units). These files are then viewed as spectra together using Labview or Matlab. This allows for trends to become visible, and enables peak differentiation for analyses. Unique peaks are recorded, and spectra is then analyzed using Matlab. The spectral points are transformed into a raster image, where each pixel in the image is a single spectra. Features are then spatially mapped by inputting the wavelength range for a peak of interest and its width. The code then finds the maximum intensity in the range and normalizes the other spectra by that intensity. When the data are displayed, the brightest points have the greatest intensity amongst the spectra in the image, and the dark points have the lowest intensity.

Points of interest from maps were analyzed using time-resolved fluorescence as well as short and long fluorescence. These spectra were then compared to that of the monomineralic database.

5.1.5 LIF monomineralic database spectra

Single spectra (long gate width), and time-resolved fluorescence spectroscopy were taken of each monomineralic sample. Several points on each sample were analyzed to ensure that the spectra was not that of an impurity or inclusion. For single spectra acquisitions, a 100 ns gate width was used with an accumulation time of 1 minute. Time-resolved spectra for these samples was collected with a TTL width of 5 ns.

5.2 Raman Spectroscopy

5.2.1 Raman 2D mapping techniques

Raman spectroscopy was carried out at the Royal Ontario Museum using a Horiba LabRAM Aramis micro-Raman spectrometer with an excitation wavelength of 532 nm. A silica standard was used for calibration. Features of interest were located using a video feed and the 10x microscope objective within the system. Once the feature was found, a stitched image was acquired of the sample area. The Raman mapping area was then selected. The microscope objective allowed for a small spot size with enough field of view to have the surface of a millimetre-sized feature in focus. A step size of 50 µm was chosen to optimize resolution and minimize data collection time. Multiple accumulations (4) were taken of each point to reduce noise. These maps took 6-30 hours to collect using a resolution of 50 µm, and an extended Raman window of 100-2000 cm^{-1}. LabSpec6 software was used to process the map data when finished. All spectra from the map were normalized and curve fitted to the lowest order polynomial possible using spectra with the most amount of noise to eliminate background noise and fluorescence. Peaks can then be highlighted using the selection tool, and spectra with high intensity values for said peak were used as standards to map out a feature. Spectral maps of the features were then saved as images, along with all the processing data and peaks used as standards for processing.

5.2.2 Raman spectral analyses

Peaks of interest were saved from spectral maps as text files with 2 columns, with the first column entries being wavenumber (cm^{-1}), and the second column as intensity (arbitrary units). These spectra were then analyzed using Crystal Sleuth software and the RRUFF database [Lafuente et al., 2016]. Each spectra was compared to the best matching spectra from the RRUFF database using the software. Often multiple minerals were found to be in one spectra, so individual peaks, or groupings of peaks were run through the RRUFF database and matched with likely spectra.

5.3 Scanning electron microscope (SEM)

A Tescan VEGA3 scanning electron microscope (SEM) was used to collect elemental maps of the same feature areas acquired by LIF and Raman. Calibration of the system was completed using a copper standard. To prevent contamination, he samples were not coated with carbon or gold. Meteorite slabs were clamped to a small stainless steel stage that was then mounted into the ESEM chamber. The chamber was then pumped to 50 Pa. High vacuum mode was used, with a charge of 20-25 kV. Beam intensity was set to 10.

5.3.1 Back-scattered electron images

A back scattered electron (BSE) detector was used to obtain qualitative, grey-scaled images of each feature by collecting high-energy electrons caused by elastic scattering from elements that have interacted with a stream of electrons. BSE images produce elemental, grey-scale images based on element weight, where high atomic number elements appear dark, and low atomic number elements appear bright. These images were collected over several minutes for higher resolution.

5.3.2 Electron dispersive spectroscopy (EDS) mapping

The SEM at York University is equipped with a Bruker energy-dispersive X-ray spectrometer (QUANTAX EDS) to obtain semi-quantitative data and elemental maps. Maps were acquired using the same ESEM parameters as previously stated. ESPRIT 2.1 software was used to collect EDS data. Maps were collected with a 2000 x 2000 pixel resolution, 16 µs dwell time, and a 30 kcps throughput. Maps were collected for two hours, with an average detection of 5000 cps. Major and abundant minor elements were chosen to be represented in each compositional map.

5.3.3 EDS point analyses

As soon as maps were completed, points of interest were selected to obtain semi-quantitative EDS point analyses. These point analyses obtained elemental abundances in specific areas to help identify major mineral phases. Point analyses were exported in atomic percent, which were then converted to weight percent oxide for rough mineral identification.

6 Results

6.1 EDS maps and quantification results

EDS maps resulted in a clear image of Allende chondrule (Figure 33), including mineral boundaries and crystal habits if the grains were large enough. Olivine end-member forsterite (Fo), and orthopyroxene member enstatite (En) were identified using EDS point analyses from the EDS map (Table 4). Not all points from the analyses matched mineral compositions due to grain size and accuracy of EDS. Even with this resolution, individual grains cannot always be resolved. However, elemental abundances provide an idea of what assemblages there may be present, even if a specific mineral isn't identified. The grain size is quite small, so in order to resolve features, a resolution of 2000 x 2000 pixels was used. EDS point analysis is semi-quantitative, therefore EDS results in rough mineral identification. Elements from emission spectra can fall near each other, and some X-rays aren't scattered back into the detector, skewing the quantitative results. Within the Allende chondrule, calcium-aluminum silicates appear to dominate the interstitial space between olivine bars within the Allende chondrule, and iron-nickel sulphides appear to surround the feature as a rim.

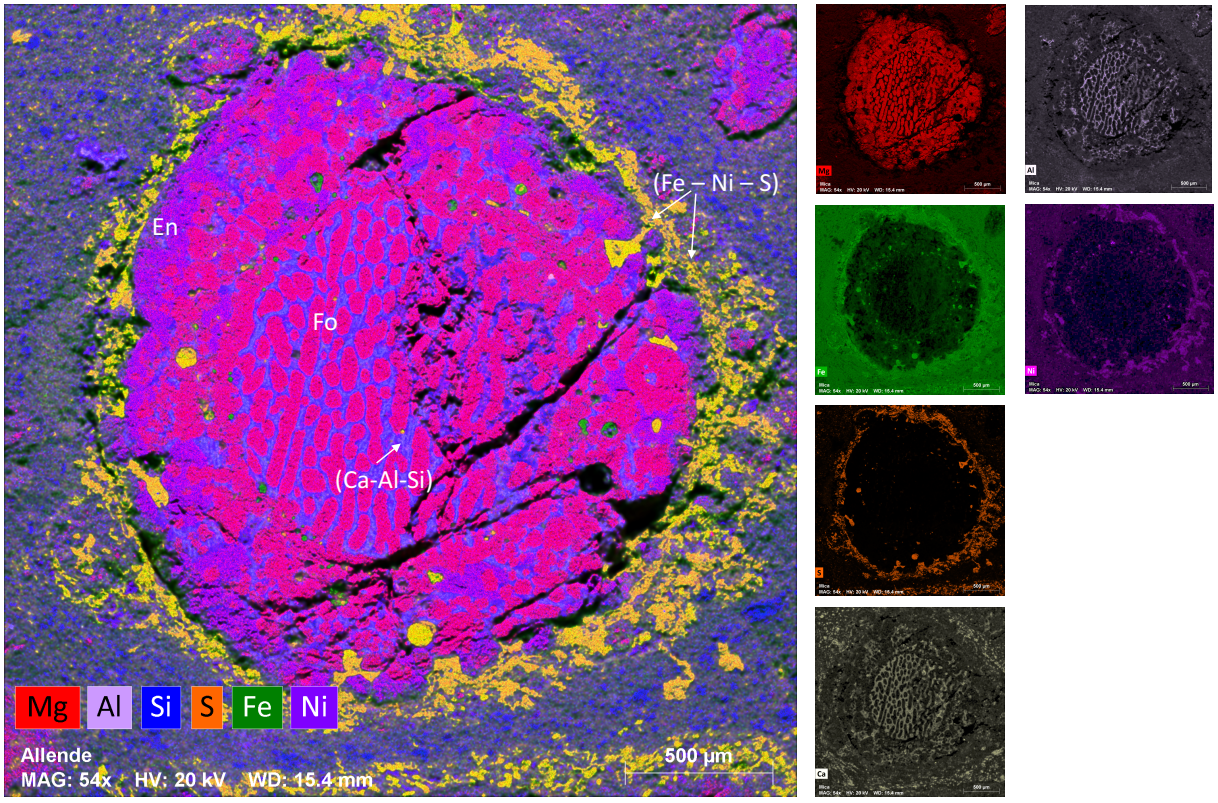


Figure 33: EDS spectral map with major and minor elements displayed for Allende chondrule. Minerals forsterite (Fo), and enstatite (En) were identified from EDS point data. nickel-iron sulphides, and calcium-aluminum rich areas are also labeled. Individual elements are displayed to the right of the main image.

Table 4: Examples of EDS point analyses resulting in mineral identification for Allende chondrule. Results reported in weight percent oxide.

Mineral	SiO_2 (%)	MgO (%)	NiO (%)
Forsterite	39	61	0
Enstatite	62	38	–

EDS maps resulted in a clear image of Allende CAI and some surrounding chondrules (Figure 34). Olivine end-member forsterite (Fo), clinopyroxene member jadeite (Jd), and nepheline (Ne) were identified using EDS point analyses from the EDS map (Table 5). Calcium-aluminum silicates appear to dominate the CAI, with some sodium. The CAI appears to be magnesium and iron poor, with magnesium dominating the surrounding features, and iron occupying the surrounding matrix.

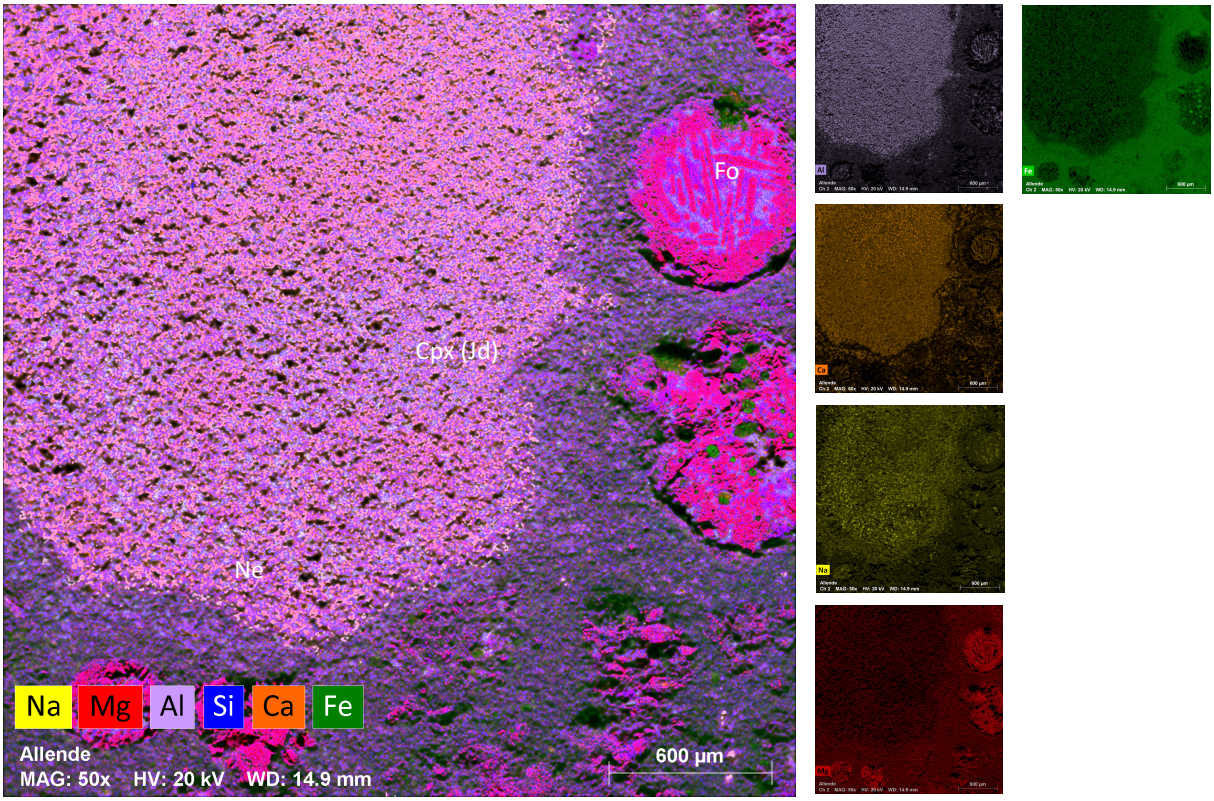


Figure 34: EDS spectral map with major and minor elements displayed for Allende CAI. Minerals forsterite (Fo), jadeite (Jd), and nepheline (Ne) were identified from EDS point data. Individual elements are displayed to the right of the main image.

Table 5: Examples of EDS point analyses resulting in mineral identification for Allende CAI. Results reported in weight percent oxide.

Mineral	SiO_2 (%)	MgO (%)	Al_2O_3 (%)	Na_2O (%)	K_2O (%)
Forsterite	39	61	–	–	–
Jadeite	63	–	26	11	–
Nepheline	65	–	–	30	6

EDS maps resulted in a clear image of Murchison chondrule (Figure 35), including mineral boundaries and crystal habits if the grains were large enough. Orthopyroxene member enstatite, and augite (Aug) were identified using EDS point analyses from the EDS map (Table 6). Calcium-rich phases are present within the surrounding matrix of Murchison chondrule.

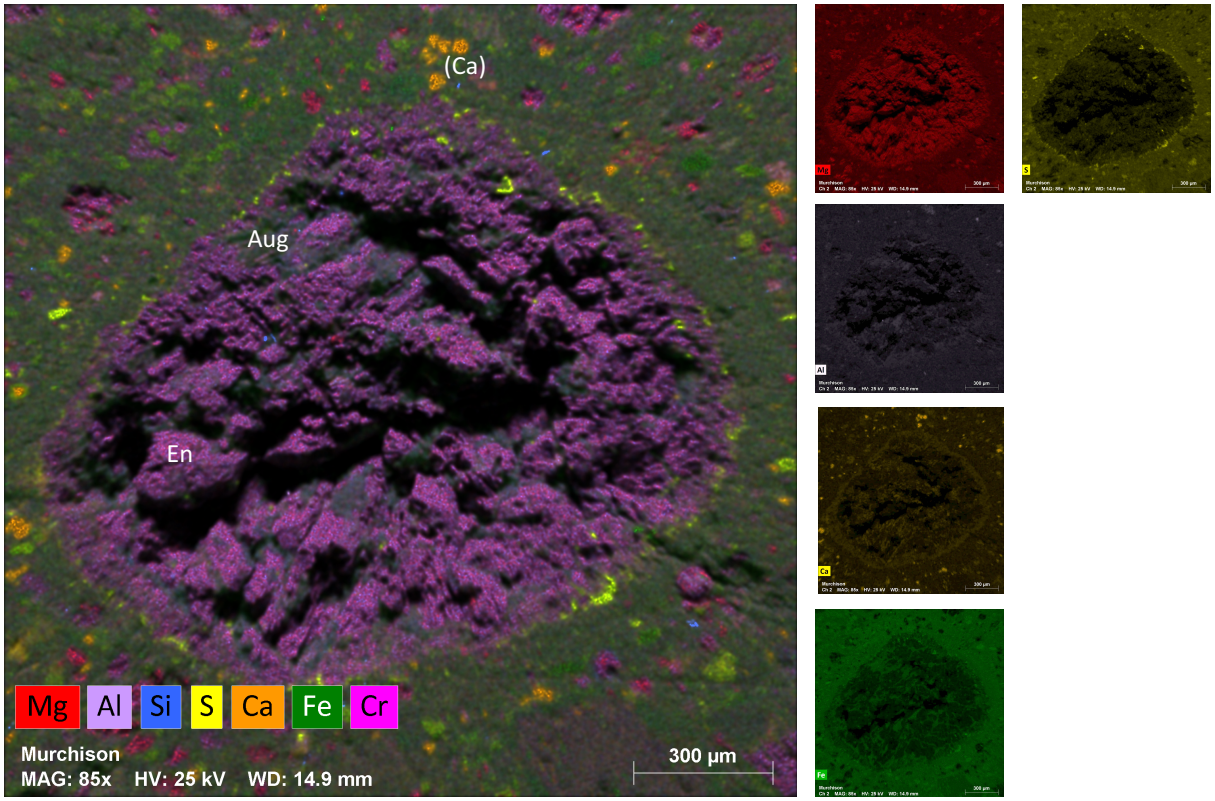


Figure 35: EDS spectral map with major and minor elements displayed for Murchison chondrule. Minerals enstatite (En), and augite (Aug) were identified from EDS point data. Individual elements are displayed to the right of the main image.

Table 6: Examples of EDS point analyses resulting in mineral identification for Murchison chondrule. Results reported in weight percent oxide.

Mineral	SiO_2 (%)	MgO (%)	NiO (%)	CaO (%)	FeO (%)
Enstatite	69	31	–	0	–
Augite	57	20	–	16	7

EDS maps resulted in a clear image of Murchison CAI (Figure 36), including mineral boundaries and crystal habits if the grains were large enough. Orthopyroxene member ferrosilite (Fs), olivine end-member forsterite (Fo), and clinopyroxene member diopside (Di) were identified using EDS point analyses from the EDS map (Table 7). Calcium-aluminum rich minerals dominate the very fine-grained CAI, whereas magnesium, iron and sulphur are abundant in the surrounding features and matrix.

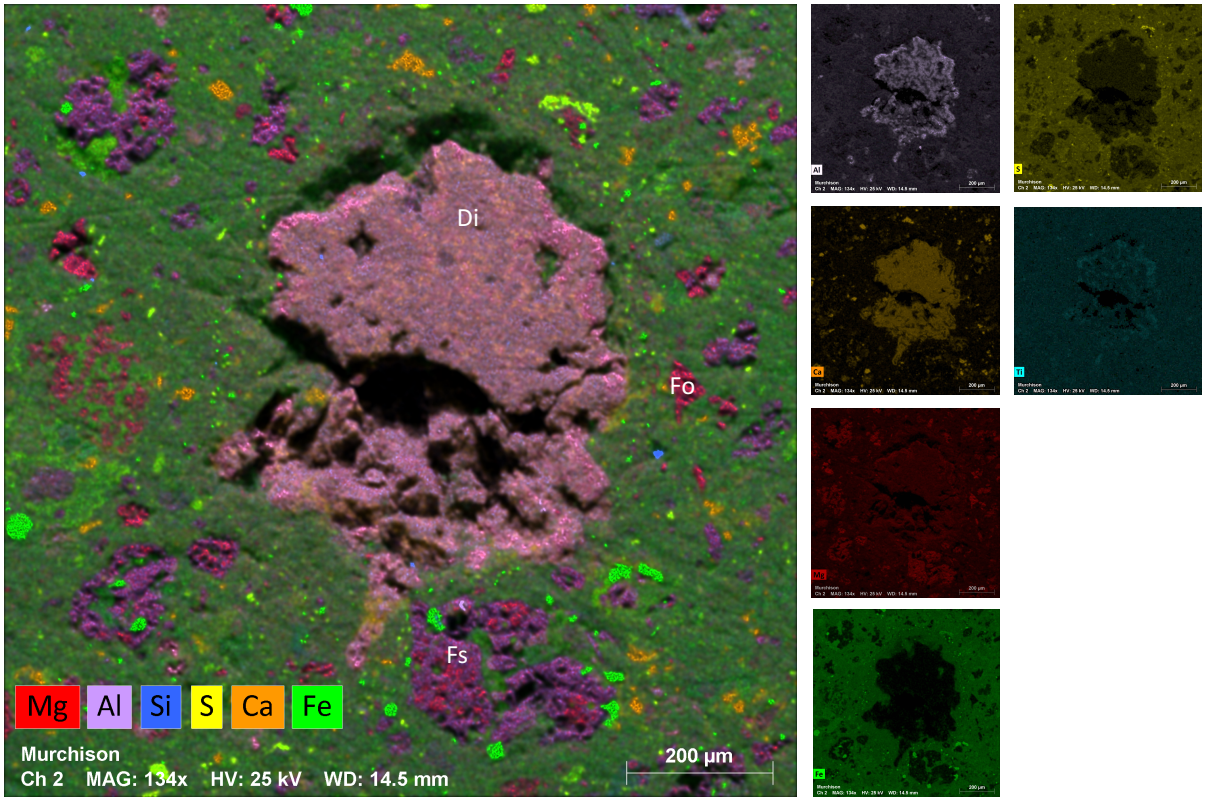


Figure 36: EDS spectral map with major and minor elements displayed for Murchison CAI. Minerals forsterite (Fo), ferrosilite (Fs), and Diopside (Di) were identified from EDS point data. Individual elements are displayed to the right of the main image.

Table 7: Examples of EDS point analyses resulting in mineral identification for Murchison CAI. Results reported in weight percent oxide.

Mineral	SiO_2 (%)	MgO (%)	FeO (%)	CaO (%)
Forsterite	30	71	–	–
Ferrosilite	32	28	41	–
Diopside	59	16	–	25

EDS maps resulted in a clear image of DGR-035 chondrule (Figure 37), including mineral boundaries and crystal habits if the grains were large enough. Orthopyroxene member enstatite (En), and ferrosilite (Fs) were identified, as well as clinopyroxene member augite (Aug), olivine (Ol), and magnetite (Mt) using EDS point analyses from the EDS map (Table 8). Iron-sulphides appear to be abundant within the DGR-035 chondrule along with the minerals identified. There also appears to be an aluminum - rich phase located interstitially between olivine and ferrosilite grains.

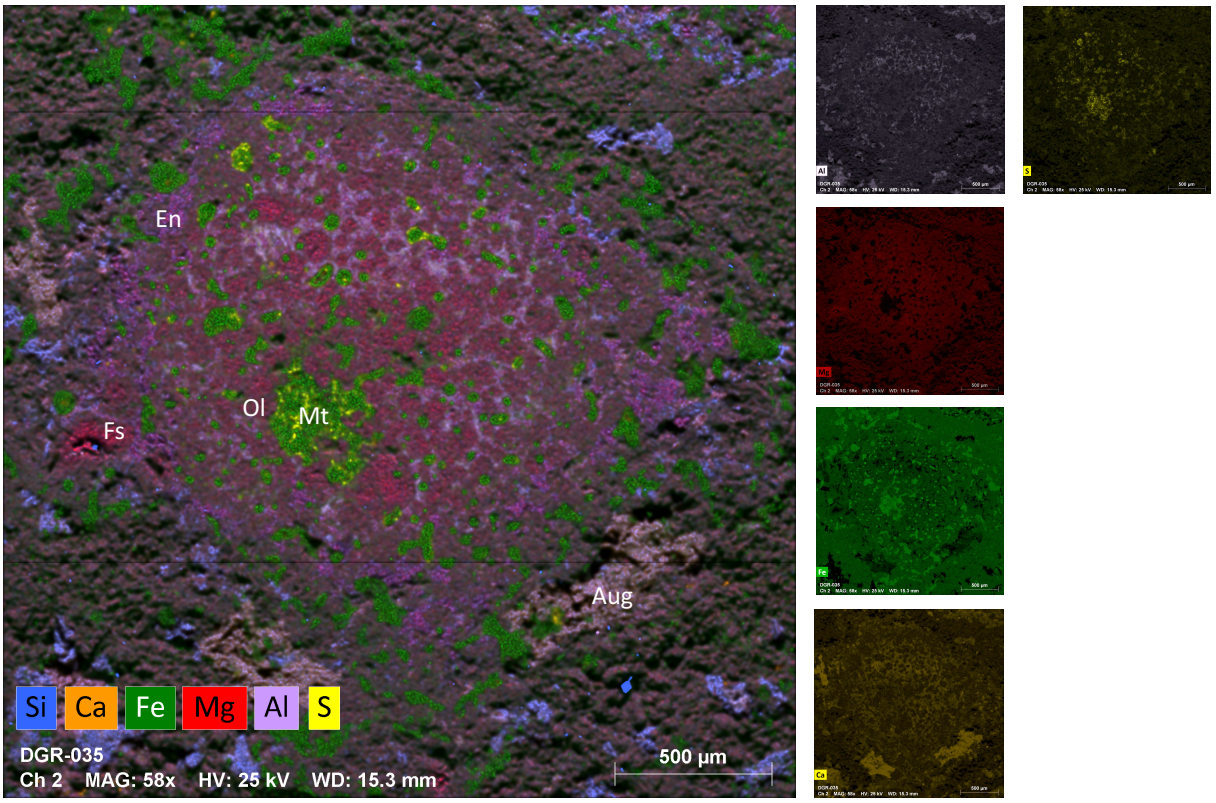


Figure 37: EDS spectral map with major and minor elements displayed for DGR-035 chondrule. Minerals olivine (Ol), enstatite (En), ferrosilite (Fs), magnetite (Mt), and augite (Aug) were identified from EDS point data. Individual elements are displayed to the right of the main image.

Table 8: Examples of EDS point analyses resulting in mineral identification for DGR-035 chondrule. Results reported in weight percent oxide.

Mineral	SiO_2 (%)	MgO (%)	FeO (%)	CaO (%)	Al_2O_3 (%)
Olivine	34	44	–	23	–
Ferrosilite	43	30	27	–	–
Enstatite	61	37	–	–	2
Augite	39	39	8	13	–
Magnetite	–	–	99	–	–

EDS maps resulted in a clear image of DGR-035 CAI (Figure 40), including mineral boundaries and crystal habits if the grains were large enough. Orthopyroxene member enstatite (En), clinopyroxene member diopside (Di), and olivine end members: fayalite (Fa), and forsterite (Fo) were identified using EDS point analyses from the EDS map (Table 9). There also appears to be an aluminum-rich phase located throughout the CAI, represented in purple.

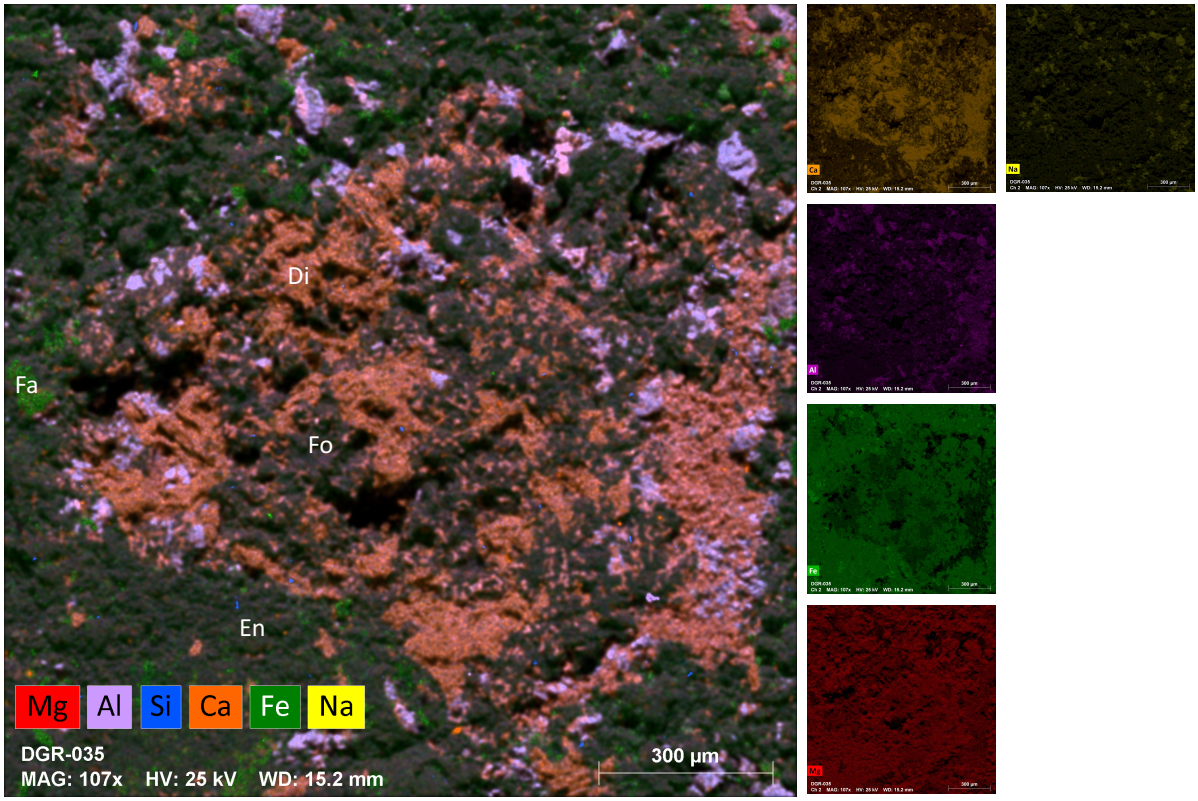


Figure 38: EDS spectral map with major and minor elements displayed for DGR-035 CAI. Minerals olivine as fayalite (Fa) and forsterite (Fo); enstatite (En), and diopside (Di) were identified from EDS point data. Individual elements are displayed to the right of the main image.

Table 9: Examples of EDS point analyses resulting in mineral identification for DGR-035 CAI. Results reported in weight percent oxide.

Mineral	SiO_2 (%)	MgO (%)	FeO (%)	CaO (%)
Fayalite	22	–	78	–
Forsterite	42	58	–	–
Enstatite	63	37	–	–
Diopside	62	17	–	21

EDS maps resulted in a clear image of DGR-034 chondrule (Figure 39), including mineral boundaries and crystal habits if the grains were large enough. Orthopyroxene member enstatite (En), and ferrosilite (Fs) were identified; as well as clinopyroxene member augite (Aug), and olivine end-member fayalite (Fa) using EDS point analyses from the EDS map (Table 10). Calcium-aluminum silicates laths are clearly visible in the centre of the chondrule, which are most likely too thin to get an accurate EDS quantification measurement, resulting in a mineral identification. These laths are believed to be a feldspar based on composition and crystal habit.

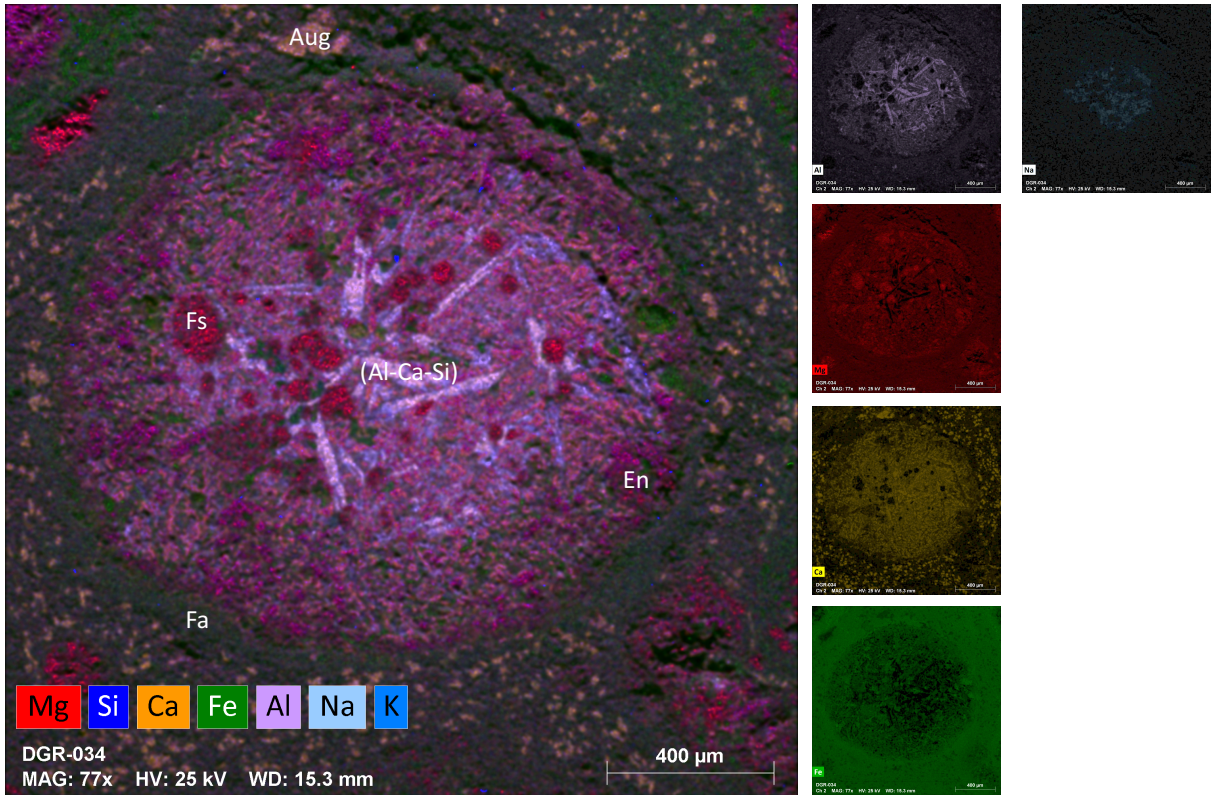


Figure 39: EDS spectral map with major and minor elements displayed for DGR-034 chondrule. Minerals fayalite (Fa), enstatite (En), ferrosilite (Fs), and augite (Aug), were identified from EDS point data. Individual elements are displayed to the right of the main image.

Table 10: Examples of EDS point analyses resulting in mineral identification for DGR-034 chondrule. Results reported in weight percent oxide.

Mineral	SiO_2 (%)	MgO (%)	FeO (%)	CaO (%)
Fayalite	33	–	66	–
Ferrosilite	54	20	26	–
Enstatite	62	34	–	–
Augite	35	20	26	19

EDS maps resulted in a clear image of DGR-035 CAI (Figure 40), including mineral boundaries and crystal habits if the grains were large enough. Orthopyroxene member enstatite (En), and ferrosilite (Fs) were identified, as well as clinopyroxene member diopside (Di), olivine end members: fayalite (Fa), and forsterite (Fo); Andradite (Adr), and perovskite (Prv) using EDS point analyses from the EDS map (Table 11). There also appears to be an aluminum - rich phase located throughout the CAI, represented in purple.

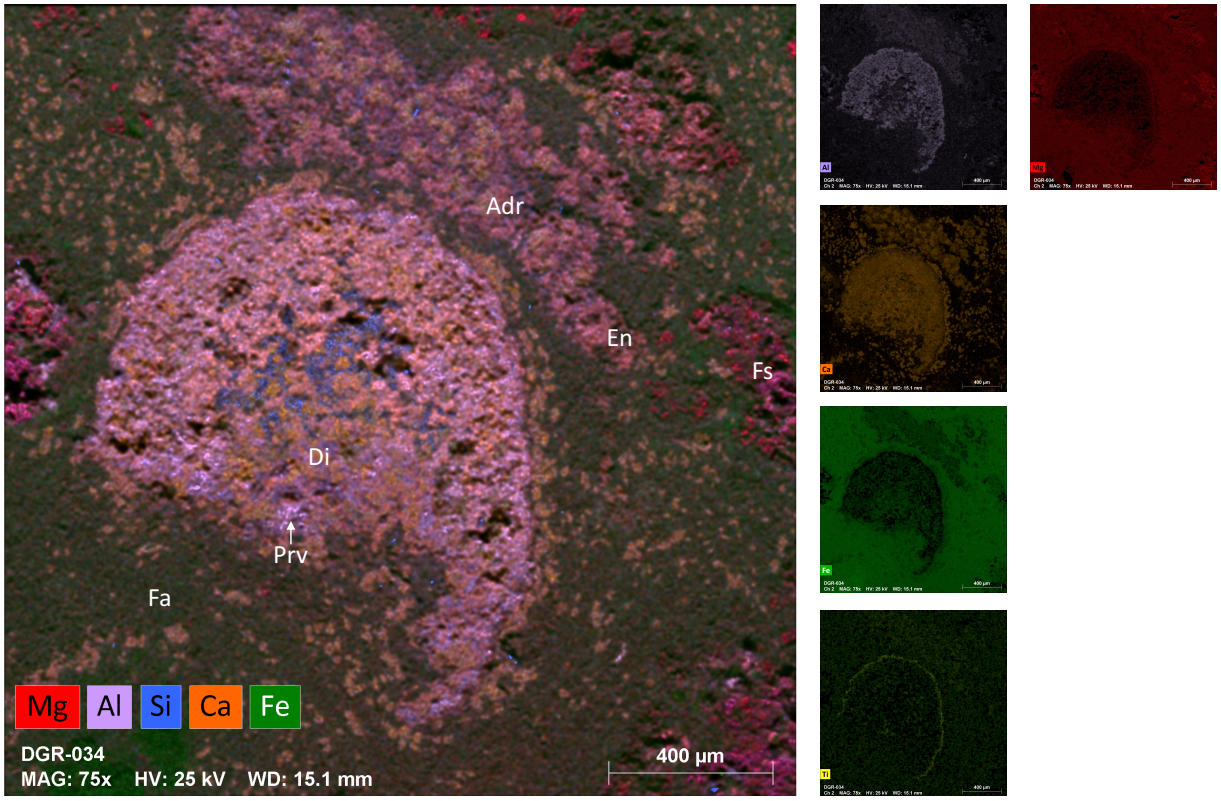


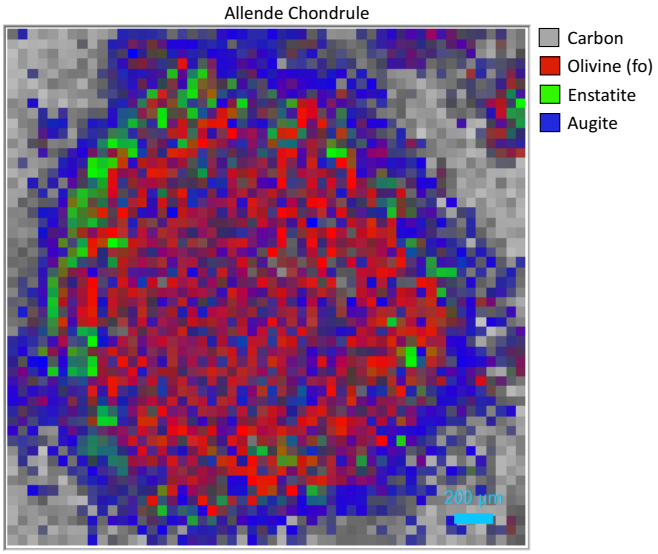
Figure 40: EDS spectral map with major and minor elements displayed for DGR-034 CAI. Minerals olivine as fayalite (Fa) and forsterite (Fo); enstatite (En), ferrosilite (Fs), Diopside (Di), Andradite (Adr), and perovskite (Prv) were identified from EDS point data. Individual elements are displayed to the right of the main image.

Table 11: Examples of EDS point analyses resulting in mineral identification for DGR-034 CAI. Results reported in weight percent oxide.

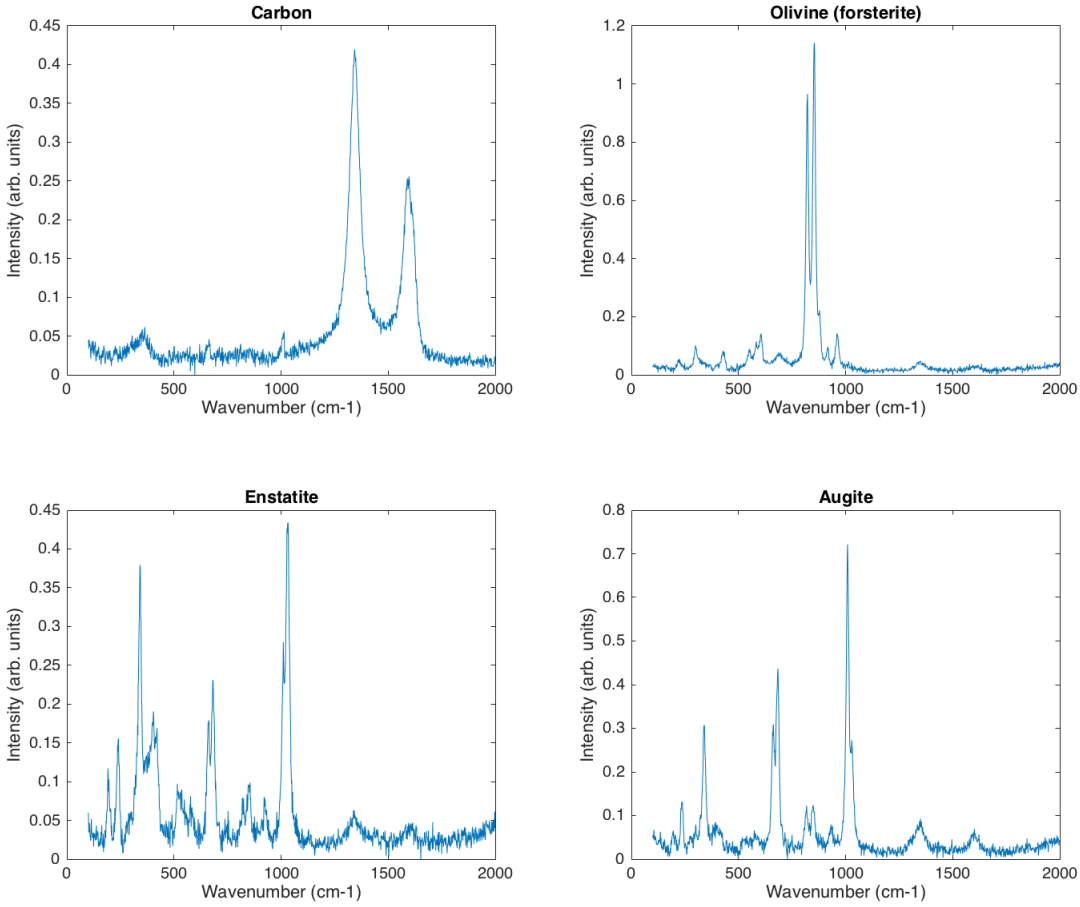
Mineral	SiO_2 (%)	MgO (%)	FeO (%)	CaO (%)	TiO_2 (%)	Cr_2O_3 (%)
Fayalite	34	–	66	–	–	–
Forsterite	37	62	–	–	–	–
Ferrosilite	33	39	27	–	–	–
Enstatite	68	32	–	–	–	–
Diopside	52	12	–	35	–	–
Perovskite	–	–	–	53	35	9
Andradite	34	2	40	25	–	–

6.2 Raman spectroscopy maps and spectral analyses

Raman spectroscopy resulted in 2D spectral maps, demonstrating the relative abundance and arrangement of minerals in a feature, and individual mineral spectra, which were identified using the RRUFF database [Lafuente et al., 2016]. A 2D Raman spectral map of Allende chondrule, and the corresponding mineral spectra are presented in Figure 41. G and D bands of carbon, olivine, enstatite, and augite were identified in the spectra for Allende chondrule. A 2D Raman spectral map of Allende CAI, and the corresponding mineral spectra are presented in Figure 42. Carbon, olivine, nepheline, augite/diopside, andradite, rutile, and silicon carbide were identified in Allende CAI. A 2D Raman spectral map of Murchison chondrule, and the corresponding mineral spectra are presented in Figure 43. Carbon, olivine, enstatite, calcite, and silicon carbide were identified within Murchison chondrule. A 2D Raman spectral map of Murchison CAI, and the corresponding mineral spectra are presented in Figure 44. Carbon, olivine, augite, and calcite were identified in Murchison CAI. One mineral phase within the feature did not match any spectra within the RRUFF database, but was prevalent within the map and labeled as 'unknown'. A 2D Raman spectral map of DGR-035 chondrule, and the corresponding mineral spectra are presented in Figure 45. Carbon, olivine, diopside, silicon carbide, labradorite, magnetite, and goethite were identified in DGR-035 chondrule. A 2D Raman spectral map of DGR-035 CAI, and the corresponding mineral spectra are presented in Figure 46. Carbon, olivine, diopside, anorthoclase, and silicon carbide were identified in DGR-035 CAI. A 2D Raman spectral map of DGR-034 chondrule, and the corresponding mineral spectra are presented in Figure 47. Carbon, olivine, anorthite, enstatite, and silicon carbide were identified in DGR-034 chondrule. A 2D Raman spectral map of DGR-034 CAI, and the corresponding mineral spectra are presented in Figure 48. Carbon, olivine, enstatite, perovskite, andradite, and augite were identified in DGR-034 CAI.

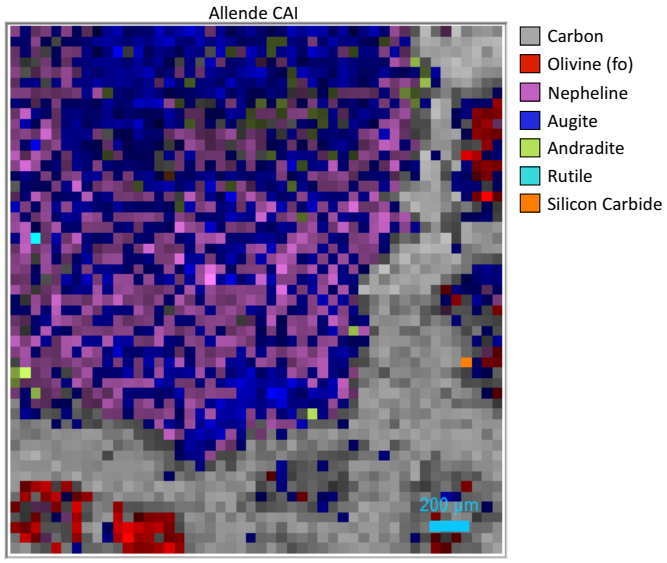


(a) Raman spectroscopy 2D map of Allende chondrule. Each colour represents a different mineral phase, and were identified as the minerals labeled in the legend to the right of the image.

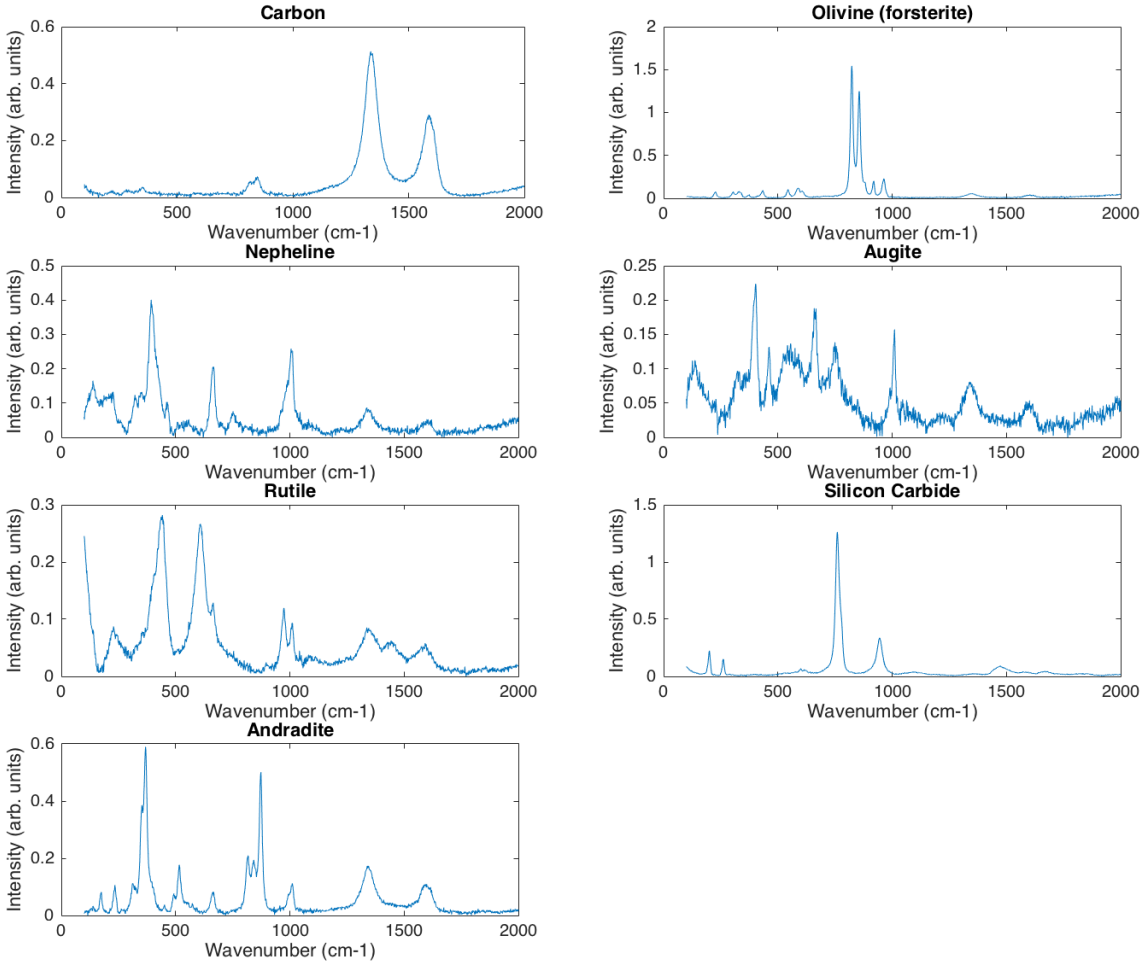


(b) Spectra obtained from Allende chondrule with unique peaks, used to map out main mineral phases within the sample. These spectra were identified using the RRUFF database.

Figure 41: Raman data as (a) 2D spectral map and (b) corresponding individual mineral spectra for Allende chondrule.

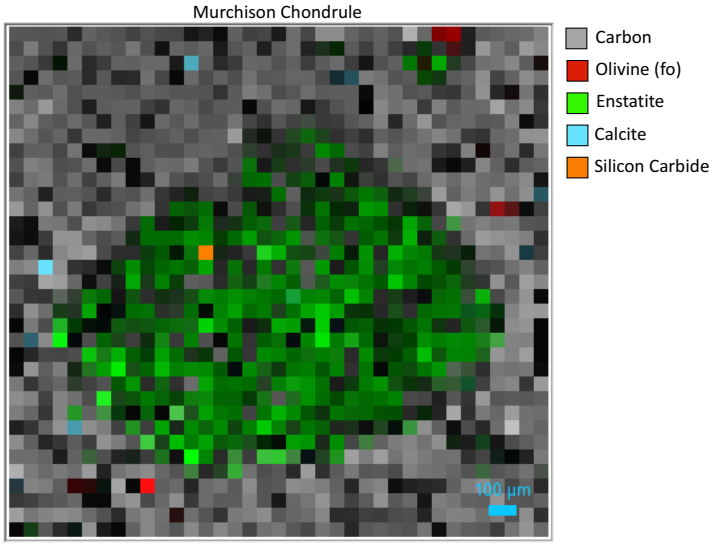


(a) Raman spectroscopy 2D map of Allende CAI. Each colour represents a different mineral phase, and were identified as the minerals labeled in the legend to the right of the image.

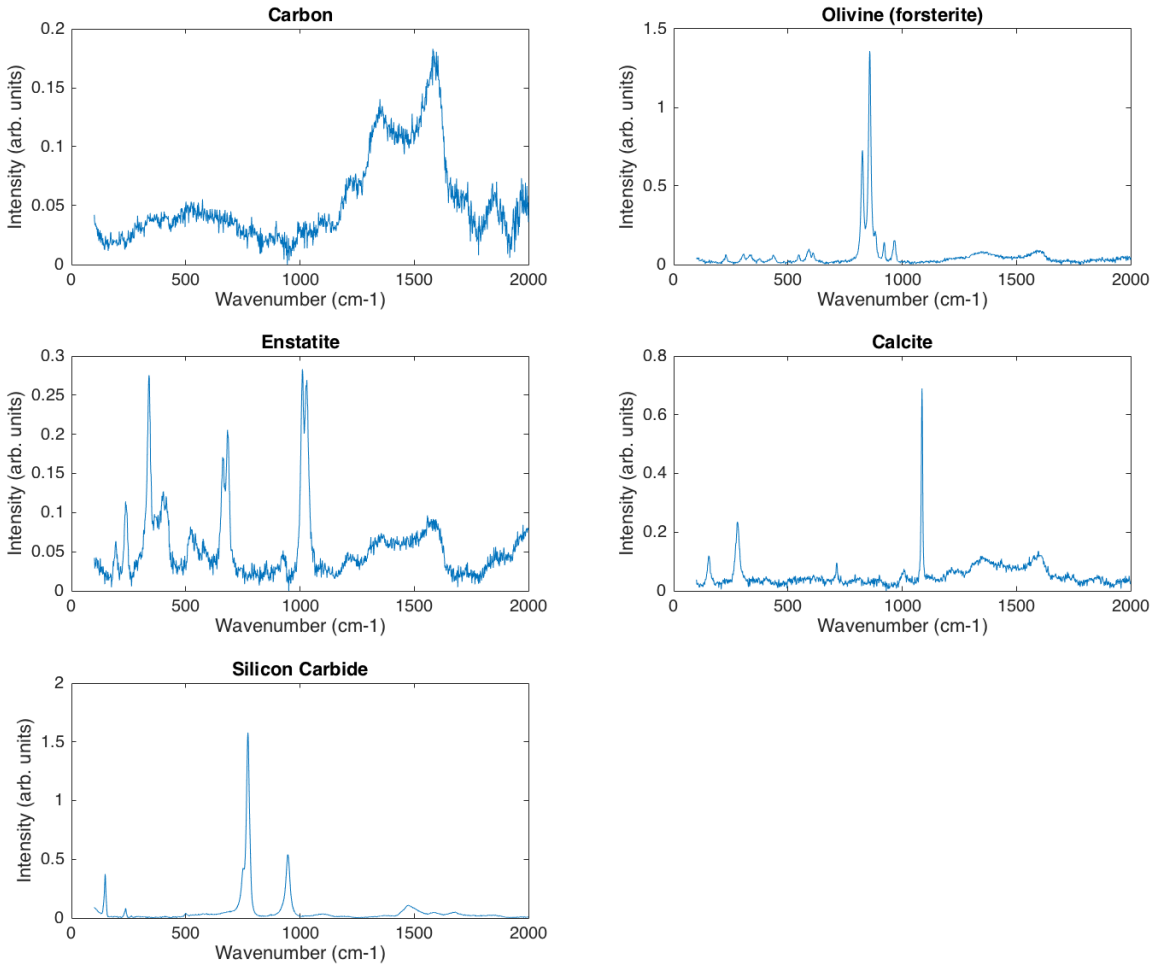


(b) Spectra obtained from Allende CAI with unique peaks, used to map out main mineral phases within the sample. These spectra were identified using the RRUFF database.

Figure 42: Raman data as (a) 2D spectral map and (b) corresponding individual mineral spectra for Allende chondrule.

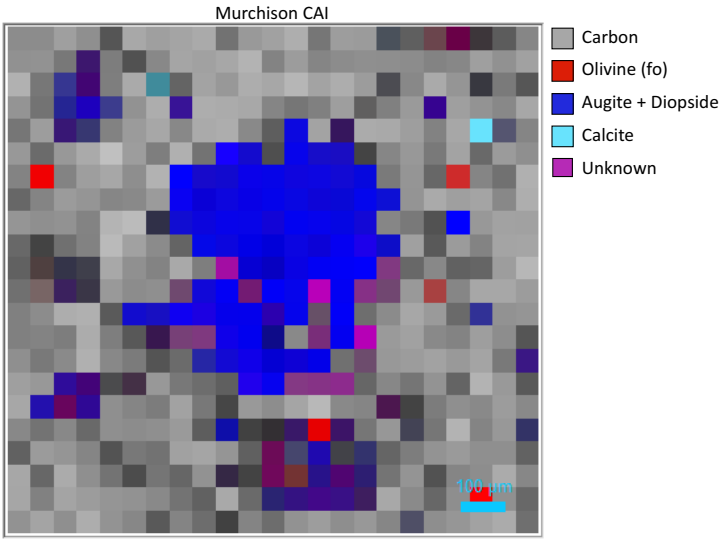


(a) Raman spectroscopy 2D map of Murchison chondrule. Each colour represents a different mineral phase, and were identified as the minerals labeled in the legend to the right of the image.

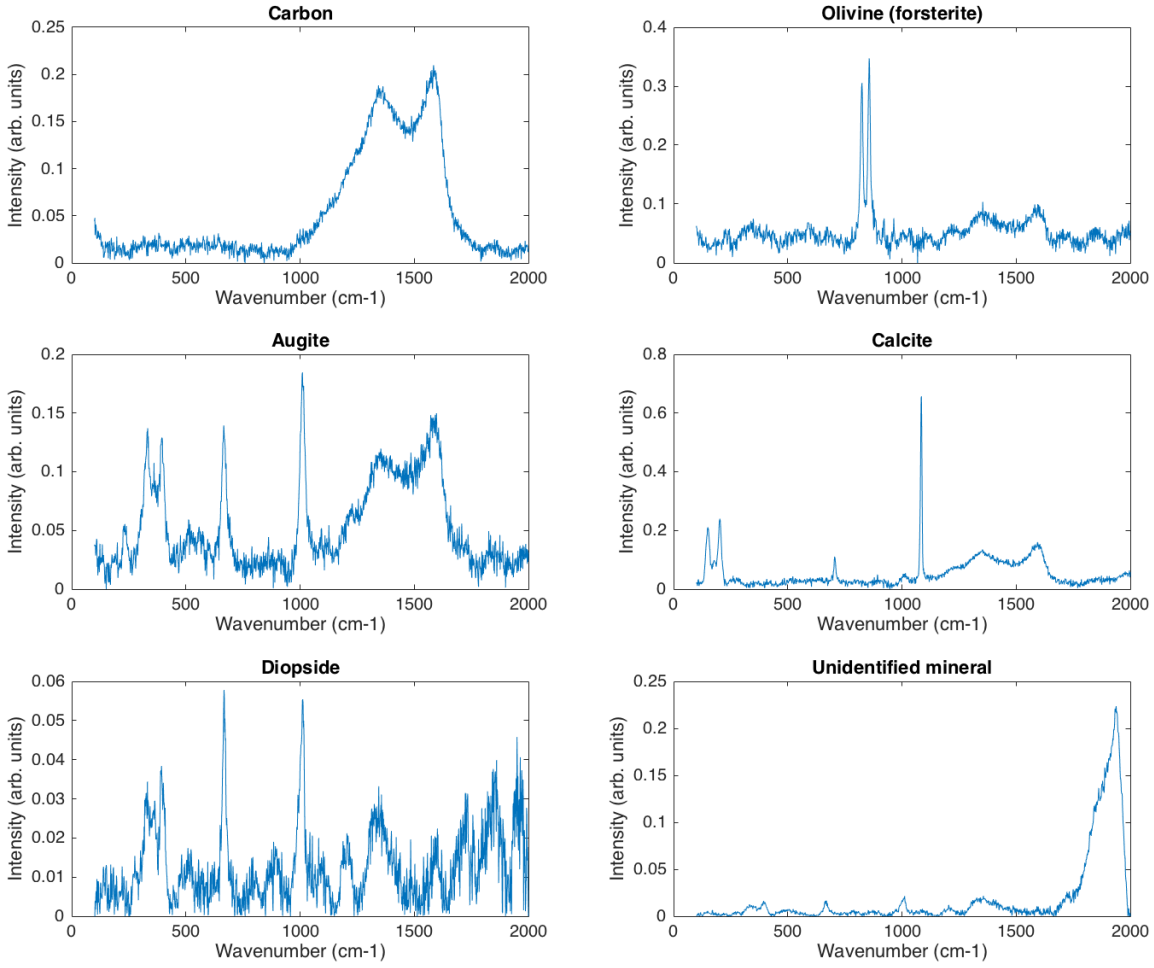


(b) Spectra obtained from Murchison chondrule with unique peaks, used to map out main mineral phases within the sample. These spectra were identified using the RRUFF database.

Figure 43: Raman data as (a) 2D spectral map and (b) corresponding individual mineral spectra for Allende chondrule.

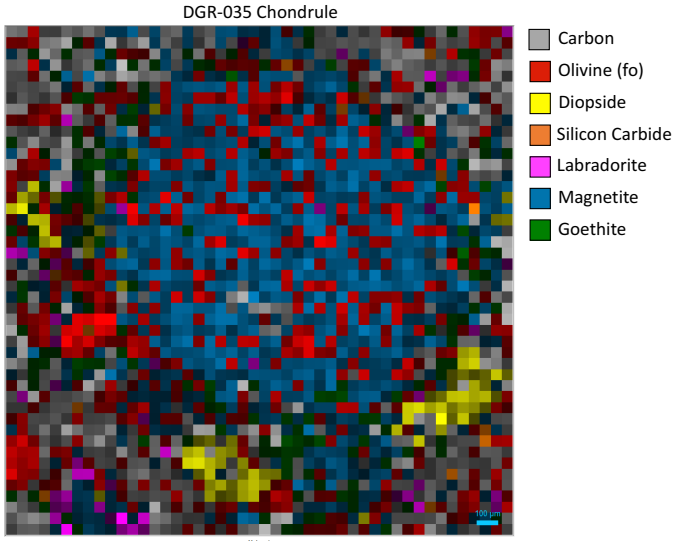


(a) Raman spectroscopy 2D map of Murchison CAI. Each colour represents a different mineral phase, and were identified as the minerals labeled in the legend to the right of the image.

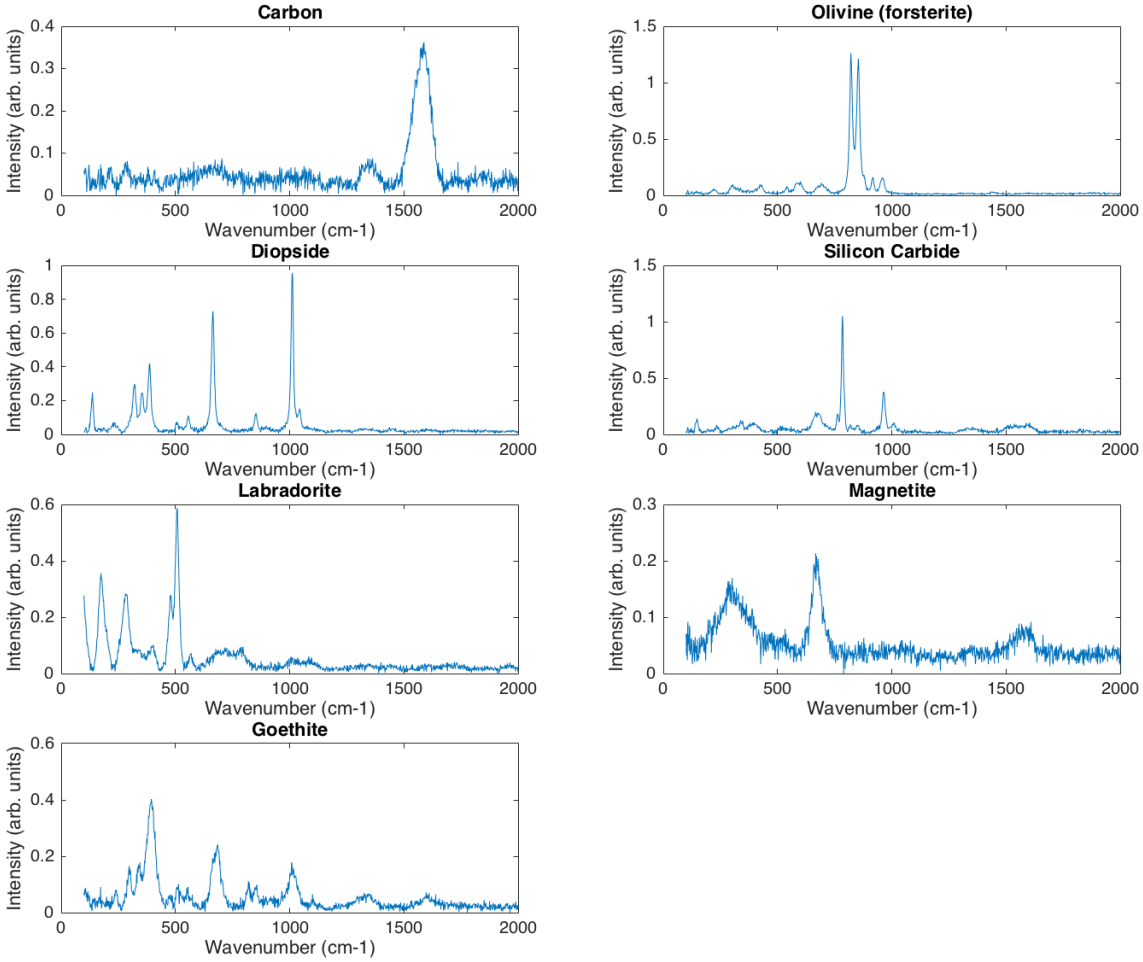


(b) Spectra obtained from Murchison CAI with unique peaks, used to map out main mineral phases within the sample. These spectra were identified using the RRUFF database.

Figure 44: Raman data as (a) 2D spectral map and (b) corresponding individual mineral spectra for Allende chondrule.

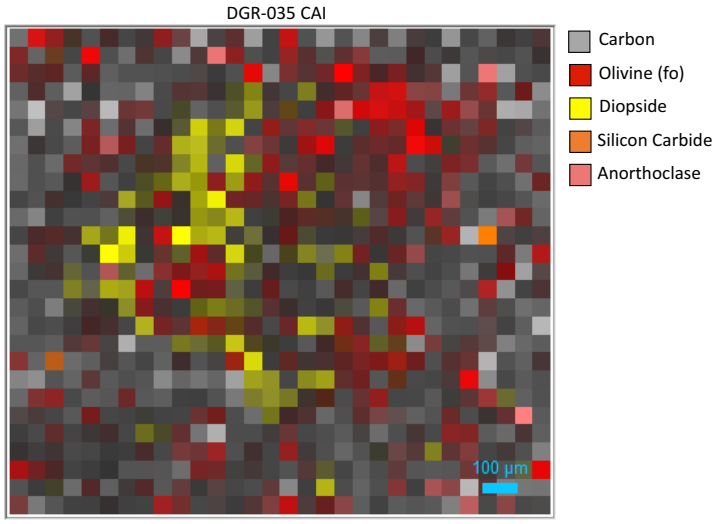


(a) Raman spectroscopy 2D map of DGR-035 chondrule. Each colour represents a different mineral phase, and were identified as the minerals labeled in the legend to the right of the image.

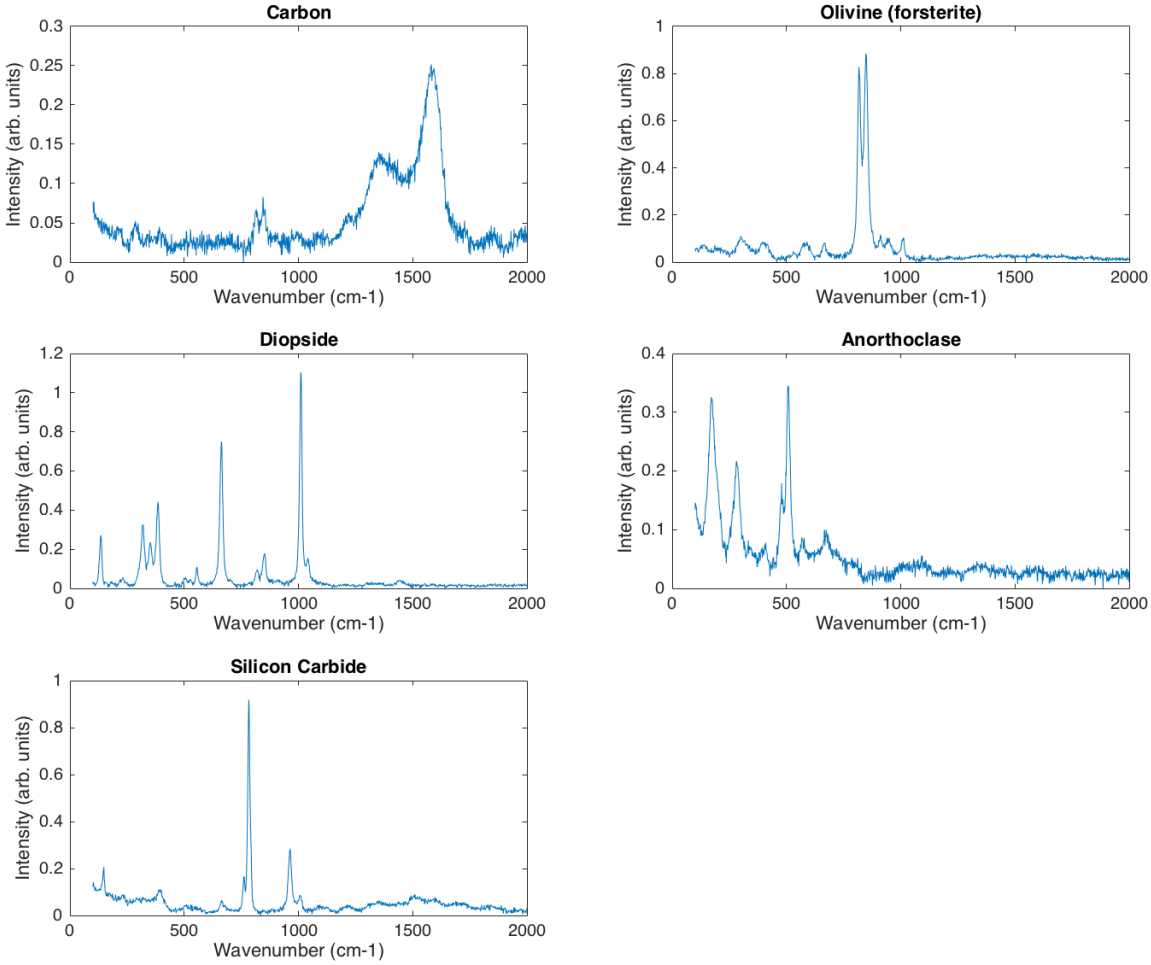


(b) Spectra obtained from DGR-035 chondrule with unique peaks, used to map out main mineral phases within the sample. These spectra were identified using the RRUFF database.

Figure 45: Raman data as (a) 2D spectral map and (b) corresponding individual mineral spectra for Allende chondrule.

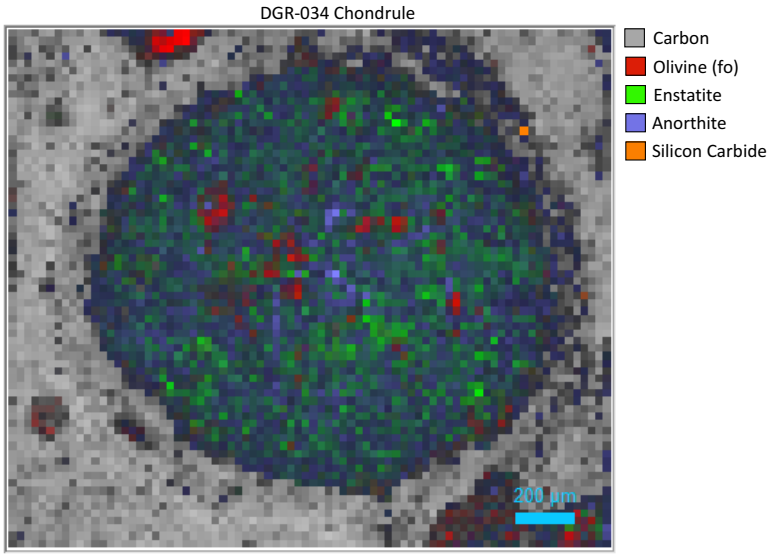


(a) Raman spectroscopy 2D map of DGR-035 CAI. Each colour represents a different mineral phase, and were identified as the minerals labeled in the legend to the right of the image.

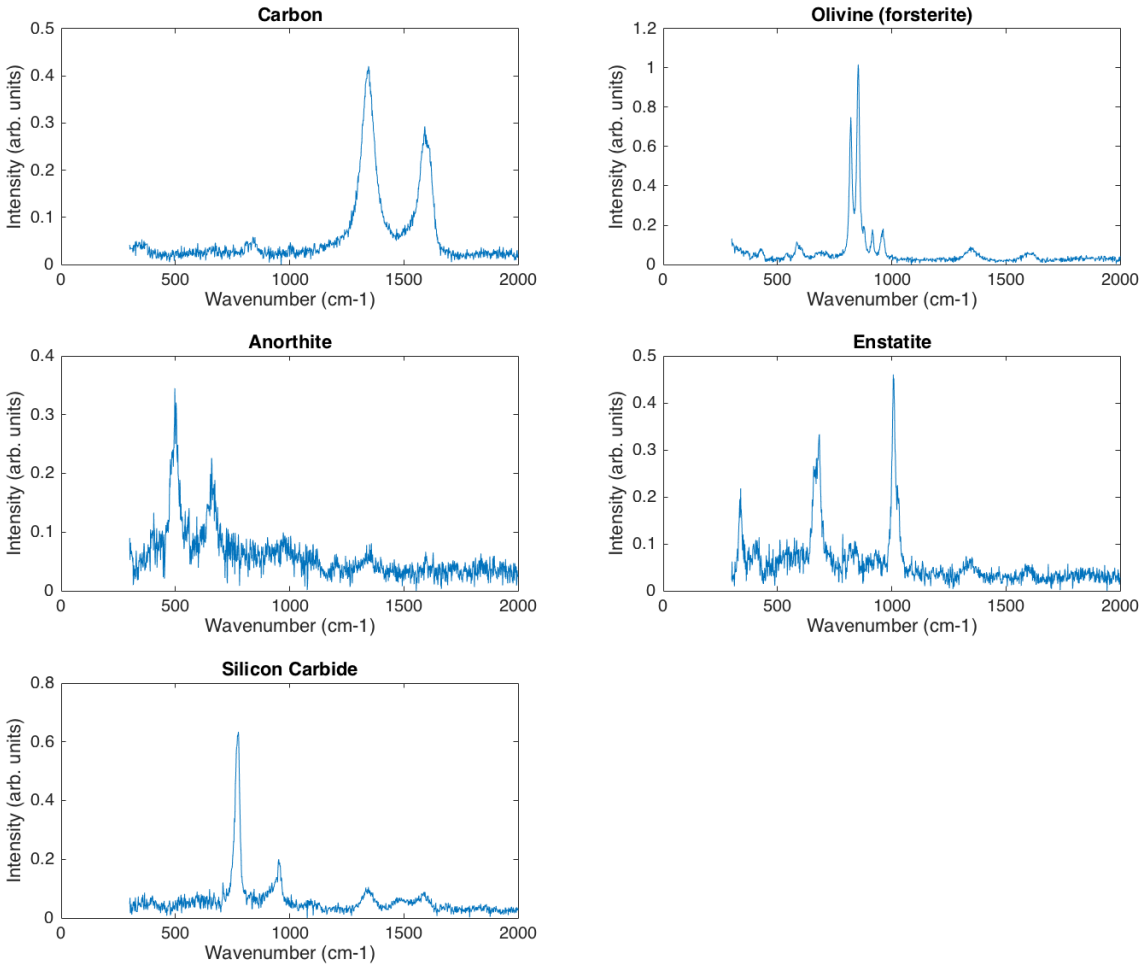


(b) Spectra obtained from DGR-035 CAI with unique peaks, used to map out main mineral phases within the sample. These spectra were identified using the RRUFF database.

Figure 46: Raman data as (a) 2D spectral map and (b) corresponding individual mineral spectra for Allende chondrule.

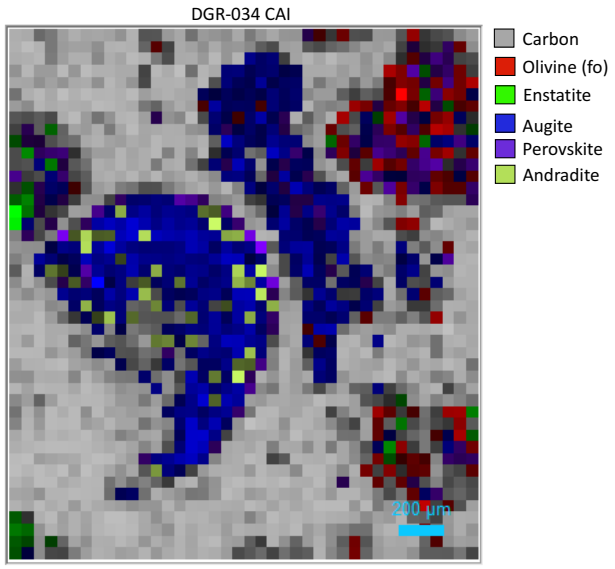


(a) Raman spectroscopy 2D map of DGR-034 chondrule. Each colour represents a different mineral phase, and were identified as the minerals labeled in the legend to the right of the image.

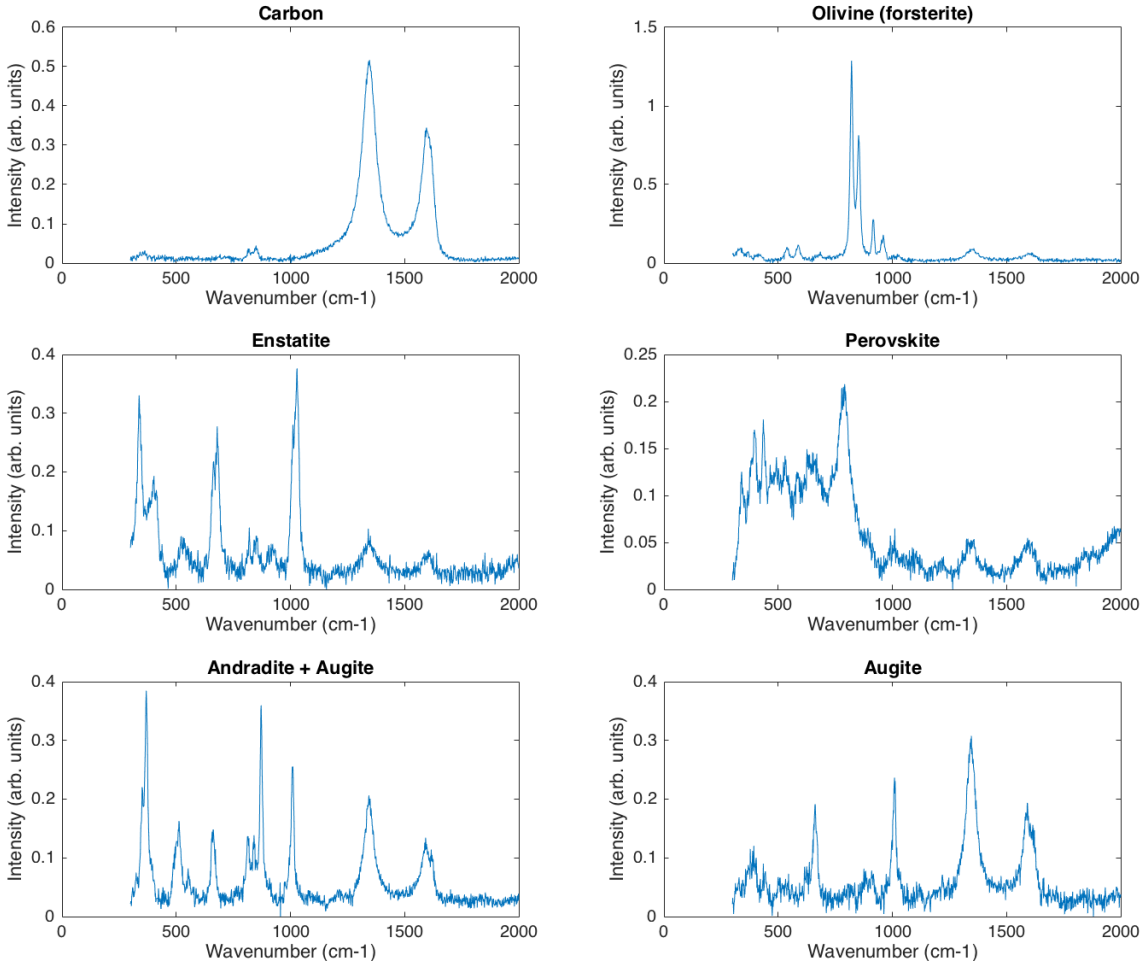


(b) Spectra obtained from DGR-034 chondrule with unique peaks, used to map out main mineral phases within the sample. These spectra were identified using the RRUFF database.

Figure 47: Raman data as (a) 2D spectral map and (b) corresponding individual mineral spectra for Allende chondrule.



(a) Raman spectroscopy 2D map of DGR-034 CAI. Each colour represents a different mineral phase, and were identified as the minerals labeled in the legend to the right of the image.



(b) Spectra obtained from DGR-034 CAI with unique peaks, used to map out main mineral phases within the sample. These spectra were identified using the RRUFF database.

Figure 48: Raman data as (a) 2D spectral map and (b) corresponding individual mineral spectra for Allende chondrule.

6.3 LIF mineral database

Laser-induced fluorescence spectroscopy produced individual, and time-resolved spectra of 10 common minerals found in carbonaceous chondrites: anorthite, augite, diopside, forsterite, labradorite, nepheline, olivine, orthopyroxene, spinel and graphite. Long fluorescence spectra, with a gate width of 100 ns is displayed in Figure 49. The resulting spectra of each mineral is often hard to distinguish from the next when looking at a single shot. However, time-resolved spectra in both surface and contour view (Figures 50 and 51) show reasonable variation between each mineral. Contour plots of time-resolved fluorescence (Figure 51) are essentially a fingerprint of the mineral, each one is unique and distinguishable. Anorthite has a broad peak from 400-450 nm, and a small, sharp peak just below 400 nm. Anorthite's peaks are strong immediately following laser interaction, and decay somewhat in the first 5 ns, with a steady peak remaining between 400-450 nm for the remainder of the 20 ns. Augite has a somewhat broad peak at 400-450 nm, but the main feature of augite is a sharp peak at 380 nm. The broader peak at 400-450 reaches its maximum around 3-5 ns, and decays steadily throughout the 20 ns. The peak at 380 nm also reaches it's peak around 5 ns, and decays before 10 ns. Diopside has a main broad peak from 400-450 nm, that steadily reaches it's maximum around 4 ns. A small peak just below 400 nm is predominant in the contour plots, which quickly reaches it's maximum just under 5 ns. Diopside also has substantial spread in wavelength before 5 ns. Forsterite, olivine, and spinel have similar 'fingerprints' with a primary peak at 415 nm, and spread from 375-500 nm between 3-5ns. Spinel has a defining extra small peak at 380 nm, making it unique from olivine and forsterite. Olivine has a more defined peak at 415 nm, with a smaller spread across wavelengths and decays more rapidly between 5-10 ns. Forsterite has a longer decay rate of the main peak from 5-6 ns and steadily towards 20 ns. Labradorite also has a dominant peak at 415 nm, and secondary peaks between 325-350 nm. Labradorite does not have much wavelength spread, resulting in thin, straight contours. Nepheline has a broad peak around 410 nm, which reaches its maximum quickly at 5 ns, and decays quickly until 15 ns. Nepheline has a similar 'fingerprint' to olivine, however the main peak at 410 nm is more symmetrical in nepheline, resulting in less spread towards 450 nm than olivine. Orthopyroxene is not easily differentiable by individual spectra, however the time-resolved contour plot results in a unique 'fingerprint' from the other minerals. Orthopyroxene has a more narrow peak at 412 nm, and a slight peak at 380 nm, that is very short lived. The peak at 412 nm reaches its maximum between 3-5 ns, and the smaller peak at 380 is short lived at 5 ns. Orthopyroxene does not have much spread into the upper wavelengths, but does spread slightly around 5 ns towards 300 nm. Graphite does not have much spread between wavelengths and has a narrow peak at 415 nm. The peak reaches its maximum at 4 ns. Graphite and labradorite time-resolved fluorescence contours look similar, however labradorite has an extra small peak around 400 nm that creates some definition.

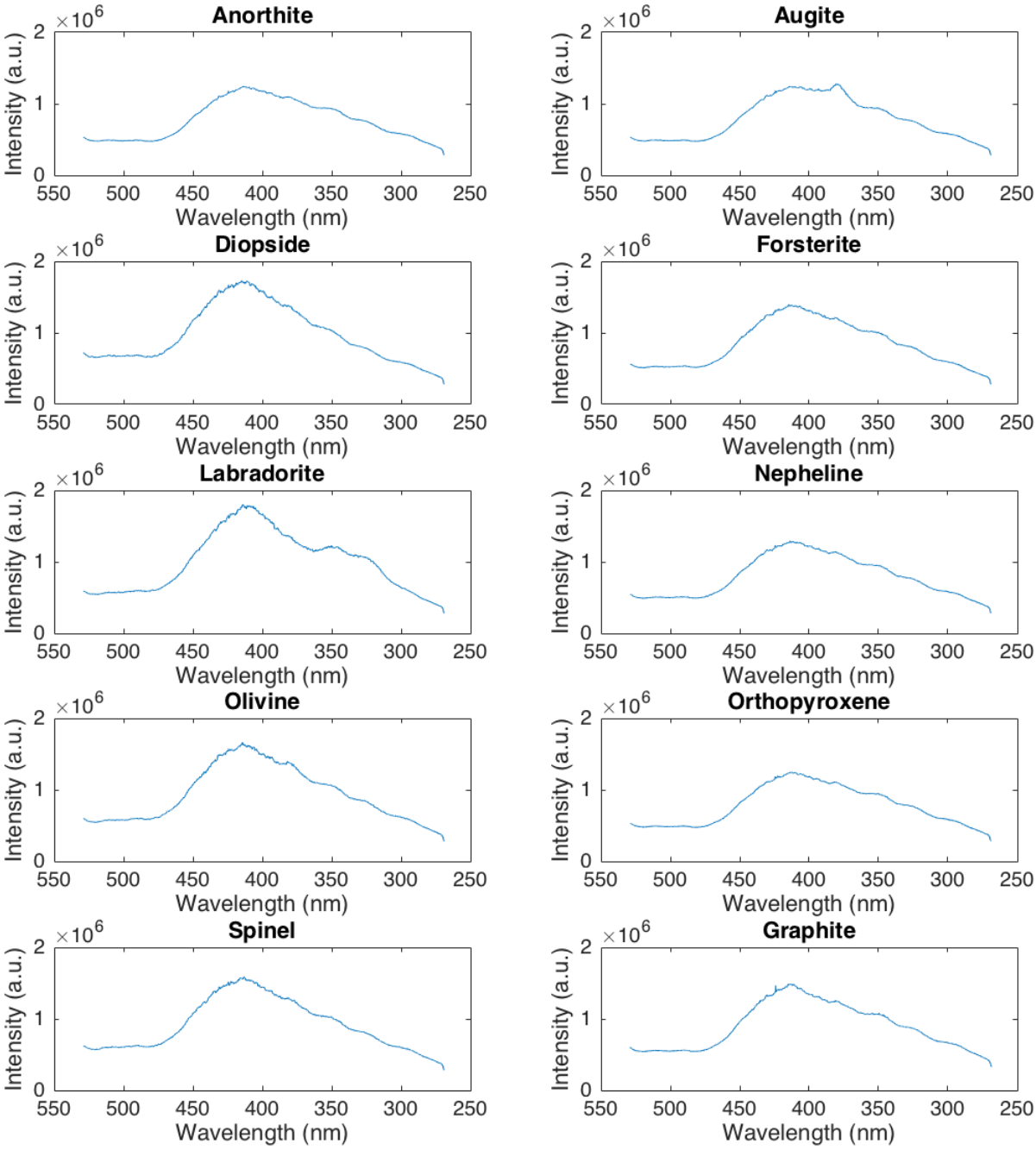


Figure 49: Mineral database: long fluorescence (100 ns gate width) spectra.

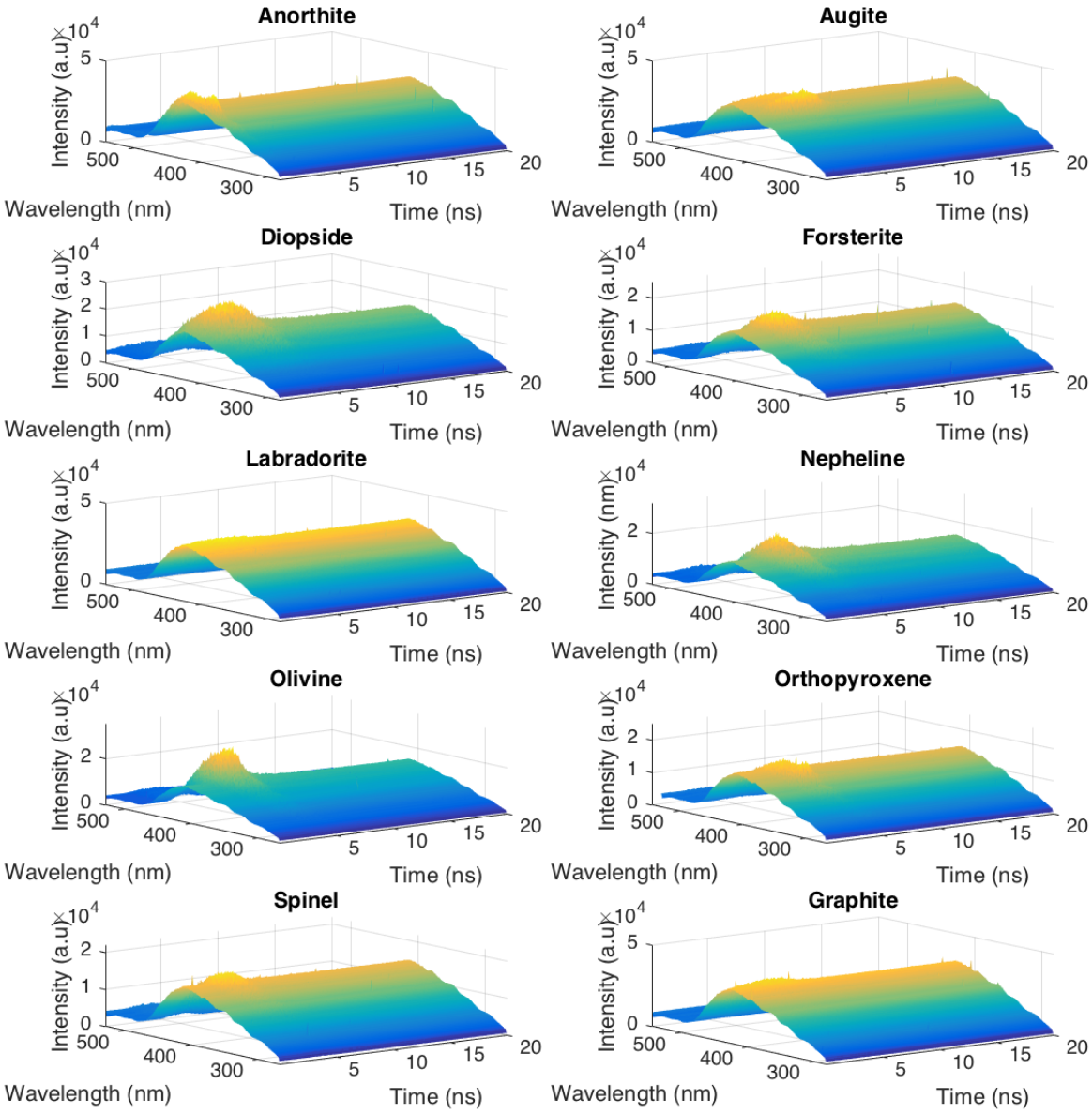


Figure 50: Mineral database: time-resolved fluorescence surface plots.

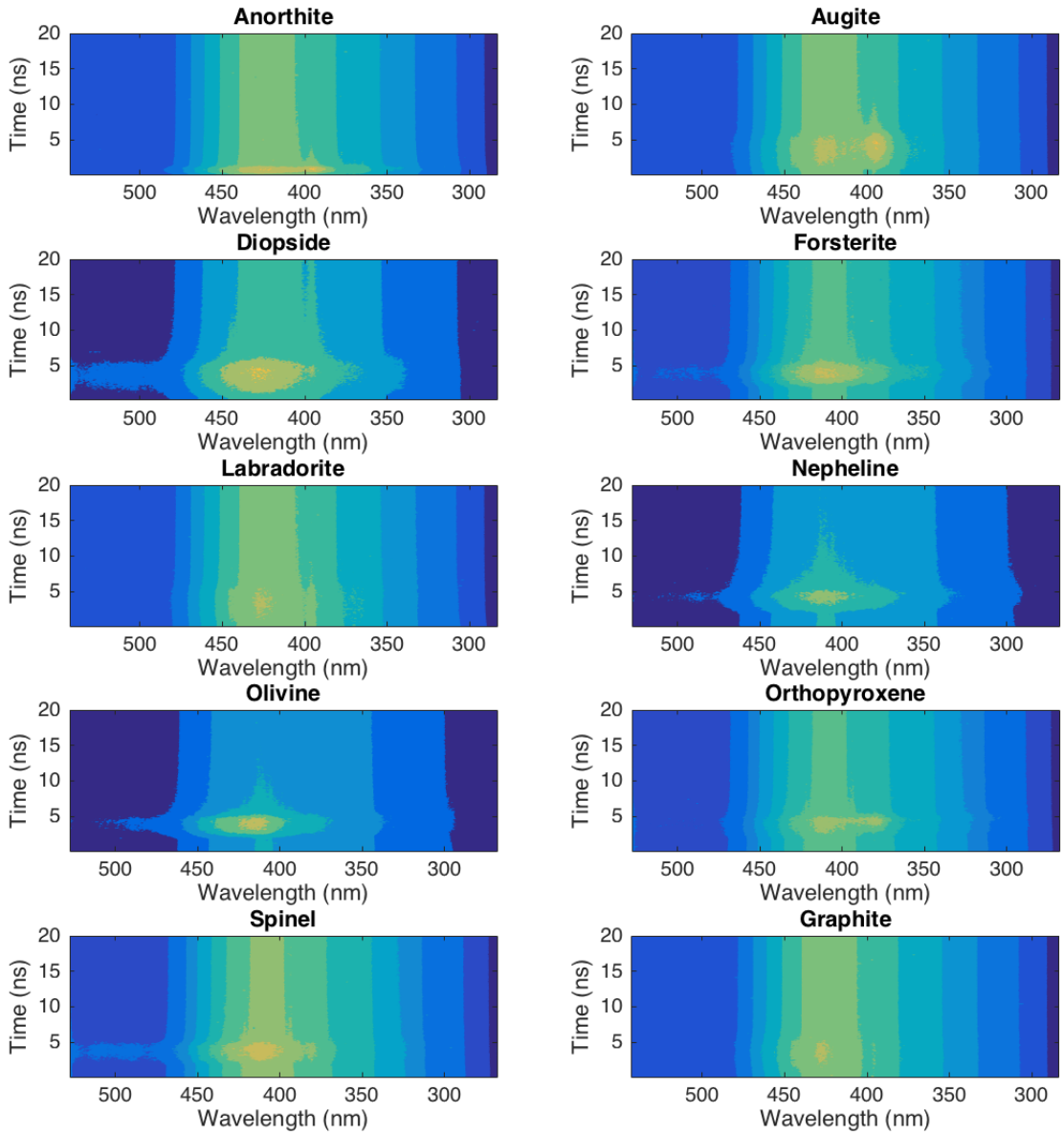


Figure 51: Mineral database: time-resolved fluorescence contour plots.

6.4 LIF 2D maps, time-resolved fluorescence and spectral analyses

6.4.1 Allende chondrule: LIF maps, individual, and time-resolved spectra

LIF 2D mapping resulted in a 1764 point spectral image covering a 2.5 mm^2 area of Allende chondrule, displaying the rim and interior of the feature (Figure 52). Two sets of peaks were predominant when viewing in the range of 400-450 nm and 300-350 nm. These peaks often occur together in the same spectra, however there is a grouping of points in the mid-lower right quadrant of the map that are dominated by 400-450 nm peak and do not include the 300-350 nm peak. Points of interest were analyzed using short and long fluorescence (10 ns and 100 ns gate width respectively) resulting in high resolution spectra of these points (Figures 53, 54 and 55).

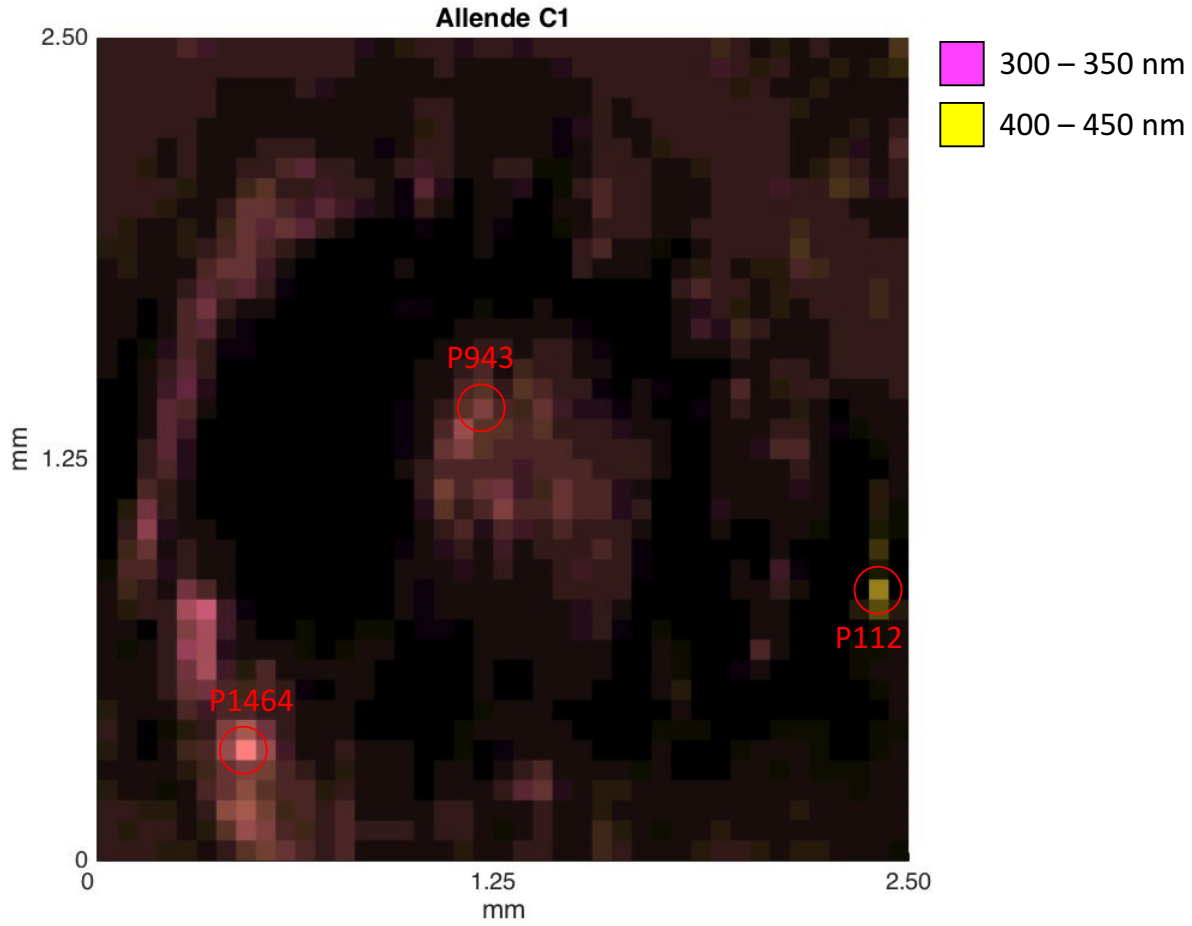


Figure 52: Allende chondrule LIF 2D map. 1764 points, covering a 2.5 mm^2 area, with a step size of 0.6 mm. Two main peaks are displayed, 300-350 nm and 400-450 nm.

Allende chondrule point of interest P112 was chosen for having significant intensity in the range of 300-350 nm, and when observing the time-resolved fluorescence contour plot, appears similar to augite (Figure 56). Point of interest P943 was chosen for having significant intensity in the range of 400-450 nm, and has similarity to forsterite (Figure 57). Point of interest P1464 was chosen as a point of interest for having

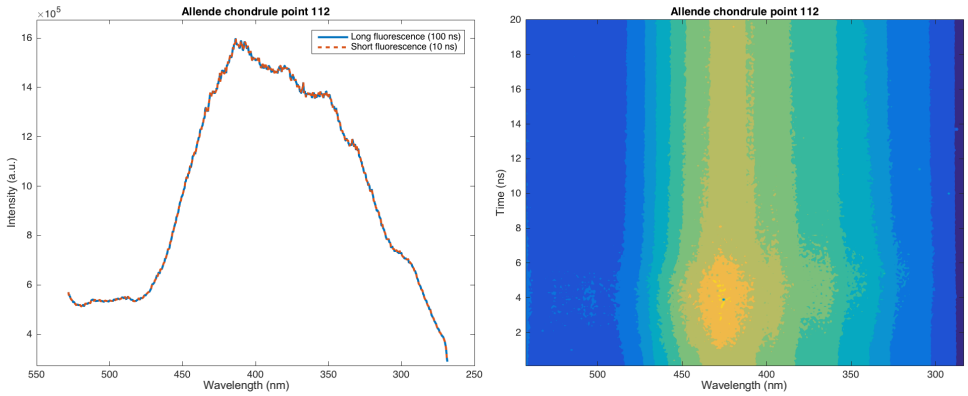


Figure 53: Allende chondrule point of interest 112 spectra and time-resolved spectral contour image.

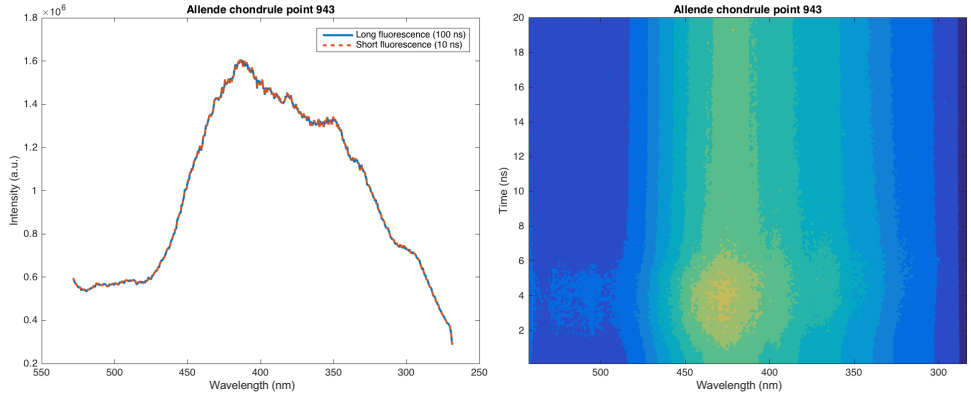


Figure 54: Allende chondrule point of interest 943 spectra and time-resolved spectral contour image.

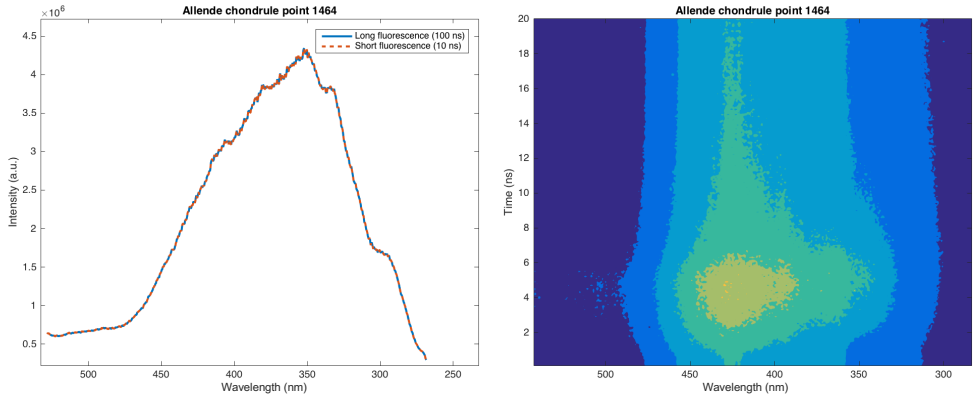


Figure 55: Allende chondrule point of interest 1464 spectra and time-resolved spectral contour image.

significant intensity in the range of 300-350 nm, however appears significantly different from P112. When observing the time-resolved fluorescence contour plot of P1464 (Figure 58), there is significant spread in wavelength between 300-400 nm. P1464 matches orthopyroxene the most, however it is not a perfect match.

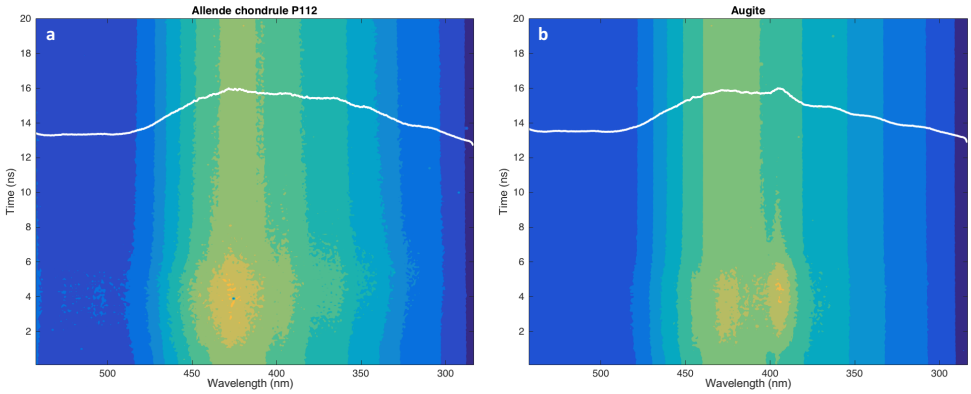


Figure 56: (a) Allende chondrule point of interest P112 spectra and time-resolved spectral contour image and overlay of long fluorescence spectra. (b) Mineral augite time-resolved fluorescence and overlay of long-fluorescence spectra.

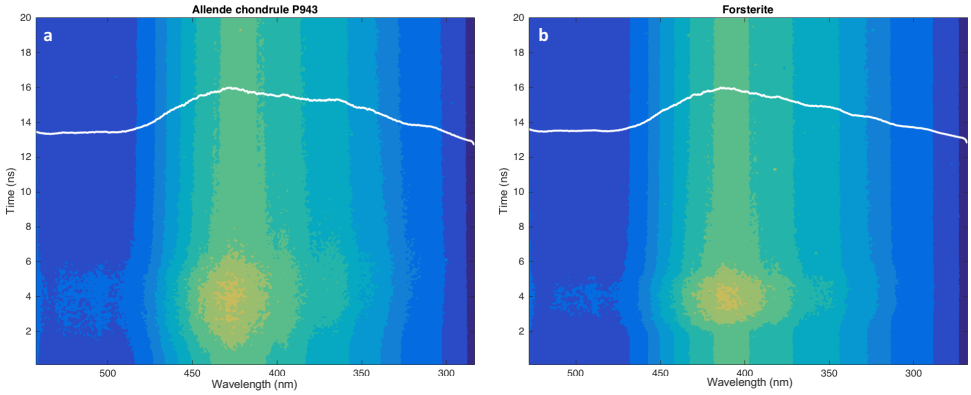


Figure 57: (a) Allende chondrule point of interest P943 spectra and time-resolved spectral contour image and overlay of long fluorescence spectra. (b) Mineral forsterite time-resolved fluorescence and overlay of long-fluorescence spectra.

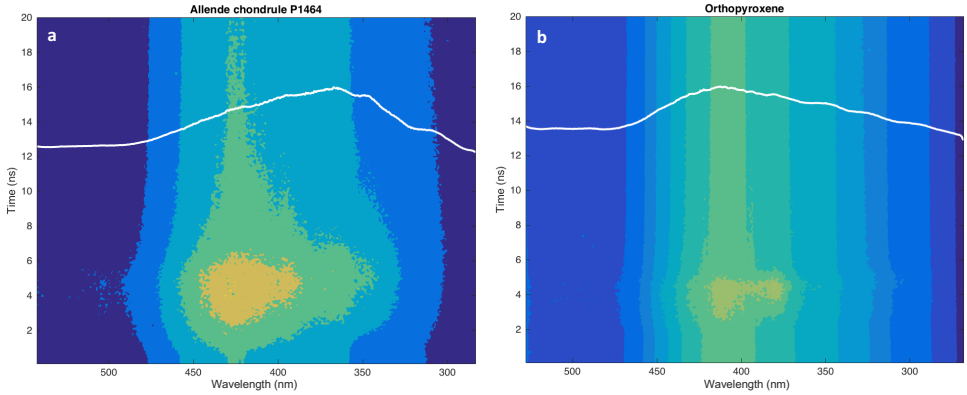


Figure 58: (a) Allende chondrule point of interest P1464 spectra and time-resolved spectral contour image and overlay of long fluorescence spectra. (b) Mineral orthopyroxene time-resolved fluorescence and overlay of long-fluorescence spectra.

6.4.2 Allende CAI: LIF maps, idividual, and time-resolved spectra

LIF 2D mapping resulted in a 1764 point spectral image covering 2.5 mm^2 of Allende CAI, displaying the shape of the feature surrounded by dark matrix (Figure 59). Two sets of peaks were predominant when viewing in the range of 275-300 nm and 330-400 nm. These peaks mainly occur together in the same spectra, however there are some areas of the map that are slightly more intense in one peak range than the other. Points of interest were analyzed using short and long fluorescence (10 ns and 100 ns gate width respectively), resulting in high resolution spectra of these points (Figures 60 and 61).

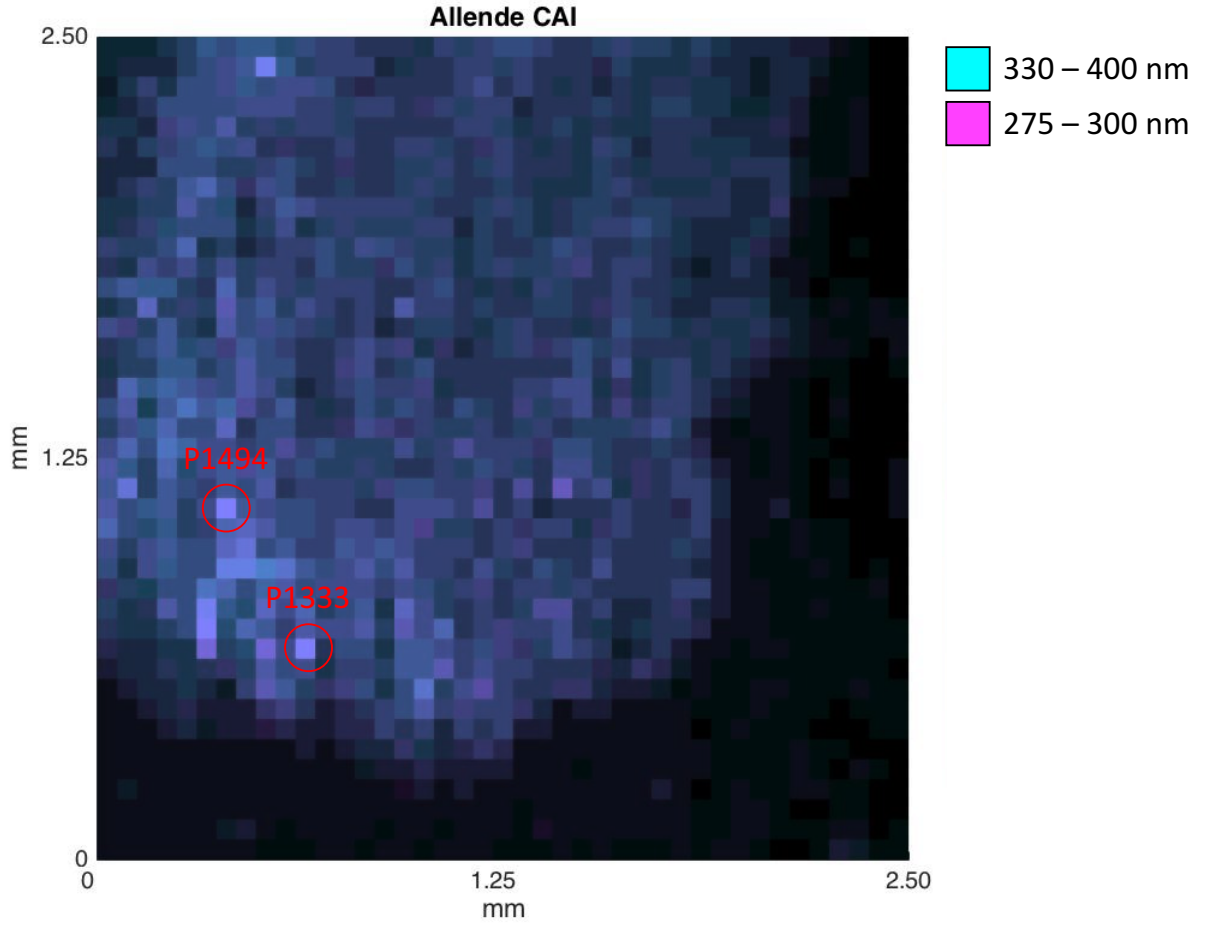


Figure 59: Allende CAI LIF 2D map. 1764 points, covering 2.5 mm^2 area, with a step size of 0.6 mm. Two main peaks are displayed, 275-300 nm and 330-400 nm.

Allende chondrule point of interest P1333 was chosen for having significant intensity in the range of 330-400 nm, and when observing the time-resolved fluorescence contour plot, appears to somewhat match augite (Figure 62). Point of interest P1494 was chosen for having significant intensity in the range of 275-300 nm, and has similarity to nepheline and augite together (Figure 63).

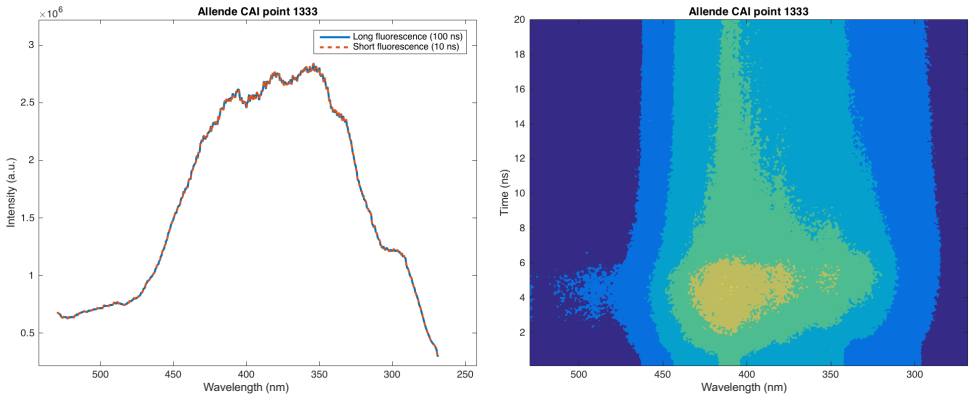


Figure 60: Allende CAI point of interest P1333 spectra and time-resolved spectral contour image.

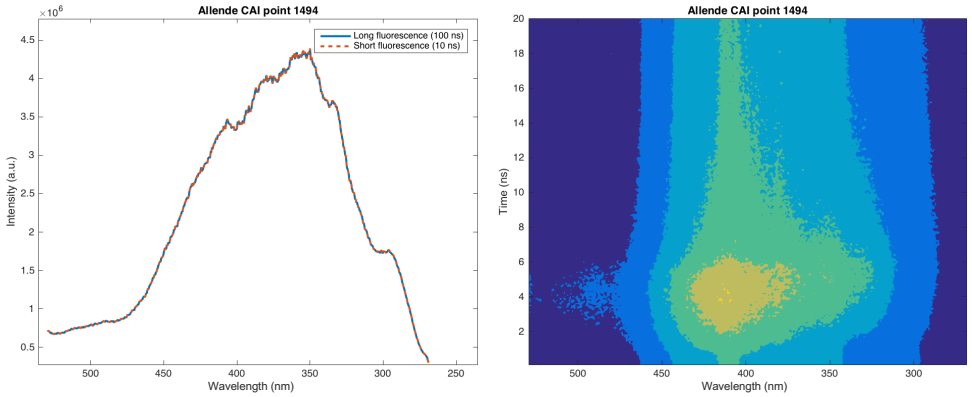


Figure 61: Allende CAI point of interest P1494 spectra and time-resolved spectral contour image.

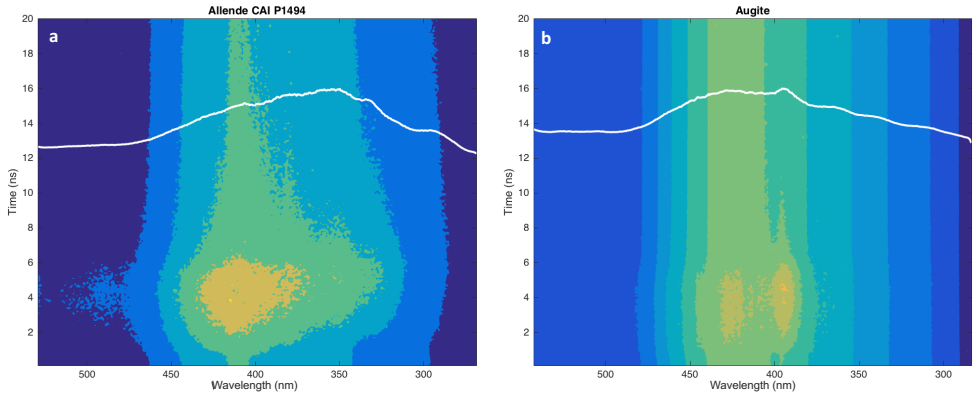


Figure 62: (a) Allende chondrule point of interest P1333 spectra and time-resolved spectral contour image and overlay of long fluorescence spectra. (b) Mineral augite time-resolved fluorescence and overlay of long-fluorescence spectra.

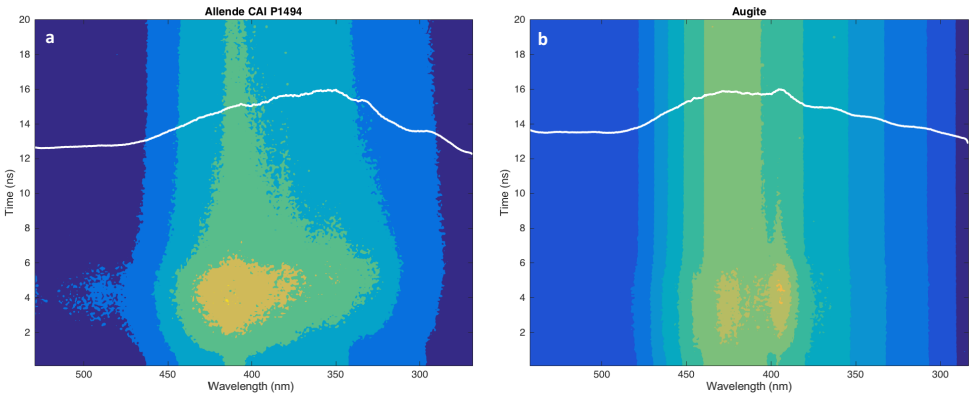


Figure 63: (a) Allende chondrule point of interest P1494 spectra and time-resolved spectral contour image and overlay of long fluorescence spectra. (b) Mineral nepheline time-resolved fluorescence and overlay of long-fluorescence spectra.

6.4.3 Murchison chondrule: LIF maps, idividual, and time-resolved spectra

LIF 2D mapping resulted in a 900 point spectral image covering 1.8 mm^2 of Murchison chondrule, displaying some features near the rim of the feature (Figure 64). Three sets of peaks were predominant when viewing in the range of 290-330 nm, 365-400 nm, and 400-475 nm. 290-330 nm and 400-475 nm peaks appear in the same spectra, however there is are points in the map that are dominated by the 365-400 nm peak and do not include the 290-330 nm peak. Points of interest were analyzed using short and long fluorescence (10 ns and 100 ns gate width respectively), resulting in high resolution spectra of these points (Figures 65, 66 and 67).

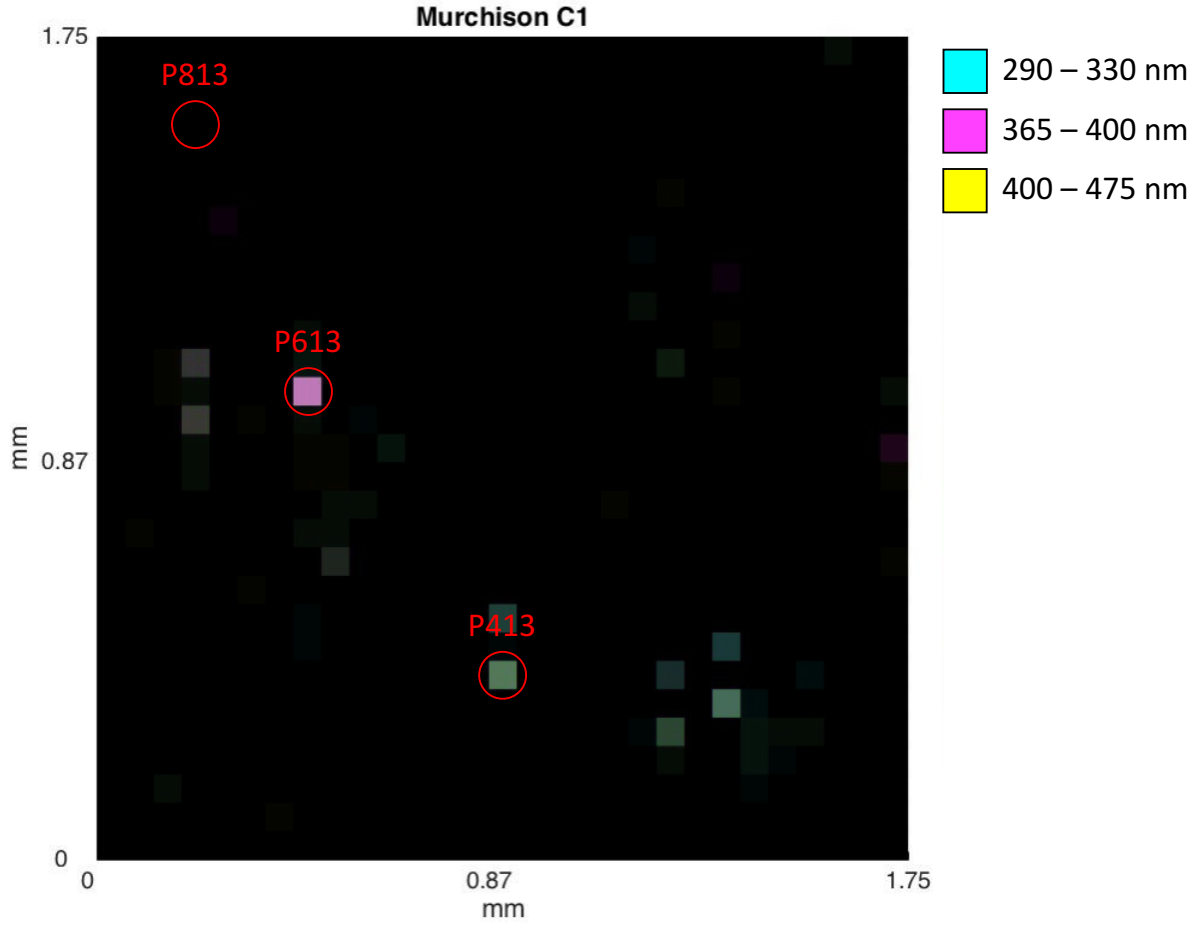


Figure 64: Murchison chondrule LIF 2D map. 900 points, covering 1.8 mm^2 area, with a step size of 0.6 mm. Three main peaks are displayed, 290-330 nm, 365-400 nm, and 400-475 nm.

Murchison chondrule point of interest P673 was chosen for having significant intensity in the range of 365-400 nm, and when observing the time-resolved fluorescence contour plot, appears similar to augite (Figure 68). Point of interest P473 was chosen for having significant intensity in the range of 400-475 nm, and appears to match forsterite (Figure 69). Point of interest P813 was chosen for having significant intensity in the range of 400-475 nm, and appears to match graphite (Figure 70).

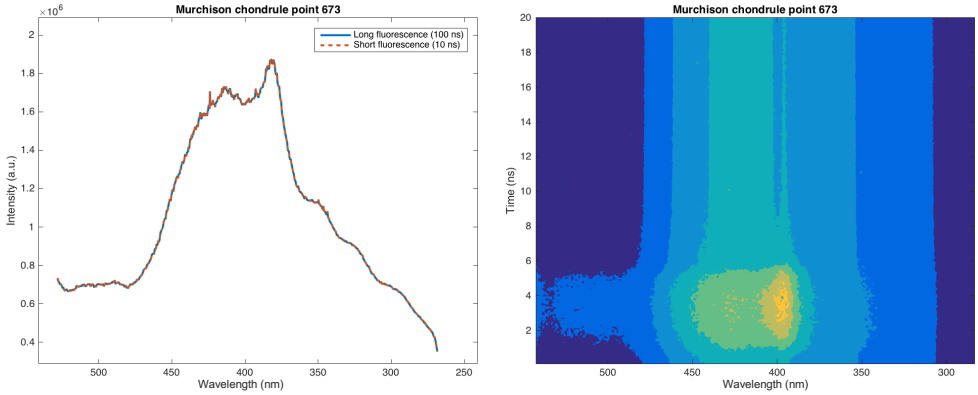


Figure 65: Murchison chondrule point of interest P673 spectra and time-resolved spectral contour image.

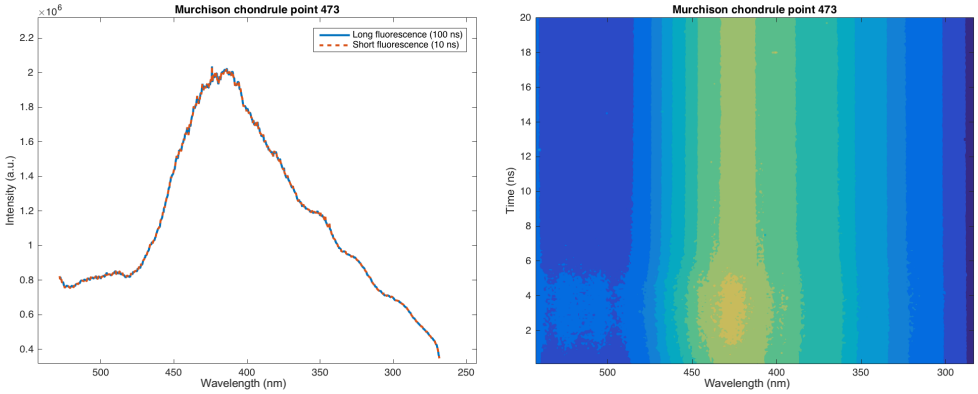


Figure 66: Murchison chondrule point of interest P473 spectra and time-resolved spectral contour image.

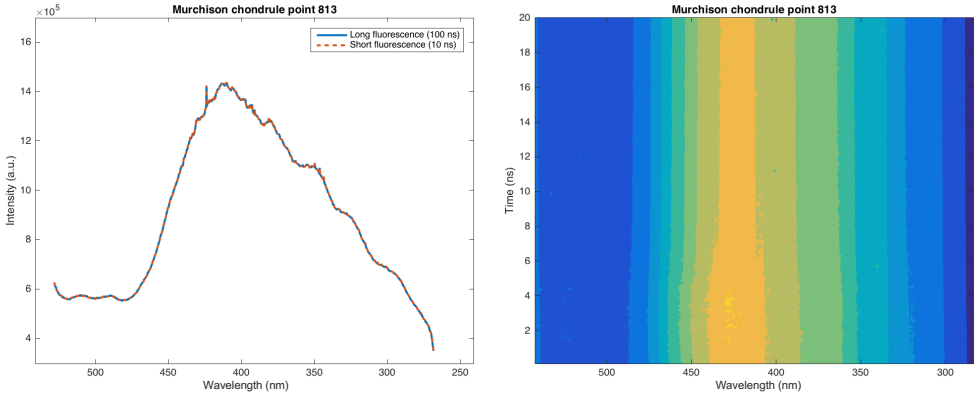


Figure 67: Murchison chondrule point of interest P813 spectra and time-resolved spectral contour image.

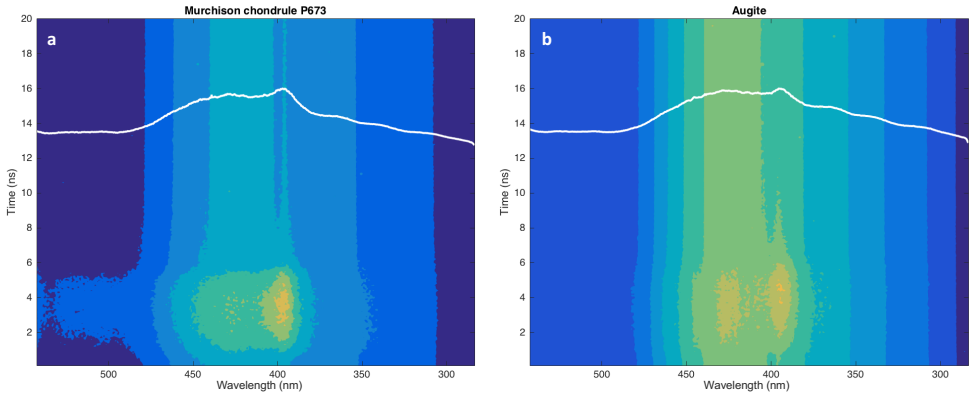


Figure 68: (a) Murchison chondrule point of interest P673 spectra and time-resolved spectral contour image and overlay of long fluorescence spectra. (b) Mineral augite time-resolved fluorescence and overlay of long-fluorescence spectra.

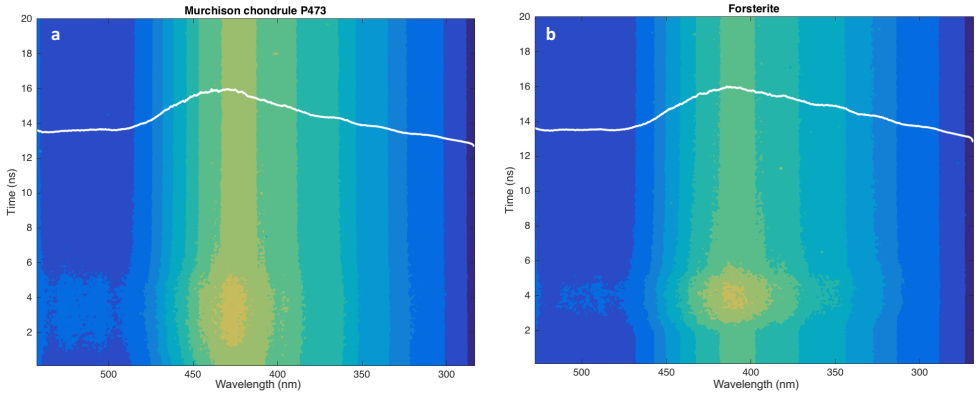


Figure 69: (a) Murchison chondrule point of interest P473 spectra and time-resolved spectral contour image and overlay of long fluorescence spectra. (b) Mineral forsterite time-resolved fluorescence and overlay of long-fluorescence spectra.

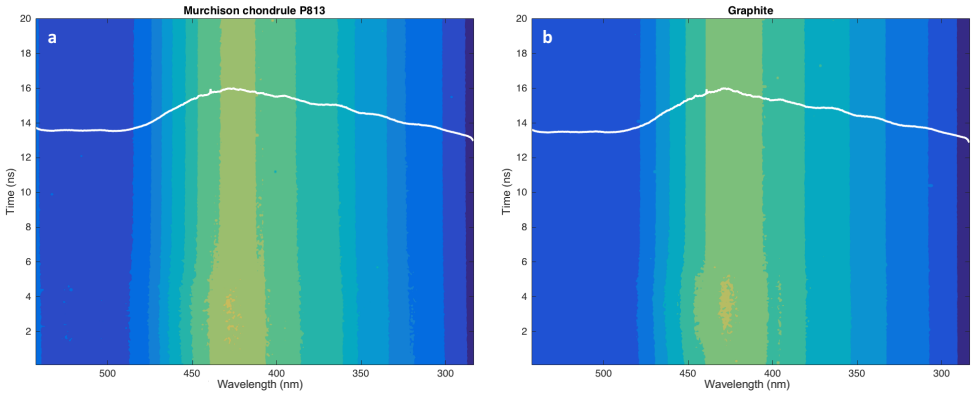


Figure 70: (a) Murchison chondrule point of interest P813 spectra and time-resolved spectral contour image and overlay of long fluorescence spectra. (b) Mineral graphite time-resolved fluorescence and overlay of long-fluorescence spectra.

6.4.4 Murchison CAI: LIF maps, idividual, and time-resolved spectra

LIF 2D mapping resulted in a 400 point spectral image covering 1.2 mm^2 of Murchison CAI, displaying the overall shape of the feature (Figure 71). Two sets of peaks were predominant when viewing, in the range of 275-300 nm and 375-400 nm. These sets of peaks appear together and separately depending on the point. Points of interest were analyzed using short and long fluorescence (10 ns and 100 ns gate width respectively), resulting in high resolution spectra of these points (Figures 72,73 and 74).

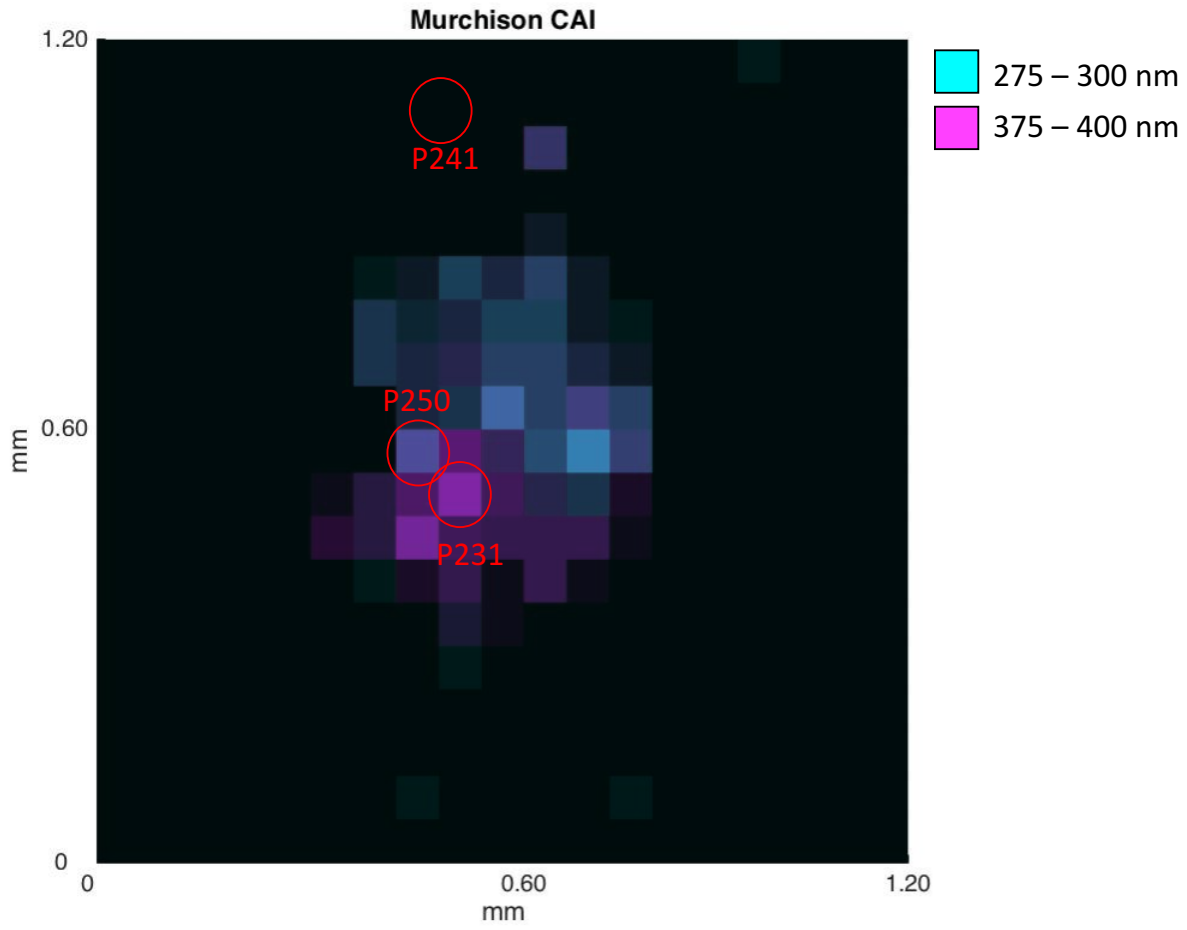


Figure 71: Murchison CAI LIF 2D map. 400 points, covering 1.2 mm^2 area, with a step size of 0.6 mm. Two main peaks are displayed, 275-300 nm and 375-400 nm.

Murchison CAI point of interest P250 was chosen for having significant intensity in the range of 275-300 nm, and when observing the time-resolved fluorescence contour plot, appears to somewhat match nepheline (Figure 75). Point of interest P241 was chosen for having significant intensity in the range of 375-400 nm, and appears to match graphite (Figure 76). Point of interest P231 was chosen for having significant intensity in the range of 375-400 nm, and appears to match diopside (Figure 77).

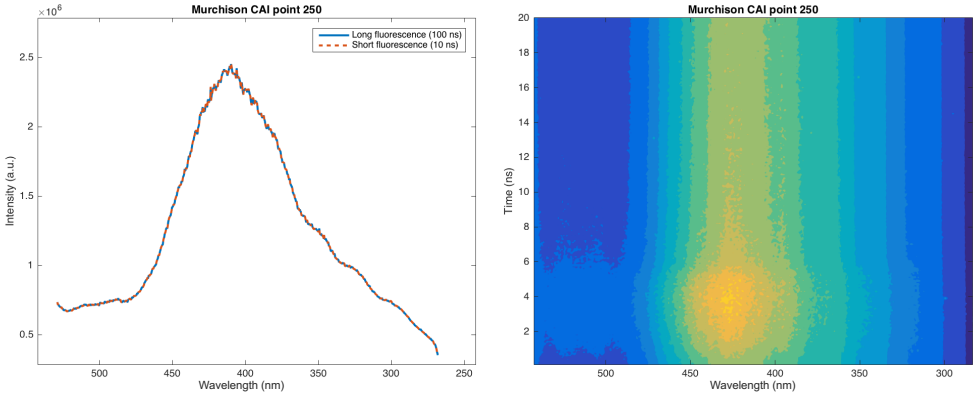


Figure 72: Murchison CAI point of interest P250 spectra and time-resolved spectral contour image.

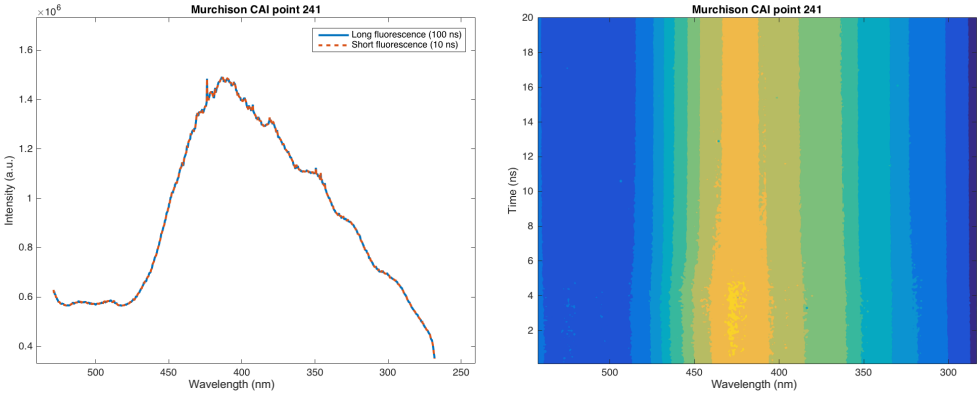


Figure 73: Murchison CAI point of interest P241 spectra and time-resolved spectral contour image.

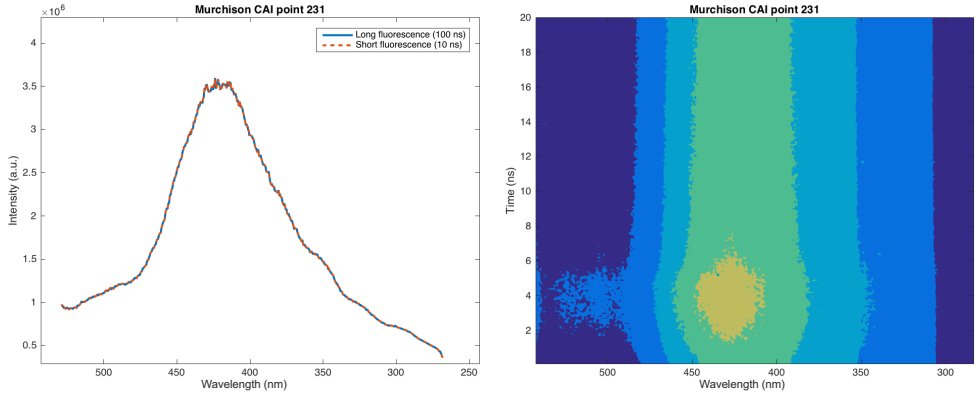


Figure 74: Murchison CAI point of interest P231 spectra and time-resolved spectral contour image.

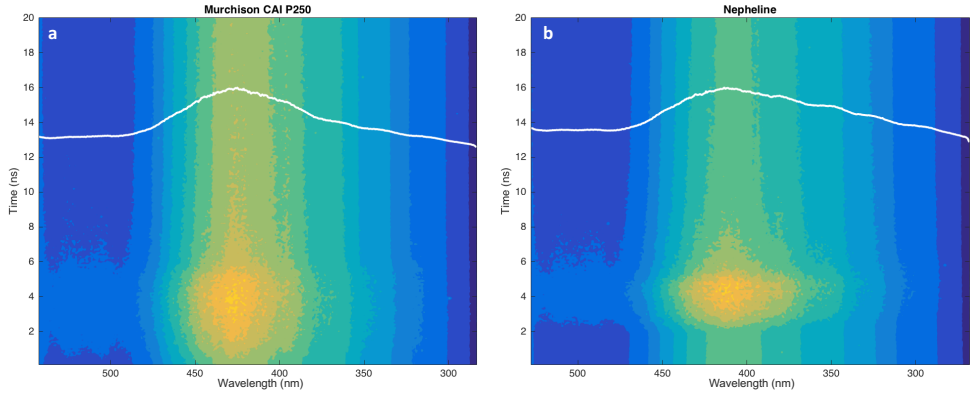


Figure 75: (a) Murchison CAI point of interest P250 spectra and time-resolved spectral contour image and overlay of long fluorescence spectra. (b) Mineral nepheline time-resolved fluorescence and overlay of long-fluorescence spectra.

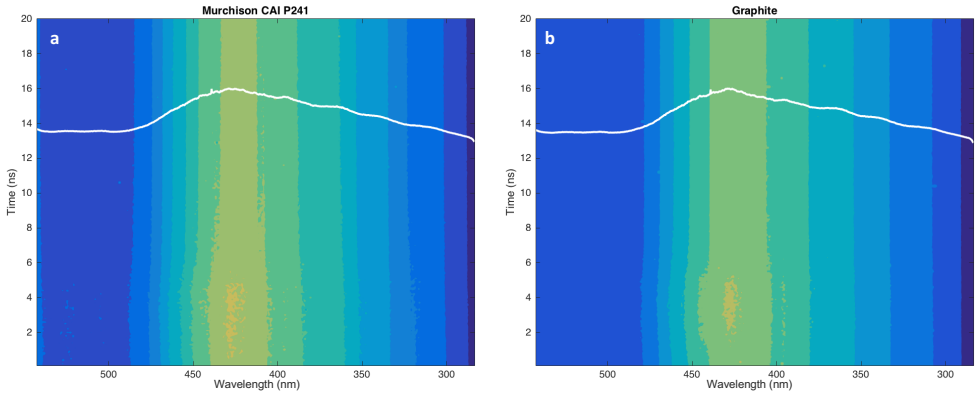


Figure 76: (a) Murchison CAI point of interest P241 spectra and time-resolved spectral contour image and overlay of long fluorescence spectra. (b) Mineral graphite time-resolved fluorescence and overlay of long-fluorescence spectra.

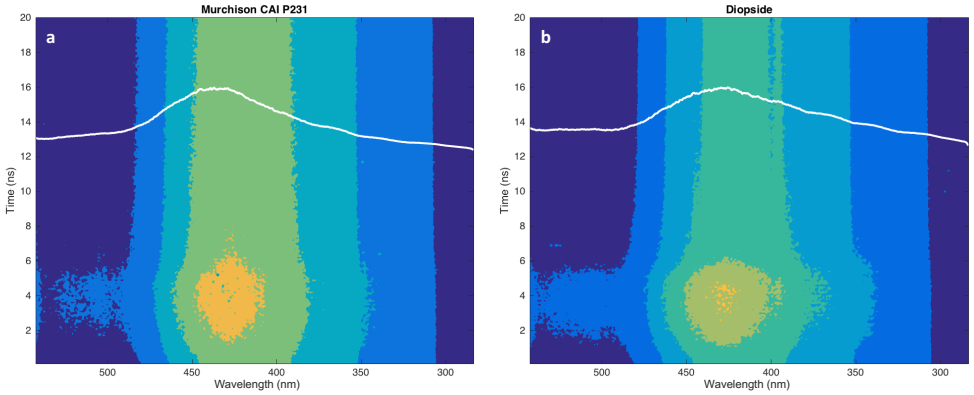


Figure 77: (a) Murchison CAI point of interest P231 spectra and time-resolved spectral contour image and overlay of long fluorescence spectra. (b) Mineral diopside time-resolved fluorescence and overlay of long-fluorescence spectra.

6.4.5 DGR-035 chondrule: LIF maps, idividual, and time-resolved spectra

LIF 2D mapping resulted in a 1764 point spectral image covering 2.5 mm^2 of DGR-035 chondrule, displaying a rim and objects surrounding the feature (Figure 78). Two sets of peaks were predominant when viewing in the range of 275-300 nm and 325-350 nm. The peaks appear to be in the same spectra for all points. Points of interest were analyzed using short and long fluorescence (10 ns and 100 ns gate width respectively), resulting in high resolution spectra of these points (Figures 79 and 80).

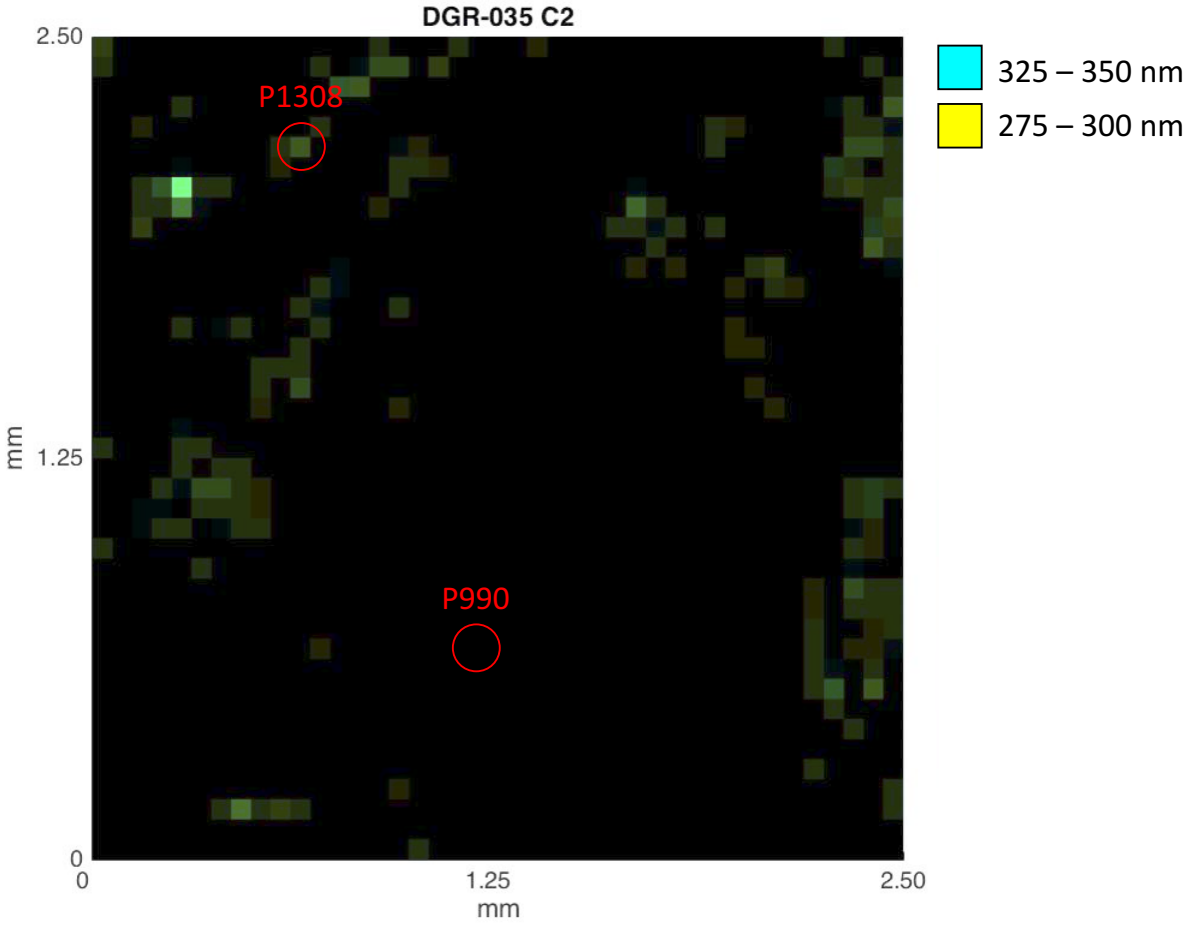


Figure 78: DGR-035 chondrule LIF 2D map. 1764 points, covering 2.5 mm^2 area, with a step size of 0.6 mm. Two main peaks are displayed, 275-300 nm and 325-350 nm.

DGR-035 chondrule point of interest P990 was chosen for having significant intensity in the range of 400-450, and some intensity from 325-350 nm. When observing the time-resolved fluorescence contour plot, appears to somewhat match graphite (Figure 81). Point of interest P1308 was chosen for having significant intensity in the range of 400-450 nm, and appears to match graphite similar to P990 (Figure 82).

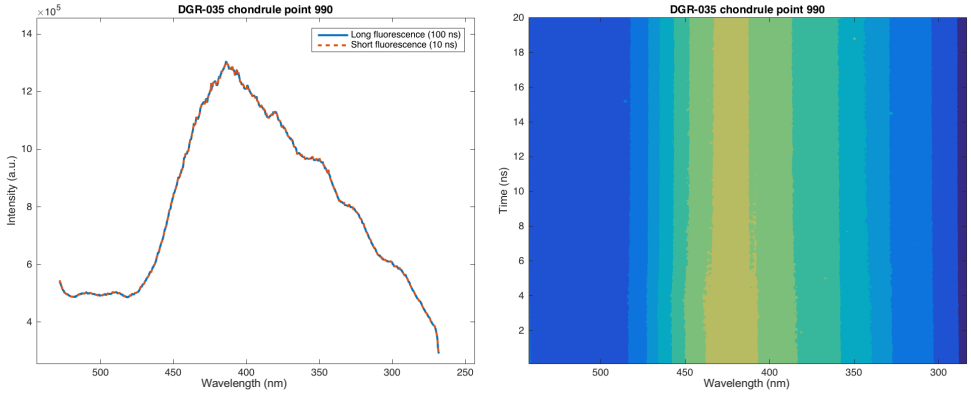


Figure 79: DGR-035 chondrule point of interest P990 spectra and time-resolved spectral contour image.

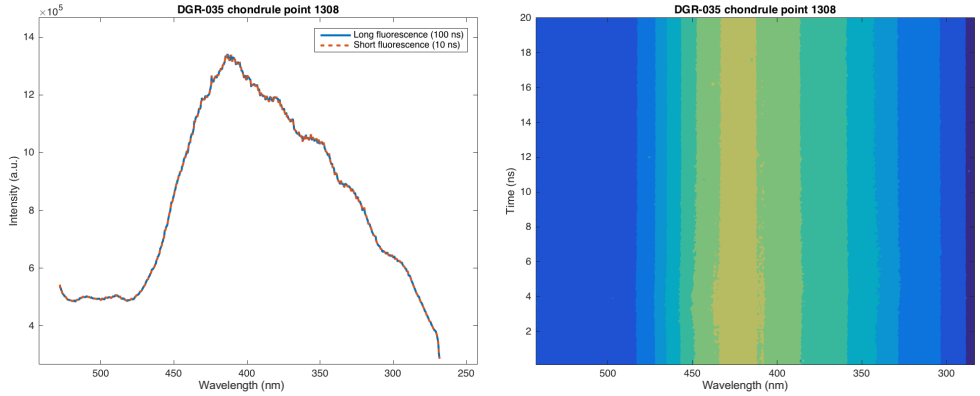


Figure 80: DGR-035 chondrule point of interest P1308 spectra and time-resolved spectral contour image.

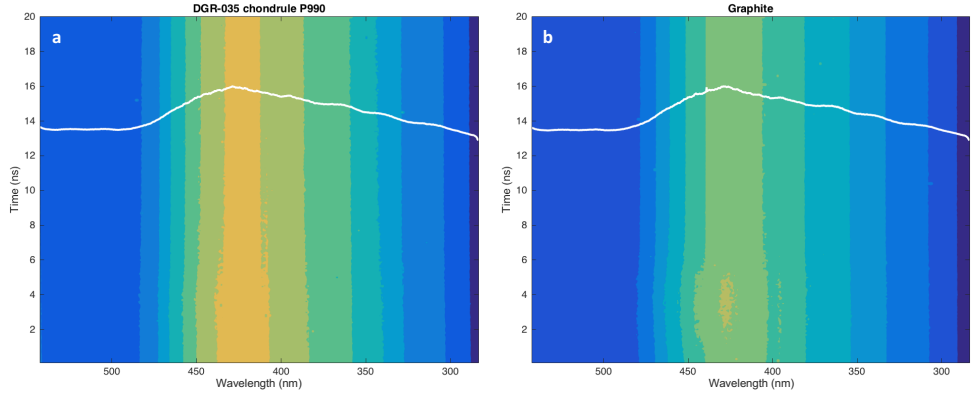


Figure 81: (a) DGR-035 chondrule point of interest P990 spectra and time-resolved spectral contour image and overlay of long fluorescence spectra. (b) Mineral graphite time-resolved fluorescence and overlay of long-fluorescence spectra.

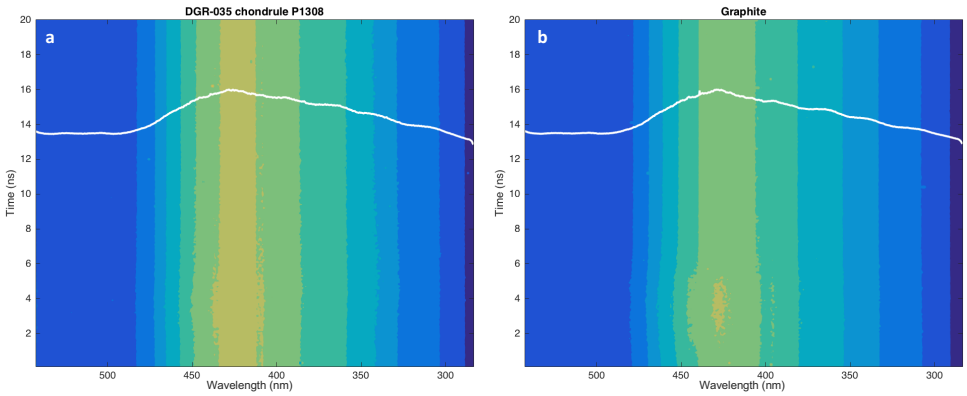


Figure 82: (a) DGR-035 chondrule point of interest P1308 spectra and time-resolved spectral contour image and overlay of long fluorescence spectra. (b) Mineral graphite time-resolved fluorescence and overlay of long-fluorescence spectra.

6.4.6 DGR-035 CAI: LIF maps, idividual, and time-resolved spectra

LIF 2D mapping resulted in a 625 point spectral image covering 1.5 mm^2 of DGR-035 CAI, displaying the general shape of the feature (Figure 83). Two sets of peaks were predominant when viewing in the range of 275-300 nm and 325-350 nm. The peaks appear to be in the same spectra for all points. Points of interest were analyzed using short and long fluorescence (10 ns and 100 ns gate width respectively), resulting in high resolution spectra of these points (Figures 84, 85 and 86).

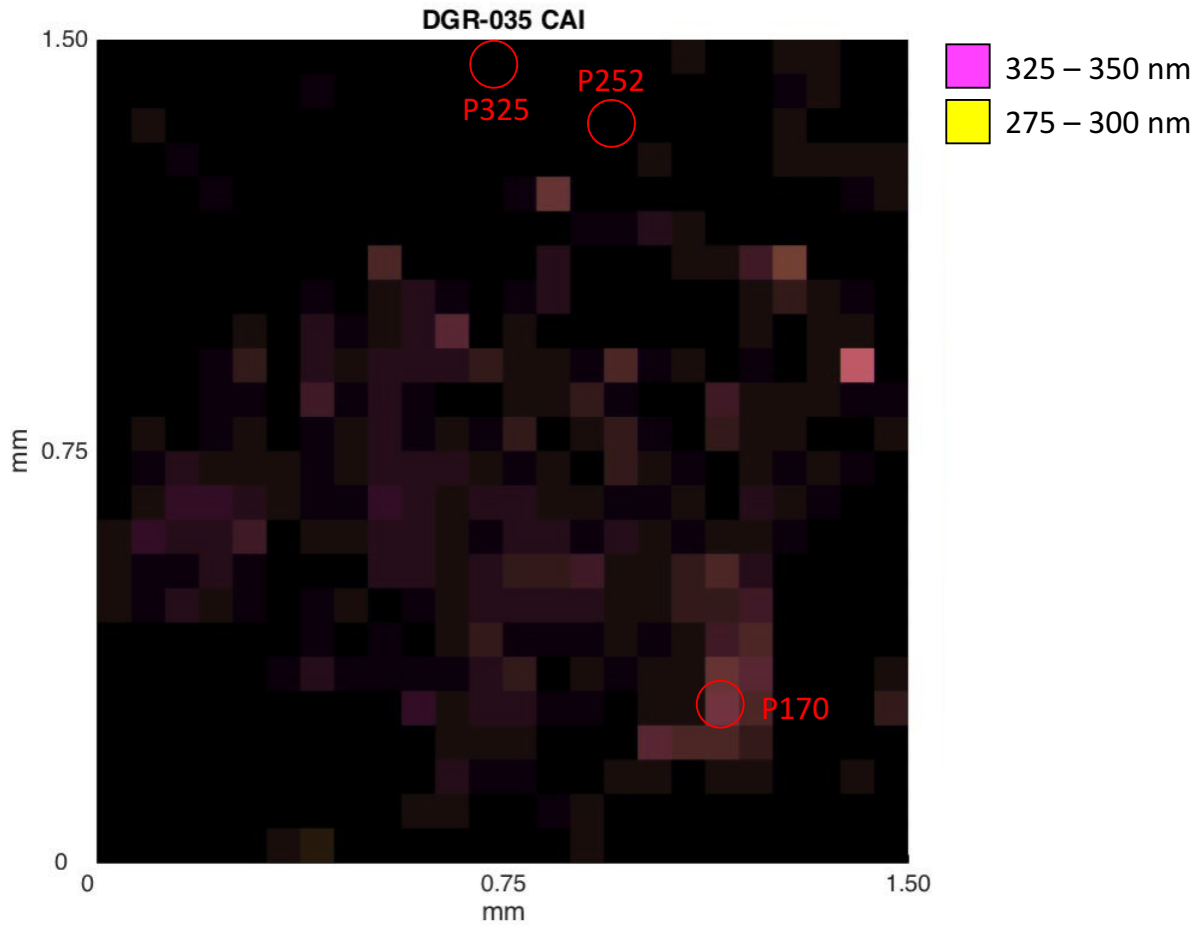


Figure 83: DGR-035 CAI LIF 2D map. 625 points, covering 1.5 mm^2 area, with a step size of 0.6 mm. Two main peaks are displayed, 275-300 nm and 325-350 nm.

DGR-035 CAI point of interest P170 was chosen for having significant intensity in the range of 400-450, and some intensity from 325-350 nm. The time-resolved fluorescence contour plot appears to match diopside (Figure 87). Point of interest P252 was chosen for having significant intensity in the range of 325-350 nm, and appears to match labradorite (Figure 88). Point of interest P325 was chosen for having significant intensity in the range of 400-450 nm, and appears to match graphite (Figure 89).

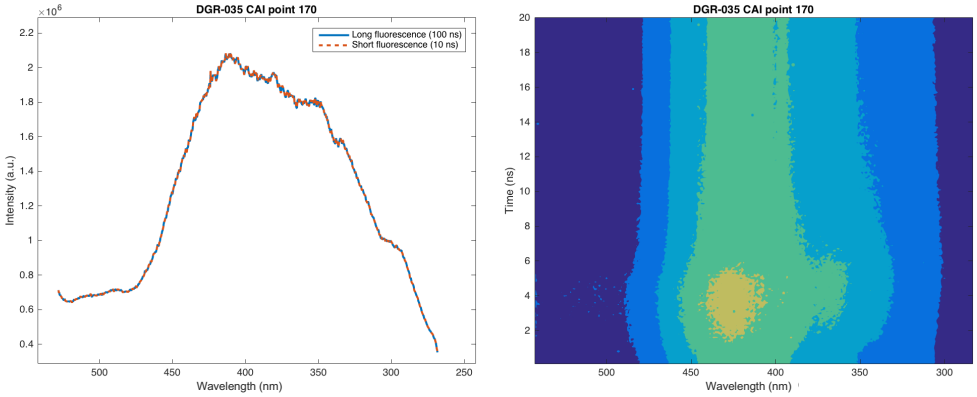


Figure 84: DGR-035 CAI point of interest P170 spectra and time-resolved spectral contour image.

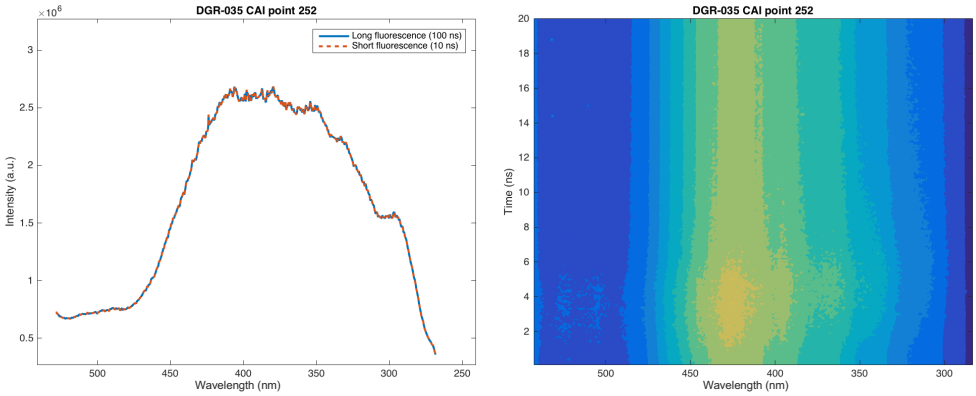


Figure 85: DGR-035 CAI point of interest P252 spectra and time-resolved spectral contour image.

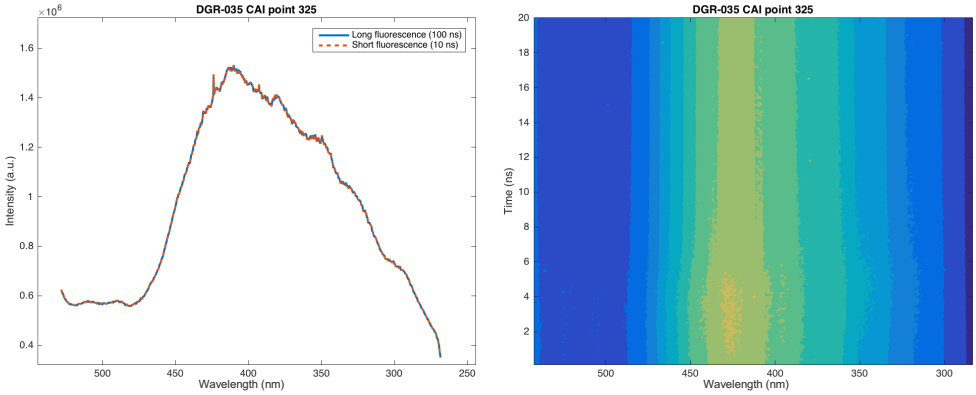


Figure 86: DGR-035 CAI point of interest P325 spectra and time-resolved spectral contour image.

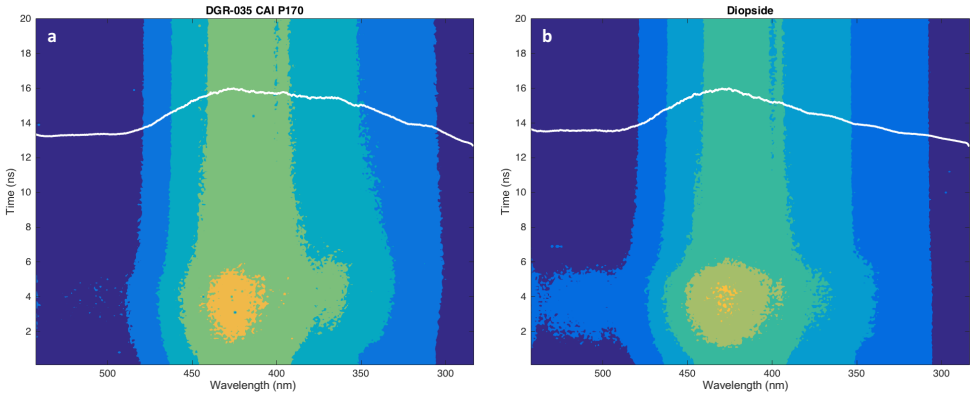


Figure 87: (a) DGR-035 CAI point of interest P170 spectra and time-resolved spectral contour image and overlay of long fluorescence spectra. (b) Mineral diopside time-resolved fluorescence and overlay of long-fluorescence spectra.

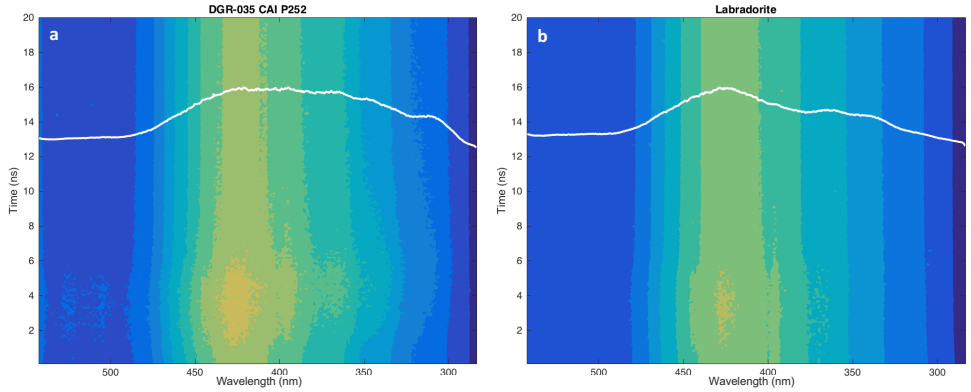


Figure 88: (a) DGR-035 CAI point of interest P252 spectra and time-resolved spectral contour image and overlay of long fluorescence spectra. (b) Mineral labradorite time-resolved fluorescence and overlay of long-fluorescence spectra.

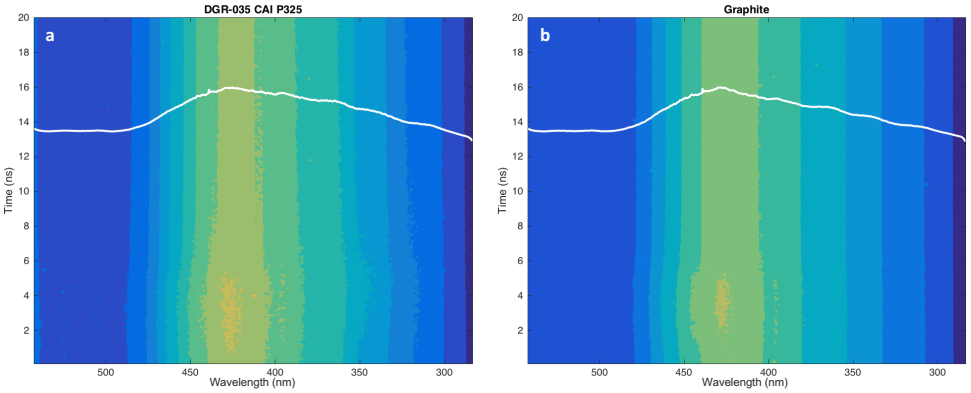


Figure 89: (a) DGR-035 CAI point of interest P325 spectra and time-resolved spectral contour image and overlay of long fluorescence spectra. (b) Mineral graphite time-resolved fluorescence and overlay of long-fluorescence spectra.

6.4.7 DGR-034 chondrule: LIF maps, idividual, and time-resolved spectra

LIF 2D mapping resulted in a 1020 point spectral image covering about a 2 mm^2 area of DGR-034 chondrule. This map resulted in not a lot of spectral information, with most peaks being cosmic rays or noise (Figure 90). Peaks were not predominant within this map, with only slight background fluorescence obtained. Two sets of peaks were mapped in the range of 285-335 nm and 400-450 nm. The peaks appear to be in the same spectra for all points.

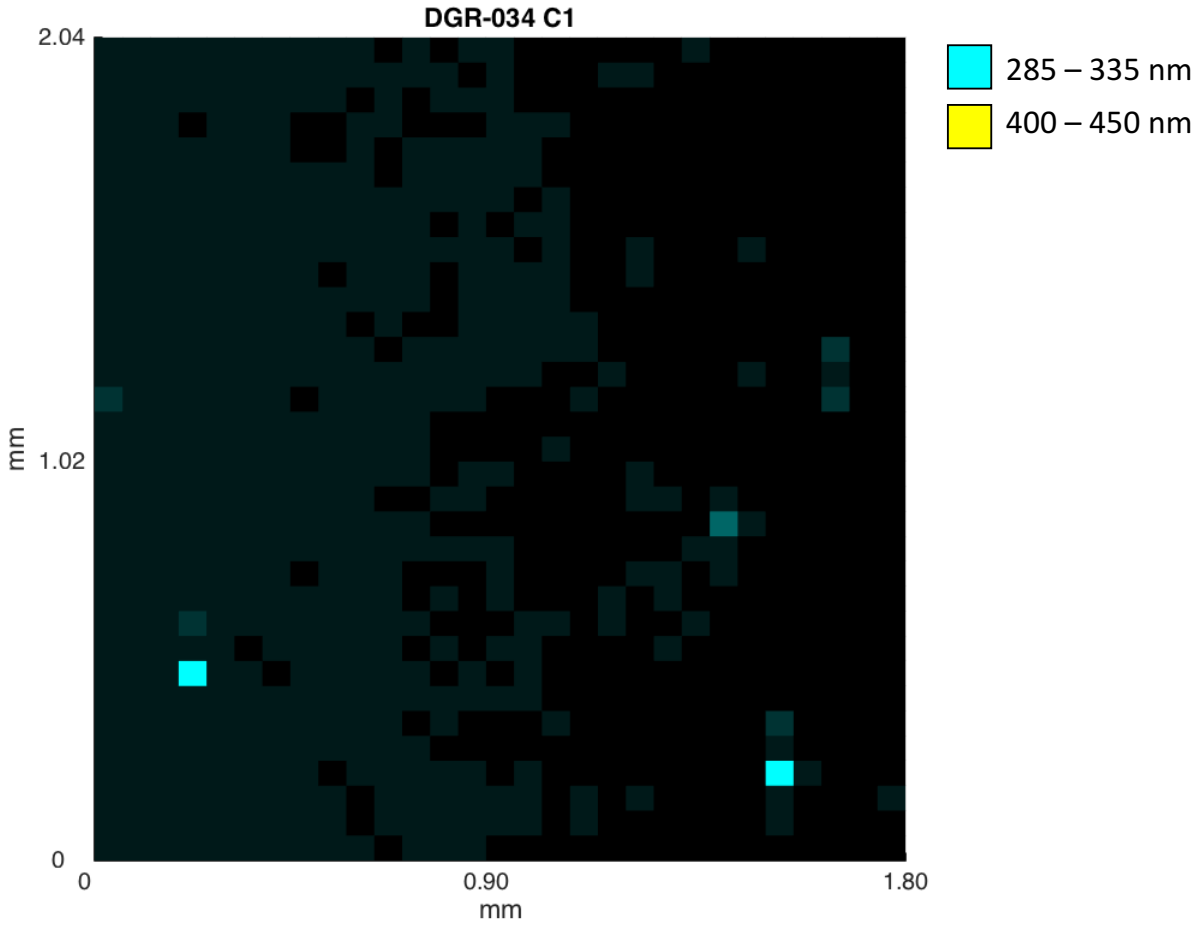


Figure 90: DGR-034 chondrule LIF 2D map. 1020 points, covering about a 2 mm^2 area, with a step size of 0.6 mm. Two main peaks are displayed, 285-335 nm and 400-450 nm.

6.4.8 DGR-034 CAI: LIF maps, idividual, and time-resolved spectra

LIF 2D mapping resulted in a 1292 point spectral image covering about a 2 mm^2 area of DGR-034 CAI. This map resulted in not a lot of spectral information, with most peaks being cosmic rays or noise (Figure 91). Peaks were not predominant within this map, with only slight background fluorescence obtained. One peak was mapped in the range of 400-450 nm.

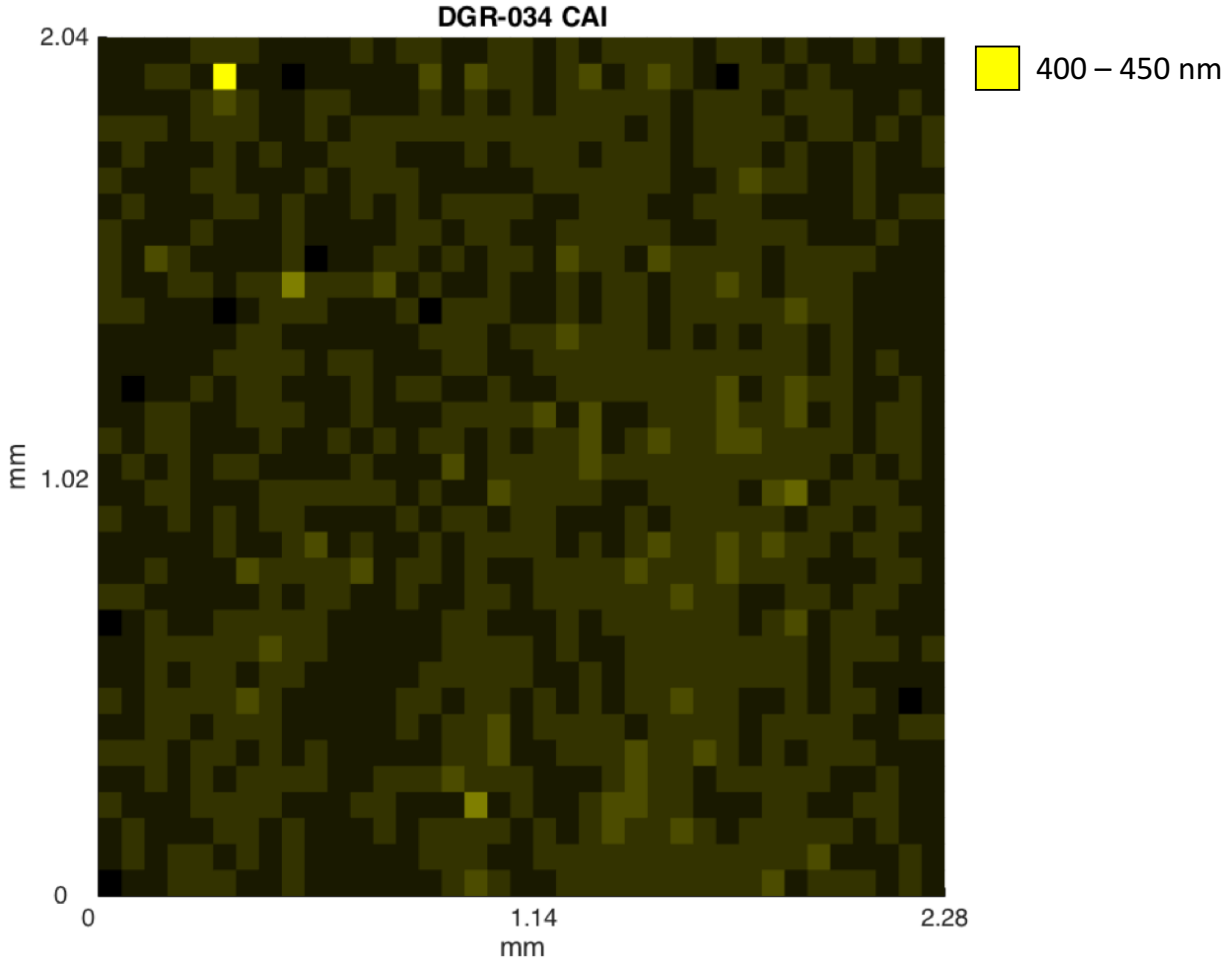
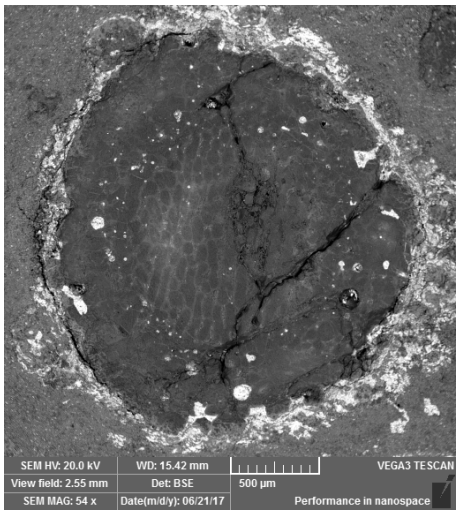


Figure 91: DGR-034 CAI LIF 2D map. 1292 points, covering about a 2 mm^2 area, with a step size of 0.6 mm. One peak is displayed and 400-450 nm.

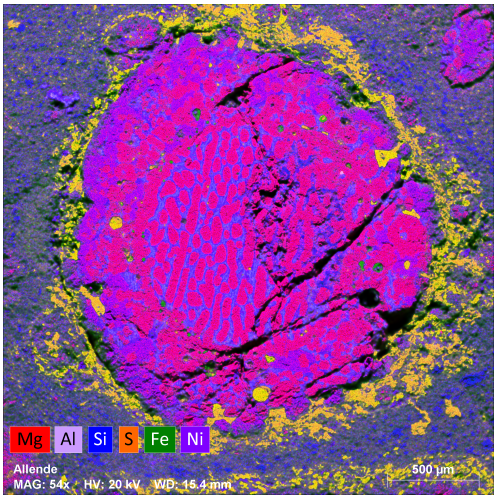
6.5 Overview of spectral maps

Presented in this section are back-scattered electron (BSE) microscope images, electron-dispersive X-ray spectroscopy images, Raman spectroscopy 2D maps, and LIF spectroscopy 2D maps of each feature for all four samples studied. This section will provide an overview of the resulting images using EDS, Raman and LIF for further comparison in Section 7.

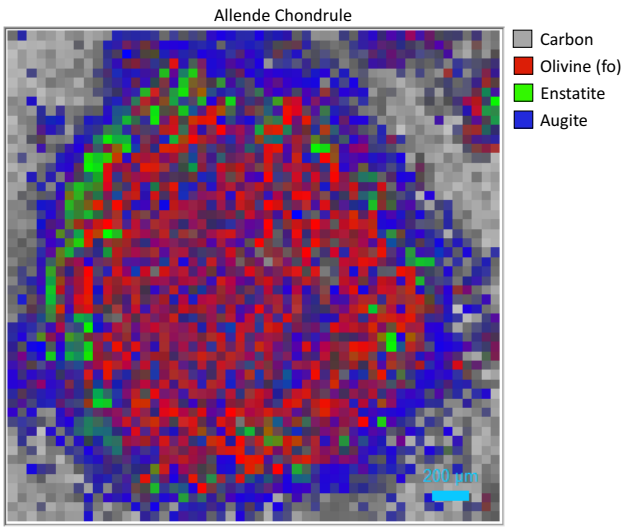
6.5.1 Allende chondrule maps



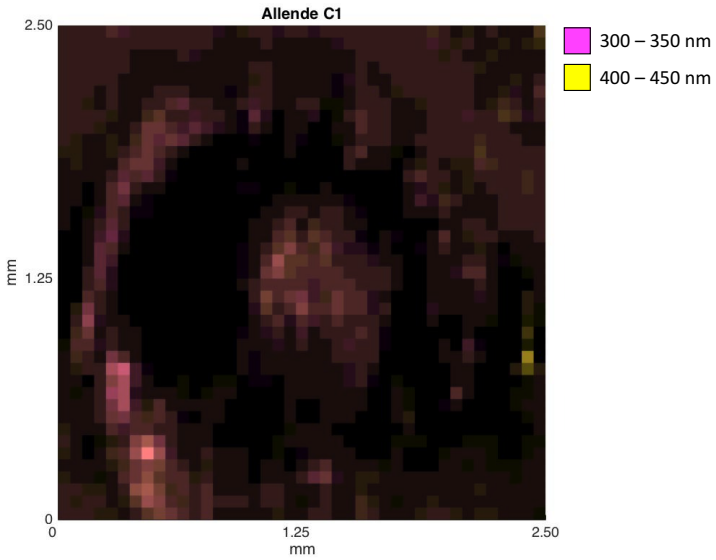
(a) BSE image of Allende chondrule



(b) EDS image of Allende chondrule



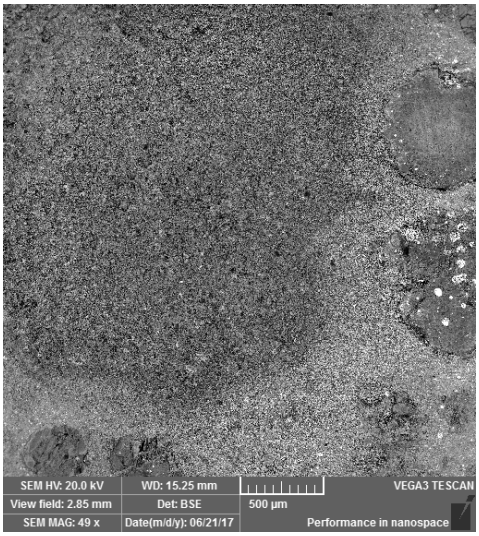
(c) Raman spectral map of Allende chondrule



(d) LIF spectral map of Allende chondrule

Figure 92: Spectral map acquisitions for Allende chondrule.

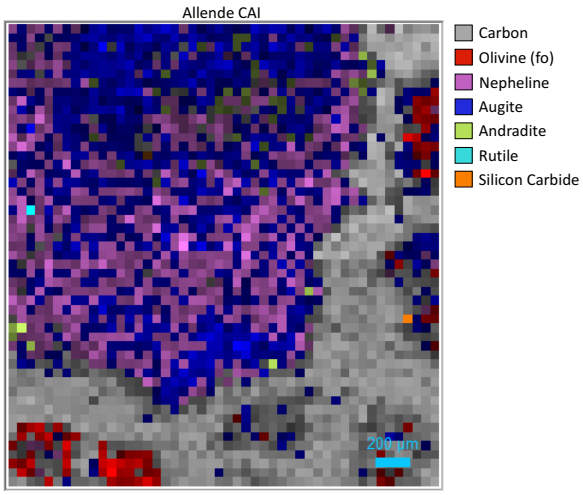
6.5.2 Allende CAI maps



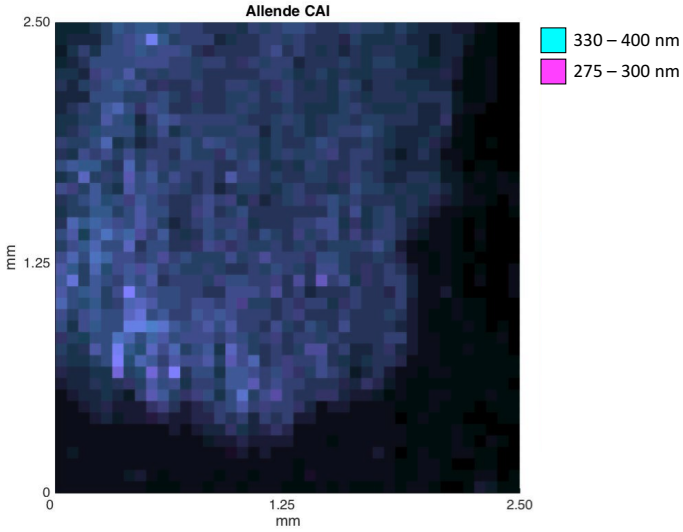
(a) BSE image of Allende CAI



(b) EDS image of Allende CAI



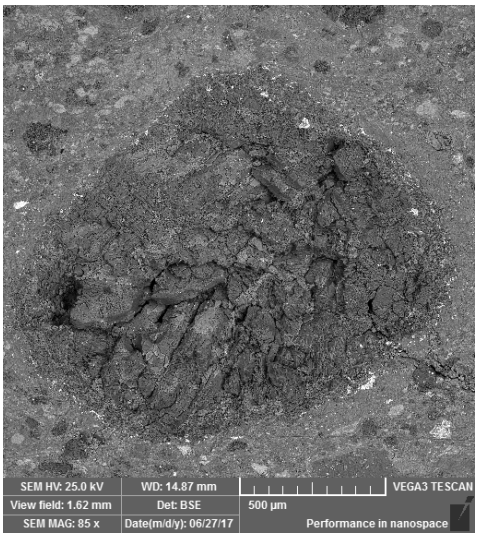
(c) Raman spectral map of Allende CAI



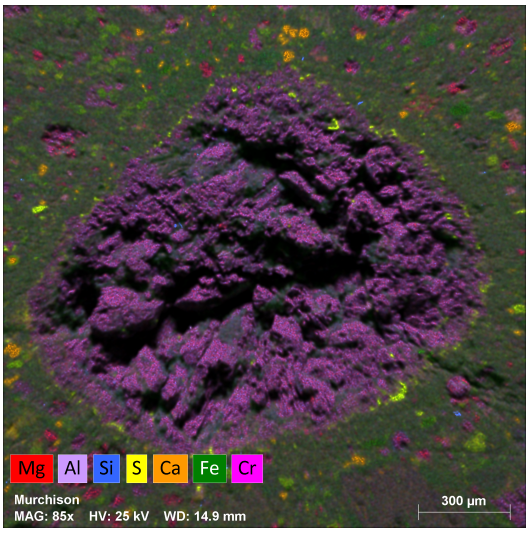
(d) LIF spectral map of Allende CAI

Figure 93: Spectral map acquisitions for Allende CAI.

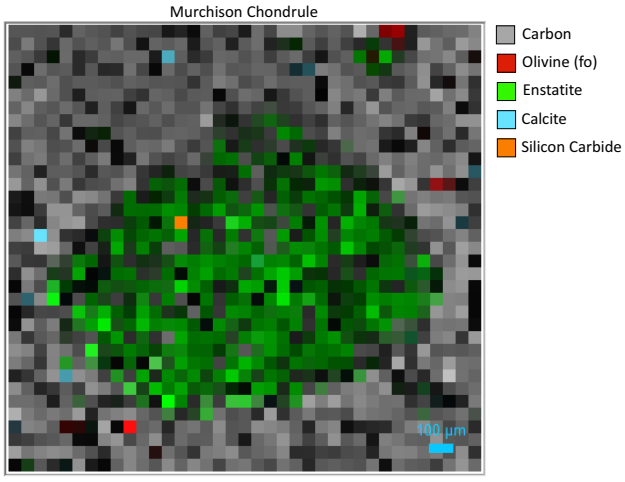
6.5.3 Murchison chondrule maps



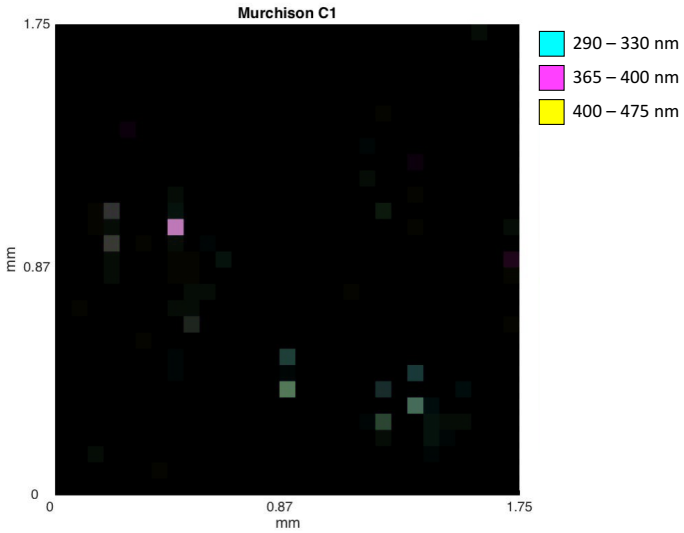
(a) BSE image of a Murchison chondrule



(b) EDS image of a Murchison chondrule



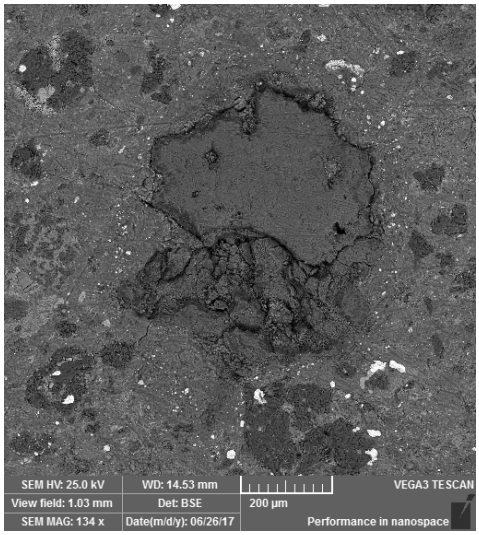
(c) Raman spectral map of a Murchison chondrule



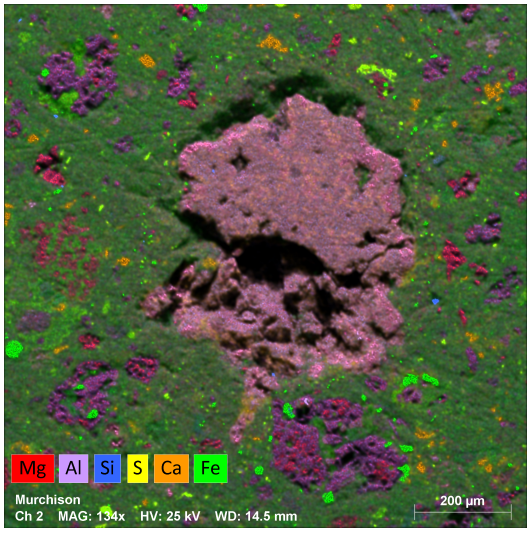
(d) LIF spectral map of a Murchison chondrule

Figure 94: Spectral map acquisitions for a Murchison chondrule.

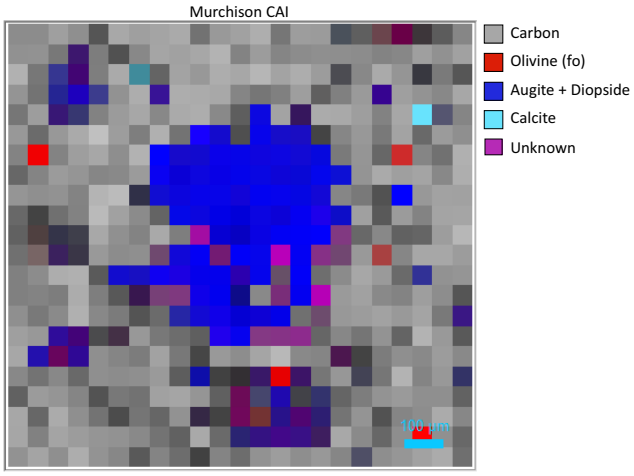
6.5.4 Murchison CAI maps



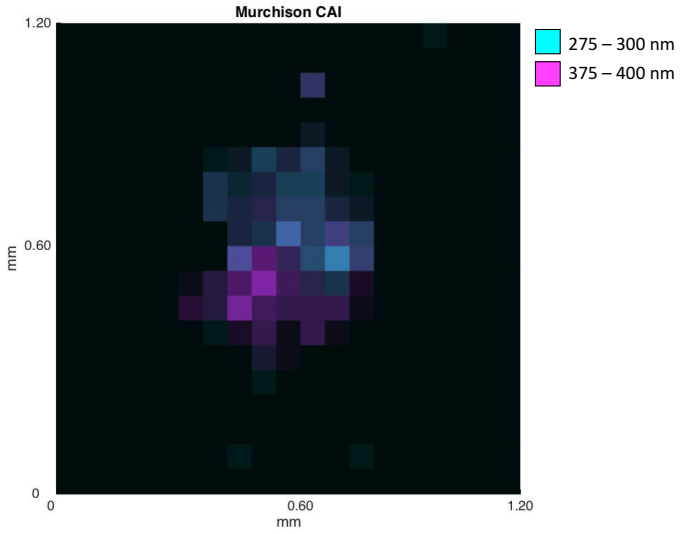
(a) BSE image of a Murchison CAI



(b) EDS image of a Murchison CAI



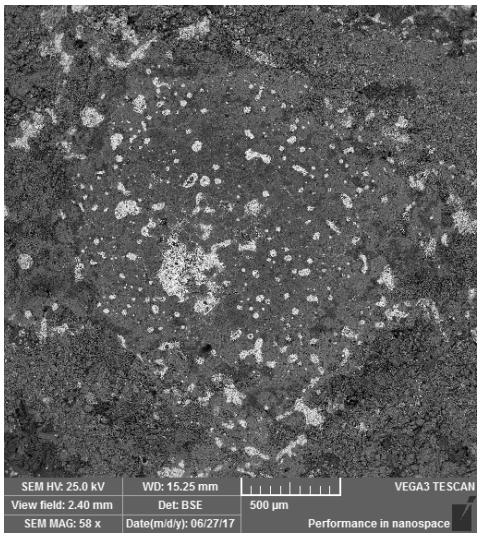
(c) Raman spectral map of a Murchison CAI



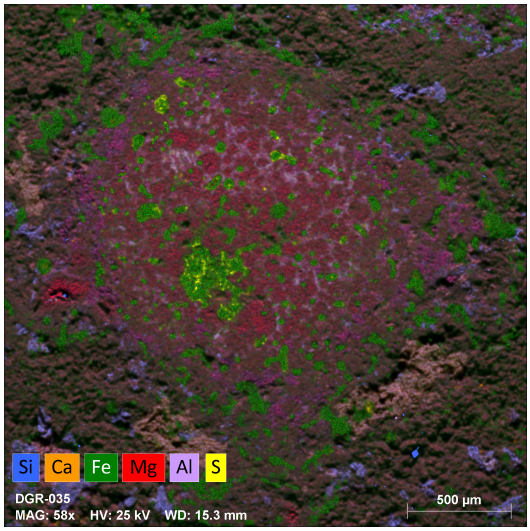
(d) LIF spectral map of a Murchison CAI

Figure 95: Spectral map acquisitions for a Murchison CAI.

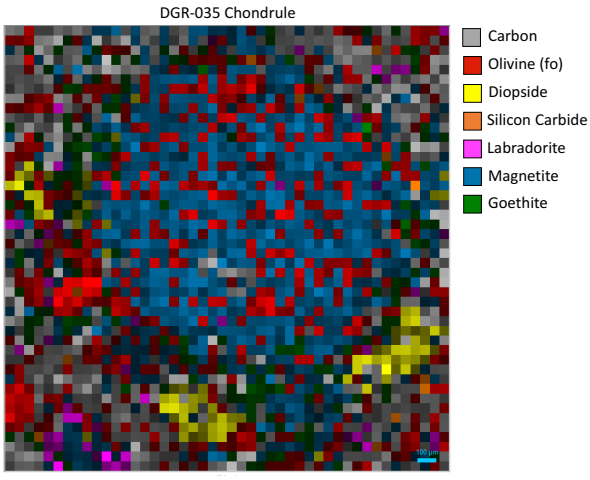
6.5.5 DGR-035 chondrule maps



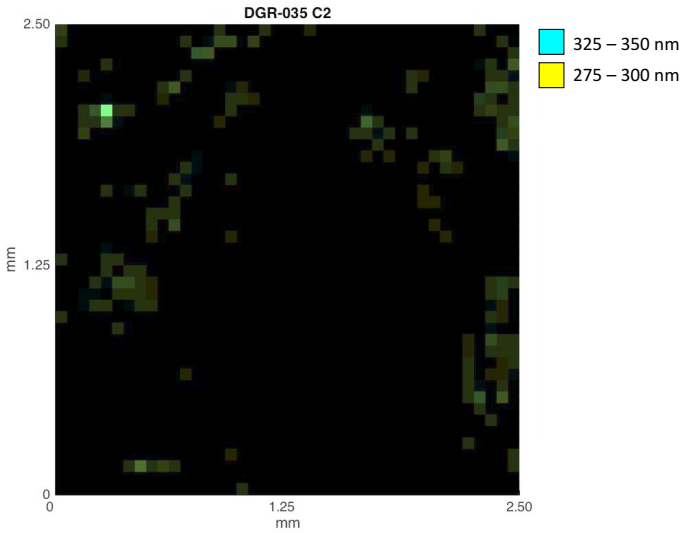
(a) BSE image of a DGR-035 chondrule



(b) EDS image of a DGR-035 chondrule



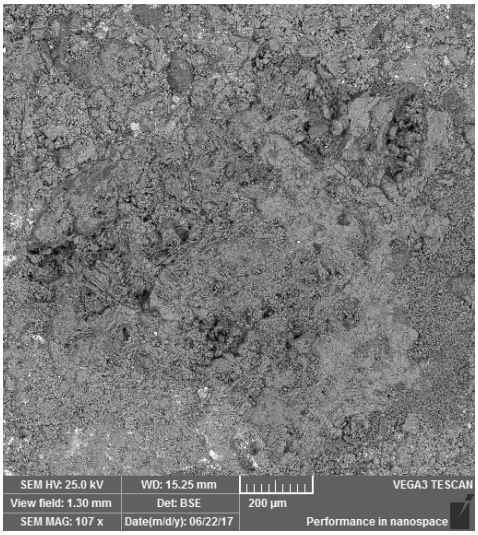
(c) Raman spectral map of a DGR-035 chondrule



(d) LIF spectral map of a DGR-035 chondrule

Figure 96: Spectral map acquisitions for a DGR-035 chondrule.

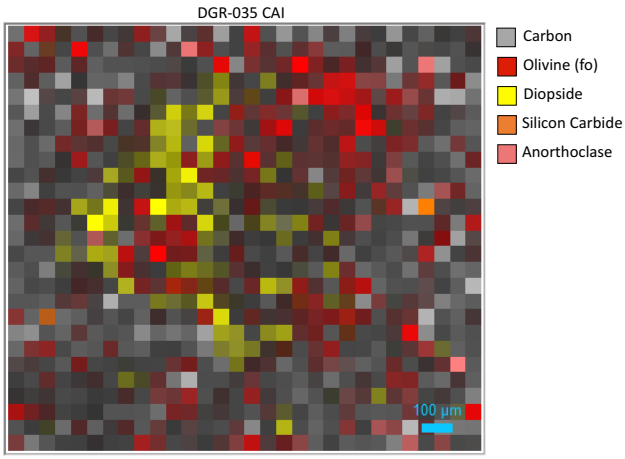
6.5.6 DGR-035 CAI maps



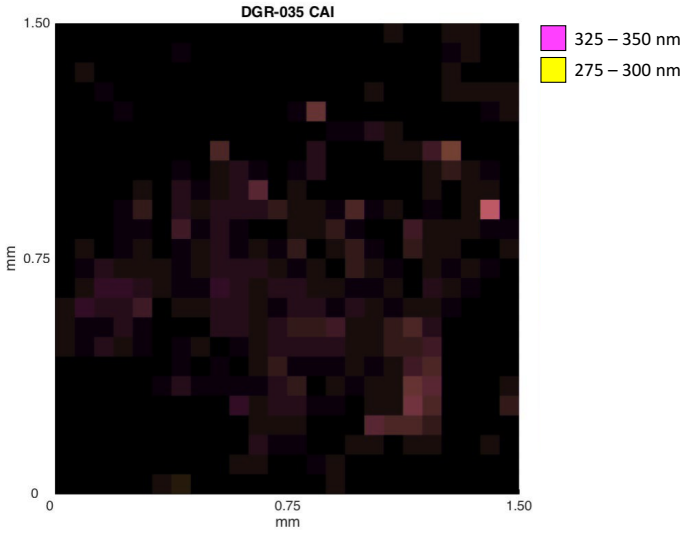
(a) BSE image of a DGR-035 CAI



(b) EDS image of a DGR-035 CAI



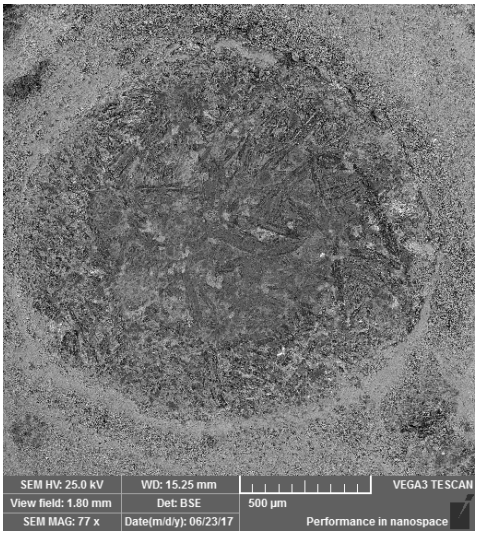
(c) Raman spectral map of a DGR-035 CAI



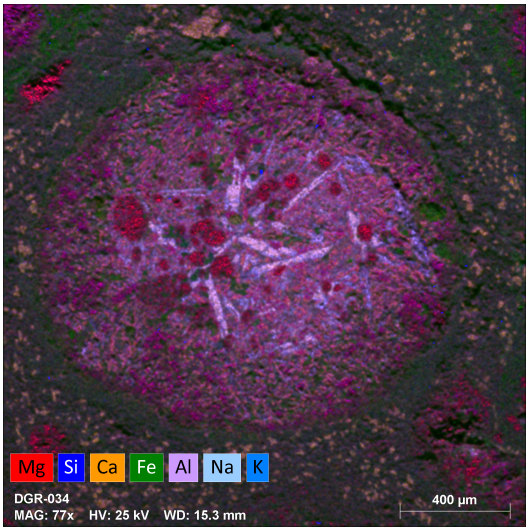
(d) LIF spectral map of a DGR-035 CAI

Figure 97: Spectral map acquisitions for a DGR-035 CAI.

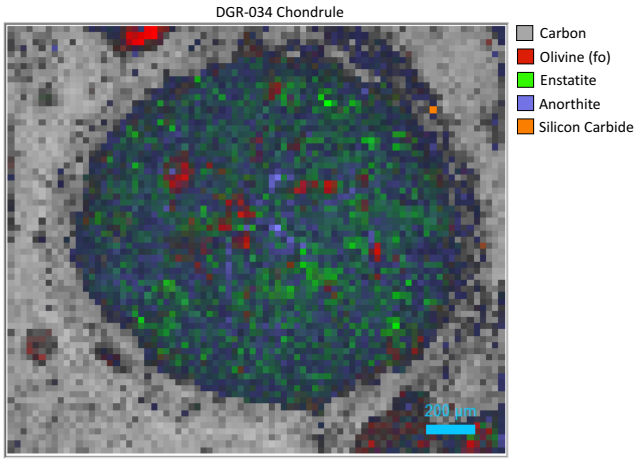
6.5.7 DGR-034 chondrule maps



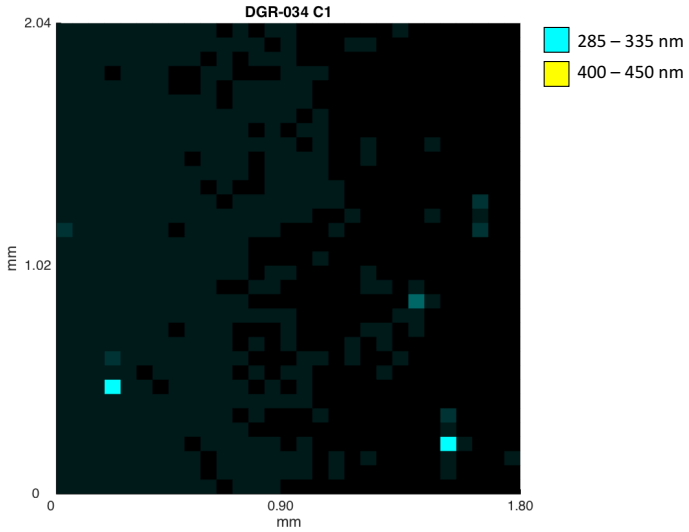
(a) BSE image of a DGR-034 chondrule



(b) EDS image of a DGR-034 chondrule



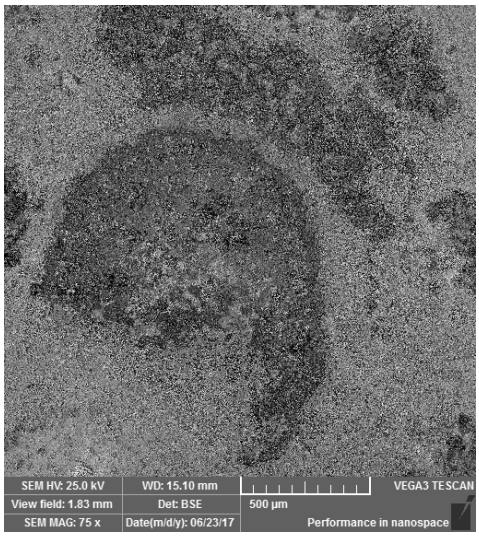
(c) Raman spectral map of a DGR-034 chondrule



(d) LIF spectral map of a DGR-034 chondrule

Figure 98: Spectral map acquisitions for a DGR-034 chondrule.

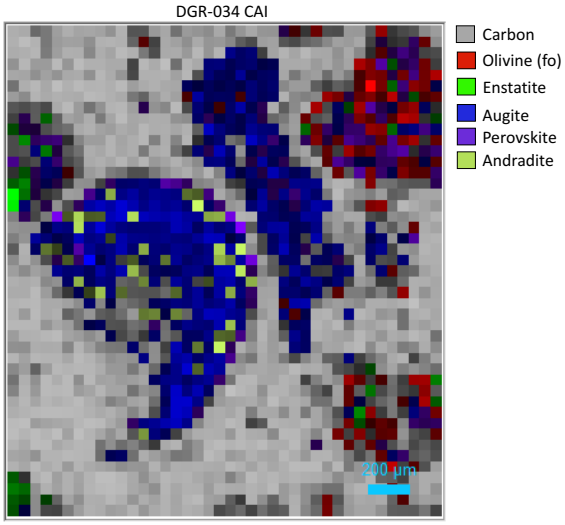
6.5.8 DGR-034 CAI maps



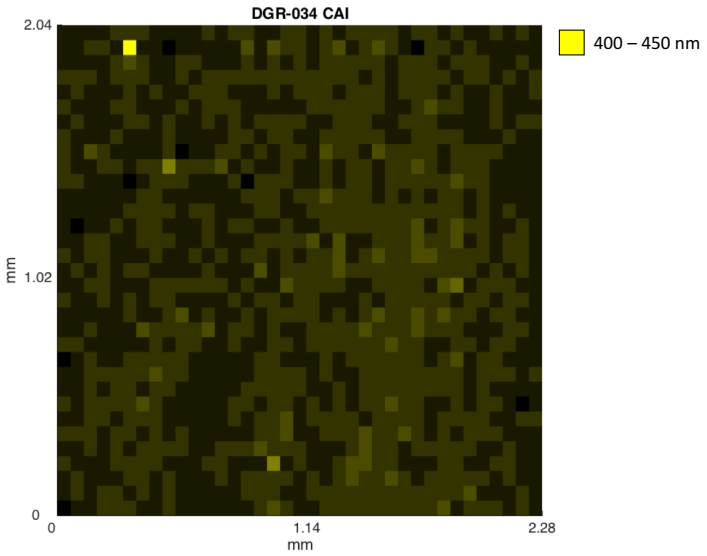
(a) BSE image of a DGR-034 CAI



(b) EDS image of a DGR-034 CAI



(c) Raman spectral map of a DGR-034 CAI



(d) LIF spectral map of a DGR-034 CAI

Figure 99: Spectral map acquisitions for a DGR-034 CAI.

6.6 Mineral ID result summary

EDS, Raman, and LIF maps resulted in mineral identification for all samples except DGR-034. The results of the mineral identification are summarized in Table 12. For all samples in which minerals were identified using EDS, Raman and LIF, there was at least one mineral identification that overlapped using all three methods and on average there were two minerals that overlapped for each sample. Both the chondrule and CAI in DGR-034 do not have minerals that were identified using LIF, and therefore lack any 'mineral overlap' between LIF and EDS/Raman.

Table 12: Summary of minerals identified from points of EDS, Raman and LIF maps. The mineral overlap column represents the number of minerals that were identified by LIF that were also identified by either Raman or EDS analyses

Sample	EDS	Raman	LIF	Mineral overlap
Allende chondrule	forsterite, enstatite	forsterite, enstatite, augite, carbon	forsterite, orthopyroxene, augite	2
Allende CAI	forsterite, clinopyroxene, nepheline	forsterite, augite, nepheline, andradite, rutile, silicon carbide, carbon	augite, nepheline	2
Murchison chondrule	augite, enstatite	enstatite, forsterite, calcite, silicon carbide, carbon	augite, forsterite, graphite	3
Murchison CAI	diopside, forsterite, ferrosilite	augite/diopside, forsterite, calcite, carbon	diopside, nepheline, graphite	2
DGR-035 chondrule	olivine, ferrosilite, enstatite, augite, magnetite	olivine, magnetite, diopside, labradorite, goethite, silicon carbide, carbon	graphite	1
DGR-035 CAI	diopside, forsterite, fayalite, enstatite	diopside, forsterite, anorthoclase, silicon carbide, carbon	diopside, labradorite, graphite	2
DGR-034 chondrule	enstatite, fayalite, ferrosilite, augite	enstatite, forsterite, anorthite, silicon carbide, carbon	–	–
DGR-034 CAI	forsterite, enstatite, perovskite, fayalite, ferrosilite, diopside, andradite	forsterite, enstatite, perovskite, andradite, carbon	–	–

7 Discussion

7.1 Characterization

Samples DGR-034 and DGR-035 were classified within this work as a CV3-S1-W3, and a CK4-S2-W2 carbonaceous chondrites respectively. Weathering and shock levels for these samples is typical of carbonaceous chondrites, with 85% being S1 or S2 [Scott et al., 1992]. Shock is often minimal within carbonaceous chondrites, which is analogous with S1 and S2 shock levels. Weathering is minimal within the samples, most likely because they were found in Morocco - a hot desert environment. If these samples were found in the Antarctic, we would expect very different terrestrial weathering features inlcuding more aqueous alteration [Bland et al., 2006]. Carbonaceous chondrites are some of the most rare meteorite types on Earth, making up approximately 5% of all meteorite falls [Hutchison, 2004]. Therefore it was important to systematically analyze and classify suspected carbonaceous chondrite samples for further scientific study. These samples have been submitted to the Meteoritical Society for naming, where the classification data will be reviewed and published for the scientific community. Characterization of these samples allowed for a meaningful investigation using other techniques such as LIF, Raman and EDS.

7.2 Spectral investigation

LIF, Raman and EDS spectral maps were collected of each millimetre sized feature in the four carbonaceous chondrite samples during this study.

EDS mapping created high-resolution, time-efficient spectral images that portray element distribution within the features. Maps were collected using a 2000 x 2000 pixel resolution, meaning for a map 2.5 mm^2, the resolution would be about 1.25 μm. Maps provided clear visibility of feature rims, body and surrounding matrix. Individual crystals were sometimes visible such as the barred olivine grains in Allende chondrule (Figure 33). EDS point data were collected, resulting in semi-quantitative analyses of each point. These data were converted from atomic percent to weight percent oxide, giving a rough indication of which mineral phases were within the features. EDS point analyses however are not very accurate as a quantitative instrument due to the nature of X-ray scattering. X-rays can be scattered off the sample and not come near the detector, which skews quantitative results. The resulting spectra can also skew results due to spectral peaks of different elements falling on or near the same energy line. EDS is a common tool for rough mineral identification in terrestrial science laboratories, much like a common petrographic microscope. EDS, however has not yet been transformed into a space instrument and would be very difficult to use in a space environment because of the sample needing to be in an enclosed environment, and size of the instrument. EDS maps and mineral identification provided a baseline for this study to compare other, more suitable for space exploration, techniques such as Raman and LIF.

Raman spectroscopy resulted in spectral images of each feature from the four carbonaceous chondrite samples. These maps are lower resolution than those collected using EDS, however they are similar resolution to LIF maps. The average step size used for each map was 50 μm. The resulting spectral maps show feature rims, bodies, and surrounding matrix, however the mineral constituents of the features are usually displayed as fine-grained mixtures instead of crystallographic structures like in some EDS maps. For example, plagioclase laths are visible within the EDS map for DGR-034 chondrule, but are small pixels within the Raman

map. Maps took a long time to collect in comparison to LIF and EDS, with map acquisition ranging from 12-30 hours. Unique peaks in the resulting map spectra were analyzed individually using Crystal Sleuth software and the RRUFF mineral database for mineral identification.

This study provides the first laser-induced fluorescence 2D maps of carbonaceous chondrite samples. LIF maps resulted in spectral images displaying either rim or interior features of chondrules and CAIs for Allende, Murchison and DGR-035. The resolution for these maps was 60 μm, resulting in large features being visible but not small crystallographic features like in EDS spectral maps. Fluorescence maps for DGR-034 however did not result in any spatial information for the chondrule or CAI. Spectral maps lead to points of interest being chosen and further analyzed using long and short fluorescence, and time resolved fluorescence for Allende, Murchison and DGR-035. The spectral information from points of interest in most cases lead to an analogous identification of minerals within the feature mapped. Using LIF, multiple minerals were usually identified in each sample except DGR-034. Raman spectroscopy was able to differentiate the most amount of minerals within a feature for each sample. EDS and LIF were able to identify a comparable number of minerals for each feature, except with respect to sample DGR-034, where LIF was unable to identify any minerals for either feature. LIF maps on average took approximately 2 hours to collect, at a resolution of 60 μm. Raman spectroscopy maps took 12-30 hours to collect at a resolution of 50 μm. This amount of time could be cut down using a smaller Raman window. Average acquisition time for one spectra using Raman would take approximately 20 seconds when using multiple accumulations to reduce noise. Fluorescence emission occurs slower than Raman phenomena, however is much more intense allowing a single fluorescence spectra to be collected in 2-4 seconds.

7.3 Database creation

This study provided a foundational LIF time-resolved spectral database, containing 10 amino acids (Appendix A), and 10 common minerals within carbonaceous chondrites, identified in previous studies. Common minerals from the olivine, pyroxene, and plagioclase groups were borrowed from the ROM and spectra was collected from each mineral. This database was used to roughly identify mineral spectra from LIF points of interest during this study. Currently, there are no public LIF spectral databases available for mineral identification. The creation of this modest, yet useful database contributed to 15 points of interest being identified as specific minerals, 12 of which were also identified using Raman or EDS. Although the LIF mineral database is not as accurate as a full mineral database and peak matching software such as Crystal Sleuth and the RRUFF database for Raman, the handmade database was useful for this study. Data pooling may be needed to build a large database for LIF such as the RRUFF database, but would be extremely useful for future studies. Conversely, there are LIF spectra available in time-resolved and non-time resolved form for many amino acids, however most of these amino acids are terrestrial and used for other fields of study such as medical and food studies [Nouadje et al., 1997, Cheng and Dovichi, 1988]. Planetary amino acids and polycyclic aromatic hydrocarbons (PAHs) have been measured previously in the York University Planetary Exploration Instrumentation Laboratory by Eshelman et al. [2017], where 24 organic compounds relevant to Mars were imaged using time-resolved LIF. Spectra such as those in Eshelman et al. [2017] could be combined with this amino acid database to create a larger suite of organic compounds relevant to planetary science, and detectable by LIF.

7.4 Identification

LIF mineral identification at the moment is more difficult and not as definitive as EDS or Raman identification due to the lack of spectral databases available. The RRUFF database [Lafuente et al., 2016] provides excellent spectra for thousands of samples of minerals, allowing fairly accurate identification of most minerals when using Raman spectroscopy. EDS is a semi-quantitative technique that is not as precise as other methods such as electron microprobe. However, using point analysis from maps, rough mineral identifcation is possible after converting results to weight percent oxide and comparing said results to known quantifications [Deer et al., 1992]. LIF spectroscopy has not yet become common enough to have mineral and organic databases, therefore in order to achieve identification a custom database is required. Nonetheless, with a small database of 10 minerals common to a carbonaceous chondrite sample suite, many identifications were made using LIF spectroscopy and time-resolved spectroscopy. Most identifications would not have been made without time-resolved fluorescence data due to the similarity between spectra in long gate-width scenarios. Time-resolved finger-printing enabled visualization of changes in each spectra over time, which formed distinction between each mineral. To enable easier and more accurate identification using LIF, larger databases such as the RRUFF database must be formed.

LIF is a difficult tool for definitive identification without a large and comprehensive database of time-resolved and non-time-resolved spectra, and because of the absence of sharp, defined features within the spectra. However, LIF can be used to identify areas of interest for more definitive identification and to eliminate many substances from the list of possibilities.

Organics in the form of amino acids were not identified during this study. A spectral databse (Appendix A) was created for 10 amino acids found within carbonaceous chondrites previously [Wing and Bada, 1991, Becker and Bunch, 1997]. Locating a point with organic carbon and obtaining an identifiable spectra within the sample suite for this study was highly unlikely. The quantity of amino acids found within meteorite samples through chemical digestion is on the order of micro-grams per gram of sample [Oró et al., 1971]. In Oró et al. [1971] , the amino acids glycine was most abundant within a sample of the Murchison meteorite, amounting to 5.3 μg/g, with the average abundance of most other amino acids reporting in the order of 0.1 μg/g. The relative abundance of amino acids within carbonaceous chondrites is fairly low, and to study amino acids, the whole sample is digested [Oró et al., 1971, Becker and Bunch, 1997, Wing and Bada, 1991]. In this study, only two objects on each sample were analyzed, which greatly reduced the probability of locating amino acids. a LIF time-resolved spectral database was created during this study, containing 10 amino acids found in previous studies within carbonaceous chondrites in the event that a spectra resulted from one of the samples resembling organic carbon.

7.5 Fluorescence quenching

LIF measurement techniques did not yield ideal results for sample DGR-034. Mapping results exhibited little to no variation between points, and when there was variation it was noise. Therefore no spectral imaging of the features shapes or characteristics were attainable, and no useful spectral point data was collected for mineral identification. Most minerals within the sample DGR-034 are within other samples, except for anorthite and perovskite. Fluorescence quenching can occur when a molecule interacts with a fluorophore through contact. The exact cause of fluorescence quenching within this sample is unknown. It is postulated

to be due to trace elements within the sample due to the main minerals being similar to that of the other carbonaceous chondrites. Well known fluorescence quenchers include halogens [Sauer et al., 2011] such as bromide and iodine, which were not very prevalent within EDS point analyses. A full analysis of trace elements within the sample would require further EPMA work. Quenching can also be caused by elements Mn^2+, Pb^2+, Cu^2+, NO_3-, and Cd^2+, which are classified as 'electron scavengers' [Sauer et al., 2011].

7.6 Raman and LIF as a combined instrument

Raman spectroscopy was suggested as a useful *in-situ* planetary science tool by various authors [Wang et al., 1998, Tarcea et al., 2008, Edwards et al., 2005, Villar et al., 2006]. Raman spectroscopy has also been selected as an instrument on NASA mission Mars2020, and ESA mission ExoMars [Beegle and Bhartia, 2016, Edwards et al., 2012]. UV Raman spectroscopy has been suggested as useful for the detection of Mars astrobiological material by Eshelman [2016], and Hamilton [2016]. The UV Raman spectroscopy instrument at York University was modified by Eshelman [2016] to include laser-induced fluorescence spectroscopy (LIF) capabilities. These modifications were minimal, and mainly required an iCCD camera with gating and a larger spectral range. UV LIF was successful in identifying mineral constituents within millimetre-sized features on carbonaceous chondrites in this study. Due to the compatibility of LIF and Raman spectroscopy in both instrumentation hardware and data analysis techniques, a combined instrument may be beneficial for planetary exploration. LIF could be used as a quick initial mapping technique, imaging target areas that could be followed by longer Raman analysis for better identification. Fluorescence provides unique information that is often unwanted or subtracted from Raman spectra, thus a combined instrument that both limits fluorescence emission in Raman spectra, and obtain independent fluorescence spectra would be ideal.

8 Conclusions

A 266 nm laser-induced fluorescence (LIF) spectrometer with time-resolved fluorescence capabilities was modified and optimized from a UV Raman spectrometer at York University to investigate the performance of LIF in mapping millimetre-sized features in chondritic material. The instrument was used to collect 2D spectral maps of four carbonaceous chondrite samples from the Royal Ontario Museum (ROM): Allende, Murchison, DGR-035, and DGR-034. Samples DGR-034 and DGR-035 were classified during this study as CV3, and CK4 carbonaceous chondrites respectively. Classification data has been sent to the Meteoritical Society for review and naming. Classification of rare carbonaceous chondrites allows future scientific study of said samples. millimetre-sized Chondrules and calcium-aluminum-rich inclusions were chosen as features to map on each sample. Fluorescence spectral maps resulted in visible features for three out of four samples, which lead to further point analyses in areas of interest. Time-resolved fluorescence, long and short fluorescence spectra were taken of each point, leading to mineral identification. A LIF time-resolved and spectral database of 10 monomineralic samples from the ROM was created to varify LIF mineral identification from the carbonaceous samples. Each feature for each sample was also mapped using 532 nm Raman spectroscopy at the ROM, resulting in detailed spectral images of structures within the chondrule and CAIs of each sample. Spectra from the Raman maps resulted in mineral identification for each sample. Electron-dispersive X-ray spectroscopy resulted in element distribution images of each sample and mineral identification by quantitative point analyses, validating Raman and LIF identification. Minerals identified using LIF, had a high rate of overlap with minerals either identified with Raman or EDS. All three methods had highly agreeable mineral identifications for each feature in all samples except DGR-034. Discrimination between minerals using a limited LIF database was difficult, and more work is required to enable LIF identification to be more precise. Sample DGR-034 did not produce fluorescence spectra, most likely due to trace element quenching. No organic carbon such as amino acids were found using LIF, EDS, or Raman spectroscopy, however the probability of amino acid identification is extremely low due to concentrations in the order of micro-grams of amino acid per gram of sample. The primary outcome of this study is the mapping capability of millimetre-sized features and the identification of minerals within most samples.

Based on the results of this work using carbonaceous chondrites, it is concluded that LIF is a useful tool for non-destructive mineral and organic detection within asteroid material. LIF spectroscopy could be used as a non-destructive *in-situ* technique for future asteroid missions, or as a laboratory technique, such as providing mineral and organic detection on samples returned from the OSIRIS-REx mission. This technique could aid in asteroid sample curation by identifying areas with higher organic or mineral constituents, while maintaining preservation of the samples.

9 Future work

Laser-induced fluorescence data for minerals is minimal. This work lays a foundation for future expansion of time-resolved, short and long fluorescnece spectral databases for better mineral identification. Due to the compatibility of Raman and LIF spectroscopy instruments, future work should include analyzing samples using both UV Raman and UV LIF spectroscopy. Samples in this study were limited to CV, CK and CM carbonaceous chondrites. Future work should include further studies into more carbonaceous chondrite types similar to asteroids of interest such as 101955 Bennu, using CK or CR meteorites.

References

Luann Becker and TE Bunch. Fullerenes, fulleranes and polycyclic aromatic hydrocarbons in the allende meteorite. *Meteoritics & planetary science*, 32(4):479–487, 1997.

Luther Beegle and Rohit Bhartia. Sherloc: An investigation for mars 2020. In *EGU General Assembly Conference Abstracts*, volume 18, page 11215, 2016.

PA Bland, ME Zolensky, GK Benedix, and MA Sephton. Weathering of chondritic meteorites. *Meteorites and the early solar system II*, pages 853–867, 2006.

Humberto Campins, Kelsey Hargrove, Noemi Pinilla-Alonso, Ellen S Howell, Michael S Kelley, Javier Licandro, T Mothé-Diniz, Y Fernández, and Julie Ziffer. Water ice and organics on the surface of the asteroid 24 themis. *Nature*, 464(7293):1320, 2010.

Yung-Fong Cheng and Norman J Dovichi. Subattomole amino acid analysis by capillary zone electrophoresis and laser-induced fluorescence. *Science*, 242(4878):562, 1988.

Roy S Clarke Jr, Eugene Jarosewich, Brian Mason, Joseph Nelen, Manuel Gomez, and Jack R Hyde. The allende, mexico, meteorite shower. *Smithsonian Contributions to the Earth Sciences*, 5:1–53, 1971.

James N Connelly, Martin Bizzarro, Alexander N Krot, Åke Nordlund, Daniel Wielandt, and Marina A Ivanova. The absolute chronology and thermal processing of solids in the solar protoplanetary disk. *Science*, 338(6107):651–655, 2012.

William Alexander Deer, Robert Andrew Howie, and Jack Zussman. *An introduction to the rock-forming minerals*, volume 2. Longman Scientific & Technical Hong Kong, 1992.

Howell GM Edwards, Caroline D Moody, Susana E Jorge Villar, and David D Wynn-Williams. Raman spectroscopic detection of key biomarkers of cyanobacteria and lichen symbiosis in extreme antarctic habitats: evaluation for mars lander missions. *Icarus*, 174(2):560–571, 2005.

Howell GM Edwards, Ian Hutchinson, and Richard Ingley. The exomars raman spectrometer and the identification of biogeological spectroscopic signatures using a flight-like prototype. *Analytical and bioanalytical chemistry*, 404(6-7):1723–1731, 2012.

E Eshelman, MG Daly, G Slater, P Dietrich, and J-F Gravel. An ultraviolet raman wavelength for the in-situ analysis of organic compounds relevant to astrobiology. *Planetary and Space Science*, 93:65–70, 2014.

E Eshelman, MG Daly, G Slater, and E Cloutis. Time-resolved detection of aromatic compounds on planetary surfaces by ultraviolet laser induced fluorescence and raman spectroscopy. *Planetary and Space Science*, 119:200–207, 2015.

E Eshelman, MG Daly, G Slater, and E Cloutis. Detecting aromatic compounds on planetary surfaces using ultraviolet time-resolved fluorescence spectroscopy. *Planetary and Space Science*, 2017.

Evan Eshelman. *Stand-off detection of organic compounds on Mars using ultraviolet Raman spectroscopy and time-resolved laser-induced fluorescence*. PhD thesis, York University, 2016.

Akira Fujiwara, J Kawaguchi, DK Yeomans, M Abe, T Mukai, T Okada, J Saito, H Yano, M Yoshikawa, DJ Scheeres, et al. The rubble-pile asteroid itokawa as observed by hayabusa. *Science*, 312(5778):1330–1334, 2006.

Springer G. Fluorescence by the x-ray continuum in multi-element targets. Technical report, Falconbridge Nickel Mines Limited, Thornhill, Ontario, Canada, 1971.

Lawrence Grossman. Petrography and mineral chemistry of ca-rich inclusions in the allende meteorite. *Geochimica et Cosmochimica Acta*, 39(4):433–454, 1975.

Lawrence Grossman and Ian M Steele. Amoeboid olivine aggregates in the allende meteorite. *Geochimica et Cosmochimica Acta*, 40(2):149IN1151–150IN2155, 1976.

David Hamilton. Biosignature detection in mars analogue aqueous alteration minerals using raman spectroscopy. Master's thesis, York University, 2016.

KFJ Heinrich. Mass absorption coefficients for electron probe microanalysis. *Proc. 11th Int. Congr. on X-Ray Optics and Microanalysis*, pages 67–119, 1986.

Robert Hutchison. *Meteorites: A petrologic, chemical and isotopic synthesis*. Cambridge University Press, 2004.

Eugene Jarosewich. Chemical analysis of the murchison meteorite. *Meteoritics & Planetary Science*, 6(1): 49–52, 1971.

Brandon C Johnson, David A Minton, HJ Melosh, and Maria T Zuber. Impact jetting as the origin of chondrules. *Nature*, 517(7534):339–341, 2015.

Gregory W Kallemeyn, Alan E Rubin, and John T Wasson. The compositional classification of chondrites: V. the karoonda (ck) group of carbonaceous chondrites. *Geochimica et Cosmochimica Acta*, 55(3):881–892, 1991.

Keith Kvenvolden, James Lawless, Katherine Pering, Etta Peterson, Jose Flores, Cyril Ponnamperuma, Isaac R Kaplan, and Carleton Moore. Evidence for extraterrestrial amino-acids and hydrocarbons in the murchison meteorite. *Nature*, 228(5275):923–926, 1970.

Barbara Lafuente, Robert T Downs, Hexiong Yang, and Nate Stone. The power of databases: the rruff project. In *Highlights in mineralogical crystallography*. Walter de Gruyter GmbH, 2016.

DS Lauretta, AE Bartels, MA Barucci, EB Bierhaus, RP Binzel, WF Bottke, H Campins, SR Chesley, BC Clark, BE Clark, et al. The osiris-rex target asteroid (101955) bennu: Constraints on its physical, geological, and dynamical nature from astronomical observations. *Meteoritics & Planetary Science*, 50(4): 834–849, 2015.

DS Lauretta, SS Balram-Knutson, E Beshore, WV Boynton, C Drouet dAubigny, DN DellaGiustina, HL Enos, DR Gholish, CW Hergenrother, ES Howell, et al. Osiris-rex: Sample return from asteroid (101955) bennu. *arXiv preprint arXiv:1702.06981*, 2017.

DA Long. The raman effect: a unified treatment of the theory of raman scattering by molecules. 2002. *West Sussex, England: John Wiley Sons Ltd*, 2002.

Ursula B Marvin, JA Wood, and JS Dickey. Ca-al rich phases in the allende meteorite. *Earth and Planetary Science Letters*, 7(4):346–350, 1970.

Daniel D Mazanek, Raymond G Merrill, Scott P Belbin, David M Reeves, Bo J Naasz, Paul A Abell, and Kevin Earle. Asteroid redirect robotic mission: Robotic boulder capture option overview. *AIAA SPACE 2014 Conference and Exposition*, page 4432, 2014.

Harry Y Mcsween. Petrographic variations among carbonaceous chondrites of the vigarano type. *Geochimica et Cosmochimica Acta*, 41(12):1777–1790, 1977.

Patrick Michel, Francesca E DeMeo, and William F Bottke. Asteroids: recent advances and new perspectives. *Asteroids IV*, 1:3, 2015.

G Nouadje, N Simeon, F Dedieu, M Nertz, Ph Puig, and F Couderc. Determination of twenty eight biogenic amines and amino acids during wine aging by micellar electrokinetic chromatography and laser-induced fluorescence detection. *Journal of Chromatography A*, 765(2):337–343, 1997.

J Oró, J Gibert, H Lichtenstein, S Wikstrom, and DA Flory. Amino-acids, aliphatic and aromatic hydrocarbons in the murchison meteorite. *Nature*, 230(5289):105–106, 1971.

Jean-Louis Pouchou and Françoise Pichoir. Quantitative analysis of homogeneous or stratified microvolumes applying the model "pap". In *Electron probe quantitation*, pages 31–75. Springer, 1991.

Vishnu Reddy, Tasha L Dunn, Cristina A Thomas, Nicholas A Moskovitz, and Thomas H Burbine. Mineralogy and surface composition of asteroids. *Asteroids IV, na*, 2015.

Markus Sauer, Johan Hofkens, and Jorg Enderlein. Basic principles of fluorescence spectroscopy. *Handbook of Fluorescence Spectroscopy and Imaging: From Single Molecules to Ensembles*, pages 1–30, 2011.

Edward RD Scott, Klaus Keil, and Dieter Stoeffler. Shock metamorphism of carbonaceous chondrites. *Geochimica et Cosmochimica Acta*, 56(12):4281–4293, 1992.

Derek WG Sears. *The origin of chondrules and chondrites*, volume 3. Cambridge University Press, 2004.

Reed SJB. Fluorescence effects in quantitative microprobe analysis. *Microbeam analysis*, pages 109–14, 1990.

M Skulinova, C Lefebvre, P Sobron, E Eshelman, M Daly, J-F Gravel, J-F Cormier, F Chateauneuf, G Slater, W Zheng, et al. Time-resolved stand-off uv-raman spectroscopy for planetary exploration. *Planetary and Space Science*, 92:88–100, 2014.

N Tarcea, T Frosch, P Rösch, M Hilchenbach, T Stuffler, S Hofer, H Thiele, Rupert Hochleitner, and J Popp. Raman spectroscopy—a powerful tool for in situ planetary science. *Space Science Reviews*, 135 (1-4):281–292, 2008.

Yuichi Tsuda, Makoto Yoshikawa, Masanao Abe, Hiroyuki Minamino, and Satoru Nakazawa. System design of the hayabusa 2—asteroid sample return mission to 1999 ju3. *Acta Astronautica*, 91:356–362, 2013.

W. R. Van Schmus. *Mineralogy, Petrology, and Classification of Types 3 and 4 Carbonaceous Chondrites*, pages 480–491. Springer Netherlands, Dordrecht, 1969. doi: 10.1007/978-94-010-3411-1_39. URL `https://doi.org/10.1007/978-94-010-3411-1_39`.

Susana E Jorge Villar, Howell GM Edwards, and Liane G Benning. Raman spectroscopic and scanning electron microscopic analysis of a novel biological colonisation of volcanic rocks. *Icarus*, 184(1):158–169, 2006.

Alian Wang, Larry A Haskin, and Enriqueta Cortez. Prototype raman spectroscopic sensor for in situ mineral characterization on planetary surfaces. *Applied Spectroscopy*, 52(4):477–487, 1998.

Michael K Weisberg, Timothy J McCoy, and Alexander N Krot. Systematics and evaluation of meteorite classification. *Meteorites and the early solar system II*, 19, 2006.

Michael R Wing and Jeffrey L Bada. The origin of the polycyclic aromatic hydrocarbons in meteorites. *Origins of Life and Evolution of the Biosphere*, 21(5-6):375–383, 1991.

F Wlotzka. A weathering scale for the ordinary chondrites. *Meteoritics*, 28, 1993.

Appendices

Appendix A: Amino acids database

This section presents the short (10 ns) and time-resolved fluorescence spectra for 10 amino acids that have been found in carbonaceous chondrites [Becker and Bunch, 1997, Wing and Bada, 1991, Oró et al., 1971]. These amino acids were not identified from the LIF spectral maps, however provided justification that the fluorescence spectra from points of interest were not organic carbon.

Table 13: Amino acids pelletized for LIF amino acids database.

Amino acid	**Sigma-Aldrich ID**
2-Aminoisobutyric acid	850993 - 25G
Alanine	A7627-100G
Aminoisobutyric acid	162663 - 25G
β - Alanine	146064 - 25G
Glycine	G5417 - 100G
L-Aspartic acid	A9256 - 100G
L-glutamic acid	G1251 - 100G
L-Proline	P5607 - 25G
Phenylalanine	P2126 - 100G
Tryptophan	T0254 - 5G

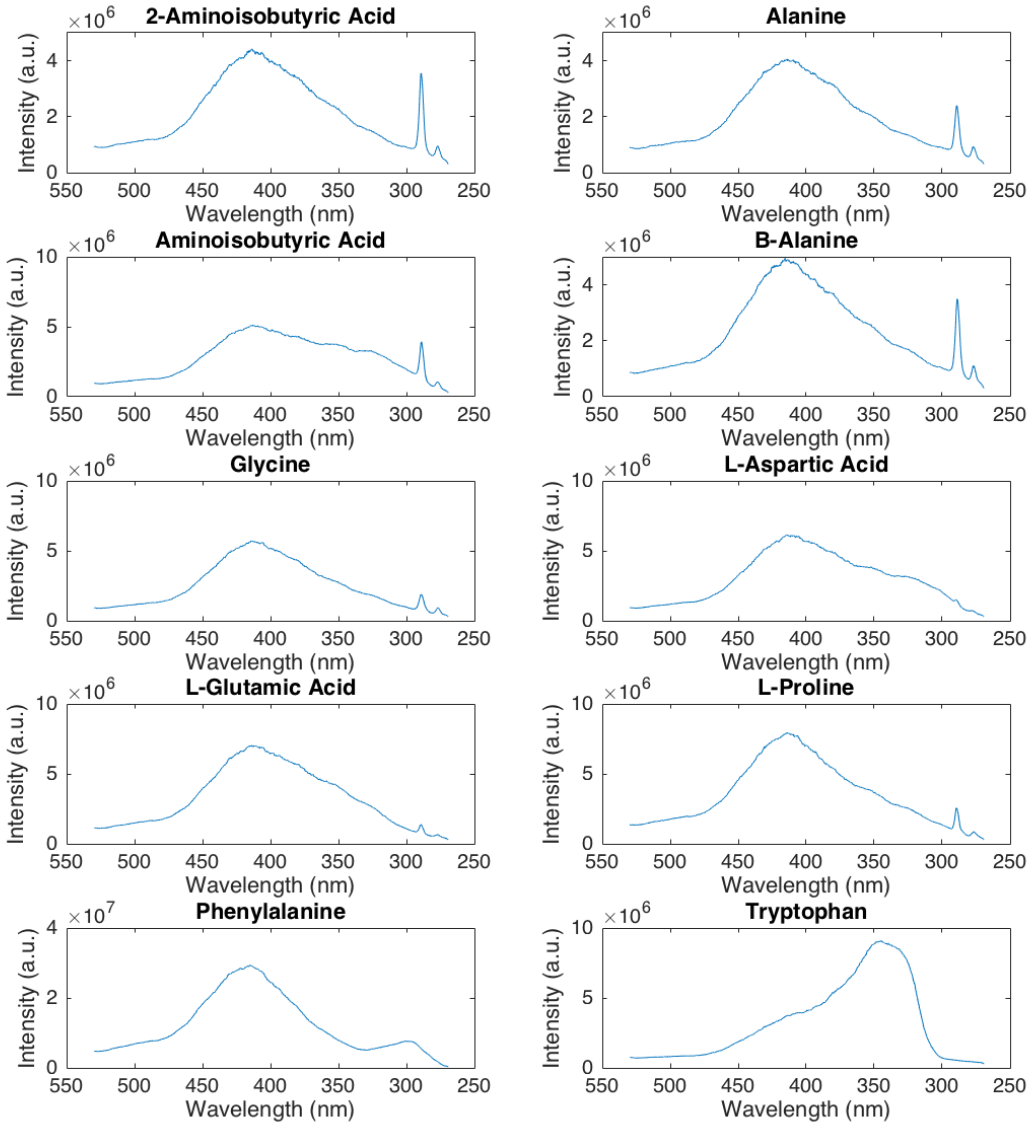


Figure 100: LIF spectra from 10 amino acids found within carbonaceous chondrites

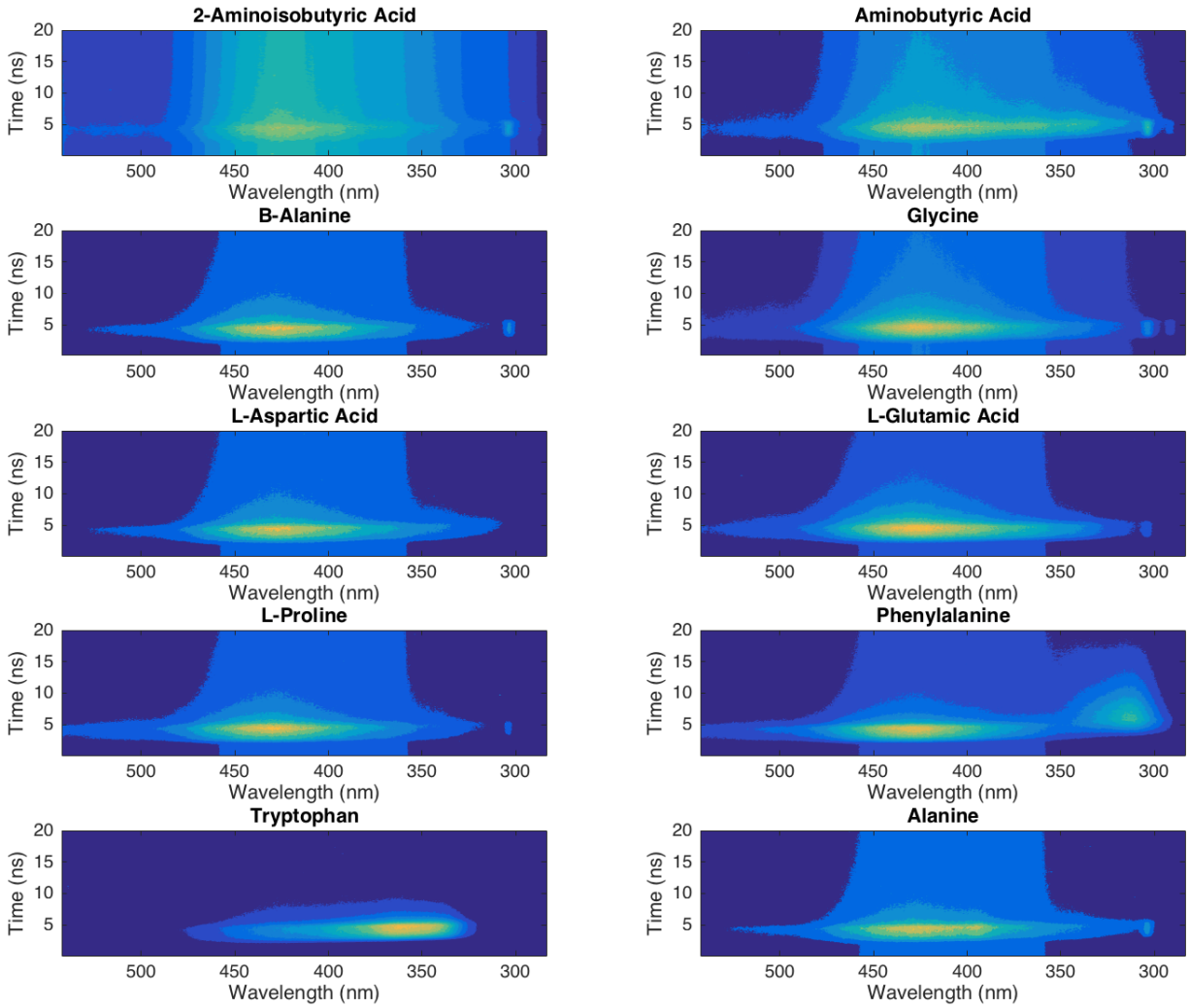


Figure 101: LIF time-resolved contour plots from 10 amino acids found within carbonaceous chondrites

Appendix B: Modal abundance determinations using Olympus STREAM

Plane-polarized light thin section images of DGR-034 and DGR-035 were imported into Olympus STREAM software to obtain modal abundances of features compared to matrix within each sample. A region of interest (ROI) was selected as the largest rectangle possible within the thin section image. Spectral ranges were chosen that segregated chondrule and CAI features from dark matrix material using the 'manual threshold' setting. False-colour images resulted from this analyses, showing areas considered to be 'features' and matrix (Figures: 102 and 103). Quantitative values resulted from these false colour images representing the modal abundance of features versus matrix within the sample (Tables: 14 and 15).

Table 14: DGR-034 matrix versus features quantification using Olympus STREAM software.

Object class	Area fraction ROI %
Matrix	41.88
Features	55.47

Table 15: DGR-035 matrix versus features quantification using Olympus STREAM software.

Object class	Area fraction ROI %
Matrix	64.09
Features	32

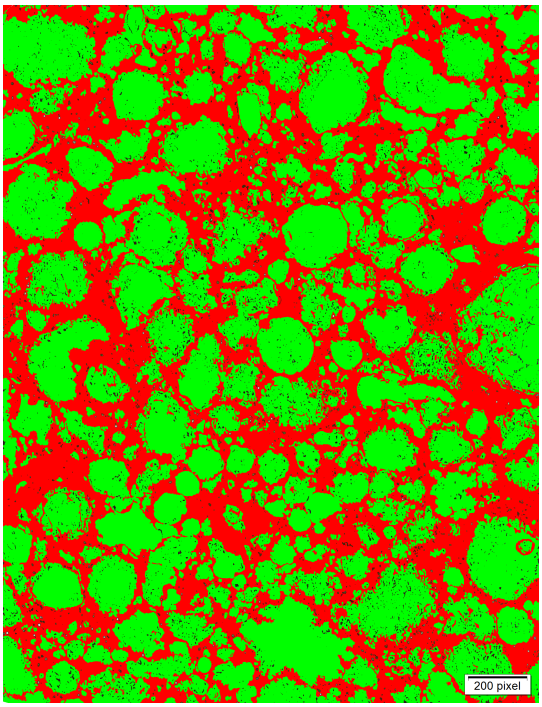


Figure 102: DGR-034 modal abundance of matrix (red) versus features (green) determined by Olympus STREAM software.

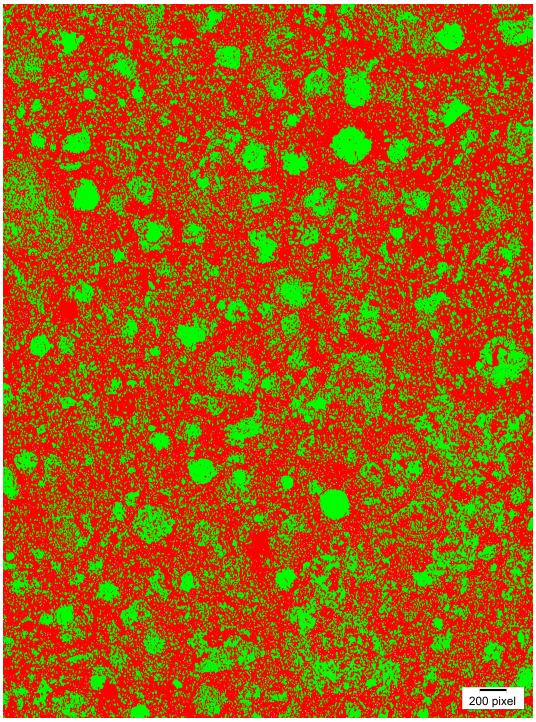


Figure 103: DGR-035 modal abundance of matrix (red) versus features (green) determined by Olympus STREAM software.

Appendix C: Chondrule and CAI measurements for DGR-034 and DGR-035

Each visible chondrule and CAI were measured in the thin sections of DGR-034 and DGR-035 to aid in classification. Olympus STREAM software was used to measure and record each feature. Images of chondrules and CAIs measured in DGR-034 are shown in Figures 104 and 105. Each measurement is recorded in Tables 16 and 17. Images of chondrules and CAIs measured in DGR-035 are shown in Figures 106 and 107. Each measurement is recorded in Tables 19 and 18.

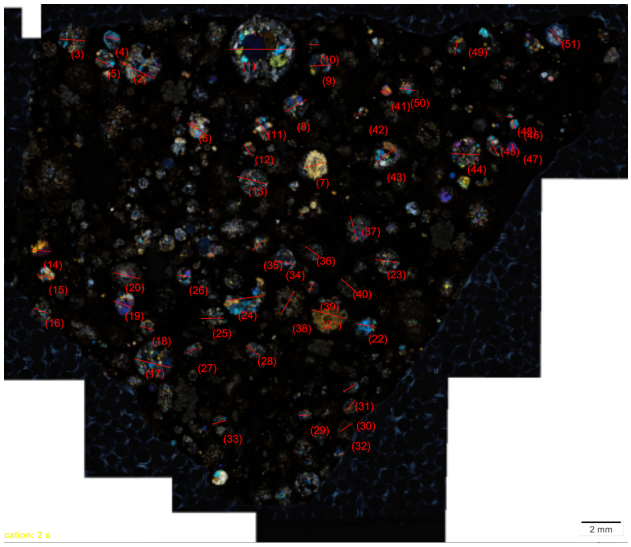


Figure 104: Crossed-polarized light image of chondrules measured in DGR-034 using Olympus STREAM software.

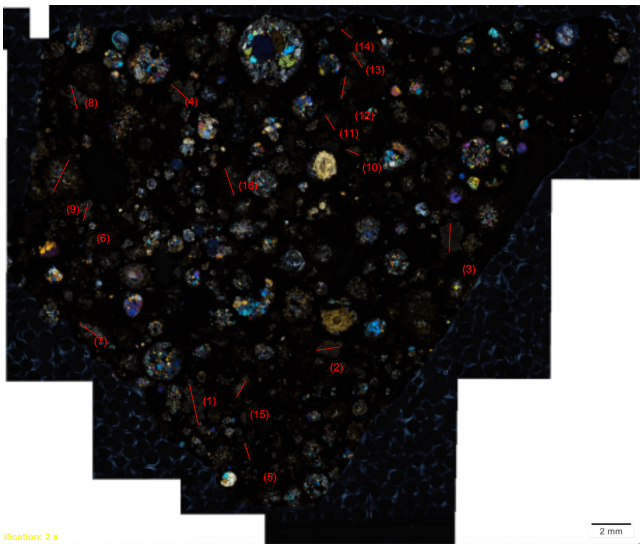


Figure 105: Crossed-polarized light image of CAIs measured in DGR-034 using Olympus STREAM software.

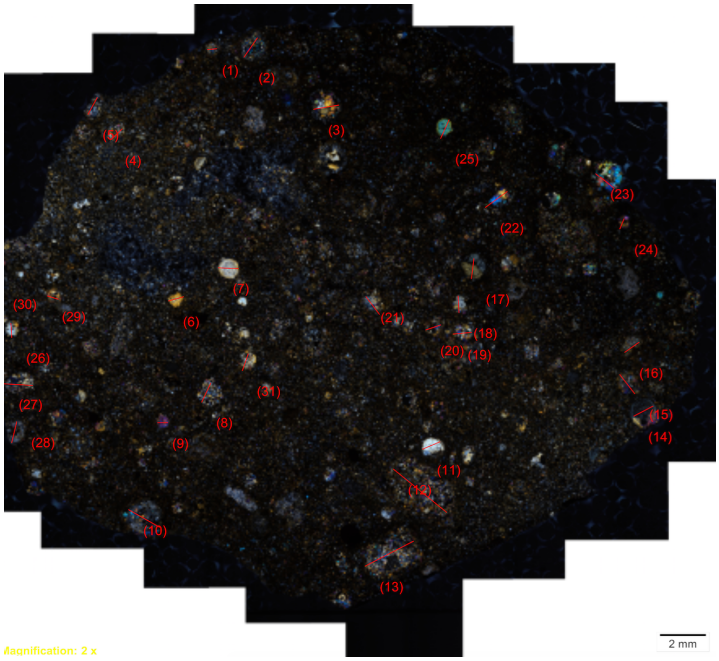


Figure 106: Crossed-polarized light image of chondrules measured in DGR-035 using Olympus STREAM software.

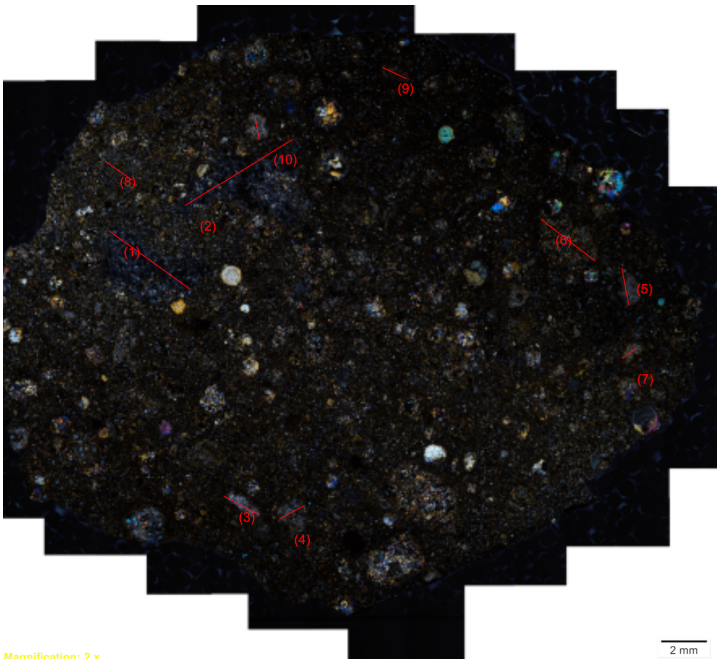


Figure 107: Crossed-polarized light image of CAIs measured in DGR-035 using Olympus STREAM software.

Table 16: Chondrule measurements in DGR-034

Feature	Length (mm)		
Chondrule 1	3313.2	Count	51
Chondrule 2	1935.820304	Minimum	330
Chondrule 3	1267.687363	Maximum	3313.2
Chondrule 4	782.1804459	Mean	992.1515702
Chondrule 5	983.8699101		
Chondrule 6	1047.168802		
Chondrule 7	1054.007234		
Chondrule 8	1209.000587		
Chondrule 9	964.0701479		
Chondrule 10	468.3081251		
Chondrule 11	1100		
Chondrule 12	688.3803164		
Chondrule 13	1507.491708		
Chondrule 14	883.8587274		
Chondrule 15	847.160699		
Chondrule 16	730.6931641		
Chondrule 17	1814.166475		
Chondrule 18	634.8868009		
Chondrule 19	904.5786312		
Chondrule 20	1328.498103		
Chondrule 21	1760.859165		
Chondrule 22	922.3780407		
Chondrule 23	1054.007234		
Chondrule 24	1831.946222		
Chondrule 25	1100.343696		
Chondrule 26	607.4948559		
Chondrule 27	580.1131355		
Chondrule 28	786.5192305		
Chondrule 29	523.2231837		
Chondrule 30	701.1151831		
Chondrule 31	679.1998969		
Chondrule 32	610.5990911		
Chondrule 33	713.9415242		
Chondrule 34	987.3227689		
Chondrule 35	759.3793255		
Chondrule 36	924.6715417		
Chondrule 37	1254.192968		
Chondrule 38	1307.416521		
Chondrule 39	480.2668529		
Chondrule 40	1130.514264		
Chondrule 41	495.7633004		
Chondrule 42	468.3081251		
Chondrule 43	1260.256803		
Chondrule 44	1404.677173		
Chondrule 45	961.54158		
Chondrule 46	400.4060439		
Chondrule 47	414.5132205		
Chondrule 48	330		
Chondrule 49	891.7642401		
Chondrule 50	777.8174593		
Chondrule 51	1014.14989		

Table 17: CAI measurements in DGR-034

Feature	Length (mm)
CAI 1	2080.949113
CAI 2	1197.838887
CAI 3	1425.032912
CAI 4	1319.564511
CAI 5	890.5585326
CAI 6	945.5394228
CAI 7	1383.504857
CAI 8	1225.387163
CAI 9	1773.991728
CAI 10	561
CAI 11	809.4460451
CAI 12	1137.058459
CAI 13	902.4881606
CAI 14	672.9312372
CAI 15	971.1972199
CAI 16	1393.489447
Count	16
Minimum	561
Maximum	2080.949113
Mean	1168.123606

Table 18: CAI measurements in DGR-035

Feature	Length (mm)
CAI 1	4306.148772
CAI 2	5464.59895
CAI 3	1707.313753
CAI 4	1224.364733
CAI 5	1610.004733
CAI 6	2952.609829
CAI 7	769.8121914
CAI 8	1447.620061
CAI 9	1111.769733
CAI 10	1023.621961
Count	10
Minimum	769.8121914
Maximum	5464.59895
Mean	2161.786472

Table 19: CAI measurements in DGR-035

Feature	Length (mm)
Chondrule 1	397.5613663
Chondrule 2	1008.489455
Chondrule 3	1095.160354
Chondrule 4	688.0409872
Chondrule 5	821.1896005
Chondrule 6	672.546333
Chondrule 7	865.3616874
Chondrule 8	917.10187
Chondrule 9	431.2
Chondrule 10	1531.52633
Chondrule 11	2350.184174
Chondrule 12	932.8415085
Chondrule 13	1050.730341
Chondrule 14	748.3234595
Chondrule 15	870.2029016
Chondrule 16	721.4138479
Chondrule 17	795.2208813
Chondrule 18	683.1788199
Chondrule 19	950.4311916
Chondrule 20	1158.839428
Chondrule 21	1023.248948
Chondrule 22	467.4158748
Chondrule 23	869.8552121
Chondrule 24	612.6763012
Chondrule 25	1226.450672
Chondrule 26	925.2693662
Chondrule 27	490.255821
Chondrule 28	656.806859
Chondrule 29	762.2269806
Count	31
Minimum	397.5613663
Maximum	2969.15023
Mean	887.0258817

Appendix D: Electron probe micro-analysis standards and calibration

EPMA analyses were completed at Queen's University, Kingston, Ontario, Canada. Major and minor element data were collected for olivine, pyroxene and plagioclase. The Electron probe used was a JEOL JXA-8230 electron probe microanalyser (EPMA) with an acceleration potential of 15 kV, and a beam current of 20 nA. A focused beam was used for olivine and pyroxene measurements, and a fixed diameter beam was used at 2-7 μm depending on grain size for plagioclase. Sodium and potassium were measured first for plagioclase grains. The 'PAP' method of Pouchou and Pichoir (1991, etc.) were used for the atomic number and absorption corrections. Mass absorption coefficients were used from Heinrich (1986). The characteristic fluorescence correction is from Reed (1990), and the continuum fluorescence correction from Springer (1971). Electron probe microanalysis results used in ternary diagrams (Figures 20, 19, 30, 29) are reported in this section. Standards used for each sample are reported in Tables 20, 21, and 22.

Table 20: Standards used to calibrated each element measured in olivine using JEOL-JXA-8230 EPMA at Queen's University, Kingston, Ontario.

Olivine standards				
X-ray line	Z	element	Standard	Reference
1	14	1	Forsterite	Oakssaung Hill, Mogok
1	15	2	Synthetic $Ca_2P_2O_7$	–
1	13	3	Anorthite	USNM 137041
1	22	4	Synthetic TiO_2	Single crystal
1	24	5	Synthetic Cr_2O_3	–
1	23	6	Synthetic V_2O_3	–
1	26	7	Synthetic Fayalite	–
1	25	8	Rhodonite	Harvard
1	12	9	Forsterite	Oakssaung Hill, Mogok
1	28	10	Synthetic Ni-olivine	Ken Domanik
1	20	11	Diopside Px-1	–
1	11	12	Albite	Calaveras co.
1	19	13	Adularia OR-1	–

Table 21: Standards used to calibrated each element measured in pyroxene using JEOL-JXA-8230 EPMA at Queen's University, Kingston, Ontario.

Pyroxene standards				
X-ray line	Z	element	Standard	Reference
1	14	1	Diopside Px-1	–
1	13	2	Anorthite	USNM 137041
1	22	3	Synthetic TiO_2	Single crystal
1	24	4	Synthetic Cr_2O_3	–
1	23	5	Synthetic V_2O_3	–
1	26	6	Synthetic Fayalite	–
1	25	7	Rhodonite	Harvard
1	12	8	Forsterite	Oakssaung Hill, Mogok
1	28	9	Synthetic Ni-olivine	Ken Domanik
1	20	10	Diopside Px-1	–
1	11	11	Albite	Calaveras co.
1	19	12	Adularia OR-1	–

Table 22: Standards used to calibrated each element measured in plagioclase using JEOL-JXA-8230 EPMA at Queen's University, Kingston, Ontario.

Plagioclase standards				
X-ray line	Z	element	Standard	Reference
1	11	1	Albite	Calaveras co.
1	13	2	Anorthite	USNM 137041
1	22	3	Synthetic TiO_2	Single crystal
1	24	4	Synthetic Cr_2O_3	–
1	23	5	Synthetic V_2O_3	–
1	26	6	Synthetic Fayalite	–
1	25	7	Rhodonite	Harvard
1	28	8	Synthetic Ni-olivine	Ken Domanik
1	13	9	Anorthite	Vesuvius ROM M11008
1	11	10	Albite	Calaveras co.
1	19	11	Adularia OR-1	–

Results_of_analyses:

		coordinates in mm		oxide weight %													
		X	Y	SiO2	P2O5	Al2O3	TiO2	Cr2O3	V2O3	FeO	MnO	MgO	NiO	CaO	Na2O	K2O	Total
1	DGR-035 chondrule 1 olivine 1	17.740	-33.832	40.66	0.01	0.07	0.05	0.11	0.00	9.22	0.06	49.42	0.00	0.25	0.01	0.01	99.87
2	DGR-035 chondrule 1 olivine 2	17.817	-33.918	39.81	0.03	0.04	0.22	0.07	0.00	13.26	0.08	46.15	0.04	0.23	0.02	0.01	99.96
3	DGR-035 chondrule 1 olivine 3	17.956	-33.986	38.90	0.02	0.03	0.04	0.07	0.00	18.45	0.13	41.77	0.22	0.23	0.00	0.00	99.86
4	DGR-035 chondrule 1 olivine 4	18.004	-34.056	38.66	0.00	0.04	0.00	0.09	0.00	19.91	0.13	40.68	0.10	0.25	0.03	0.01	99.90
5	DGR-035 chondrule 1 olivine 5	18.093	-34.098	36.94	0.00	0.01	0.02	0.04	0.00	29.52	0.20	32.74	0.31	0.05	0.00	0.00	99.83
6	DGR-035 chondrule 2 olivine 1	23.873	-35.430	40.86	0.00	0.04	0.08	0.07	0.00	8.78	0.07	49.90	0.11	0.21	0.01	0.00	100.13
7	DGR-035 chondrule 2 olivine 2	23.879	-35.464	39.57	0.00	0.04	0.07	0.04	0.00	16.14	0.13	43.53	0.30	0.18	0.00	0.01	100.01
8	DGR-035 chondrule 2 olivine 3	23.927	-35.513	39.61	0.00	0.00	0.08	0.00	0.00	14.12	0.09	44.95	0.12	0.12	0.00	0.00	99.11
9	DGR-035 chondrule 2 olivine 4	24.106	-35.565	39.54	0.00	0.02	0.05	0.02	0.00	15.71	0.09	44.10	0.06	0.12	0.00	0.00	99.71
10	DGR-035 chondrule 2 olivine 5	24.130	-35.560	37.61	0.00	0.02	0.03	0.04	0.01	26.28	0.18	35.40	0.30	0.15	0.00	0.00	100.03
11	DGR-035 chondrule 2 olivine 6	24.164	-35.627	37.69	0.00	0.01	0.02	0.04	0.00	26.35	0.20	35.57	0.27	0.11	0.00	0.01	100.27
12	DGR-035 chondrule 2 olivine 7	24.228	-35.727	36.93	0.03	0.01	0.01	0.01	0.00	29.34	0.26	33.47	0.34	0.02	0.01	0.00	100.42
13	DGR-035 chondrule 3 olivine 1	35.670	-39.861	40.32	0.01	0.02	0.06	0.02	0.04	12.05	0.08	47.02	0.02	0.29	0.00	0.01	99.96
14	DGR-035 chondrule 3 olivine 2	35.561	-40.044	40.61	0.01	0.04	0.08	0.01	0.00	11.87	0.10	47.35	0.07	0.21	0.01	0.02	100.41
15	DGR-035 chondrule 3 olivine 3	36.213	-40.053	41.41	0.00	0.02	0.00	0.04	0.00	8.80	0.03	50.03	0.01	0.14	0.00	0.01	100.49
16	DGR-035 chondrule 3 olivine 4	36.272	-40.284	37.43	0.00	0.03	0.10	0.03	0.01	28.53	0.19	33.78	0.33	0.17	0.00	0.00	100.61
17	DGR-035 chondrule 3 olivine 5	36.361	-40.378	36.70	0.21	0.01	0.01	0.05	0.01	29.98	0.25	32.29	0.35	0.04	0.00	0.00	99.90
18	DGR-035 matrix 1 olivine 1	22.902	-40.228	36.61	0.00	0.01	0.04	0.06	0.01	29.94	0.25	32.69	0.34	0.05	0.00	0.00	99.99
19	DGR-035 matrix 1 olivine 2	22.787	-40.223	36.92	0.00	0.01	0.00	0.01	0.02	30.10	0.22	32.50	0.33	0.10	0.00	0.00	100.20
20	DGR-035 matrix 1 olivine 3	22.541	-40.367	36.76	0.00	0.00	0.01	0.04	0.01	30.20	0.21	33.02	0.35	0.06	0.02	0.00	100.68
21	DGR-035 matrix 1 olivine 4	22.894	-40.486	36.81	0.02	0.00	0.02	0.00	0.00	30.39	0.25	32.49	0.34	0.02	0.02	0.00	100.37
22	DGR-035 CAI 1 olivine 1	13.382	-32.874	36.65	0.79	0.01	0.01	0.00	0.00	27.38	0.20	34.46	0.32	0.04	0.06	0.00	99.91
23	DGR-035 CAI 1 olivine 2	13.517	-32.911	37.12	0.14	0.00	0.00	0.03	0.00	26.82	0.20	35.15	0.29	0.03	0.03	0.00	99.81
24	DGR-035 CAI 1 olivine 3	13.386	-32.826	36.80	0.38	0.73	0.03	0.03	0.01	26.53	0.22	34.68	0.29	0.05	0.04	0.00	99.78
25	DGR-035 CAI 1 olivine 4	13.576	-32.734	37.40	0.16	0.07	0.01	0.02	0.00	26.55	0.22	34.52	0.33	0.08	0.04	0.00	99.40
26	DGR-034 chondrule 1 olivine 1	-29.131	-40.047	41.83	0.00	0.02	0.02	0.08	0.00	3.57	0.24	54.51	0.02	0.15	0.00	0.00	100.44
27	DGR-034 chondrule 1 olivine 2	-29.080	-40.097	39.77	0.01	0.00	0.00	0.00	0.02	14.71	0.21	45.34	0.10	0.18	0.01	0.00	100.35
28	DGR-034 chondrule 1 olivine 3	-29.193	-40.076	37.06	0.02	0.25	0.01	0.06	0.00	29.62	0.26	33.85	0.04	0.09	0.02	0.01	101.28
29	DGR-034 chondrule 1 olivine 4	-29.127	-40.143	37.60	0.04	0.01	0.00	0.02	0.01	28.37	0.24	34.44	0.12	0.06	0.01	0.00	100.91
30	DGR-034 chondrule 1 olivine 5	-29.166	-40.151	38.73	0.00	0.02	0.02	0.06	0.02	20.55	0.23	40.48	0.06	0.16	0.00	0.01	100.34
31	DGR-034 chondrule 1 olivine 6	-29.256	-40.181	42.08	0.00	0.01	0.00	0.06	0.00	3.83	0.23	54.08	0.02	0.15	0.01	0.01	100.48
32	DGR-034 chondrule 2 olivine 1	-27.290	-33.222	41.62	0.00	0.02	0.03	0.04	0.01	5.60	0.09	52.51	0.00	0.21	0.00	0.01	100.15
33	DGR-034 chondrule 2 olivine 2	-27.332	-33.299	41.58	0.00	0.02	0.04	0.01	0.00	6.21	0.08	52.15	0.02	0.24	0.01	0.00	100.36
34	DGR-034 chondrule 2 olivine 3	-27.084	-33.420	42.15	0.03	0.01	0.01	0.05	0.00	3.52	0.04	54.55	0.01	0.12	0.01	0.00	100.51
35	DGR-034 chondrule 2 olivine 4	-27.009	-33.511	40.97	0.00	0.06	0.00	0.04	0.01	7.54	0.07	51.02	0.02	0.26	0.01	0.00	100.02
36	DGR-034 chondrule 2 olivine 5	-26.944	-33.494	41.04	0.01	0.03	0.03	0.07	0.01	9.71	0.09	50.14	0.02	0.20	0.00	0.00	101.36
37	DGR-034 chondrule 2 olivine 6	-26.997	-33.583	34.60	0.06	0.47	0.05	0.45	0.00	37.96	0.23	25.70	0.01	0.17	0.07	0.02	99.79
38	DGR-034 chondrule 3 olivine 1	-27.729	-34.023	41.09	0.00	0.02	0.00	0.05	0.00	7.80	0.13	50.81	0.02	0.22	0.00	0.00	100.13
39	DGR-034 chondrule 3 olivine 2	-27.666	-34.008	40.88	0.02	0.02	0.04	0.06	0.01	9.15	0.14	49.88	0.02	0.24	0.00	0.00	100.46
40	DGR-034 chondrule 3 olivine 3	-27.689	-34.067	40.08	0.01	0.01	0.01	0.07	0.02	13.78	0.14	46.24	0.02	0.20	0.02	0.00	100.61
41	DGR-034 chondrule 3 olivine 4	-28.010	-33.944	41.44	0.00	0.10	0.05	0.15	0.02	5.94	0.12	52.00	0.00	0.34	0.00	0.00	100.15
42	DGR-034 chondrule 3 olivine 5	-28.042	-33.895	41.09	0.00	0.02	0.06	0.05	0.00	7.46	0.15	50.96	0.01	0.27	0.00	0.01	100.10
43	DGR-034 matrix 1 olivine 1	-28.484	-33.276	34.04	0.01	0.08	0.00	0.14	0.00	42.37	0.26	22.37	0.04	0.12	0.00	0.00	99.43
44	DGR-034 matrix 1 olivine 2	-28.517	-33.283	33.77	0.05	0.17	0.03	0.11	0.01	40.09	0.19	24.46	0.09	0.12	0.00	0.00	99.10
45	DGR-034 matrix 1 olivine 3	-28.512	-33.286	33.41	0.03	0.20	0.02	0.09	0.00	42.88	0.29	22.29	0.19	0.16	0.01	0.00	99.55
46	DGR-034 matrix 1 olivine 4	-28.449	-33.231	31.94	0.23	2.11	0.08	0.99	0.01	42.39	0.25	20.86	0.19	0.33	0.06	0.00	99.43
47	DGR-034 chondrule 4 olivine 1	-17.908	-32.310	33.91	0.21	0.02	0.01	0.06	0.01	41.29	0.34	23.57	0.03	0.15	0.04	0.00	99.64
48	DGR-034 chondrule 4 olivine 2	-17.600	-32.435	34.03	0.19	0.04	0.00	0.06	0.03	42.12	0.29	23.23	0.03	0.12	0.07	0.00	100.21
49	DGR-034 chondrule 4 olivine 3	-17.415	-32.478	29.44	0.07	0.03	0.01	0.06	0.00	25.47	0.19	20.35	0.01	0.15	0.00	0.01	75.78
50	DGR-034 chondrule 4 olivine 4	-17.334	-32.478	34.39	0.02	0.03	0.00	0.01	0.00	42.79	0.28	22.85	0.06	0.20	0.02	0.00	100.66
51	DGR-035 chondrule 4 olivine 1	28.314	-34.006	42.33	0.00	0.31	0.03	0.11	0.01	0.34	0.02	56.36	0.01	0.56	0.01	0.01	100.09
52	DGR-035 chondrule 4 olivine 2	28.397	-34.174	42.58	0.01	0.24	0.06	0.08	0.00	0.37	0.01	56.51	0.00	0.54	0.00	0.00	100.39
53	DGR-035 chondrule 4 olivine 3	28.438	-34.250	42.06	0.00	0.18	0.06	0.15	0.02	2.45	0.01	55.05	0.00	0.42	0.00	0.00	100.41
54	DGR-035 chondrule 4 olivine 4	28.474	-34.338	38.70	0.00	0.08	0.07	0.13	0.01	20.14	0.14	40.40	0.22	0.14	0.01	0.00	100.04
55	DGR-035 chondrule 4 olivine 5	28.467	-34.386	36.58	0.00	0.06	0.03	0.15	0.02	29.14	0.24	33.44	0.33	0.07	0.01	0.00	100.08
56	DGR-035 chondrule 4 olivine 6	28.667	-33.903	42.49	0.00	0.21	0.08	0.24	0.00	0.90	0.03	55.91	0.00	0.49	0.00	0.00	100.35
57	DGR-035 chondrule 4 olivine 7	28.752	-33.919	41.58	0.00	0.17	0.08	0.16	0.00	2.56	0.05	54.91	0.00	0.47	0.01	0.00	99.99
58	DGR-035 chondrule 4 olivine 8	28.823	-33.943	41.97	0.01	0.16	0.06	0.16	0.00	3.64	0.02	54.17	0.01	0.48	0.00	0.01	100.69
59	DGR-035 chondrule 4 olivine 9	28.864	-33.966	36.92	0.01	0.10	0.06	0.14	0.00	25.92	0.17	35.29	0.28	0.35	0.00	0.00	99.24
60	DGR-035 chondrule 4 olivine 10	28.898	-33.997	36.58	0.05	0.06	0.01	0.08	0.00	30.05	0.23	32.84	0.29	0.04	0.01	0.00	100.23
61	DGR-035 matrix 2 olivine 1	27.275	-31.523	35.21	0.02	0.03	0.00	0.03	0.01	26.97	0.22	31.61	0.28	0.01	0.00	0.00	94.39
62	DGR-035 matrix 2 olivine 2	27.357	-31.445	36.66	0.00	0.00	0.00	0.02	0.00	31.28	0.25	31.90	0.34	0.02	0.00	0.01	100.48
63	DGR-035 matrix 2 olivine 3	27.701	-31.542	36.51	0.01	0.12	0.04	0.16	0.00	30.57	0.22	31.90	0.33	0.05	0.02	0.00	99.92
64	DGR-035 chondrule 5 olivine 1	22.177	-29.540	42.07	0.00	0.26	0.10	0.24	0.04	1.92	0.05	55.88	0.01	0.43	0.00	0.00	100.98
65	DGR-035 chondrule 5 olivine 2	22.131	-29.545	41.98	0.01	0.60	0.23	0.23	0.06	1.02	0.04	55.90	0.00	0.53	0.00	0.01	100.61
66	DGR-035 chondrule 5 olivine 3	22.089	-29.564	37.65	0.00	0.13	0.10	0.08	0.00	23.82	0.15	37.71	0.30	0.23	0.00	0.00	100.18
67	DGR-035 chondrule 5 olivine 4	22.100	-29.584	36.29	0.05	7.73	0.13	0.39	0.03	23.94	0.12	27.70	0.33	0.05	0.13	2.19	99.09
68	DGR-034 matrix 2 olivine 1	-23.415	-42.479	21.19	0.08	0.19	0.04	0.08	0.00	23.51	0.13	9.55	0.07	0.38	0.12	0.05	55.39
69	DGR-034 matrix 2 olivine 2	-23.425	-42.486	34.91	0.04	0.26	0.04	0.25	0.01	39.34	0.21	24.78	0.07	0.11	0.00	0.00	100.02
70	DGR-034 matrix 2 olivine 3	-23.425	-42.493	25.93	0.30	1.59	0.07	0.49	0.00	36.34	0.18	15.70	0.53	0.42	0.03	0.03	81.61
71	DGR-034 chondrule 5 olivine 1	-13.745	-29.588	42.06	0.00	0.36	0.11	0.08	0.03	0.36	0.01	56.17	0.01	0.62	0.00	0.00	99.82
72	DGR-034 chondrule 5 olivine 2	-13.793	-29.586	42.22	0.01	1.27	0.15	0.25	0.01	0.82	0.06	54.73	0.00	1.11	0.03	0.00	100.66
73	DGR-034 chondrule 5 olivine 3	-13.860	-29.571	41.86	0.00	0.16	0.04	0.14	0.00	4.12	0.07	53.92	0.00	0.14	0.06	0.01	100.51
74	DGR-034 chondrule 5 olivine 4	-13.913	-29.571	41.51	0.01	0.13	0.07	0.21	0.00	5.56	0.07	52.60	0.01	0.28	0.00	0.01	100.47
75	DGR-034 chondrule 5 olivine 5	-13.961	-29.584	40.36	0.01	0.06	0.08	0.12	0.00	11.42	0.11	48.06	0.02	0.19	0.00	0.00	100.44
76	DGR-034 chondrule 5 olivine 6	-14.020	-29.629	28.44	0.03	5.56	0.15	3.94	0.21	29.00	0.14	24.78	0.03	0.27	0.02	0.03	92.62
77	DGR-034 chondrule 6 olivine 1	-28.715	-37.412	41.96	0.01	0.03	0.05	0.06	0.02	4.98	0.12	53.46	0.02	0.12	0.01	0.00	100.85
78	DGR-034 chondrule 6 olivine 2	-28.683	-37.433	41.62	0.01	2.02	0.24	1.01	0.11	12.04	0.17	42.81	0.03	0.47	0.11	0.02	100.67
79	DGR-034 matrix 3 olivine 1	-15.289	-35.473	36.29	0.04	0.03	0.00	0.08	0.01	32.51	0.28	31.06	0.04	0.09	0.01	0.00	100.45
80	DGR-034 matrix 3 olivine 2	-15.274	-35.439	36.03	0.01	0.01	0.01	0.05	0.01	34.34	0.23	29.94	0.01	0.07	0.00	0.00	100.70
81	DGR-034 matrix 3 olivine 3	-15.274	-35.402	35.38	0.00	0.02	0.01	0.08	0.00	36.62	0.27	28.02	0.06	0.09	0.02	0.00	100.55
82	DGR-034 matrix 3 olivine 4	-15.280	-35.378	35.33	0.01	0.02	0.00	0.07	0.00	39.14	0.32	25.89	0.04	0.08	0.04	0.01	100.93
83	DGR-034 matrix 3 olivine 5	-15.259	-35.362	35.06	0.01	0.01	0.00	0.05	0.00	41.62	0.26	23.75	0.06	0.10	0.02	0.00	100.95

Figure 108: Olivine point results in weight percent oxide from EPMA. Results highlighted were not used due to error.

sigma_relative = Sqrt((I_unk,peak/t_peak + I_unk,bkg/t_bkg)/curr)/I_unk,net

1-sigma relative precision based on Poisson distribution

	Si	P	Al	Ti	Cr	V	Fe	Mn	Mg	Ni	Ca	Na	K	
1	DGR-035 chondrule 1 olivine 1	0.0041	0.8766	0.1053	0.2977	0.1376	0.0000	0.0075	0.2030	0.0032	0.0000	0.0413	1.0231	0.5177
2	DGR-035 chondrule 1 olivine 2	0.0041	0.3422	0.1942	0.0687	0.1915	4.3346	0.0062	0.1680	0.0034	0.3345	0.0439	0.5635	0.5763
3	DGR-035 chondrule 1 olivine 3	0.0042	0.4964	0.2431	0.3160	0.1865	0.0000	0.0052	0.1091	0.0036	0.0601	0.0449	2.6007	0.0000
4	DGR-035 chondrule 1 olivine 4	0.0042	4.2711	0.2181	0.0000	0.1577	0.0000	0.0050	0.1066	0.0037	0.1200	0.0417	0.3689	0.6336
5	DGR-035 chondrule 1 olivine 5	0.0043	4.6589	0.5380	0.6386	0.3437	0.0000	0.0041	0.0763	0.0042	0.0477	0.1835	0.0000	0.0000
6	DGR-035 chondrule 2 olivine 1	0.0041	0.0000	0.1810	0.1764	0.2168	0.0000	0.0077	0.1752	0.0032	0.1060	0.0479	0.7545	0.0000
7	DGR-035 chondrule 2 olivine 2	0.0042	0.0000	0.2165	0.2016	0.2967	4.1900	0.0056	0.1064	0.0035	0.0459	0.0535	0.0000	1.1002
8	DGR-035 chondrule 2 olivine 3	0.0042	0.0000	0.0000	0.1676	5.0078	4.3942	0.0060	0.1415	0.0034	0.1028	0.0769	0.0000	0.0000
9	DGR-035 chondrule 2 olivine 4	0.0042	0.0000	0.4000	0.2784	0.7948	0.0000	0.0057	0.1451	0.0035	0.1872	0.0752	0.0000	0.0000
10	DGR-035 chondrule 2 olivine 5	0.0042	0.0000	0.4831	0.4474	0.3494	0.8619	0.0044	0.0825	0.0040	0.0478	0.0615	2.5301	0.0000
11	DGR-035 chondrule 2 olivine 6	0.0042	4.3901	0.6332	0.6528	0.3496	4.5670	0.0044	0.0776	0.0040	0.0518	0.0824	4.9788	1.1427
12	DGR-035 chondrule 2 olivine 7	0.0043	0.3062	1.1389	2.3775	1.0885	0.0000	0.0041	0.0601	0.0042	0.0429	0.3758	0.9987	0.0000
13	DGR-035 chondrule 3 olivine 1	0.0041	0.7033	0.4160	0.2211	0.5582	0.3115	0.0066	0.1560	0.0033	0.5907	0.0378	0.0000	0.5743
14	DGR-035 chondrule 3 olivine 2	0.0041	0.8184	0.1743	0.1821	0.8569	4.2510	0.0066	0.1264	0.0033	0.1766	0.0486	0.6309	0.2702
15	DGR-035 chondrule 3 olivine 3	0.0041	0.0000	0.4234	3.6529	0.3845	0.0000	0.0077	0.3528	0.0032	1.0525	0.0647	0.0000	0.5255
16	DGR-035 chondrule 3 olivine 4	0.0043	0.0000	0.2551	0.1442	0.3995	0.8849	0.0042	0.0786	0.0041	0.0439	0.0567	0.0000	0.0000
17	DGR-035 chondrule 3 olivine 5	0.0043	0.0616	0.6789	1.3261	0.2621	1.5576	0.0041	0.0637	0.0043	0.0419	0.2025	2.6588	1.5825
18	DGR-035 matrix 1 olivine 1	0.0043	0.0000	1.0478	0.3700	0.2280	1.5305	0.0041	0.0625	0.0042	0.0438	0.1802	0.0000	0.0000
19	DGR-035 matrix 1 olivine 2	0.0043	0.0000	0.9082	0.0000	1.3890	0.7110	0.0041	0.0703	0.0042	0.0441	0.0881	0.0000	0.0000
20	DGR-035 matrix 1 olivine 3	0.0043	0.0000	0.0000	1.0902	0.3326	1.1704	0.0041	0.0752	0.0042	0.0425	0.1340	0.6336	0.0000
21	DGR-035 matrix 1 olivine 4	0.0043	0.4217	0.0000	0.7594	0.0000	4.3718	0.0040	0.0628	0.0042	0.0431	0.4458	0.6294	2.0048
22	DGR-035 CAI 1 olivine 1	0.0043	0.0244	1.1805	2.4151	0.0000	0.0000	0.0043	0.0778	0.0041	0.0449	0.1960	0.1950	1.5544
23	DGR-035 CAI 1 olivine 2	0.0043	0.0855	0.0000	0.0000	0.3958	0.0000	0.0043	0.0783	0.0040	0.0504	0.2433	0.3805	0.0000
24	DGR-035 CAI 1 olivine 3	0.0043	0.0396	0.0177	0.5437	0.4747	1.4935	0.0043	0.0712	0.0041	0.0484	0.1719	0.3017	0.0000
25	DGR-035 CAI 1 olivine 4	0.0043	0.0761	0.1108	1.0565	0.7279	4.6727	0.0043	0.0704	0.0041	0.0431	0.1153	0.2904	1.9944
26	DGR-034 chondrule 1 olivine 1	0.0041	4.2555	0.4076	0.5607	0.1833	0.0000	0.0125	0.0625	0.0030	0.4702	0.0616	0.0000	0.0000
27	DGR-034 chondrule 1 olivine 2	0.0041	1.0928	2.6193	0.0000	0.0000	0.6222	0.0059	0.0744	0.0034	0.1240	0.0536	1.2773	0.0000
28	DGR-034 chondrule 1 olivine 3	0.0043	0.5401	0.0398	1.3109	0.2141	0.0000	0.0041	0.0623	0.0041	0.3520	0.0937	0.5754	1.1628
29	DGR-034 chondrule 1 olivine 4	0.0042	0.2761	0.5554	0.0000	0.6210	1.5214	0.0042	0.0662	0.0041	0.1117	0.1467	1.0541	0.0000
30	DGR-034 chondrule 1 olivine 5	0.0042	2.2332	0.3167	0.8850	0.2280	0.5446	0.0050	0.0689	0.0037	0.1988	0.0590	5.1257	0.6391
31	DGR-034 chondrule 1 olivine 6	0.0040	0.0000	0.9664	0.0000	0.2125	0.0000	0.0120	0.0687	0.0030	0.4387	0.0642	1.7247	0.4736
32	DGR-034 chondrule 2 olivine 1	0.0041	2.0493	0.3080	0.4547	0.2911	1.0329	0.0098	0.1423	0.0031	0.0000	0.0482	0.0000	0.5542
33	DGR-034 chondrule 2 olivine 2	0.0041	4.2161	0.3067	0.3068	1.2834	0.0000	0.0093	0.1565	0.0031	0.6349	0.0428	1.2976	0.0000
34	DGR-034 chondrule 2 olivine 3	0.0040	0.2919	0.5117	1.4885	0.3042	0.0000	0.0126	0.3210	0.0030	0.8389	0.0733	1.0445	1.7693
35	DGR-034 chondrule 2 olivine 4	0.0041	0.0000	0.1197	0.0000	0.3298	0.9537	0.0084	0.1773	0.0031	0.5202	0.0405	0.6512	0.0000
36	DGR-034 chondrule 2 olivine 5	0.0041	1.4116	0.2246	0.4655	0.2028	1.0175	0.0073	0.1507	0.0032	0.6448	0.0504	0.0000	7.3459
37	DGR-034 chondrule 2 olivine 6	0.0044	0.1722	0.0240	0.3097	0.0442	0.0000	0.0036	0.0681	0.0049	1.2012	0.0582	0.1805	0.3630
38	DGR-034 chondrule 3 olivine 1	0.0041	0.0000	0.3287	0.0000	0.2496	0.0000	0.0082	0.1092	0.0031	0.7391	0.0466	0.0000	0.0000
39	DGR-034 chondrule 3 olivine 2	0.0041	0.5962	0.4347	0.3567	0.2248	1.0247	0.0076	0.1016	0.0032	0.7560	0.0427	0.0000	1.5089
40	DGR-034 chondrule 3 olivine 3	0.0041	1.4623	0.5021	1.8455	0.1920	0.7276	0.0061	0.1022	0.0034	0.5633	0.0489	0.5145	1.8949
41	DGR-034 chondrule 3 olivine 4	0.0041	0.0000	0.0820	0.2633	0.1052	0.6624	0.0095	0.1182	0.0031	0.0000	0.0334	0.0000	0.0000
42	DGR-034 chondrule 3 olivine 5	0.0041	0.0000	0.3303	0.2346	0.2486	0.0000	0.0084	0.0926	0.0031	0.7980	0.0388	0.0000	0.6129
43	DGR-034 matrix 1 olivine 1	0.0044	1.2235	0.1124	0.0000	0.1067	0.0000	0.0034	0.0617	0.0053	0.3288	0.0794	0.0000	0.0000
44	DGR-034 matrix 1 olivine 2	0.0045	0.1997	0.0530	0.5405	0.1322	1.5826	0.0035	0.0784	0.0050	0.1569	0.0778	2.5192	2.1152
45	DGR-034 matrix 1 olivine 3	0.0045	0.3634	0.0477	0.8865	0.1672	4.6441	0.0034	0.0581	0.0053	0.0754	0.0613	1.7077	2.1253
46	DGR-034 matrix 1 olivine 4	0.0046	0.0583	0.0093	0.1876	0.0267	0.9341	0.0034	0.0666	0.0055	0.0748	0.0351	0.2440	1.4514
47	DGR-034 chondrule 4 olivine 1	0.0044	0.0635	0.4882	1.3912	0.2128	2.3352	0.0034	0.0507	0.0052	0.4457	0.0673	0.2958	8.5093
48	DGR-034 chondrule 4 olivine 2	0.0044	0.0695	0.2156	4.1995	0.2187	0.4688	0.0034	0.0594	0.0052	0.4876	0.0794	0.1806	1.3998
49	DGR-034 chondrule 4 olivine 3	0.0048	0.1505	0.3063	0.9783	0.2281	0.0000	0.0044	0.0773	0.0054	2.2270	0.0628	0.0000	0.6152
50	DGR-034 chondrule 4 olivine 4	0.0044	0.4939	0.2974	0.0000	1.9599	0.0000	0.0034	0.0607	0.0053	0.2197	0.0518	0.6339	1.6833
51	DGR-035 chondrule 4 olivine 1	0.0040	4.0020	0.0314	0.3863	0.1347	1.4044	0.0551	0.5690	0.0029	1.2497	0.0237	0.8607	0.6405
52	DGR-035 chondrule 4 olivine 2	0.0040	1.0025	0.0392	0.2184	0.1841	3.7772	0.0533	1.1275	0.0029	0.0000	0.0241	0.0000	0.0000
53	DGR-035 chondrule 4 olivine 3	0.0040	0.0000	0.0502	0.2319	0.1020	0.5764	0.0155	0.8037	0.0030	0.0000	0.0286	5.1691	0.0000
54	DGR-035 chondrule 4 olivine 4	0.0042	2.1743	0.1001	0.1959	0.1129	1.0908	0.0050	0.0993	0.0037	0.0626	0.0689	1.7391	0.0000
55	DGR-035 chondrule 4 olivine 5	0.0043	4.4543	0.1366	0.5290	0.1004	0.5869	0.0041	0.0668	0.0042	0.0444	0.1158	0.9842	4.0455
56	DGR-035 chondrule 4 olivine 6	0.0040	0.0000	0.0419	0.1660	0.0704	0.0000	0.0289	0.4289	0.0029	0.0000	0.0262	0.0000	1.1691
57	DGR-035 chondrule 4 olivine 7	0.0041	4.1290	0.0504	0.1739	0.1007	3.9090	0.0151	0.2412	0.0030	0.0000	0.0266	0.8561	0.0000
58	DGR-035 chondrule 4 olivine 8	0.0040	0.6900	0.0553	0.2130	0.0966	0.0000	0.0124	0.5961	0.0030	1.0192	0.0262	0.0000	0.6037
59	DGR-035 chondrule 4 olivine 9	0.0043	0.8947	0.0859	0.2268	0.1011	0.0000	0.0044	0.0849	0.0040	0.0516	0.0330	0.0000	2.0081
60	DGR-035 chondrule 4 olivine 10	0.0043	0.2143	0.1385	2.4045	0.1746	0.0000	0.0041	0.0686	0.0042	0.0504	0.2297	0.8258	2.0150
61	DGR-035 matrix 2 olivine 1	0.0044	0.5003	0.2662	0.0000	0.4873	2.2534	0.0043	0.0687	0.0043	0.0506	0.5453	5.0572	2.0579
62	DGR-035 matrix 2 olivine 2	0.0043	0.0000	0.0000	0.0000	0.7634	0.0000	0.0040	0.0643	0.0043	0.0436	0.3430	0.0000	1.0122
63	DGR-035 matrix 2 olivine 3	0.0043	0.9373	0.0725	0.3978	0.0962	0.0000	0.0040	0.0695	0.0043	0.0447	0.1683	0.6327	0.0000
64	DGR-035 chondrule 5 olivine 1	0.0041	0.0000	0.0369	0.1433	0.0737	0.3882	0.0178	0.2267	0.0029	1.6838	0.0287	0.0000	0.0000
65	DGR-035 chondrule 5 olivine 2	0.0041	0.7823	0.0198	0.0673	0.0727	0.2318	0.0263	0.3042	0.0029	0.0000	0.0249	1.7130	0.7196
66	DGR-035 chondrule 5 olivine 3	0.0042	2.2852	0.0674	0.1523	0.1727	0.0000	0.0046	0.0979	0.0039	0.0472	0.0455	0.0000	0.0000
67	DGR-035 chondrule 5 olivine 4	0.0043	0.1950	0.0045	0.1152	0.0512	0.4470	0.0046	0.1168	0.0045	0.0440	0.1580	0.0946	0.0099
68	DGR-034 matrix 2 olivine 1	0.0056	0.1119	0.0406	0.2939	0.1529	0.0000	0.0046	0.1030	0.0082	0.1628	0.0295	0.1134	0.1218
69	DGR-034 matrix 2 olivine 2	0.0044	0.2814	0.0379	0.3210	0.0671	1.6441	0.0035	0.0753	0.0050	0.1874	0.0805	0.0000	0.0000
70	DGR-034 matrix 2 olivine 3	0.0051	0.0464	0.0108	0.1985	0.0407	4.8031	0.0037	0.0850	0.0064	0.0297	0.0288	0.4053	0.2402
71	DGR-034 chondrule 5 olivine 1	0.0041	0.0000	0.0291	0.1267	0.1740	0.5264	0.0538	0.8100	0.0029	1.4333	0.0222	0.0000	1.3879
72	DGR-034 chondrule 5 olivine 2	0.0040	0.9587	0.0124	0.0989	0.0692	1.4274	0.0306	0.2097	0.0030	2.5110	0.0156	0.2861	2.3358
73	DGR-034 chondrule 5 olivine 3	0.0041	0.0000	0.0554	0.3592	0.1044	0.0000	0.0116	0.1738	0.0030	0.0000	0.0667	0.1595	0.6033
74	DGR-034 chondrule 5 olivine 4	0.0041	1.0424	0.0627	0.2073	0.0792	0.0000	0.0099	0.1832	0.0031	1.0173	0.0394	0.0000	0.3916
75	DGR-034 chondrule 5 olivine 5	0.0041	0.8579	0.1334	0.1748	0.1215	4.0084	0.0067	0.1233	0.0033	0.5126	0.0514	4.9930	0.0000
76	DGR-034 chondrule 5 olivine 6	0.0049	0.3051	0.0054	0.0986	0.0125	0.0877	0.0041	0.0979	0.0049	0.4301	0.0394	0.6492	0.2099
77	DGR-034 chondrule 6 olivine 1	0.0041	1.3088	0.2438	0.2750	0.1970	0.6882	0.0105	0.1059	0.0030	0.6900	0.0768	0.6449	2.4385
78	DGR-034 chondrule 6 olivine 2	0.0040	1.0556	0.0094	0.0656	0.0271	0.1470	0.0066	0.0865	0.0035	0.3413	0.0267	0.0986	0.3486
79	DGR-034 matrix 3 olivine 1	0.0043	0.2318	0.2735	5.9881	0.1613	1.5388	0.0039	0.0586	0.0044	0.2851	0.0991	1.0278	0.0000
80	DGR-034 matrix 3 olivine 2	0.0043	0.9334	1.3982	0.9326	0.2553	1.6183	0.0038	0.0698	0.0045	2.3508	0.1254	0.0000	0.0000
81	DGR-034 matrix 3 olivine 3	0.0044	0.0000	0.3693	2.0168	0.1746	0.0000	0.0037	0.0605	0.0047	0.2292	0.1046	0.6388	0.0000
82	DGR-034 matrix 3 olivine 4	0.0044	1.6433	0.5045	0.0000	0.1920	0.0000	0.0035	0.0532	0.0049	0.3360	0.1075	0.3218	0.9203
83	DGR-034 matrix 3 olivine 5	0.0044	0.7039	0.9541	0.0000	0.2783	0.0000	0.0034	0.0657	0.0051	0.2263	0.0914	0.5698	0.0000

Figure 109: Olivine point precision results from EPMA. Results highlighted were not used due to error.

LLD(3-sigma) = 3*ZAF*(C_std/I_std,net)*Sqrt(2)*Sqrt(I_unk,bkg /(t_unk,bkg*curr_unk))

3-sigma lower limit of detection (wt% oxide)

	SiO2	P2O5	Al2O3	TiO2	Cr2O3	V2O3	FeO	MnO	MgO	NiO	CaO	Na2O	K2O
1 DGR-035 chondrule 1 olivine 1	0.0624	0.0280	0.0207	0.0393	0.0369	0.0410	0.0441	0.0318	0.0510	0.0340	0.0218	0.0266	0.0182
2 DGR-035 chondrule 1 olivine 2	0.0609	0.0272	0.0216	0.0387	0.0373	0.0397	0.0454	0.0344	0.0520	0.0353	0.0220	0.0272	0.0175
3 DGR-035 chondrule 1 olivine 3	0.0621	0.0276	0.0221	0.0399	0.0339	0.0401	0.0468	0.0342	0.0506	0.0349	0.0224	0.0301	0.0184
4 DGR-035 chondrule 1 olivine 4	0.0639	0.0272	0.0220	0.0410	0.0347	0.0384	0.0469	0.0348	0.0532	0.0354	0.0228	0.0291	0.0176
5 DGR-035 chondrule 1 olivine 5	0.0624	0.0293	0.0219	0.0411	0.0355	0.0428	0.0485	0.0351	0.0521	0.0376	0.0232	0.0339	0.0188
6 DGR-035 chondrule 2 olivine 1	0.0614	0.0269	0.0216	0.0382	0.0377	0.0394	0.0451	0.0325	0.0509	0.0334	0.0217	0.0273	0.0181
7 DGR-035 chondrule 2 olivine 2	0.0658	0.0277	0.0219	0.0400	0.0357	0.0380	0.0462	0.0337	0.0528	0.0347	0.0227	0.0295	0.0181
8 DGR-035 chondrule 2 olivine 3	0.0629	0.0291	0.0222	0.0397	0.0366	0.0401	0.0439	0.0339	0.0507	0.0353	0.0227	0.0287	0.0179
9 DGR-035 chondrule 2 olivine 4	0.0606	0.0277	0.0218	0.0390	0.0396	0.0415	0.0464	0.0341	0.0509	0.0347	0.0224	0.0289	0.0184
10 DGR-035 chondrule 2 olivine 5	0.0643	0.0290	0.0223	0.0410	0.0342	0.0369	0.0493	0.0348	0.0503	0.0362	0.0229	0.0315	0.0195
11 DGR-035 chondrule 2 olivine 6	0.0632	0.0277	0.0225	0.0401	0.0342	0.0403	0.0491	0.0355	0.0509	0.0369	0.0235	0.0310	0.0186
12 DGR-035 chondrule 2 olivine 7	0.0638	0.0253	0.0219	0.0407	0.0369	0.0384	0.0481	0.0330	0.0500	0.0369	0.0238	0.0315	0.0192
13 DGR-035 chondrule 3 olivine 1	0.0628	0.0267	0.0216	0.0400	0.0356	0.0365	0.0466	0.0341	0.0500	0.0344	0.0229	0.0281	0.0174
14 DGR-035 chondrule 3 olivine 2	0.0626	0.0259	0.0211	0.0400	0.0371	0.0391	0.0436	0.0335	0.0520	0.0337	0.0234	0.0268	0.0177
15 DGR-035 chondrule 3 olivine 3	0.0645	0.0281	0.0221	0.0395	0.0380	0.0419	0.0444	0.0330	0.0504	0.0342	0.0222	0.0271	0.0172
16 DGR-035 chondrule 3 olivine 4	0.0649	0.0294	0.0231	0.0397	0.0367	0.0377	0.0483	0.0352	0.0511	0.0371	0.0230	0.0318	0.0189
17 DGR-035 chondrule 3 olivine 5	0.0647	0.0287	0.0222	0.0407	0.0365	0.0402	0.0484	0.0346	0.0517	0.0367	0.0234	0.0342	0.0183
18 DGR-035 matrix 1 olivine 1	0.0630	0.0284	0.0230	0.0408	0.0355	0.0395	0.0512	0.0337	0.0489	0.0375	0.0232	0.0332	0.0188
19 DGR-035 matrix 1 olivine 2	0.0651	0.0295	0.0224	0.0411	0.0378	0.0360	0.0508	0.0353	0.0518	0.0369	0.0237	0.0320	0.0186
20 DGR-035 matrix 1 olivine 3	0.0653	0.0287	0.0221	0.0409	0.0365	0.0403	0.0488	0.0369	0.0490	0.0371	0.0226	0.0320	0.0190
21 DGR-035 matrix 1 olivine 4	0.0640	0.0280	0.0235	0.0412	0.0361	0.0380	0.0523	0.0344	0.0515	0.0375	0.0229	0.0318	0.0186
22 DGR-035 CAI 1 olivine 1	0.0650	0.0287	0.0227	0.0417	0.0383	0.0406	0.0492	0.0356	0.0509	0.0366	0.0232	0.0318	0.0181
23 DGR-035 CAI 1 olivine 2	0.0640	0.0295	0.0226	0.0408	0.0338	0.0409	0.0494	0.0360	0.0505	0.0373	0.0234	0.0298	0.0189
24 DGR-035 CAI 1 olivine 3	0.0666	0.0292	0.0226	0.0407	0.0347	0.0389	0.0485	0.0351	0.0510	0.0365	0.0229	0.0324	0.0187
25 DGR-035 CAI 1 olivine 4	0.0635	0.0294	0.0227	0.0399	0.0345	0.0411	0.0482	0.0348	0.0514	0.0361	0.0234	0.0311	0.0186
26 DGR-034 chondrule 1 olivine 1	0.0605	0.0279	0.0213	0.0382	0.0365	0.0400	0.0432	0.0306	0.0510	0.0331	0.0219	0.0252	0.0177
27 DGR-034 chondrule 1 olivine 2	0.0626	0.0278	0.0219	0.0410	0.0373	0.0382	0.0458	0.0351	0.0522	0.0343	0.0224	0.0282	0.0184
28 DGR-034 chondrule 1 olivine 3	0.0640	0.0297	0.0233	0.0403	0.0344	0.0394	0.0483	0.0351	0.0509	0.0371	0.0229	0.0323	0.0188
29 DGR-034 chondrule 1 olivine 4	0.0646	0.0295	0.0227	0.0411	0.0376	0.0395	0.0490	0.0356	0.0510	0.0365	0.0238	0.0329	0.0186
30 DGR-034 chondrule 1 olivine 5	0.0655	0.0283	0.0222	0.0400	0.0368	0.0373	0.0479	0.0347	0.0513	0.0351	0.0225	0.0303	0.0177
31 DGR-034 chondrule 1 olivine 6	0.0612	0.0270	0.0216	0.0397	0.0359	0.0377	0.0427	0.0347	0.0507	0.0322	0.0223	0.0256	0.0167
32 DGR-034 chondrule 2 olivine 1	0.0609	0.0266	0.0209	0.0388	0.0342	0.0378	0.0433	0.0321	0.0514	0.0338	0.0221	0.0268	0.0170
33 DGR-034 chondrule 2 olivine 2	0.0630	0.0275	0.0208	0.0388	0.0381	0.0392	0.0441	0.0318	0.0514	0.0328	0.0220	0.0263	0.0181
34 DGR-034 chondrule 2 olivine 3	0.0630	0.0250	0.0212	0.0380	0.0387	0.0398	0.0416	0.0337	0.0499	0.0324	0.0218	0.0256	0.0171
35 DGR-034 chondrule 2 olivine 4	0.0632	0.0282	0.0212	0.0398	0.0344	0.0345	0.0445	0.0341	0.0528	0.0335	0.0221	0.0265	0.0179
36 DGR-034 chondrule 2 olivine 5	0.0637	0.0272	0.0211	0.0394	0.0376	0.0368	0.0451	0.0354	0.0518	0.0334	0.0222	0.0271	0.0177
37 DGR-034 chondrule 2 olivine 6	0.0654	0.0300	0.0226	0.0414	0.0354	0.0414	0.0480	0.0356	0.0501	0.0387	0.0230	0.0341	0.0193
38 DGR-034 chondrule 3 olivine 1	0.0616	0.0275	0.0206	0.0398	0.0355	0.0430	0.0439	0.0336	0.0518	0.0334	0.0222	0.0272	0.0181
39 DGR-034 chondrule 3 olivine 2	0.0642	0.0263	0.0215	0.0387	0.0344	0.0371	0.0447	0.0354	0.0512	0.0343	0.0223	0.0267	0.0180
40 DGR-034 chondrule 3 olivine 3	0.0612	0.0280	0.0220	0.0393	0.0359	0.0386	0.0461	0.0336	0.0517	0.0346	0.0220	0.0277	0.0180
41 DGR-034 chondrule 3 olivine 4	0.0636	0.0278	0.0209	0.0385	0.0370	0.0356	0.0417	0.0342	0.0507	0.0335	0.0221	0.0267	0.0177
42 DGR-034 chondrule 3 olivine 5	0.0615	0.0271	0.0216	0.0389	0.0354	0.0417	0.0437	0.0335	0.0516	0.0336	0.0218	0.0263	0.0173
43 DGR-034 matrix 1 olivine 1	0.0663	0.0298	0.0238	0.0422	0.0351	0.0419	0.0515	0.0360	0.0498	0.0385	0.0238	0.0366	0.0200
44 DGR-034 matrix 1 olivine 2	0.0665	0.0295	0.0230	0.0409	0.0354	0.0397	0.0499	0.0355	0.0493	0.0388	0.0240	0.0351	0.0193
45 DGR-034 matrix 1 olivine 3	0.0662	0.0299	0.0233	0.0409	0.0377	0.0390	0.0499	0.0364	0.0527	0.0384	0.0242	0.0364	0.0193
46 DGR-034 matrix 1 olivine 4	0.0666	0.0309	0.0234	0.0414	0.0374	0.0383	0.0525	0.0373	0.0497	0.0387	0.0240	0.0379	0.0196
47 DGR-034 chondrule 4 olivine 1	0.0657	0.0301	0.0237	0.0416	0.0354	0.0391	0.0510	0.0362	0.0500	0.0383	0.0246	0.0357	0.0194
48 DGR-034 chondrule 4 olivine 2	0.0673	0.0304	0.0232	0.0419	0.0366	0.0374	0.0521	0.0387	0.0528	0.0388	0.0244	0.0364	0.0190
49 DGR-034 chondrule 4 olivine 3	0.0635	0.0294	0.0226	0.0396	0.0350	0.0386	0.0450	0.0334	0.0471	0.0360	0.0227	0.0345	0.0181
50 DGR-034 chondrule 4 olivine 4	0.0655	0.0294	0.0229	0.0420	0.0384	0.0410	0.0498	0.0381	0.0502	0.0385	0.0246	0.0352	0.0191
51 DGR-035 chondrule 4 olivine 1	0.0601	0.0264	0.0204	0.0387	0.0359	0.0395	0.0401	0.0324	0.0504	0.0320	0.0213	0.0244	0.0168
52 DGR-035 chondrule 4 olivine 2	0.0620	0.0260	0.0209	0.0381	0.0372	0.0359	0.0421	0.0328	0.0528	0.0322	0.0208	0.0250	0.0174
53 DGR-035 chondrule 4 olivine 3	0.0605	0.0269	0.0212	0.0372	0.0357	0.0363	0.0427	0.0323	0.0520	0.0325	0.0220	0.0254	0.0179
54 DGR-035 chondrule 4 olivine 4	0.0644	0.0276	0.0224	0.0404	0.0366	0.0384	0.0470	0.0341	0.0508	0.0359	0.0233	0.0306	0.0181
55 DGR-035 chondrule 4 olivine 5	0.0640	0.0280	0.0229	0.0411	0.0371	0.0393	0.0459	0.0357	0.0485	0.0373	0.0228	0.0310	0.0188
56 DGR-035 chondrule 4 olivine 6	0.0604	0.0271	0.0206	0.0375	0.0337	0.0377	0.0444	0.0313	0.0538	0.0324	0.0222	0.0253	0.0169
57 DGR-035 chondrule 4 olivine 7	0.0604	0.0271	0.0210	0.0375	0.0365	0.0369	0.0433	0.0324	0.0507	0.0328	0.0218	0.0249	0.0178
58 DGR-035 chondrule 4 olivine 8	0.0592	0.0264	0.0211	0.0384	0.0361	0.0371	0.0428	0.0339	0.0516	0.0328	0.0220	0.0264	0.0172
59 DGR-035 chondrule 4 olivine 9	0.0648	0.0277	0.0236	0.0397	0.0335	0.0409	0.0494	0.0349	0.0508	0.0371	0.0229	0.0332	0.0187
60 DGR-035 chondrule 4 olivine 10	0.0637	0.0272	0.0225	0.0411	0.0382	0.0402	0.0490	0.0349	0.0504	0.0377	0.0235	0.0313	0.0187
61 DGR-035 matrix 2 olivine 1	0.0655	0.0274	0.0227	0.0402	0.0355	0.0392	0.0472	0.0339	0.0513	0.0363	0.0228	0.0322	0.0191
62 DGR-035 matrix 2 olivine 2	0.0642	0.0291	0.0225	0.0407	0.0356	0.0396	0.0494	0.0351	0.0506	0.0378	0.0241	0.0335	0.0186
63 DGR-035 matrix 2 olivine 3	0.0654	0.0289	0.0231	0.0412	0.0350	0.0397	0.0504	0.0342	0.0498	0.0375	0.0248	0.0321	0.0190
64 DGR-035 chondrule 5 olivine 1	0.0617	0.0265	0.0210	0.0394	0.0370	0.0376	0.0429	0.0315	0.0511	0.0326	0.0224	0.0250	0.0179
65 DGR-035 chondrule 5 olivine 2	0.0635	0.0251	0.0209	0.0382	0.0354	0.0389	0.0427	0.0317	0.0524	0.0322	0.0223	0.0247	0.0172
66 DGR-035 chondrule 5 olivine 3	0.0635	0.0288	0.0224	0.0406	0.0361	0.0387	0.0471	0.0371	0.0521	0.0368	0.0231	0.0308	0.0188
67 DGR-035 chondrule 5 olivine 4	0.0653	0.0280	0.0231	0.0402	0.0393	0.0374	0.0494	0.0359	0.0483	0.0370	0.0237	0.0323	0.0192
68 DGR-034 matrix 2 olivine 1	0.0581	0.0219	0.0167	0.0359	0.0316	0.0363	0.0450	0.0323	0.0382	0.0320	0.0206	0.0352	0.0170
69 DGR-034 matrix 2 olivine 2	0.0661	0.0295	0.0232	0.0408	0.0366	0.0414	0.0499	0.0367	0.0500	0.0380	0.0232	0.0359	0.0202
70 DGR-034 matrix 2 olivine 3	0.0588	0.0282	0.0216	0.0406	0.0341	0.0401	0.0485	0.0361	0.0471	0.0372	0.0230	0.0341	0.0184
71 DGR-034 chondrule 5 olivine 1	0.0634	0.0271	0.0217	0.0388	0.0372	0.0381	0.0422	0.0328	0.0506	0.0323	0.0217	0.0253	0.0168
72 DGR-034 chondrule 5 olivine 2	0.0616	0.0247	0.0210	0.0385	0.0359	0.0401	0.0442	0.0311	0.0510	0.0324	0.0223	0.0236	0.0170
73 DGR-034 chondrule 5 olivine 3	0.0625	0.0267	0.0211	0.0395	0.0336	0.0389	0.0431	0.0324	0.0528	0.0332	0.0220	0.0253	0.0172
74 DGR-034 chondrule 5 olivine 4	0.0619	0.0268	0.0212	0.0394	0.0367	0.0390	0.0430	0.0335	0.0514	0.0329	0.0228	0.0264	0.0164
75 DGR-034 chondrule 5 olivine 5	0.0634	0.0272	0.0218	0.0395	0.0349	0.0369	0.0439	0.0338	0.0556	0.0347	0.0224	0.0269	0.0181
76 DGR-034 chondrule 5 olivine 6	0.0659	0.0267	0.0225	0.0403	0.0363	0.0416	0.0489	0.0343	0.0492	0.0370	0.0230	0.0339	0.0185
77 DGR-034 chondrule 6 olivine 1	0.0638	0.0254	0.0210	0.0385	0.0323	0.0373	0.0446	0.0316	0.0502	0.0333	0.0226	0.0255	0.0177
78 DGR-034 chondrule 6 olivine 2	0.0625	0.0268	0.0220	0.0401	0.0336	0.0404	0.0457	0.0338	0.0501	0.0349	0.0229	0.0282	0.0175
79 DGR-034 matrix 3 olivine 1	0.0645	0.0282	0.0226	0.0408	0.0341	0.0395	0.0492	0.0350	0.0517	0.0371	0.0225	0.0333	0.0196
80 DGR-034 matrix 3 olivine 2	0.0694	0.0286	0.0230	0.0408	0.0366	0.0414	0.0481	0.0378	0.0520	0.0380	0.0234	0.0346	0.0191
81 DGR-034 matrix 3 olivine 3	0.0670	0.0300	0.0228	0.0407	0.0350	0.0404	0.0501	0.0359	0.0520	0.0375	0.0239	0.0339	0.0190
82 DGR-034 matrix 3 olivine 4	0.0642	0.0303	0.0231	0.0409	0.0365	0.0430	0.0495	0.0351	0.0502	0.0384	0.0239	0.0339	0.0188
83 DGR-034 matrix 3 olivine 5	0.0667	0.0297	0.0233	0.0415	0.0376	0.0405	0.0504	0.0396	0.0520	0.0383	0.0242	0.0353	0.0193

Figure 110: Olivine limit of detection point results from EPMA. Results highlighted were not used due to error.

Results_of_analyses:

	coordinates in mm		oxide weight %												
	X	Y	SiO2	Al2O3	TiO2	Cr2O3	V2O3	FeO	MnO	MgO	NiO	CaO	Na2O	K2O	Total
84 DGR-035 chondrule 1 cpx 1	17.701	-33.856	51.71	4.37	0.89	1.20	0.04	2.29	0.00	18.35	0.01	20.86	0.00	0.00	99.72
85 DGR-035 chondrule 1 cpx 2	17.747	-33.876	51.79	4.20	0.83	1.15	0.05	2.50	0.01	19.06	0.00	20.05	0.02	0.01	99.66
86 DGR-035 chondrule 1 cpx 3	17.719	-33.685	50.69	6.07	0.96	1.41	0.05	2.90	0.05	19.66	0.03	17.91	0.02	0.01	99.76
87 DGR-035 chondrule 1 cpx 4	17.626	-33.801	51.87	3.99	0.77	1.12	0.06	2.36	0.04	19.04	0.01	20.07	0.01	0.01	99.34
88 DGR-035 chondrule 1 opx 1	17.926	-33.842	50.22	11.85	0.84	1.46	0.04	4.71	0.04	29.85	0.02	1.65	0.01	0.00	100.70
89 DGR-035 chondrule 1 opx 2	17.553	-33.678	51.01	10.67	0.78	1.46	0.02	4.67	0.06	30.39	0.02	1.75	0.02	0.00	100.83
90 DGR-035 chondrule 1 opx 3	17.479	-33.837	49.93	11.99	0.81	1.55	0.03	4.55	0.05	29.71	0.01	1.55	0.00	0.01	100.21
91 DGR-035 chondrule 1 opx 4	17.518	-34.140	50.69	10.82	0.86	1.56	0.05	4.75	0.05	30.07	0.01	1.81	0.00	0.00	100.68
92 DGR-035 chondrule 1 cpx 5	18.062	-34.068	52.18	4.46	0.95	1.24	0.06	2.97	0.04	19.42	0.02	19.54	0.02	0.01	100.91
93 DGR-035 chondrule 1 opx 5	17.751	-34.293	55.63	2.33	0.36	1.08	0.05	4.52	0.11	28.99	0.02	7.93	0.02	0.00	101.05
94 DGR-035 chondrule 1 cpx 6	17.324	-33.754	47.30	11.10	1.73	0.88	0.02	2.67	0.06	15.89	0.02	20.70	0.00	0.00	100.37
95 DGR-035 chondrule 1 cpx 7	17.610	-33.515	48.30	9.38	2.20	1.71	0.08	3.32	0.08	19.38	0.03	15.83	0.01	0.00	100.31
96 DGR-035 chondrule 3 cpx 1	35.465	-40.489	52.67	4.35	1.65	0.79	0.03	0.73	0.14	19.25	0.02	20.73	0.01	0.00	100.36
97 DGR-035 chondrule 3 cpx 2	35.443	-40.501	52.80	4.12	1.62	0.84	0.02	0.85	0.16	20.64	0.03	19.39	0.03	0.00	100.50
98 DGR-035 chondrule 3 cpx 3	35.513	-40.472	56.62	2.53	0.71	0.85	0.00	0.91	0.27	32.46	0.00	6.58	0.02	0.00	100.95
99 DGR-035 chondrule 3 cpx 4	35.502	-40.462	56.62	2.69	0.82	0.89	0.03	0.91	0.25	32.39	0.01	6.34	0.01	0.00	100.96
100 DGR-035 matrix 1 cpx 1	22.766	-40.144	54.01	0.02	0.00	0.01	0.02	6.66	0.04	14.42	0.01	25.14	0.03	0.00	100.35
101 DGR-035 matrix 1 cpx 2	22.737	-40.129	52.54	0.02	0.00	0.03	0.00	10.11	0.08	12.15	0.02	24.73	0.02	0.00	99.69
102 DGR-035 matrix 1 cpx 3	22.745	-40.114	53.02	0.56	0.01	0.01	0.00	8.91	0.11	14.92	0.04	21.36	0.40	0.00	99.33
103 DGR-035 matrix 1 cpx 4	22.642	-40.121	51.13	0.01	0.02	0.00	0.02	5.54	0.09	14.51	0.00	23.56	0.01	0.00	94.88
104 DGR-035 CAI 1 opx 1	13.410	-32.803	52.77	4.74	0.12	0.04	0.00	13.93	0.16	27.59	0.05	0.50	0.02	0.00	99.91
105 DGR-035 CAI 1 opx 2	13.410	-32.834	52.56	4.91	0.07	0.02	0.02	14.60	0.17	27.11	0.04	0.31	0.03	0.01	99.86
106 DGR-034 chondrule 1 opx 1	-28.984	-40.155	59.03	1.08	0.21	0.79	0.01	0.68	0.28	37.87	0.02	0.99	0.01	0.01	101.00
107 DGR-034 chondrule 1 opx 2	-28.926	-40.159	58.48	1.73	0.18	0.85	0.00	0.84	0.29	36.46	0.01	1.70	0.05	0.00	100.61
108 DGR-034 chondrule 1 opx 3	-28.825	-40.106	59.08	0.91	0.16	0.79	0.01	1.27	0.13	38.00	0.01	0.41	0.01	0.00	100.80
109 DGR-034 chondrule 1 opx 4	-28.720	-40.061	58.77	0.98	0.10	0.81	0.01	1.79	0.16	37.47	0.01	0.74	0.02	0.00	100.87
110 DGR-034 CAI 1 cpx 1	-29.096	-35.319	53.69	2.54	0.18	0.12	0.01	0.49	0.08	18.09	0.12	24.27	0.03	0.01	99.63
111 DGR-034 CAI 1 cpx 2	-29.106	-35.356	53.12	3.60	0.09	0.14	0.05	0.98	0.01	17.09	0.02	25.33	0.06	0.00	100.49
112 DGR-034 CAI 1 cpx 3	-29.214	-35.371	53.23	2.82	0.13	0.07	0.04	0.67	0.07	17.84	0.04	25.13	0.03	0.00	100.04
113 DGR-034 CAI 1 cpx 4	-29.264	-35.286	47.33	0.70	0.04	0.00	0.03	28.30	0.36	0.27	0.06	21.58	0.06	0.01	98.74
114 DGR-034 CAI 1 cpx 5	-29.107	-35.438	47.43	0.25	0.05	0.01	0.03	28.44	0.37	0.15	0.04	21.93	0.06	0.01	98.76
115 DGR-034 chondrule 3 opx 1	-27.710	-33.934	57.17	2.60	0.22	1.18	0.00	2.12	0.15	35.14	0.01	1.74	0.01	0.00	100.35
116 DGR-034 chondrule 3 opx 2	-27.634	-33.944	57.82	1.73	0.18	0.96	0.02	2.31	0.12	36.21	0.03	1.37	0.01	0.00	100.76
117 DGR-034 chondrule 3 opx 3	-27.786	-33.913	56.99	1.82	0.16	0.95	0.04	2.89	0.19	35.09	0.01	1.69	0.00	0.01	99.85
118 DGR-034 chondrule 3 opx 4	-27.908	-33.916	56.34	1.04	0.36	0.65	0.01	5.32	0.42	31.20	0.03	4.25	0.00	0.00	99.62
119 DGR-034 chondrule 3 opx 5	-27.932	-33.911	56.77	1.35	0.34	0.86	0.01	4.55	0.36	31.96	0.02	3.97	0.00	0.00	100.19
120 DGR-034 chondrule 3 opx 6	-28.004	-33.866	56.59	1.97	0.40	0.98	0.01	4.35	0.34	32.93	0.02	2.79	0.00	0.01	100.38
121 DGR-034 chondrule 3 cpx 1	-27.986	-33.886	51.10	3.90	2.82	0.89	0.05	2.62	0.25	18.65	0.03	19.57	0.01	0.00	99.88
122 DGR-034 chondrule 3 cpx 2	-27.963	-33.883	52.80	3.65	0.81	1.21	0.03	2.59	0.26	20.94	0.00	17.03	0.02	0.01	99.34
123 DGR-034 chondrule 3 cpx 3	-27.948	-33.918	52.49	3.98	1.13	0.98	0.02	3.27	0.31	20.73	0.01	17.11	0.09	0.00	100.11
124 DGR-034 chondrule 4 opx 1	-17.534	-32.551	49.84	0.81	0.04	0.83	0.03	22.28	0.25	18.90	0.02	1.30	0.04	0.00	94.36
125 DGR-034 chondrule 4 opx 2	-17.551	-32.534	50.04	1.15	0.08	1.02	0.03	23.74	0.29	17.84	0.00	2.27	0.06	0.00	96.53
126 DGR-034 chondrule 4 opx 3	-17.676	-32.539	50.91	1.31	0.15	1.00	0.01	25.05	0.35	17.00	0.02	3.99	0.09	0.00	99.87
127 DGR-034 chondrule 4 cpx 1	-17.513	-32.554	48.85	3.37	0.53	1.40	0.03	13.94	0.19	11.67	0.02	18.57	0.50	0.00	99.06
128 DGR-034 chondrule 4 cpx 2	-18.209	-32.414	47.15	2.88	0.29	1.00	0.02	12.64	0.20	11.96	0.00	15.46	0.39	0.01	92.00
129 DGR-034 chondrule 4 cpx 3	-18.262	-32.292	50.23	2.33	0.40	1.15	0.04	13.88	0.18	12.08	0.01	19.07	0.40	0.00	99.77
130 DGR-035 matrix 2 cpx 1	27.640	-31.517	54.02	0.03	0.01	0.03	0.01	4.45	0.06	16.10	0.07	25.31	0.02	0.00	100.12
131 DGR-035 matrix 2 cpx 2	27.602	-31.536	54.59	0.05	0.00	0.00	0.00	6.20	0.03	14.56	0.02	24.62	0.05	0.01	100.13
132 DGR-035 matrix 2 cpx 3	27.589	-31.549	53.02	0.36	0.09	0.00	0.01	8.16	0.06	13.76	0.02	23.87	0.17	0.01	99.51
133 DGR-035 matrix 2 cpx 4	27.588	-31.570	52.73	0.44	0.07	0.00	0.01	8.58	0.05	14.71	0.04	22.25	0.26	0.01	99.16
134 DGR-035 matrix 2 cpx 5	27.574	-31.564	45.74	0.91	0.03	0.01	0.00	10.49	0.07	12.49	0.13	18.46	0.35	0.00	88.68
135 DGR-035 chondrule 5 opx 1	21.932	-29.772	58.94	1.30	0.30	0.50	0.00	0.46	0.05	38.39	0.01	0.58	0.00	0.00	100.53
136 DGR-035 chondrule 5 opx 2	22.022	-29.839	55.61	1.20	0.25	0.46	0.02	1.01	0.07	36.21	0.02	0.55	0.00	0.01	95.41
137 DGR-035 chondrule 5 opx 3	22.029	-29.873	58.65	1.47	0.31	0.46	0.04	1.13	0.05	38.32	0.04	0.50	0.01	0.00	100.99
138 DGR-034 chondrule 6 opx 1	-28.428	-37.356	57.25	4.82	0.66	0.56	0.09	0.54	0.07	37.04	0.02	0.41	0.02	0.00	101.50
139 DGR-034 chondrule 6 opx 2	-28.446	-37.357	55.91	5.88	0.58	0.55	0.07	0.91	0.08	36.05	0.03	1.02	0.04	0.00	101.12
140 DGR-034 chondrule 6 opx 3	-28.455	-37.342	54.46	8.56	0.87	0.63	0.10	0.32	0.07	35.27	0.02	0.91	0.00	0.00	101.19
141 DGR-034 chondrule 6 opx 4	-28.569	-37.220	52.52	11.15	1.10	0.83	0.02	0.74	0.12	33.32	0.01	1.02	0.03	0.01	100.87
142 DGR-034 chondrule 6 opx 5	-28.603	-37.221	53.62	9.98	0.95	0.66	0.06	0.41	0.09	34.52	0.01	1.01	0.00	0.01	101.33
143 DGR-034 chondrule 6 opx 6	-28.627	-37.230	55.33	7.19	0.68	0.64	0.05	0.38	0.11	35.63	0.02	0.90	0.00	0.01	100.94

Figure 111: Pyroxene point results in weight percent oxide from EPMA. Results highlighted were not used due to error.

sigma_relative = Sqrt((I_unk,peak/t_peak + I_unk,bkg/t_bkg)/curr)/I_unk,net

1-sigma relative precision based on Poisson distribution

		Si	Al	Ti	Cr	V	Fe	Mn	Mg	Ni	Ca	Na	K
84	DGR-035 chondrule 1 cpx 1	0.0035	0.0081	0.0242	0.0254	0.3950	0.0163	3.0989	0.0053	1.3728	0.0037	0.0000	0.0000
85	DGR-035 chondrule 1 cpx 2	0.0035	0.0083	0.0254	0.0264	0.2932	0.0155	0.8829	0.0052	0.0000	0.0038	0.4559	1.0698
86	DGR-035 chondrule 1 cpx 3	0.0035	0.0068	0.0228	0.0233	0.3014	0.0142	0.2288	0.0051	0.3049	0.0040	0.4947	0.6906
87	DGR-035 chondrule 1 cpx 4	0.0035	0.0085	0.0271	0.0267	0.2751	0.0161	0.3420	0.0052	1.3753	0.0038	1.2393	0.5362
88	DGR-035 chondrule 1 opx 1	0.0036	0.0049	0.0246	0.0224	0.3114	0.0108	0.3323	0.0041	0.4425	0.0142	0.9914	1.4409
89	DGR-035 chondrule 1 opx 2	0.0036	0.0052	0.0260	0.0225	0.8615	0.0108	0.2108	0.0041	0.5619	0.0139	0.5625	0.0000
90	DGR-035 chondrule 1 opx 3	0.0037	0.0049	0.0252	0.0217	0.4165	0.0110	0.2342	0.0041	1.3228	0.0148	4.9572	0.4352
91	DGR-035 chondrule 1 opx 4	0.0036	0.0052	0.0242	0.0216	0.2680	0.0108	0.2610	0.0041	0.6503	0.0135	0.0000	1.4493
92	DGR-035 chondrule 1 cpx 5	0.0035	0.0080	0.0230	0.0252	0.2512	0.0140	0.3131	0.0052	0.5931	0.0039	0.5161	1.1110
93	DGR-035 chondrule 1 opx 5	0.0034	0.0117	0.0466	0.0268	0.2811	0.0111	0.1189	0.0042	0.4227	0.0062	0.4501	7.4219
94	DGR-035 chondrule 1 cpx 6	0.0037	0.0049	0.0155	0.0302	0.7694	0.0148	0.2336	0.0058	0.5900	0.0037	4.9907	0.0000
95	DGR-035 chondrule 1 cpx 7	0.0036	0.0054	0.0133	0.0207	0.2019	0.0132	0.1742	0.0052	0.3035	0.0043	1.0020	0.0000
96	DGR-035 chondrule 3 cpx 1	0.0034	0.0081	0.0159	0.0328	0.5335	0.0335	0.0984	0.0052	0.5871	0.0038	0.9914	1.8596
97	DGR-035 chondrule 3 cpx 2	0.0034	0.0084	0.0161	0.0315	0.7418	0.0298	0.0915	0.0050	0.3417	0.0039	0.3486	1.3149
98	DGR-035 chondrule 3 cpx 3	0.0034	0.0112	0.0278	0.0313	0.0000	0.0283	0.0581	0.0039	0.0000	0.0068	0.3736	2.5000
99	DGR-035 chondrule 3 cpx 4	0.0034	0.0108	0.0248	0.0302	0.4060	0.0288	0.0647	0.0039	1.5853	0.0069	1.3090	0.0000
100	DGR-035 matrix 1 cpx 1	0.0033	0.4177	0.0000	2.6378	0.7649	0.0090	0.3057	0.0061	1.0636	0.0034	0.3884	0.0000
101	DGR-035 matrix 1 cpx 2	0.0034	0.6042	0.0000	0.4404	0.0000	0.0072	0.1685	0.0068	0.4523	0.0034	0.5579	0.0000
102	DGR-035 matrix 1 cpx 3	0.0034	0.0280	0.9339	1.7497	0.0000	0.0077	0.1292	0.0061	0.2614	0.0037	0.0373	0.0000
103	DGR-035 matrix 1 cpx 4	0.0034	1.7553	0.7339	0.0000	0.6274	0.0099	0.1558	0.0061	4.0933	0.0035	1.2429	0.0000
104	DGR-035 CAI 1 opx 1	0.0035	0.0080	0.1223	0.3589	0.0000	0.0061	0.0881	0.0044	0.1955	0.0299	0.3933	0.0000
105	DGR-035 CAI 1 opx 2	0.0035	0.0079	0.2115	0.6621	0.6024	0.0059	0.0830	0.0044	0.2055	0.0416	0.3028	0.7583
106	DGR-034 chondrule 1 opx 1	0.0033	0.0184	0.0715	0.0325	1.4449	0.0343	0.0566	0.0036	0.5562	0.0193	0.8342	0.5116
107	DGR-034 chondrule 1 opx 2	0.0033	0.0141	0.0828	0.0315	0.0000	0.0300	0.0562	0.0037	1.1196	0.0141	0.1831	1.4285
108	DGR-034 chondrule 1 opx 3	0.0033	0.0206	0.0885	0.0320	2.1088	0.0228	0.1031	0.0036	0.9557	0.0336	0.9875	0.0000
109	DGR-034 chondrule 1 opx 4	0.0033	0.0196	0.1397	0.0317	0.9930	0.0188	0.0884	0.0036	0.5979	0.0229	0.4354	0.0000
110	DGR-034 CAI 1 cpx 1	0.0034	0.0108	0.0889	0.1313	1.0313	0.0452	0.1696	0.0054	0.0767	0.0035	0.3679	0.6629
111	DGR-034 CAI 1 cpx 2	0.0034	0.0089	0.1572	0.1095	0.3234	0.0277	0.8926	0.0055	0.5207	0.0034	0.1618	0.0000
112	DGR-034 CAI 1 cpx 3	0.0034	0.0103	0.1160	0.2297	0.4168	0.0356	0.1849	0.0054	0.2153	0.0034	0.3736	3.8999
113	DGR-034 CAI 1 cpx 4	0.0036	0.0245	0.3378	0.0000	0.5500	0.0042	0.0494	0.0675	0.1654	0.0036	0.1983	0.9499
114	DGR-034 CAI 1 cpx 5	0.0036	0.0529	0.3210	1.0955	0.4568	0.0042	0.0496	0.1130	0.2599	0.0036	0.2098	0.5449
115	DGR-034 chondrule 3 opx 1	0.0034	0.0110	0.0701	0.0258	0.0000	0.0169	0.0923	0.0037	0.8699	0.0139	0.7023	0.0000
116	DGR-034 chondrule 3 opx 2	0.0033	0.0140	0.0830	0.0291	0.6145	0.0161	0.1121	0.0037	0.3115	0.0159	0.9899	1.4933
117	DGR-034 chondrule 3 opx 3	0.0034	0.0135	0.0915	0.0289	0.3607	0.0141	0.0770	0.0038	0.7801	0.0141	0.0000	0.7803
118	DGR-034 chondrule 3 opx 4	0.0034	0.0190	0.0455	0.0368	1.0308	0.0101	0.0429	0.0040	0.2666	0.0085	0.0000	1.4978
119	DGR-034 chondrule 3 opx 5	0.0034	0.0162	0.0488	0.0306	1.0680	0.0110	0.0484	0.0040	0.4944	0.0088	0.0000	0.0000
120	DGR-034 chondrule 3 opx 6	0.0034	0.0130	0.0432	0.0287	1.0313	0.0113	0.0515	0.0039	0.4129	0.0107	5.0852	0.9119
121	DGR-034 chondrule 3 cpx 1	0.0035	0.0086	0.0115	0.0305	0.2926	0.0150	0.0636	0.0053	0.3609	0.0039	0.8475	0.0000
122	DGR-034 chondrule 3 cpx 2	0.0034	0.0090	0.0257	0.0254	0.4095	0.0153	0.0631	0.0050	8.2321	0.0042	0.5167	0.6975
123	DGR-034 chondrule 3 cpx 3	0.0034	0.0086	0.0206	0.0288	0.8665	0.0133	0.0553	0.0050	1.1753	0.0041	0.1114	2.6218
124	DGR-034 chondrule 4 opx 1	0.0036	0.0226	0.3501	0.0299	0.4557	0.0048	0.0634	0.0055	0.4620	0.0162	0.2443	0.0000
125	DGR-034 chondrule 4 opx 2	0.0036	0.0180	0.1859	0.0267	0.5386	0.0046	0.0565	0.0057	4.2603	0.0118	0.1866	0.0000
126	DGR-034 chondrule 4 opx 3	0.0035	0.0165	0.1038	0.0271	0.9644	0.0045	0.0488	0.0059	0.6214	0.0087	0.1336	0.0000
127	DGR-034 chondrule 4 cpx 1	0.0036	0.0094	0.0355	0.0231	0.4288	0.0061	0.0798	0.0070	0.4803	0.0039	0.0335	2.6123
128	DGR-034 chondrule 4 cpx 2	0.0036	0.0103	0.0571	0.0277	0.5523	0.0064	0.0764	0.0069	0.0000	0.0043	0.0396	1.1242
129	DGR-034 chondrule 4 cpx 3	0.0035	0.0115	0.0438	0.0256	0.3546	0.0061	0.0825	0.0069	0.6643	0.0039	0.0389	0.0000
130	DGR-035 matrix 2 cpx 1	0.0033	0.2966	0.9297	0.5072	1.4930	0.0112	0.2213	0.0058	0.1269	0.0034	0.5145	2.5659
131	DGR-035 matrix 2 cpx 2	0.0033	0.2202	0.0000	0.0000	0.0000	0.0094	0.4091	0.0061	0.4026	0.0034	0.2090	0.7228
132	DGR-035 matrix 2 cpx 3	0.0034	0.0385	0.1671	0.0000	1.4261	0.0081	0.2236	0.0063	0.4307	0.0035	0.0743	0.6505
133	DGR-035 matrix 2 cpx 4	0.0034	0.0332	0.2026	0.0000	2.3220	0.0079	0.2649	0.0061	0.2149	0.0036	0.0512	0.4462
134	DGR-035 matrix 2 cpx 5	0.0037	0.0199	0.5359	1.3367	0.0000	0.0071	0.1851	0.0067	0.0773	0.0040	0.0417	1.3125
135	DGR-035 chondrule 5 opx 1	0.0033	0.0166	0.0541	0.0434	4.0994	0.0450	0.2354	0.0036	0.9624	0.0264	0.0000	0.0000
136	DGR-035 chondrule 5 opx 2	0.0034	0.0175	0.0621	0.0447	0.6780	0.0264	0.1780	0.0037	0.4738	0.0277	5.1064	0.7748
137	DGR-035 chondrule 5 opx 3	0.0033	0.0154	0.0515	0.0448	0.3692	0.0242	0.2281	0.0036	0.2112	0.0294	1.0015	1.7996
138	DGR-034 chondrule 6 opx 1	0.0034	0.0079	0.0292	0.0396	0.1795	0.0407	0.1671	0.0036	0.3889	0.0331	0.4194	0.0000
139	DGR-034 chondrule 6 opx 2	0.0034	0.0071	0.0324	0.0405	0.2004	0.0282	0.1658	0.0037	0.2709	0.0189	0.2112	3.5974
140	DGR-034 chondrule 6 opx 3	0.0035	0.0058	0.0240	0.0368	0.1599	0.0601	0.1811	0.0037	0.4079	0.0202	0.0000	0.0000
141	DGR-034 chondrule 6 opx 4	0.0036	0.0051	0.0204	0.0315	0.7323	0.0328	0.1095	0.0038	0.9851	0.0188	0.2941	0.5115
142	DGR-034 chondrule 6 opx 5	0.0035	0.0054	0.0226	0.0365	0.2456	0.0487	0.1375	0.0038	1.0983	0.0190	0.0000	0.8000
143	DGR-034 chondrule 6 opx 6	0.0035	0.0064	0.0287	0.0367	0.2531	0.0520	0.1203	0.0037	0.4253	0.0203	4.8894	0.7234

Figure 112: Pyroxene point precision results from EPMA. Results highlighted were not used due to error.

LLD(3-sigma) = 3*ZAF*(C_std/I_std,net)*Sqrt(2)*Sqrt(I_unk,bkg /(t_unk,bkg*curr_unk))

3-sigma lower limit of detection (wt% oxide)

		SiO2	Al2O3	TiO2	Cr2O3	V2O3	FeO	MnO	MgO	NiO	CaO	Na2O	K2O
84	DGR-035 chondrule 1 cpx 1	0.0639	0.0287	0.0411	0.0376	0.0425	0.0463	0.0366	0.0409	0.0268	0.0269	0.0285	0.0183
85	DGR-035 chondrule 1 cpx 2	0.0622	0.0288	0.0406	0.0396	0.0409	0.0449	0.0359	0.0421	0.0271	0.0279	0.0268	0.0172
86	DGR-035 chondrule 1 cpx 3	0.0631	0.0293	0.0406	0.0387	0.0421	0.0455	0.0333	0.0424	0.0264	0.0285	0.0264	0.0174
87	DGR-035 chondrule 1 cpx 4	0.0623	0.0302	0.0417	0.0390	0.0431	0.0471	0.0344	0.0436	0.0269	0.0283	0.0270	0.0170
88	DGR-035 chondrule 1 opx 1	0.0643	0.0311	0.0394	0.0360	0.0373	0.0439	0.0349	0.0470	0.0256	0.0253	0.0257	0.0172
89	DGR-035 chondrule 1 opx 2	0.0624	0.0303	0.0393	0.0366	0.0393	0.0426	0.0324	0.0455	0.0254	0.0265	0.0260	0.0177
90	DGR-035 chondrule 1 opx 3	0.0639	0.0301	0.0394	0.0358	0.0404	0.0435	0.0326	0.0442	0.0257	0.0256	0.0260	0.0172
91	DGR-035 chondrule 1 opx 4	0.0615	0.0305	0.0394	0.0360	0.0384	0.0450	0.0340	0.0475	0.0252	0.0254	0.0267	0.0173
92	DGR-035 chondrule 1 cpx 5	0.0620	0.0292	0.0403	0.0405	0.0408	0.0439	0.0348	0.0452	0.0269	0.0279	0.0278	0.0179
93	DGR-035 chondrule 1 opx 5	0.0600	0.0289	0.0398	0.0358	0.0384	0.0441	0.0333	0.0460	0.0259	0.0262	0.0257	0.0178
94	DGR-035 chondrule 1 cpx 6	0.0617	0.0300	0.0409	0.0345	0.0427	0.0445	0.0356	0.0429	0.0268	0.0277	0.0276	0.0177
95	DGR-035 chondrule 1 cpx 7	0.0615	0.0305	0.0407	0.0372	0.0420	0.0449	0.0369	0.0421	0.0263	0.0290	0.0273	0.0178
96	DGR-035 chondrule 3 cpx 1	0.0609	0.0294	0.0401	0.0379	0.0390	0.0447	0.0333	0.0436	0.0266	0.0279	0.0266	0.0173
97	DGR-035 chondrule 3 cpx 2	0.0609	0.0292	0.0403	0.0374	0.0413	0.0439	0.0346	0.0414	0.0264	0.0275	0.0272	0.0183
98	DGR-035 chondrule 3 cpx 3	0.0639	0.0288	0.0392	0.0371	0.0414	0.0431	0.0314	0.0437	0.0260	0.0262	0.0259	0.0180
99	DGR-035 chondrule 3 cpx 4	0.0600	0.0290	0.0382	0.0366	0.0359	0.0457	0.0344	0.0473	0.0257	0.0265	0.0267	0.0180
100	DGR-035 matrix 1 cpx 1	0.0610	0.0287	0.0425	0.0402	0.0423	0.0480	0.0356	0.0427	0.0278	0.0291	0.0281	0.0184
101	DGR-035 matrix 1 cpx 2	0.0611	0.0279	0.0425	0.0347	0.0425	0.0474	0.0361	0.0421	0.0278	0.0286	0.0292	0.0189
102	DGR-035 matrix 1 cpx 3	0.0610	0.0293	0.0408	0.0394	0.0420	0.0470	0.0350	0.0430	0.0277	0.0287	0.0291	0.0187
103	DGR-035 matrix 1 cpx 4	0.0592	0.0288	0.0403	0.0380	0.0402	0.0445	0.0347	0.0433	0.0268	0.0272	0.0282	0.0182
104	DGR-035 CAI 1 opx 1	0.0623	0.0311	0.0387	0.0371	0.0389	0.0444	0.0342	0.0477	0.0267	0.0264	0.0280	0.0182
105	DGR-035 CAI 1 opx 2	0.0680	0.0308	0.0402	0.0375	0.0368	0.0460	0.0335	0.0475	0.0268	0.0263	0.0279	0.0178
106	DGR-034 chondrule 1 opx 1	0.0623	0.0285	0.0381	0.0366	0.0407	0.0427	0.0324	0.0457	0.0250	0.0258	0.0247	0.0170
107	DGR-034 chondrule 1 opx 2	0.0622	0.0304	0.0396	0.0392	0.0413	0.0438	0.0330	0.0446	0.0253	0.0257	0.0254	0.0172
108	DGR-034 chondrule 1 opx 3	0.0632	0.0289	0.0381	0.0342	0.0398	0.0424	0.0324	0.0479	0.0247	0.0254	0.0245	0.0171
109	DGR-034 chondrule 1 opx 4	0.0617	0.0283	0.0393	0.0356	0.0367	0.0451	0.0336	0.0469	0.0250	0.0251	0.0256	0.0175
110	DGR-034 CAI 1 cpx 1	0.0618	0.0286	0.0418	0.0391	0.0388	0.0468	0.0359	0.0420	0.0264	0.0275	0.0269	0.0181
111	DGR-034 CAI 1 cpx 2	0.0625	0.0287	0.0405	0.0370	0.0400	0.0465	0.0365	0.0416	0.0270	0.0281	0.0264	0.0180
112	DGR-034 CAI 1 cpx 3	0.0607	0.0299	0.0397	0.0404	0.0415	0.0450	0.0322	0.0429	0.0267	0.0276	0.0274	0.0181
113	DGR-034 CAI 1 cpx 4	0.0639	0.0309	0.0429	0.0417	0.0427	0.0512	0.0370	0.0399	0.0296	0.0303	0.0341	0.0189
114	DGR-034 CAI 1 cpx 5	0.0632	0.0307	0.0429	0.0385	0.0429	0.0508	0.0374	0.0408	0.0297	0.0302	0.0336	0.0190
115	DGR-034 chondrule 3 opx 1	0.0621	0.0281	0.0398	0.0387	0.0429	0.0444	0.0320	0.0478	0.0253	0.0255	0.0246	0.0179
116	DGR-034 chondrule 3 opx 2	0.0622	0.0289	0.0389	0.0379	0.0390	0.0442	0.0332	0.0478	0.0248	0.0257	0.0249	0.0180
117	DGR-034 chondrule 3 opx 3	0.0625	0.0284	0.0393	0.0366	0.0378	0.0425	0.0327	0.0472	0.0252	0.0254	0.0252	0.0167
118	DGR-034 chondrule 3 opx 4	0.0631	0.0295	0.0380	0.0374	0.0379	0.0439	0.0327	0.0489	0.0255	0.0265	0.0266	0.0179
119	DGR-034 chondrule 3 opx 5	0.0630	0.0298	0.0400	0.0359	0.0394	0.0453	0.0343	0.0497	0.0255	0.0253	0.0282	0.0180
120	DGR-034 chondrule 3 opx 6	0.0617	0.0289	0.0393	0.0384	0.0380	0.0433	0.0349	0.0465	0.0252	0.0254	0.0268	0.0173
121	DGR-034 chondrule 3 cpx 1	0.0604	0.0285	0.0401	0.0386	0.0378	0.0451	0.0332	0.0446	0.0267	0.0293	0.0278	0.0183
122	DGR-034 chondrule 3 cpx 2	0.0620	0.0293	0.0408	0.0383	0.0362	0.0473	0.0354	0.0444	0.0269	0.0281	0.0275	0.0176
123	DGR-034 chondrule 3 cpx 3	0.0615	0.0294	0.0415	0.0379	0.0401	0.0447	0.0354	0.0431	0.0268	0.0272	0.0263	0.0184
124	DGR-034 chondrule 4 opx 1	0.0645	0.0311	0.0404	0.0340	0.0384	0.0457	0.0344	0.0474	0.0268	0.0268	0.0301	0.0188
125	DGR-034 chondrule 4 opx 2	0.0639	0.0306	0.0404	0.0354	0.0413	0.0455	0.0348	0.0460	0.0278	0.0266	0.0327	0.0190
126	DGR-034 chondrule 4 opx 3	0.0639	0.0302	0.0409	0.0361	0.0420	0.0478	0.0341	0.0472	0.0281	0.0267	0.0309	0.0194
127	DGR-034 chondrule 4 cpx 1	0.0662	0.0302	0.0421	0.0396	0.0412	0.0478	0.0343	0.0413	0.0279	0.0282	0.0313	0.0179
128	DGR-034 chondrule 4 cpx 2	0.0630	0.0307	0.0410	0.0361	0.0391	0.0481	0.0342	0.0415	0.0277	0.0269	0.0314	0.0180
129	DGR-034 chondrule 4 cpx 3	0.0632	0.0296	0.0411	0.0363	0.0397	0.0478	0.0353	0.0435	0.0280	0.0285	0.0312	0.0184
130	DGR-035 matrix 2 cpx 1	0.0603	0.0288	0.0411	0.0374	0.0423	0.0461	0.0347	0.0441	0.0270	0.0286	0.0284	0.0177
131	DGR-035 matrix 2 cpx 2	0.0629	0.0294	0.0432	0.0395	0.0418	0.0470	0.0370	0.0426	0.0273	0.0300	0.0302	0.0180
132	DGR-035 matrix 2 cpx 3	0.0628	0.0290	0.0410	0.0387	0.0399	0.0484	0.0349	0.0416	0.0279	0.0292	0.0298	0.0176
133	DGR-035 matrix 2 cpx 4	0.0634	0.0294	0.0410	0.0384	0.0437	0.0472	0.0362	0.0428	0.0274	0.0276	0.0295	0.0179
134	DGR-035 matrix 2 cpx 5	0.0586	0.0277	0.0404	0.0396	0.0433	0.0490	0.0339	0.0415	0.0272	0.0288	0.0289	0.0180
135	DGR-035 chondrule 5 opx 1	0.0603	0.0290	0.0388	0.0364	0.0390	0.0419	0.0331	0.0473	0.0248	0.0239	0.0260	0.0174
136	DGR-035 chondrule 5 opx 2	0.0606	0.0295	0.0394	0.0340	0.0371	0.0427	0.0315	0.0450	0.0243	0.0248	0.0256	0.0167
137	DGR-035 chondrule 5 opx 3	0.0614	0.0290	0.0381	0.0338	0.0356	0.0402	0.0332	0.0480	0.0246	0.0246	0.0248	0.0175
138	DGR-034 chondrule 6 opx 1	0.0628	0.0295	0.0391	0.0347	0.0393	0.0440	0.0320	0.0464	0.0248	0.0237	0.0242	0.0178
139	DGR-034 chondrule 6 opx 2	0.0608	0.0295	0.0395	0.0353	0.0377	0.0426	0.0336	0.0455	0.0249	0.0253	0.0256	0.0175
140	DGR-034 chondrule 6 opx 3	0.0612	0.0305	0.0387	0.0338	0.0378	0.0432	0.0333	0.0450	0.0247	0.0247	0.0259	0.0176
141	DGR-034 chondrule 6 opx 4	0.0627	0.0300	0.0381	0.0367	0.0403	0.0443	0.0328	0.0449	0.0254	0.0254	0.0253	0.0169
142	DGR-034 chondrule 6 opx 5	0.0606	0.0301	0.0391	0.0370	0.0395	0.0423	0.0309	0.0454	0.0247	0.0252	0.0254	0.0173
143	DGR-034 chondrule 6 opx 6	0.0635	0.0300	0.0388	0.0356	0.0362	0.0429	0.0325	0.0449	0.0244	0.0245	0.0244	0.0173

Figure 113: Pyroxene limit of detection point results from EPMA. Results highlighted were not used due to error.

Results_of_analyses:

	coordinates in mm		oxide weight %											
	X	Y	SiO2	Al2O3	TiO2	Cr2O3	V2O3	FeO	MnO	MgO	CaO	Na2O	K2O	Total
144 DGR-035 chondrule 2 plagioclase 1	23.980	-35.559	59.36	25.73	0.03	0.00	0.00	0.39	0.00	0.01	6.96	7.73	0.22	100.44
145 DGR-035 chondrule 2 plagioclase 2	23.948	-35.553	61.81	23.57	0.04	0.00	0.00	0.45	0.03	0.12	4.84	8.62	0.38	99.84
146 DGR-035 chondrule 2 plagioclase 3	23.719	-35.262	59.81	25.41	0.00	0.00	0.02	0.42	0.00	0.02	6.68	7.52	0.23	100.11
147 DGR-035 chondrule 2 plagioclase 4	24.062	-35.654	60.34	24.75	0.04	0.04	0.01	0.67	0.00	0.21	6.13	7.94	0.24	100.37
148 DGR-035 chondrule 2 plagioclase 5	23.833	-35.700	59.58	25.50	0.02	0.00	0.00	0.46	0.01	0.13	6.68	7.54	0.23	100.14
149 DGR-035 chondrule 3 plagioclase 1	35.404	-40.518	61.80	24.19	0.00	0.00	0.03	0.32	0.00	0.06	5.22	8.53	0.29	100.44
150 DGR-035 chondrule 3 plagioclase 2	35.393	-40.460	63.34	23.45	0.02	0.00	0.01	0.31	0.02	0.07	4.23	9.16	0.34	100.94
151 DGR-035 chondrule 3 plagioclase 3	35.326	-40.450	62.75	23.42	0.00	0.00	0.00	0.33	0.01	0.05	4.30	9.03	0.37	100.27
152 DGR-035 chondrule 3 plagioclase 4	35.524	-40.576	44.99	35.28	0.01	0.01	0.02	0.34	0.00	0.00	18.34	1.06	0.01	100.05
153 DGR-035 chondrule 3 plagioclase 5	35.837	-40.518	43.91	36.22	0.00	0.01	0.01	0.32	0.01	0.00	18.91	0.74	0.00	100.15
154 DGR-035 chondrule 3 plagioclase 6	35.811	-40.241	61.54	24.28	0.01	0.05	0.00	0.29	0.01	0.24	5.37	8.50	0.33	100.61
155 DGR-035 matrix 1 plagioclase 1	22.444	-40.220	61.34	24.26	0.00	0.00	0.01	0.34	0.00	0.00	5.21	8.58	0.27	100.01
156 DGR-035 matrix 1 plagioclase 2	22.742	-40.456	58.37	26.52	0.01	0.04	0.01	0.53	0.00	0.00	7.87	7.14	0.15	100.63
157 DGR-035 matrix 1 plagioclase 3	22.979	-40.301	59.58	25.63	0.01	0.01	0.00	0.42	0.00	0.01	7.04	7.52	0.20	100.42
158 DGR-035 matrix 1 plagioclase 4	22.625	-40.298	61.34	24.05	0.01	0.02	0.00	0.90	0.00	0.02	5.16	8.53	0.28	100.31
159 DGR-035 CAI 1 plagioclase 1	13.468	-32.778	45.02	35.33	0.00	0.03	0.00	0.30	0.01	0.12	18.44	1.03	0.01	100.30
160 DGR-035 CAI 1 plagioclase 2	13.440	-32.780	58.46	26.07	0.01	0.01	0.00	0.22	0.00	0.09	7.63	7.18	0.16	99.83
161 DGR-035 CAI 1 plagioclase 3	13.520	-32.777	44.69	35.63	0.00	0.00	0.01	0.14	0.00	0.01	18.82	0.89	0.01	100.22
162 DGR-035 CAI 1 plagioclase 4	13.562	-32.774	51.52	30.98	0.00	0.01	0.00	0.20	0.01	0.01	13.12	4.22	0.06	100.12
163 DGR-035 CAI 1 plagioclase 5	13.559	-32.706	61.11	25.07	0.02	0.01	0.00	0.23	0.00	0.01	6.12	7.97	0.25	100.79
164 DGR-035 CAI 1 gehlenite 1 (actually grossular)	13.448	-33.196	39.31	20.95	0.00	0.00	0.00	2.33	0.06	0.06	36.69	0.02	0.00	99.41
165 DGR-034 chondrule 1 plagioclase 1	-29.806	-40.288	46.42	33.01	0.01	0.02	0.00	0.89	0.02	0.66	17.16	1.79	0.00	99.99
166 DGR-034 chondrule 1 plagioclase 2	-29.873	-40.263	46.14	33.80	0.03	0.02	0.00	0.35	0.00	0.54	17.57	1.59	0.01	100.05
167 DGR-034 CAI 1 plagioclase 1	-29.053	-35.492	42.25	36.86	0.01	0.01	0.02	0.20	0.00	0.01	19.50	0.15	0.00	99.02
168 DGR-034 CAI 1 plagioclase 2	-29.090	-35.418	42.23	37.39	0.02	0.00	0.00	0.21	0.00	0.01	19.88	0.06	0.00	99.81
169 DGR-034 CAI 1 plagioclase 3	-29.080	-35.389	42.22	36.98	0.00	0.00	0.00	0.19	0.00	0.04	19.78	0.08	0.02	99.32
170 DGR-034 chondrule 3 plagioclase 1	-27.823	-33.999	45.46	33.87	0.01	0.00	0.01	0.89	0.00	0.52	18.11	1.32	0.00	100.18
171 DGR-034 chondrule 3 plagioclase 2	-27.813	-33.985	45.07	34.05	0.04	0.00	0.00	0.78	0.01	0.49	18.16	1.28	0.00	99.88
172 DGR-034 chondrule 5 plagioclase 1	-12.765	-30.067	47.12	32.52	0.02	0.02	0.04	0.85	0.02	0.33	16.63	2.13	0.01	99.69
173 DGR-034 chondrule 5 plagioclase 2	-12.786	-30.054	45.87	33.07	0.01	0.03	0.00	0.92	0.02	0.30	17.12	1.82	0.00	99.16
174 DGR-034 chondrule 5 plagioclase 3	-12.841	-30.141	46.70	32.73	0.02	0.03	0.01	0.88	0.00	0.34	16.99	1.96	0.00	99.66
175 DGR-034 chondrule 5 plagioclase 4	-12.869	-30.130	46.58	32.66	0.01	0.04	0.00	0.92	0.02	0.45	16.96	1.90	0.00	99.52
176 DGR-034 chondrule 5 plagioclase 5	-12.927	-30.179	47.07	32.11	0.01	0.00	0.00	1.28	0.02	0.27	16.55	2.12	0.00	99.44
177 DGR-035 matrix 2 plagioclase 1	28.558	-30.602	61.34	24.78	0.01	0.02	0.00	0.32	0.01	0.06	5.65	8.35	0.26	100.79
178 DGR-035 matrix 2 plagioclase 2	28.565	-30.637	61.43	24.59	0.00	0.00	0.01	0.31	0.00	0.03	5.94	8.23	0.24	100.78
179 DGR-035 matrix 2 plagioclase 3	28.577	-30.650	58.51	26.94	0.00	0.01	0.00	0.49	0.00	0.04	8.14	7.08	0.16	101.36
180 DGR-035 matrix 2 plagioclase 4	28.580	-30.578	57.45	27.04	0.00	0.00	0.00	0.23	0.00	0.00	8.86	6.70	0.15	100.44
181 DGR-035 matrix 2 plagioclase 5	28.397	-30.511	60.93	24.69	0.03	0.01	0.00	0.24	0.00	0.08	5.92	8.23	0.23	100.38
182 DGR-035 matrix 2 plagioclase 6	28.390	-30.539	60.30	25.10	0.00	0.03	0.00	0.60	0.01	0.07	6.04	8.03	0.27	100.45
183 DGR-035 matrix 2 plagioclase 7	28.383	-30.546	58.46	26.63	0.00	0.00	0.01	0.51	0.00	0.01	7.95	7.05	0.16	100.77
184 DGR-034 chondrule 6 plagioclase 1	-28.587	-37.309	47.46	32.71	0.02	0.04	0.00	0.76	0.00	0.30	16.22	2.30	0.01	99.83
185 DGR-034 chondrule 6 plagioclase 2	-28.530	-37.337	47.39	32.97	0.04	0.03	0.01	0.80	0.01	0.35	16.17	2.24	0.01	100.02
186 DGR-034 chondrule 6 plagioclase 3	-28.743	-37.424	47.13	32.09	0.05	0.03	0.00	0.88	0.00	0.34	16.28	2.38	0.01	99.18
187 DGR-034 chondrule 6 plagioclase 4	-28.556	-37.449	47.87	32.58	0.03	0.03	0.00	0.85	0.01	0.37	16.10	2.36	0.00	100.20

Figure 114: Plagioclase point results in weight percent oxide from EPMA. Results highlighted were not used due to error.

sigma_relative = Sqrt((I_unk,peak/t_peak + I_unk,bkg/t_bkg)/curr)/I_unk,net

1-sigma relative precision based on Poisson distribution

		Si	Al	Ti	Cr	V	Fe	Mn	Mg	Ca	Na	K
144	DGR-035 chondrule 2 plagioclase 1	0.0033	0.0053	0.4424	0.0000	0.0000	0.0299	0.0000	1.5462	0.0081	0.0108	0.0395
145	DGR-035 chondrule 2 plagioclase 2	0.0032	0.0055	0.4334	0.0000	0.0000	0.0265	0.4972	0.0797	0.0098	0.0102	0.0280
146	DGR-035 chondrule 2 plagioclase 3	0.0033	0.0053	0.0000	0.0000	0.7997	0.0278	0.0000	0.3471	0.0083	0.0110	0.0388
147	DGR-035 chondrule 2 plagioclase 4	0.0032	0.0054	0.4113	0.3444	1.1733	0.0202	0.0000	0.0518	0.0086	0.0107	0.0379
148	DGR-035 chondrule 2 plagioclase 5	0.0033	0.0053	0.8232	0.0000	0.0000	0.0262	1.3096	0.0755	0.0082	0.0110	0.0395
149	DGR-035 chondrule 3 plagioclase 1	0.0032	0.0055	0.0000	0.0000	0.4764	0.0345	0.0000	0.1457	0.0094	0.0103	0.0336
150	DGR-035 chondrule 3 plagioclase 2	0.0032	0.0055	0.8050	0.0000	1.1733	0.0356	0.6962	0.1272	0.0105	0.0099	0.0298
151	DGR-035 chondrule 3 plagioclase 3	0.0032	0.0055	4.0663	0.0000	0.0000	0.0343	1.0670	0.1801	0.0104	0.0099	0.0280
152	DGR-035 chondrule 3 plagioclase 4	0.0038	0.0044	2.4966	1.8164	0.9597	0.0339	0.0000	0.0000	0.0049	0.0325	0.4520
153	DGR-035 chondrule 3 plagioclase 5	0.0039	0.0044	0.0000	1.1026	1.1737	0.0359	1.6558	0.0000	0.0048	0.0401	3.9054
154	DGR-035 chondrule 3 plagioclase 6	0.0032	0.0054	1.7456	0.3060	0.0000	0.0372	1.6642	0.0465	0.0092	0.0103	0.0307
155	DGR-035 matrix 1 plagioclase 1	0.0032	0.0054	2.9525	0.0000	1.5879	0.0328	6.8553	7.4528	0.0094	0.0102	0.0350
156	DGR-035 matrix 1 plagioclase 2	0.0033	0.0052	2.0659	0.3924	1.4922	0.0237	0.0000	0.0000	0.0076	0.0113	0.0531
157	DGR-035 matrix 1 plagioclase 3	0.0033	0.0053	1.7611	1.3553	0.0000	0.0281	0.0000	0.6247	0.0080	0.0110	0.0428
158	DGR-035 matrix 1 plagioclase 4	0.0032	0.0055	1.3509	0.6925	0.0000	0.0165	3.2333	0.4209	0.0094	0.0103	0.0344
159	DGR-035 CAI 1 plagioclase 1	0.0038	0.0044	0.0000	0.4239	4.7984	0.0365	1.1385	0.0803	0.0049	0.0332	0.7638
160	DGR-035 CAI 1 plagioclase 2	0.0033	0.0052	1.3766	1.3392	0.0000	0.0467	3.2483	0.1013	0.0077	0.0112	0.0506
161	DGR-035 CAI 1 plagioclase 3	0.0038	0.0044	0.0000	5.5435	1.6460	0.0703	0.0000	1.0171	0.0048	0.0361	0.4085
162	DGR-035 CAI 1 plagioclase 4	0.0035	0.0048	0.0000	1.8367	0.0000	0.0524	1.3816	1.3344	0.0058	0.0150	0.1130
163	DGR-035 CAI 1 plagioclase 5	0.0032	0.0053	0.8657	1.7550	0.0000	0.0448	0.0000	0.6237	0.0086	0.0107	0.0361
164	DGR-035 CAI 1 gehlenite 1 (actually grossular)	0.0040	0.0059	13.1280	0.0000	0.0000	0.0094	0.2577	0.1633	0.0034	0.7867	0.0000
165	DGR-034 chondrule 1 plagioclase 1	0.0037	0.0046	2.5638	0.6642	4.8700	0.0167	0.5922	0.0231	0.0051	0.0239	1.2353
166	DGR-034 chondrule 1 plagioclase 2	0.0037	0.0046	0.4778	0.8379	0.0000	0.0329	6.8665	0.0260	0.0050	0.0259	0.5862
167	DGR-034 CAI 1 plagioclase 1	0.0039	0.0043	1.0634	1.1494	0.9803	0.0500	3.3601	0.8311	0.0047	0.1312	0.0000
168	DGR-034 CAI 1 plagioclase 2	0.0039	0.0043	0.8395	0.0000	4.8693	0.0507	6.5046	1.6506	0.0047	0.2866	1.2366
169	DGR-034 CAI 1 plagioclase 3	0.0039	0.0043	0.0000	0.0000	0.0000	0.0534	0.0000	0.2115	0.0047	0.2114	0.3615
170	DGR-034 chondrule 3 plagioclase 1	0.0038	0.0046	1.4120	0.0000	1.1821	0.0168	0.0000	0.0272	0.0049	0.0286	0.0000
171	DGR-034 chondrule 3 plagioclase 2	0.0038	0.0045	0.3904	5.9187	0.0000	0.0183	2.2302	0.0283	0.0049	0.0296	0.0000
172	DGR-034 chondrule 5 plagioclase 1	0.0037	0.0047	0.9876	0.6189	0.3744	0.0172	0.5610	0.0378	0.0051	0.0218	0.4277
173	DGR-034 chondrule 5 plagioclase 2	0.0038	0.0046	1.5687	0.5805	0.0000	0.0165	0.6691	0.0389	0.0051	0.0238	1.5045
174	DGR-034 chondrule 5 plagioclase 3	0.0037	0.0046	0.7371	0.5715	2.3805	0.0170	0.0000	0.0363	0.0051	0.0227	0.0000
175	DGR-034 chondrule 5 plagioclase 4	0.0037	0.0046	1.6154	0.4041	0.0000	0.0164	0.8344	0.0300	0.0051	0.0236	0.0000
176	DGR-034 chondrule 5 plagioclase 5	0.0037	0.0047	1.1736	0.0000	0.0000	0.0133	0.6232	0.0427	0.0052	0.0221	0.0000
177	DGR-035 matrix 2 plagioclase 1	0.0032	0.0054	1.2234	0.9813	0.0000	0.0347	1.3199	0.1602	0.0090	0.0104	0.0356
178	DGR-035 matrix 2 plagioclase 2	0.0032	0.0054	0.0000	0.0000	1.1896	0.0358	0.0000	0.2518	0.0088	0.0105	0.0381
179	DGR-035 matrix 2 plagioclase 3	0.0033	0.0051	0.0000	1.3988	0.0000	0.0249	0.0000	0.2226	0.0074	0.0113	0.0502
180	DGR-035 matrix 2 plagioclase 4	0.0033	0.0051	0.0000	5.5352	0.0000	0.0460	6.5076	1.9020	0.0071	0.0117	0.0515
181	DGR-035 matrix 2 plagioclase 5	0.0032	0.0054	0.5002	1.0827	0.0000	0.0434	0.0000	0.1067	0.0088	0.0105	0.0388
182	DGR-035 matrix 2 plagioclase 6	0.0032	0.0053	0.0000	0.4461	0.0000	0.0219	0.9235	0.1313	0.0087	0.0106	0.0343
183	DGR-035 matrix 2 plagioclase 7	0.0033	0.0052	0.0000	0.0000	2.2161	0.0244	0.0000	1.0816	0.0075	0.0114	0.0501
184	DGR-034 chondrule 6 plagioclase 1	0.0037	0.0046	0.8097	0.4039	0.0000	0.0187	0.0000	0.0394	0.0052	0.0210	0.4700
185	DGR-034 chondrule 6 plagioclase 2	0.0037	0.0046	0.3715	0.5167	2.4482	0.0178	0.9150	0.0355	0.0052	0.0213	1.0619
186	DGR-034 chondrule 6 plagioclase 3	0.0037	0.0047	0.3548	0.5888	0.0000	0.0169	0.0000	0.0358	0.0052	0.0207	0.9345
187	DGR-034 chondrule 6 plagioclase 4	0.0037	0.0047	0.5081	0.4787	0.0000	0.0172	1.1194	0.0340	0.0052	0.0208	0.0000

Figure 115: Plagioclase point precision results from EPMA. Results highlighted were not used due to error.

		LLD(3-sigma) = 3*ZAF*(C_std/I_std,net)*Sqrt(2)*Sqrt(I_unk,bkg /(t_unk,bkg*curr_unk))										
		3-sigma lower limit of detection (wt% oxide)										
		SiO2	Al2O3	TiO2	Cr2O3	V2O3	FeO	MnO	MgO	CaO	Na2O	K2O
144	DGR-035 chondrule 2 plagioclase 1	0.0622	0.0537	0.0428	0.0422	0.0437	0.0247	0.0392	0.0239	0.0322	0.0569	0.0174
145	DGR-035 chondrule 2 plagioclase 2	0.0624	0.0556	0.0450	0.0445	0.0476	0.0247	0.0363	0.0229	0.0316	0.0548	0.0178
146	DGR-035 chondrule 2 plagioclase 3	0.0645	0.0556	0.0462	0.0408	0.0440	0.0247	0.0380	0.0238	0.0322	0.0562	0.0171
147	DGR-035 chondrule 2 plagioclase 4	0.0643	0.0534	0.0441	0.0387	0.0436	0.0253	0.0406	0.0239	0.0299	0.0567	0.0175
148	DGR-035 chondrule 2 plagioclase 5	0.0646	0.0538	0.0450	0.0441	0.0444	0.0246	0.0381	0.0235	0.0309	0.0559	0.0174
149	DGR-035 chondrule 3 plagioclase 1	0.0636	0.0536	0.0449	0.0434	0.0422	0.0251	0.0399	0.0237	0.0309	0.0596	0.0177
150	DGR-035 chondrule 3 plagioclase 2	0.0621	0.0552	0.0439	0.0415	0.0436	0.0251	0.0357	0.0223	0.0320	0.0562	0.0177
151	DGR-035 chondrule 3 plagioclase 3	0.0644	0.0528	0.0450	0.0439	0.0454	0.0251	0.0371	0.0232	0.0315	0.0575	0.0171
152	DGR-035 chondrule 3 plagioclase 4	0.0616	0.0568	0.0463	0.0417	0.0446	0.0259	0.0384	0.0250	0.0322	0.0462	0.0175
153	DGR-035 chondrule 3 plagioclase 5	0.0603	0.0574	0.0483	0.0417	0.0439	0.0266	0.0388	0.0252	0.0336	0.0448	0.0183
154	DGR-035 chondrule 3 plagioclase 6	0.0633	0.0552	0.0449	0.0383	0.0477	0.0246	0.0389	0.0233	0.0307	0.0555	0.0180
155	DGR-035 matrix 1 plagioclase 1	0.0636	0.0554	0.0435	0.0443	0.0447	0.0243	0.0405	0.0234	0.0307	0.0581	0.0172
156	DGR-035 matrix 1 plagioclase 2	0.0612	0.0546	0.0456	0.0423	0.0419	0.0248	0.0401	0.0241	0.0335	0.0555	0.0175
157	DGR-035 matrix 1 plagioclase 3	0.0641	0.0547	0.0453	0.0411	0.0464	0.0250	0.0394	0.0228	0.0313	0.0554	0.0168
158	DGR-035 matrix 1 plagioclase 4	0.0626	0.0549	0.0445	0.0410	0.0439	0.0247	0.0380	0.0243	0.0320	0.0586	0.0180
159	DGR-035 CAI 1 plagioclase 1	0.0648	0.0560	0.0467	0.0397	0.0460	0.0255	0.0398	0.0238	0.0341	0.0477	0.0176
160	DGR-035 CAI 1 plagioclase 2	0.0610	0.0532	0.0455	0.0406	0.0503	0.0243	0.0383	0.0233	0.0310	0.0538	0.0175
161	DGR-035 CAI 1 plagioclase 3	0.0611	0.0586	0.0479	0.0429	0.0467	0.0263	0.0367	0.0242	0.0328	0.0467	0.0176
162	DGR-035 CAI 1 plagioclase 4	0.0608	0.0541	0.0465	0.0421	0.0498	0.0255	0.0404	0.0243	0.0338	0.0510	0.0174
163	DGR-035 CAI 1 plagioclase 5	0.0625	0.0531	0.0442	0.0401	0.0461	0.0250	0.0388	0.0228	0.0284	0.0596	0.0168
164	DGR-035 CAI 1 gehlenite 1 (actually grossular)	0.0588	0.0515	0.0493	0.0476	0.0507	0.0271	0.0420	0.0254	0.0360	0.0483	0.0184
165	DGR-034 chondrule 1 plagioclase 1	0.0605	0.0572	0.0474	0.0444	0.0466	0.0251	0.0371	0.0241	0.0332	0.0458	0.0173
166	DGR-034 chondrule 1 plagioclase 2	0.0610	0.0556	0.0468	0.0441	0.0453	0.0256	0.0407	0.0234	0.0341	0.0494	0.0175
167	DGR-034 CAI 1 plagioclase 1	0.0634	0.0569	0.0470	0.0436	0.0456	0.0251	0.0397	0.0245	0.0349	0.0459	0.0180
168	DGR-034 CAI 1 plagioclase 2	0.0631	0.0564	0.0463	0.0448	0.0467	0.0267	0.0386	0.0246	0.0340	0.0461	0.0172
169	DGR-034 CAI 1 plagioclase 3	0.0609	0.0595	0.0472	0.0432	0.0470	0.0259	0.0402	0.0236	0.0354	0.0445	0.0170
170	DGR-034 chondrule 3 plagioclase 1	0.0596	0.0591	0.0469	0.0477	0.0442	0.0257	0.0408	0.0244	0.0335	0.0464	0.0178
171	DGR-034 chondrule 3 plagioclase 2	0.0612	0.0543	0.0464	0.0458	0.0482	0.0256	0.0394	0.0246	0.0330	0.0514	0.0177
172	DGR-034 chondrule 5 plagioclase 1	0.0616	0.0572	0.0471	0.0411	0.0424	0.0253	0.0382	0.0252	0.0328	0.0472	0.0165
173	DGR-034 chondrule 5 plagioclase 2	0.0609	0.0588	0.0463	0.0428	0.0472	0.0257	0.0383	0.0229	0.0348	0.0476	0.0176
174	DGR-034 chondrule 5 plagioclase 3	0.0609	0.0596	0.0458	0.0421	0.0452	0.0263	0.0418	0.0244	0.0344	0.0452	0.0176
175	DGR-034 chondrule 5 plagioclase 4	0.0589	0.0548	0.0477	0.0406	0.0481	0.0255	0.0385	0.0244	0.0349	0.0529	0.0175
176	DGR-034 chondrule 5 plagioclase 5	0.0608	0.0543	0.0474	0.0468	0.0441	0.0252	0.0391	0.0242	0.0339	0.0512	0.0182
177	DGR-035 matrix 2 plagioclase 1	0.0603	0.0545	0.0448	0.0443	0.0418	0.0247	0.0384	0.0241	0.0306	0.0554	0.0172
178	DGR-035 matrix 2 plagioclase 2	0.0601	0.0529	0.0463	0.0448	0.0443	0.0247	0.0387	0.0229	0.0312	0.0581	0.0171
179	DGR-035 matrix 2 plagioclase 3	0.0628	0.0515	0.0449	0.0425	0.0457	0.0242	0.0412	0.0232	0.0315	0.0535	0.0171
180	DGR-035 matrix 2 plagioclase 4	0.0619	0.0571	0.0465	0.0427	0.0447	0.0251	0.0385	0.0235	0.0322	0.0562	0.0169
181	DGR-035 matrix 2 plagioclase 5	0.0622	0.0545	0.0431	0.0408	0.0415	0.0251	0.0368	0.0228	0.0323	0.0587	0.0173
182	DGR-035 matrix 2 plagioclase 6	0.0600	0.0538	0.0454	0.0419	0.0450	0.0251	0.0373	0.0236	0.0326	0.0578	0.0167
183	DGR-035 matrix 2 plagioclase 7	0.0631	0.0535	0.0456	0.0415	0.0418	0.0246	0.0384	0.0233	0.0316	0.0563	0.0166
184	DGR-034 chondrule 6 plagioclase 1	0.0619	0.0539	0.0474	0.0406	0.0458	0.0261	0.0427	0.0243	0.0318	0.0511	0.0172
185	DGR-034 chondrule 6 plagioclase 2	0.0620	0.0573	0.0466	0.0416	0.0465	0.0249	0.0370	0.0243	0.0340	0.0505	0.0173
186	DGR-034 chondrule 6 plagioclase 3	0.0621	0.0557	0.0470	0.0435	0.0494	0.0259	0.0401	0.0240	0.0323	0.0518	0.0174
187	DGR-034 chondrule 6 plagioclase 4	0.0623	0.0558	0.0460	0.0418	0.0481	0.0253	0.0391	0.0236	0.0326	0.0520	0.0185

Figure 116: Plagioclase limit of detection point results from EPMA. Results highlighted were not used due to error.

DGR-035	Max	Average	Mean Deviation	Chondrule Average	Matrix Average	CAI Average
fa	35.488%	20.83%	11.343%	16.842%	34.485%	30.244%
fo	99.663%	79.171%	11.343%	83.158%	65.515%	69.756%
DGR-034	Max	Average	Mean Deviation	Chondrule Average	Matrix Average	CAI Average
fa	51.905%	23.544%	18.301%	15.834%	45.816%	0.000%
fo	99.642%	76.456%	18.301%	84.166%	54.184%	0.000%

Figure 117: Olivine end member (forsterite-fayalite) results reported in mol% from EPMA analyses.

DGR-035	Max	Average	Mean Deviation	Chondrule Average	Matrix Average	CAI Average
fs	23.057%	9.440%	5.784%	5.722%	0.000%	22.454%
En	98.272%	86.863%	6.500%	89.758%	0.000%	76.730%
Wo	15.311%	3.697%	2.609%	4.521%	0.000%	0.816%
DGR-034	Max	Average	Mean Deviation	Chondrule Average	Matrix Average	CAI Average
fs	41.429%	5.020%	5.027%	5.020%	0.000%	0.000%
En	98.412%	91.663%	6.954%	91.663%	0.000%	0.000%
Wo	8.454%	3.318%	1.929%	3.318%	0.000%	0.000%

Figure 118: Orthopyroxene end member (ferrosilite-enstatite-wollastonite) results reported in mol% from EPMA analyses.

DGR-035	Max	Average	Mean Deviation	Chondrule Average	Matrix Average	CAI Average
An	99.901%	42.413%	19.651%	38.623%	31.907%	68.625%
Ab	78.148%	56.471%	19.210%	60.014%	66.873%	30.908%
Or	2.166%	1.115%	0.523%	1.363%	1.221%	0.467%

DGR-034	Max	Average	Mean Deviation	Chondrule Average	Matrix Average	CAI Average
An	99.457%	85.865%	5.620%	82.816%	0.000%	99.080%
Ab	20.964%	14.109%	5.623%	17.162%	0.000%	0.881%
Or	0.119%	0.026%	0.032%	0.022%	0.000%	0.040%

Figure 119: Clinopyroxene end member (clinoferrosilite-clinoenstatite-wollastonite) results reported in mol% from EPMA analyses.

DGR-035	Max	Average	Mean Deviation	Chondrule Average	Matrix Average	CAI Average
An	99.901%	42.413%	19.651%	38.623%	31.907%	68.625%
Ab	78.148%	56.471%	19.210%	60.014%	66.873%	30.908%
Or	2.166%	1.115%	0.523%	1.363%	1.221%	0.467%

DGR-034	Max	Average	Mean Deviation	Chondrule Average	Matrix Average	CAI Average
An	99.457%	85.865%	5.620%	82.816%	0.000%	99.080%
Ab	20.964%	14.109%	5.623%	17.162%	0.000%	0.881%
Or	0.119%	0.026%	0.032%	0.022%	0.000%	0.040%

Figure 120: Plagioclase end member (anorthite-albite-orthoclase) results reported in mol% from EPMA analyses.